The Warm-Hot Circumgalactic Medium and its Co-Evolution with the Galaxy Disk

by

Zhijie Qu

A dissertation submitted in partial fulfillment
of the requirements for the degree of
Doctor of Philosophy
(Astronomy and Astrophysics)
in The University of Michigan
2021

Doctoral Committee:

Professor Joel N. Bregman, Chair
Professor Eric F. Bell
Professor August E. Evrard
Associate Professor Christopher J. Miller

Zhijie Qu

quzhijie@umich.edu

ORCID iD: 0000-0002-2941-646X

To my parents, my teachers, and friends.

ACKNOWLEDGEMENTS

First of all, I would like to express my greatest gratitude to my advisor Joel Bregman for his tremendous support and patient guidance during my entire Ph.D. journey. Joel provided me many opportunities to explore different directions and gave me complete freedom to choose projects to work on. I also really enjoyed all the thoughtful discussions in front of the whiteboard in his office. Unfortunately, the last in-person meeting with him was mostly one and half years ago because of the COVID-19. During the pandemic, we have many virtual meetings, but I wish we could have in-person meetings before I leave Ann Arbor.

Joel not only guided me on how to be a good researcher, but also other skills and capabilities benefiting my further career, such as how to mentor students, and even how to write a promotion recommendation letter for others as a senior professor. He also instructed me on how to interact with collaborators, how to write papers by patiently going through my draft manuscripts with me, and how to make good presentations by helping me prepare the slides.

I greatly thank my dissertation committee members, Eric Bell, Gus Evrard, and Chris Miller, for their thoughtful suggestions in every committee meeting. They have also always been very responsible to make sure that I made enough progress and could succeed to finish the degree.

I am very grateful to have Jiangtao Li and Edmund Hodges-Kluck as my major collaborators and academic siblings. They always provided helpful discussions and suggestions on multi-wavelength observations related to my projects in our group

meetings. I also want to thank many colleagues, especially Hsiao-Wen Chen, Sean Johnson, Chris Howk, Nicolas Lehner, Benjamin Oppenheimer, Yong Zheng, Blair Savage, Bart Wakker, and Phil Kaaret for their supports in the field.

The University of Michigan Astronomy Department has given me the greatest opportunity to grow and mature into a junior researcher. I want to thank the faculty here for creating an encouraging and friendly academic environment. I really appreciate the timely and professional supports from the IT, the admin staff in the department, the LSA, and the International Center. I also thank my classmates, Ryan Farber, Adi Foord, Adam Smercina, and Renee Ludlam for their company in the department. It was a great time to have classes, discussions, and work on homework together.

I feel sincerely fortunate to be loved and supported by my Chinese friends Wenzheng Shi, Jiabing Huang, Siyao Jia, Mengxiao Lin, Ping Chen, Yimeng Liu, Yuguang Chen, and many many across the world. Especially, I would like to express special thank to friends made at Ann Arbor, Song Yiying, Hui Li, Jiangtao Li, Xi Meng, Rongxin Lin, Ke Zhang, Shen Li, Fujun Du, Hang Yang, Rui Huang, Xu Liu, and Zhuangyuan Yin, who make the past six years so enjoyable.

At last, but not least, I would like to genuinely thank my parents, Min Xie and Youqiang Qu. They are warmhearted, diligent, and trustworthy. They are the kind of people I want to become. They have also given me tremendous love and support all the years. They always say to me that "Do whatever makes you happy and we will always be there for you". No words can ever fully express my gratitude for their unconditional support.

This dissertation is financially supported by NASA ADAP grants NNX15AM93G, NNX16AF23G, and 80NSSC19K1013, NASA *HST* grants HST-GO-12904 and HST-AR-15806. I also would like to acknowledge the support of the Rackham One-Term Dissertation Fellowship, the Rackham Travel Grant, and the Department of Astron-

omy Graduate Research Grant at the University of Michigan.

Zhijie Qu Ann Arbor, Michigan

TABLE OF CONTENTS

LIST OF FIGURES

Figure

LIST OF TABLES

Table

ABSTRACT

In the past decade, multi-wavelength observations revealed that the galaxy disk is surrounded by a massive, low-density, and multi-phase gaseous medium – the circumgalactic medium (CGM; see the review by Tumlinson et al. 2017). This massive baryon reservoir feeds galaxy growth through the accretion of radiatively cooling gas, which fuels star formation in the disk. Stellar feedback in the disk ejects metals, momentum, and energy into and beyond the CGM. These feedback and accretion processes are the most uncertain pieces in our picture of galaxy evolution. These processes can be constrained by the properties of the CGM surrounding the galaxy, because the CGM is co-evolving with the disk. This dissertation focuses on observations of the warm-hot CGM at low redshift $z \lesssim 1$ and its connection with galactic disks.

The warm-hot CGM is observed in multi-wavelength bands including the ultraviolet (UV), the X-ray, and the Sunyaev-Zeldovich (SZ). Using archival UV spectra, I studied the warm gas in the Milky Way (MW) and a nearby galaxy NGC 891 traced by intermediate ionization state ions (e.g., Si IV and O VI). For the MW, I developed a kinematical model, which could constrain both the density distribution and the bulk velocity field of the warm gas simultaneously. We applied this model to the line shape sample of Si IV absorption lines, and found that most observed column densities are close to the disk ($d < 20$ kpc) rather than at large radii. This spatial distribution leads to a total warm gas mass of $\log_{10} M/M_{\odot} \approx 9$ around the MW disk, which is about one order of magnitude lower than the hot gas mass in the MW measured in the X-ray band. However, the warm gas has a short lifetime, leading to rapid

radiative cooling, so it has more active interactions with the disk. The net accretion of the warm gas is detected in the northern hemisphere with a mass accretion rate comparable to the star formation rate in the MW disk. Galactic fountain features are seen in the warm gas disk, which is co-rotating with the stellar disk. Similarly, in NGC 891, inflows and outflows are also detected close to the disk. These phenomena suggest that the warm gas is dominated by feedback originating from the disk.

I also developed a new extraction method for the large-scale SZ features aiming at the hot gas in the local universe (i.e., the MW and the Local Group). This method was applied to the archival *Planck* and *WMAP* data, which led to the discovery of a massive hot bridge connecting the MW and M31. This structure is also confirmed in X-ray emission after subtracting the MW hot halo contribution. This method will be further developed in the future to detect the MW contribution to the SZ signal by suppressing dust contamination.

To understand the connection between the warm-hot CGM and the disk, I developed a semi-analytic model, which assumes that the star formation is supplied by accretion from radiative cooling of the hot CGM. In this theoretical model, the star formation in the disk is balanced by the net accretion rate from the CGM, which is also modified by photoionization and stellar feedback. For the cooling flow, we consider a stable solution, where the mass cooling rate is a constant over all temperatures. The derived temperature distribution could match various observations of galaxy-absorber pairs at different redshifts: O VII and O VIII at $z = 0$ (MW); O VI absorption at $z \approx 0.2$; Ne VIII and Mg X at $z \approx 1$. By combining this model with the spatial distribution of galaxies, I predict the observed cosmic column density distribution for these high ionization state ions. In this model, most high column density absorption systems are associated with the warm-hot CGM, by comparing the model prediction to the measured cosmic column density distribution for UV ions (e.g., O VI and Ne VIII). However, the model prediction underestimates the detection

rate of low column density absorption systems (e.g., log $N \lesssim 13.5$ for O VI), which suggests that these systems are hosted by unvirialized dark matter structures (e.g., cosmic filaments).

CHAPTER I

Introduction

1.1 Missing Baryons and the Circumgalactic Medium

In one galaxy, the most prominent component is the visible galaxy disk, which contains millions of stars. However, the galaxy disk only occupies a small volume of the galaxy compared to the galaxy dark matter halo, where the galaxy disk is formed. Then, questions raise as whether there is normal material beyond the disk within the dark matter halo, and how much? These questions are hard to answer, but one could find some hints in the stellar mass-halo mass relationship (Fig. 1.1; Behroozi et al. 2019). This fundamental relationship has been extensively explored in the past decades, which revealed that the disk baryonic fraction is not a constant for all galaxies (i.e., the mass ratio between the baryons in the disk and the dark matter halo). Among all galaxies, Milky-Way-like (MW-like) galaxies have the highest disk baryonic fraction of $\approx 4\%$, while some low mass galaxies are lower than 1% (Behroozi et al., 2019). Therefore, at least some galaxies (low-mass and massive galaxies) are missing some of their baryons in the galaxy disk.

However, it became clear that all galaxies are missing their baryons in the disk, thanks to the development of the Λ-CDM cosmology in the past decades. With more and more constraints, the cosmic baryonic fraction is determined to be $16-17\%$ in the Universe (Planck Collaboration et al., 2020), the remainder being dark matter. This

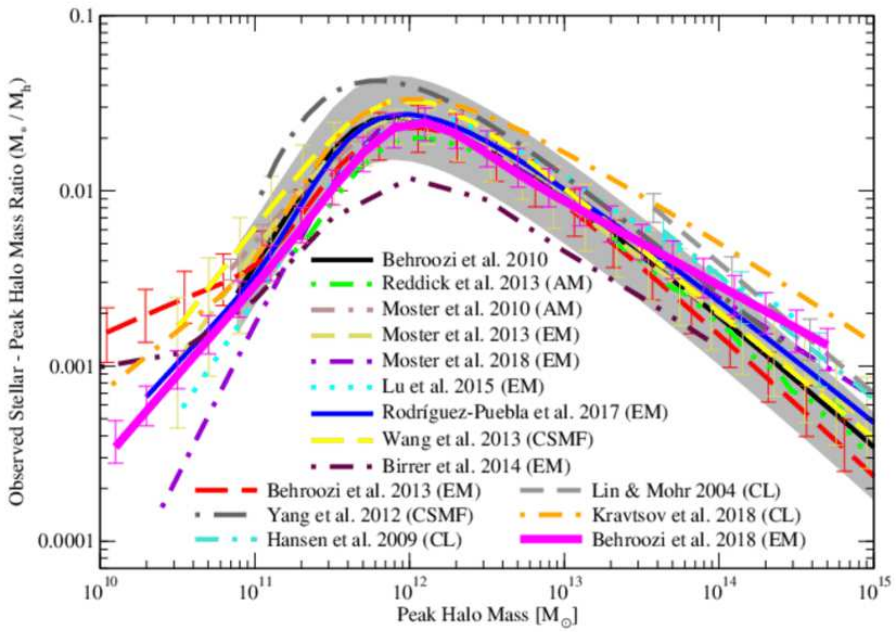

Figure 1.1: The stellar mass-halo mass relationship adopted from Behroozi et al. (2019). The stellar mass-halo mass ratio is not a constant over all galaxies. The Milky Way is at the peak of this relationship with a ratio of 0.04. However, the Λ-CDM cosmology suggests the cosmic average baryonic fraction is 0.168 (Planck Collaboration et al., 2020), so there is a significant gap between the baryonic fraction in the galaxy disk and the cosmic average. Therefore, lots of baryons are missing in the disk, which may be detected in the dark matter halo as the circumgalactic medium.

cosmic baryonic fraction is about four times higher than the peak of the stellar mass-halo mass ratio (Fig. 1.1 and Table 1.1). For example, the expected total baryon mass is $\approx 3 \times 10^{11} M_{\odot}$ for a MW-like galaxy with a halo mass of $\approx 2 \times 10^{12} M_{\odot}$. However, the total baryons in the disk is about $8 \times 10^{10} M_{\odot}$ by adding the stellar mass and the interstellar medium (ISM) mass, so $\approx 70\%$ of the baryons are missing from the disk (e.g., McGaugh et al., 2010; Bregman, 2007; Bregman et al., 2018).

One solution to the missing baryon problem is that there is an invisible gaseous component beyond the disk but within the dark matter halo of the galaxy. This invisible gaseous halo component is also known as the circumgalactic medium (CGM; Putman et al. 2012; Tumlinson et al. 2017). However, due to the observational diffi-

Table 1.1: The Baryon Budget in the Galaxy

Component	Dwarf Galaxy $M_\odot$	L^* Galaxy (MW-like) $M_\odot$	Galaxy Cluster $M_\odot$
Dark Matter Halo	10^{11}	10^{12}	10^{14}
Galaxy Disk	10^8	5×10^{10}	3×10^{11}
CGM/ICM [a]	...[b]	$(1-10) \times 10^{10} M_\odot$	10^{13}

[a] The circumgalactic medium (CGM) is the gaseous component surround the dwarf galaxy and the L^* galaxy. For the galaxy cluster, the gas within the dark matter is between the galaxy members, so it may be beyond dark matter halos of individual galaxies. [b] Studies on the CGM of dwarf are still preliminary without a census of multi-phase medium in the CGM of the dwarf galaxy.

culty, it is still of great uncertainty that whether the CGM can make up for all of the missing baryons. Some studies argued that all of missing baryons are within the typical boundary of the halo (the virial radius; §1.2.1). Meanwhile, other studies argued that the gas is expelled beyond the galaxy dark matter halo by feedback originating from the disk, then there is an intrinsic deficit of baryons in the galaxy. Despite these controversies, the CGM is found to be massive ($> 10^{10} M_\odot$) for L^* galaxies, and it is more massive for a more massive halo (i.e., the hot gas accounts for $> 95\%$ of the total baryons in the richest clusters with halo masses of $\approx 10^{15} M_\odot$).

Recent observations revealed that the CGM is multi-phase, covering a wide temperature range from the dust and molecular gas ($\lesssim$ 100 K), the cool neutral gas ($\approx 10^3$ K), the cool ionized gas ($\approx 10^4$ K), the warm gas ($\approx 10^5$), and the hot gas ($\gtrsim 10^6$ K; §1.2.2; also see the review in Tumlinson et al. 2017 and reference therein). The hot gas is believed to be the equilibrium phase balancing the thermal pressure and the gravity (Mo et al., 2010), so it is buoyant in the dark matter halo. The lower temperature phases cannot be buoyant, so they will be outflowing ejected by feedback from the disk or inflowing accreted from CGM or surrounding intergalactic medium (IGM; §1.2.3). However, the temperature distribution of the CGM is of a great uncertainty. Among all of the phases, the warm-hot component is the most uncertain part, which is limited by instruments. In this dissertation, I develop models

and methods to constrain warm-hot CGM properties mainly in the local Universe, and investigate the connection between the disk and the warm-hot CGM.

1.2 The CGM-Disk Co-Evolution

The CGM is actively interacting with the disk, which has two types of processes – feedback and accretion. Baryonic interactions in the disk (e.g., stellar wind and supernovae) could eject materials (and metals), energy, and momentum beyond the disk, thus affecting the surrounding environment of the disk (including the CGM and IGM). Feedback processes can be manifested in various ways, such as photoionization by escaping ionizing flux (Wakker et al., 2015), galactic winds (e.g., Thompson et al., 2016; Fielding et al., 2017a,b; Li & Tonnesen, 2020; Li & Bryan, 2020), galactic fountains (e.g., Bregman, 1980; Kim & Ostriker, 2018), and active galactic nucleus (AGN) feedback (Li et al., 2015; Gaspari et al., 2017; Prasad et al., 2020; Voit et al., 2020). The accretion processes include two steps – accretion from the IGM into the CGM and accretion from the CGM onto the disk. In the first step, the accreted materials may be heated up to a maximum temperature (the virial temperature; §1.2.1), which leads to accretion shocks (e.g., Ryu et al., 2003). Radiative cooling in the CGM leads to accretion onto the disk, which has two modes – the hot mode and the cold mode (described in §1.2.3; Kereš et al. 2005, 2009; Nelson et al. 2013). These interactions are summarized in Fig. 5.4.

Currently, these interaction processes are still uncertain in both theory and observation. As one of the most important parts of the baryonic cycle in galaxy evolution, the uncertainty in interaction processes leads to uncertainty in understanding of galaxy evolution – such as how does galaxy sustain its star formation, how does a galaxy lose its baryons, and what quenches a star-forming galaxy? These processes are imprinted in the CGM, motivating observational and theoretical studies. In this section, I introduce why the CGM should exist and how it co-evolves with the disk.

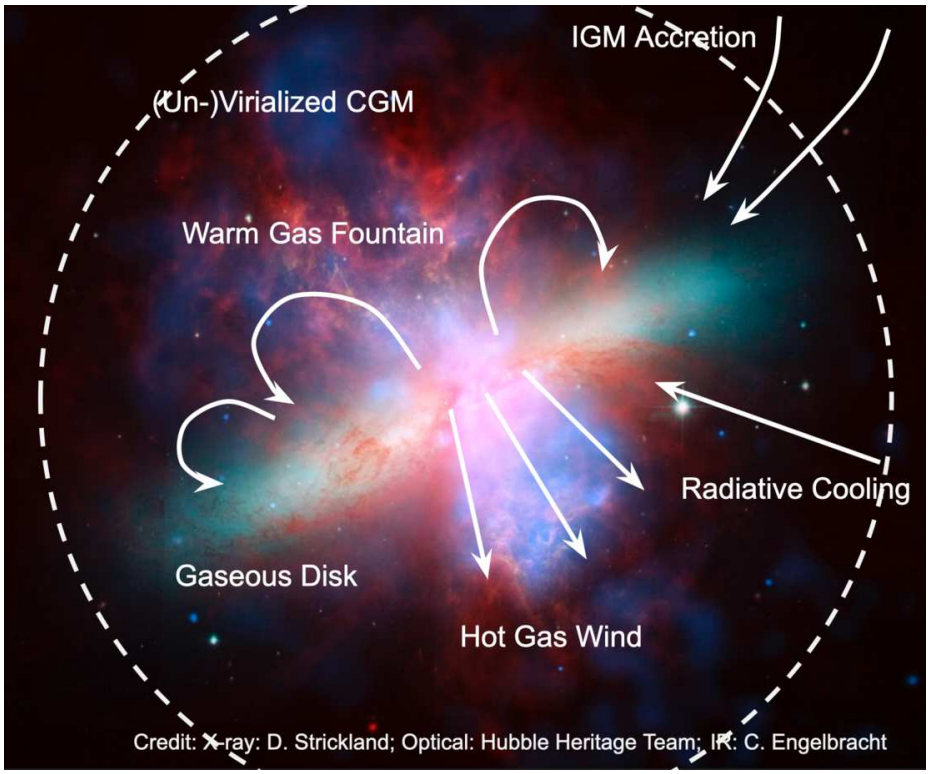

Figure 1.2: This figure is adopted from NASA/CXC gallery with multi-wavelength data from NASA/CXC/JHU/D.Strickland; Optical: NASA/ESA/ STScI/AURA/The Hubble Heritage Team; IR: NASA/JPL-Caltech/ Univ. of AZ/C. Engelbracht. The dashed circle represents the size of the CGM (not scaled; the CGM should be $10-20$ times larger than the disk). The CGM feeds the disk through radiative cooling, and prevent direct accretion from IGM. The feedback from the disk modulates the surrounding CGM and nearby IGM through gaseous fountains and galactic winds depending on whether the ejected gas can leave the dark matter halo potential.

1.2.1 The Virialized Hot Halo

Galaxy (halo) formation is driven by evolution of the dark matter density perturbation. In the early universe, density perturbations grow linearly until they reach a critical density, after which they collapse to form virialized dark matter halos (Mo et al., 2010). This collapse will stop when it reaches another critical density as it becomes virialized, as suggested by the virial theorem. Finally, the gas in the CGM reaches a hydrostatic equilibrium phase, but it may deviate from this equilibrium state due to inevitable radiative cooling and possible heating from the disk (described in §1.2.2 and §1.2.3).

The critical density of the virial equilibrium is about 200 times the cosmic critical density ($\rho_{\rm crit}$): $\rho_\Delta = \Delta_{\rm vir}\rho_{\rm crit}$, where $\Delta_{\rm vir}$ is about 200. Therefore, we will determine the characteristic size of the dark matter halo as

$$R_{\rm vir}^3 = R_{200}^3 = \frac{M_{\rm h}}{4\pi\Delta_{\rm vir}\rho_{\rm crit}/3}, \tag{1.1}$$

where $M_{\rm h}$ is the dark matter halo mass. Then, the circular velocity of the dark matter halo at the boundary is derived as

$$V_{\rm c}^2 = \frac{GM_{\rm h}}{R_{\rm vir}} = 100H_0^2R_{\rm vir}^2, \tag{1.2}$$

where H_0 is the Hubble constant.

The virial temperature is calculated by adopting the virial theorem, where the gravitational potential (U) of the system is balanced by twice its internal thermal energy (E) and the work done by the system surface (W): $U + 2E + W = 0$. This calculation involves the density distribution of the dark matter halo. For an order-of-magnitude estimation, a uniform spatial distribution within a sphere is assumed

to calculate the gravitational potential

$$U = -\frac{3}{5}\frac{GM_{\rm h}M_{\rm gas}}{R_{\rm vir}}. \tag{1.3}$$

The internal thermal energy is calculated under the isothermal assumption:

$$E = \frac{3}{2}\frac{M_{\rm gas}}{\mu m_{\rm p}}k_{\rm B}T, \tag{1.4}$$

where μ is the mean weight (in the units of the hydrogen mass per particle), T is a constant temperature, and $k_{\rm B}$ is the Boltzmann constant. Then, the derived virial temperature is

$$T_{\rm vir} = \frac{\mu m_{\rm p}}{5k_{\rm B}}V_{\rm c}^2, \tag{1.5}$$

when the work W is zero.

A more realistic case is assuming that the dark matter halo follows the singular isothermal sphere (Mo et al., 2010), where the dark matter density distribution and the corresponding U are

$$\begin{aligned} \rho(r) &= \frac{V_{\rm c}^2}{4\pi G r^2}, \\ U &= -V_{\rm c}^2 M_{\rm gas} \end{aligned} \tag{1.6}$$

The work done by the system is calculated by integrating the surface pressure

$$W = -\int_0^{R_{\rm vir}} \rho(r)\frac{k_{\rm B}T}{\mu m_{\rm p}}4\pi r^2 {\rm d}r = -M_{\rm gas}\frac{k_{\rm B}T}{\mu m_{\rm p}}. \tag{1.7}$$

Substituting W and U into $U + 2E + W = 0$, the derived virial temperature is

$$T_{\rm vir} = \frac{\mu m_{\rm p}}{2k_{\rm B}}V_{\rm c}^2 = 1.4 \times 10^6 {\rm K}\left(\frac{V_{\rm c}}{200\ {\rm km\ s^{-1}}}\right)^2, \tag{1.8}$$

where 200 km s^{-1} is the typical circular velocity of L^* galaxies.

Therefore, the virial theorem suggests the existence of a hot halo with a temperature higher than 10^6 K for an L^* galaxy. The typical density of the hot halo is $\Omega_{\rm b}\rho_{\rm vir}\Delta_{\rm vir} \approx 5 \times 10^{-5}$ $\rm cm^{-3}$, where $\Omega_{\rm b} = 0.0486$ is the cosmic baryonic fraction (Planck Collaboration et al., 2020). Combining these values together, the radiative cooling timescale of the hot gas is longer than 10 Gyr. If there is no other processes, the hot halo is expected to be stable during the Hubble time ($\approx$ 13 Gyr).

1.2.2 The Multi-Phase Medium

Although the virial theorem predicts that all gas in the CGM will be virialized to the hot phase for a L^* galaxy, feedback and accretion processes induce perturbations leading to a multi-phase CGM medium. These interaction processes can trigger thermal or gravitational instabilities, which generate high-density clouds, which can cool down rapidly and form cooler gas. The multi-phase medium has been detected in multi-wavelength bands, and different phases are associated with different processes. In this section, I summarize the existing efforts in the observation of multi-phase medium from the lowest to the highest temperature phase.

1.2.2.1 The Cold and Cool Medium

Normally, the cold gas cannot be buoyant in the CGM because of its high density. For example, the MW cold gas thin disk (e.g., CO gas) has a scale height of ≈ 0.1 kpc, which is much smaller than the warm gas (e.g., Si IV and C IV) of $3 - 4$ kpc (Savage & Wakker, 2009). However, energetic feedback may expel the cold gas from the disk into the CGM.

In the CGM, the cold phase is detected as the dust and molecular gas that have temperatures of $\lesssim 100$ K. This circumgalactic dust has been detected in both the low redshift universe at $z \lesssim 0.5$ or at high redshift of $z \approx 3 - 4$ (e.g., Ménard

et al., 2010; Ginolfi et al., 2017; Falkendal et al., 2021). By analyzing the color cross-correlation between galaxies and background QSOs, Ménard et al. (2010) found that the CGM dust can extend to several Mpc (also see Smith et al. 2016a, who argued this circumgalactic dust is due to nearby galaxies). This extended dust CGM is believed to be launched from the interstellar medium by energetic super-galactic winds (Leroy et al., 2015). In turn, the existence of the dust in the CGM is also suggested to provide a large radiation cross-section to launch super-galactic winds (Murray et al., 2011).

With a higher temperature, the cool gas ($T \approx 10^4$ K) may be the radiatively cooled-down gas from the hot halo or directly accretion from the IGM. However, the fate of the cool gas is of a large uncertainty in both observation and theory. As shown in Fig. 7.1, the radiative cooling rate of the cool gas drops dramatically at lower temperature, and sometimes it can even be in a radiative heating phase if photoionization is considered. In this case, the cool gas could be a long lifetime phase, when photoionization is sufficient (i.e., the density is low) to balance radiative cooling (Werk et al., 2014), or it may lead to significant accretion onto the disk of $\approx 100 M_\odot$ yr^{-1} in some studies (e.g., McQuinn & Werk, 2018). However, different scenarios lead to controversy of the total mass of the cool gas in the CGM. Some studies argued a massive cool CGM with a mass of $\log M(M_\odot) \approx 11$ for L^* galaxies, which is the dominant mass contributor in the CGM (Prochaska et al., 2017). There are other studies suggested a lower mass for the cool phase of $\log M \approx 10$ for the MW and M31 (e.g., Lehner et al., 2015; Zheng et al., 2019a; Lehner et al., 2020).

Observationally, the cool gas ($\approx 10^3 - 10^{4.5}$ K) can be traced by low ionization state ions, such as H I, and various metal ions (e.g., Mg II, Fe II, and C II). These ions can be detected in different bands at a wide range of redshifts.

In the local universe, the H I 21 cm line is mainly detected in emission for strong diffuse H I systems ($\log N_{\rm HI} \gtrsim 18$ and angular size of $\gtrsim 10'$; e.g., Oosterloo et al. 2007;

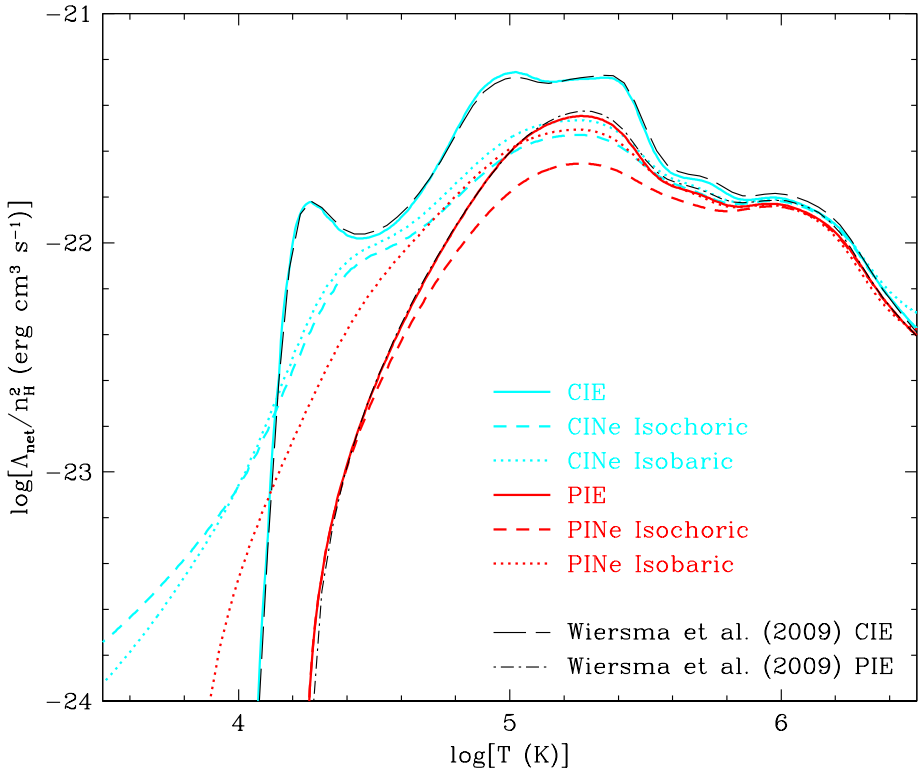

Figure 1.3: The optically thin radiative cooling curve adopted from Oppenheimer & Schaye (2013). Collisional ionization dominates the curves at high temperatures $T \gtrsim 10^6$ K, while photoionization significantly modulates the low temperature phase ($T \lesssim 10^5$ K). At low-temperature phases (the cool gas at$T \approx 10^3 - 10^4$ K), the gas is in purely heating phase, which makes the gas have long-lifetime. At high temperature ($T > 10^6$ K), the cooling timescale is long (even longer than Hubble time in some cases) combining the low emissivity and the low density. Because of its long lifetime and low density, the hot gas is expected to be the ambient phase filling in the CGM. Between the cool and the hot gases, the warm gas ($T \approx 10^5$) has the highest emissivity, which makes it short-lifetime. Therefore, the warm gas is a great tracer for interaction processes, such as accretion and feedback between the disk and the CGM.

Kalberla & Dedes 2008; Marasco & Fraternali 2011). With recent improvements of radio telescope, strong H I 21 cm absorption lines ($\log N_{\rm HI} > 20$) can be detected against background radio sources (e.g., Zhang et al. 2021a; also see non-detection of intervening H I 21 cm absorption lines in Darling et al. 2011)

At low redshift of $z < 0.5$, against rest-frame UV-bright background sources, extensive studies have focused on absorption lines of H I Lyα and associated metal lines mainly using the *FUSE* telescope, the *Hubble Space Telescope*/Cosmic Origin Spectroscopy (*HST*/COS), and STIS (e.g., Stocke et al., 2013; Borthakur et al., 2015; Zahedy et al., 2016; Johnson et al., 2015; Keeney et al., 2017; Burchett et al., 2019), and at high redshift of $z \approx 0.5-6$ using ground-based optical telescopes (e.g., Muzahid et al., 2016a; Rubin et al., 2018; Simcoe et al., 2020). These studies investigated the CGM and galaxy connection in different environments such as normal spirals (Stocke et al., 2013; Werk et al., 2014), high-z star forming galaxies (Chen et al., 2020b), large red galaxies (Lan & Mo, 2018; Zahedy et al., 2019), dwarf galaxies (Bordoloi et al., 2014; Johnson et al., 2017; Zheng et al., 2019b, 2020), and even member galaxies in galaxy groups and clusters (Yoon et al., 2012; Stocke et al., 2014; Yoon & Putman, 2017; Burchett et al., 2018).

The development of integral field spectroscopy in the past decade make it possible to observe the low-temperature CGM in emission at moderate redshift of $z \approx 2-5$ (shifting UV lines into optical). Surrounding star-forming galaxies or bright QSOs, giant Lyα nebulae are illuminated by ionizing flux from the disk (e.g., Arrigoni Battaia et al., 2018; Cantalupo et al., 2019; Cai et al., 2019; O'Sullivan et al., 2020; Chen et al., 2021). Sometimes, the Lyα nebulae have associated warm gas clouds traced by higher ionization state ions (e.g., C IV) indicating a warm-hot CGM (Guo et al., 2020; Travascio et al., 2020). It is also possible to trace cool gas filaments accreted into the dark matter halo (Martin et al., 2019).

1.2.2.2 The Warm and Hot Medium

As introduced in §1.2.1, the hot gas in the CGM is expected to be low-density, so it has a long lifetime considering the low radiative cooling rate. Therefore, it is predicted to be the volume-filling phase in the CGM of a L^* galaxy (Bregman, 2007). Different from the hot gas, the warm gas has a temperature around the peak of the radiative cooling curve (Fig. 7.1), which leads to short cooling timescales of $\lesssim 10$ Myr around $\log T \approx 5$. Therefore, the observed warm gas in the CGM should be refreshed frequently by various interaction processes (e.g., accretion shocks and galactic fountains; Bregman 1980).

There are four bands to detect the warm-hot CGM, mainly in the high-energy band. First, the warm-hot gas can be detected in the UV band traced by intermediate to high ionization state ions, such as Si IV ($\log T \approx 4.8$; e.g., Zheng et al. 2019a), C IV ($\log T \approx 5.0$; e.g., Burchett et al. 2015; Yu et al. 2021), O VI ($\log T \approx 5.5$; e.g., Shull & Slavin 1994; Savage et al. 2003; Sembach et al. 2003; Shull et al. 2009; Savage & Wakker 2009; Wakker et al. 2012; Savage et al. 2014), Ne VIII ($\log T \approx 5.8$; e.g., Savage et al. 2005; Mulchaey & Chen 2009; Narayanan et al. 2011; Muzahid et al. 2012b,a; Burchett et al. 2019), and Mg X ($\log T \approx 6.1$; Qu & Bregman 2016).

Second, absorption or emission in the X-ray band are adopted to characterize gas with temperature of $\log T > 6$ traced by O VII and O VIII. For the MW, X-ray observations revealed the existence of an extended hot halo surrounding the disk in both emission and absorption (e.g. Henley & Shelton, 2012; Gupta et al., 2012; Henley & Shelton, 2013; Fang et al., 2015; Miller & Bregman, 2015; Nevalainen et al., 2017; Luo et al., 2018; Kaaret et al., 2020). A recent study revealed the existence of two huge X-ray bubbles ≈ 10 kpc around the MW Galactic center, known as the eROSITA Bubble (Predehl et al., 2020). X-ray observations on external galaxies are mostly in local universe limited by instruments (e.g., Anderson & Bregman, 2010; Anderson et al., 2013; Bogdán et al., 2013a; Li & Wang, 2013; Li et al., 2018a, 2019), while the

absorption is only detected for the one intervening system reported by Nicastro et al. (2018) and for a stacking study of tens of galaxies (Kovács et al., 2019).

The γ-ray emission is another way to detect the hot gas, but mainly for the MW and nearby structures (e.g., M31). The most famous γ-ray detection of the hot gas is the Fermi Bubble in the MW (Su et al., 2010), which can be modeled as a shock-induced remnant by past AGN activities (Li et al., 2015; Miller & Bregman, 2016). Recently, it is also suggested that the hot halo can be constrained by the γ-ray photons produced in interactions between high-energy cosmic rays with baryons in the halo of the MW or M31 (Liu et al., 2019; Karwin et al., 2019, 2021; Zhang et al., 2021b).

The last means to detect the hot gas is through the Sunyaev-Zeldovich (SZ) effect. The thermal SZ effect occurs when the hot gas up-scatters cosmic microwave background (CMB) photons, which creates a decrement relative to the CMB black-body at low frequencies and an excess at higher frequencies (Rephaeli, 1995). The amount of scattering along a line of sight is proportional to the integral of the electron pressure $P_{\rm e} = n_{\rm e}kT$. Previous efforts mainly focused on distant galaxy clusters (mostly point sources) using the *Planck* telescope, ACT, and SPT (Planck Collaboration et al., 2013, 2016b,c; Hilton et al., 2021). Recently, it became clear that archival data can also be used to study nearby galaxies or galaxy groups (Pratt et al., 2021), and the hot gas within the Local Group (Qu et al., 2021).

1.2.3 Accretion and Feedback – Inflows and Outflows

Simulations predict that there are two accretion modes from the IGM to the disk – the hot mode and the cold mode (Kereš et al., 2005; Nelson et al., 2013). These two accretion modes are distinguished by whether the accreted cool IGM is heated to the virial temperature during accretion. In the hot mode, the IGM was shock-heated at about the virial radius, and mixed with the hot CGM. The accreted gas on the disk has cooled-down from the hot CGM. In the cold mode, the cold IGM was never

heated up to the virial temperature, so it kept cold in the galaxy halo before it fell onto the disk. The cold mode is predicted to be more significant at high redshifts, which may be detected in observations (e.g., Martin et al., 2019), while the hot mode dominates the local universe (Nelson et al., 2013).

Another question on accretion is how does the accreted gas fall onto the disk. Some simulations (e.g., EAGLE and TNG) predicts that most accretion occurs along the galactic XY plane (i.e., along the major axis; Péroux & Howk 2020), while Fraternali (2017) proposed another accretion model induced by galactic fountains (i.e., along the minor axis), which will affect the spatial distribution of star formation.

Stellar and AGN activities lead to feedback, modulating the CGM in various ways. When the feedback is energetic enough (e.g., star burst; M82), the ejected materials can leave the dark matter halo, leading to a deficit of baryons within the virial radius. This is known as galactic winds, which enrich the metallicity of IGM, and may be a solution to the galaxy missing baryon problem. When the ejected materials cannot leave the gravitational potential of the galaxy, it will enrich the CGM (i.e., metals and densities) and may be accreted back to the disk, which is known as the recycled gas. The combination of ejection, accretion, and recycle around the disk is sometimes referred to as the galactic fountain of baryons.

AGN feedback originates from the super-massive black hole at the galaxy center. There are two modes of AGN feedback – the quasar mode and the kinematic mode. The quasar mode provides a high radiative pressure to the surrounding gas, when the accretion rate is high. The kinematic mode is common at a low accretion rate of the black hole, which can be observed as radio jets and hot gas bubbles in the CGM or the intra-cluster medium (Su et al., 2010; Fabian, 2012; Miller & Bregman, 2016; Li et al., 2019).

To understand these uncertain processes, the kinematics of the CGM is of great importance. Observationally, inflows and outflows are detected in different phases by

measuring line centroids of various spectral lines. Using the MW as an example, the cold gas traced by H I shows a net accretion velocity of $20 - 30$ km s^{-1} (Marasco & Fraternali, 2011). The warm gas traced by Si IV and C IV shows similar accretion features but with a slightly larger velocity of ≈ 70 km s^{-1} (Fox et al., 2019; Zheng et al., 2019a; Qu et al., 2021). In contrast, the hot gas traced by the O VII and O VIII does not have a significant inflow or outflow (< 50 km s^{-1}; Hodges-Kluck et al. 2016b). These inflowing cool-warm gases provide a mass accretion rate of $0.5 - 1 M_{\odot}$ yr^{-1}, which is about the star formation rate of the MW. Another gas contributor of the MW halo is the accreted satellites (i.e., the Large and Small Magellanic Cloud; LMC/SMC), which will eventually supply the MW disk. There is a massive ($\log M(M_{\odot}) \approx 9$) warm gas envelope surrounding the LMC (Fox et al., 2014), which dominates the warm gas in the MW halo (Qu et al., 2020).

In the MW, outflows are mainly detected around the Galactic Center (GC; i.e., the Fermi Bubble). UV absorption line and H I 21 cm emission line studies revealed the acceleration of cold H I clouds and their warm gas envelopes (Fox et al., 2015; Bordoloi et al., 2017b; Savage et al., 2017; Karim et al., 2018; Lockman et al., 2020). These clouds were ejected by the super-massive black hole (or nuclear star burst) at the GC, and accelerated within the first 1 kpc to reach an outflow velocity of ≈ 300 km s^{-1} in the Fermi Bubble.

Similarly to the MW, inflows and outflows in external galaxies can be detected in the velocity distribution of spectral lines compared to the galaxy velocities (e.g., Leroy et al., 2015; Rubin & MaNGA Team, 2016; Chen et al., 2020a). Another method to detect feedback effects is to consider the azimuthal dependence of the gas and metal distribution (Bordoloi et al., 2011; Ho et al., 2017; Lan & Mo, 2018; Luo et al., 2021), since outflows have higher metallicities than the accreted gas from the IGM. This method is difficult to apply to the MW because of the viewing – most observed gas is close to the disk, so it is hard to observe variation of the metallicity or the gas

density at large radii.

1.3 Physical Modeling of the Warm-Hot CGM

Various models are built to connect observations with theories of the disk-CGM co-evolution. There are two types of models – numerical simulations and analytic models. Ideally, numerical simulations can include all physical processes involved in the disk-CGM co-evolution, such as feedback (winds, photoionization, cosmic rays, and radio jets), accretion, mixing of gas (turbulence), radiation, and even magnetic fields. The biggest difficulty is the large dynamic range of the these processes from sub-pc scale (mixing layer between different phases) to the Mpc scale (the size of the CGM and nearby IGM). Therefore, sub-grid models and assumptions at small scale are needed for cosmological simulations in practice, which involve extra uncertainties in the model predictions.

Currently, numerical simulations can be divided into three classes roughly based on their box sizes and associated resolutions – cosmological simulations (≈ 100 Mpc; e.g., EAGLE, Illustris, and IllustrisTNG; Vogelsberger et al. 2014; Schaye et al. 2015; Pillepich et al. 2018; Martizzi et al. 2019; Wijers et al. 2020), galaxy simulations ($\approx 1-10$ Mpc; e.g., zoomed-in EAGLE; Oppenheimer et al. 2016; Fielding et al. 2017a; Li & Tonnesen 2020), zoom-in (disk) simulations ($\approx 1-10$ kpc; e.g., Farber et al. 2018; Kim & Ostriker 2018). These simulations focus on several fundamental astrophysical questions in galaxy evolution, such as how to launch galactic winds by supernovae (e.g., Fielding et al., 2017a; Li & Tonnesen, 2020), and investigating the role of cosmic-rays in feedback (e.g. Farber et al., 2018; Ji et al., 2019b; Butsky et al., 2020). There are also technical questions, such as whether the simulation resolution affects the predictions of the CGM (Hummels et al., 2019; Peeples et al., 2019).

These simulations have agreements, but there remain lots of inconsistencies between different codes and observations. For example, the EAGLE and the Illustris

simulations predict significantly different baryonic fraction dependences on the halo mass (Schaller et al., 2015; Suresh et al., 2017). This baryonic fraction increases with more massive halos in the EAGLE simulation, while it is decreasing in the Illustris simulation. This difference is mainly due to these two simulations having different galactic wind launch prescriptions. However, testing different prescriptions is time-consuming in numerical simulations, so one needs a more effective alternative to test different prescriptions in the modeling of the CGM.

The analytic model is effective since it uses formalized relationships to describe the CGM evolution rather than to model all interaction processes. Analytic models typically focus on one dominant process to determine the first order tendency, which is different from numerical simulations implementing all processes The existing models have been focused on radiative cooling models (e.g., Bordoloi et al., 2017a; McQuinn & Werk, 2018; Qu & Bregman, 2018b,a), hydrostatic CGM models (e.g., Stern et al., 2016; Faerman et al., 2017, 2020), accretion shocks (e.g., Stern et al., 2019), and precipitation models (e.g., Voit et al., 2019).

1.4 The Structure of the Dissertation

This dissertation is dedicated to understanding the warm-hot CGM, including its spatial distribution, kinematics, and connection with the galaxy disk in both observation and modeling. This dissertation can be divided into two large parts - observations of warm-hot CGM at low redshift $z \lesssim 1$ (§2 to §6), and a CGM model dominant by radiative cooling and stellar feedback (§7 and §8):

- In §2, I report the first (and the only) detection of the intervening Mg X absorption system toward LBQS 1435-0134, which is the only feasible UV tracer of the hot gas in hydrostatic equilibrium. This section is published independently on the Astrophysical Journal as Qu & Bregman (2016, ApJ, 832, 189).

- In §3, I report the discovery of a massive hot gas bridge between the MW and M31 detected in the X-ray and SZ bands. This section is published independently on the Astrophysical Journal as Qu & Bregman (2021, ApJ, 907, 14).

- In §4, I develop a density distribution model for the warm gas in the MW traced by Si IV and O VI absorption lines, based on the column density dependence on the Galactic longitude and latitude. This section is published independently on the Astrophysical Journal as Qu & Bregman (2019, ApJ, 880, 89).

- In §5, kinematics is introduced into the warm gas density model in §4 to reproduce the observed line shapes of Si IV. This section is published independently on the Astrophysical Journal as Qu & Bregman (2020, ApJ, 894, 142).

- In §6, I study the cool-warm CGM in a nearby MW-like galaxy NGC 891, where both feedback and accreted gas are detected around the NGC 891 disk. This section is published independently on the Astrophysical Journal as Qu & Bregman (2019, ApJ, 876, 101).

- In §7, I develop an analytic warm-hot CGM model by balancing between the star formation rate and the accretion rate due to radiative cooling of the hot CGM. This section is published independently on the Astrophysical Journal as Qu & Bregman (2018, ApJ, 856, 5).

- In §8, I consider the warm-hot gas distribution in the Universe by combining the analytic warm-hot CGM model with the galaxy spatial distribution. This section is published independently on the Astrophysical Journal as Qu & Bregman (2018, ApJ, 862, 23).

The summary and the future work are in §9.

CHAPTER II

A Hot Gaseous Galaxy Halo Candidate with Mg X Absorption

2.1 Introduction

The baryon masses of galaxies are significantly smaller than expectations based on the cosmological baryon to total mass ratio (0.16; Planck Collaboration et al. 2016a) where the total mass is inferred from the galaxy rotation curve. In particular, the stellar mass and the galactic gas mass can only account for $\sim 15-25\%$ of the total baryon mass (Mateo, 1998; Bell et al., 2003; Dai et al., 2010; Martin et al., 2010; Anderson & Bregman, 2010; Behroozi et al., 2010; McGaugh & Schombert, 2015). A solution to this missing baryon problem in galaxies is that there exists a massive extended hot gaseous halo (Fukugita & Peebles, 2006; Bregman & Lloyd-Davies, 2007; Kaufmann et al., 2009).

The gaseous content of halos is predicted to evolve during galaxy formation and evolution. Early in the history of the universe ($z \sim 4$), baryons are expected to be cool ($\sim 10^4$ K; Weinberg et al. 1997), while during galaxy formation ($z \sim 3$ to 1), the cool gas is transformed into the warm-hot medium ($10^5 - 10^7$ K) and the hot medium ($> 10^7$ K) in halos as a consequence of the gravitational collapse and the shock heating (Cen & Ostriker, 1999). For low redshift galaxies ($z \lesssim 1$), the

predicted cool gas accounts for $\sim 20\% - 40\%$ of the total baryons, while more than 30% should be in the warm-hot intergalactic medium (WHIM; Cen & Ostriker 2006). The gaseous halo depends on the mass of the galaxy, with extensive hot halos present around massive galaxies but not around low-mass galaxies (Kereš et al., 2005, 2009).

These theoretical works stimulated observational searches for the halo gas, determining masses and temperatures. The cool halo gas ($\sim 10^3 - 10^5$ K) can be traced by low ionization metal ion absorption, which is detected in spectra of background active galactic nuclei (AGN; e.g. Werk et al. 2014). The COS-Halo team carried out a survey of ultraviolet (UV) absorption lines of low redshift galaxies ($z \approx 0.2$) mainly using the Cosmic Origins Spectrograph (COS; Green et al. 2012) on the *Hubble Space Telescope* (*HST*). They found that $\approx 90\%$ of their target galaxies show cool gas absorption due to galaxy halos (Werk et al., 2012, 2013; Tumlinson et al., 2013). Based on their observations, the COS-Halo team found the cool gas in the halo can account for $\sim 40\%$ of the total baryons for $L \approx L^*$ galaxies (Werk et al., 2014), while a recent study showed that this component can only account for $\sim 6\%$ (Stern et al., 2016). These cool absorption systems are believed to be separate clouds similar to high velocity clouds in the Milky Way (Sembach et al., 2003; Zahedy et al., 2016). In addition to the atomic gas, cooler molecular gas can be present in higher column density systems, such as the damped Lyα absorbers, which could also be hosted by galaxy halos (Srianand et al., 2005; Muzahid et al., 2015, 2016a).

Besides the cool gas, the theory predicts the presence of a hot volume-filling medium at about the virial temperature in a galaxy halo, and such gas has been detected. For an L^* galaxy, the virial temperature is about $10^{6.3}$ K, so the most prominent emission and absorption lines are in the X-ray band (see Bregman 2007 for review). X-ray emission line studies of external galaxies detect extended hot halos to $0.1R_{200}$, beyond which the surface brightness falls to undetectable levels, when the gas density is around $n_{200} \sim 5 \times 10^{-5}$ cm^{-3} (Anderson & Bregman 2010; Boroson et al.

2011; Bogdán et al. 2015; Anderson et al. 2016). Within $0.1R_{200}$, smaller than 5% of total galactic baryons are detected, and an extrapolation to R_{200} increases this mass by about an order of magnitude, still not accounting for all the baryons. Absorption line studies of intervening gas (hosted by galaxy halos) have not been fruitful due to the short redshift search space (Bregman et al., 2015) and to the contamination by weak Galactic lines (Nicastro et al., 2016a,b). X-ray studies of the Milky Way utilize both emission lines and absorption lines of O VII and O VIII, and also detect a hot halo extending to at least 50 kpc (Miller & Bregman, 2015; Miller et al., 2016; Hodges-Kluck et al., 2016b). When extrapolated to R_{200}, the gaseous mass is $\sim 4.3 \times 10^{10} M_{\odot}$ within 250 kpc, which is comparable to the total stellar mass (Miller & Bregman, 2015).

Another approach focuses on high ionization species in the UV band to detect the hot halo. Typically, low ionization species are ionized by photons from background AGNs. Meanwhile, ions with ionizational potentials greater than O VI (113.9 eV) are collisionally ionized in a halo environment, and can be employed to trace the warm-hot gas (Tripp et al., 2008; Tepper-García et al., 2013; Stocke et al., 2014). The two most useful ions are Ne VIII and Mg X, which have resonance double lines in the extreme UV band (Verner et al., 1994). The first intergalactic Ne VIII absorption feature was discovered by Savage et al. (2005) with the Far Ultraviolet Spectroscopic Explorer (FUSE). Subsequently, several Ne VIII doublets have been detected with matched O VI doublets (Tripp et al., 2011; Narayanan et al., 2011; Meiring et al., 2013). Thus, assuming all O VI ions are also collisional ionized, intergalactic Ne VIII systems can be described as a single temperature collisional equilibrium model with temperatures of $\sim 10^{5.7}$ K and total column densities of $\sim 10^{18.8} - 10^{20.1}$ cm^{-2} (Narayanan et al., 2012). Although the column density is within the range expected for a volume-filling galaxy halo, this temperature is lower than the expectation ($\gtrsim 10^6$ K), so it is suggested that the detected gas originates from interaction layers, which are the

interfaces between cool clouds and the hot halo (Gnat et al., 2010; Kwak et al., 2015), rather than the isolated hot halo (Narayanan et al., 2011; Meiring et al., 2013). Even for the Milky Way, a multi-temperature model might be more physically relevant, with one component at the virial temperature (as is found for the Milky Way; Miller & Bregman 2015), yet obtaining a unique model fit would require additional data.

One way to solve this dilemma is to expand the probed temperature range by including Mg X as a diagnostic, because it reaches a peak ionization at about twice the temperature of Ne VIII ($\sim 10^{6.1}$ K, compared to $\sim 10^{5.8}$ K) and four times that of O VI ($\sim 10^{5.5}$ K; Bryans et al. 2006). The gas traced by Mg X is approximately at the virial temperature for a $\sim L^*$ galaxy, making this the ideal diagnostic for studies of hot gaseous halos. A blind search of Mg X was carried out with *HST*/COS (*HST* proposal ID 11741; Tripp as PI). However, currently discovered Mg X doublets in their spectra have been identified only from AGN outflows (Muzahid et al., 2013). AGN outflows show several differences from a hot galactic halo, so distinguishing between the two possibilities is viable in some but not all cases. First, AGN outflows show larger observed column densities of Mg X than predicted for galactic halos ($\gtrsim 10^{14.5}$ cm^{-2}), and even less abundant species, such as Na IX may be detectable. If one assumed these lines come from gaseous halos, the expected hydrogen column density is $\gtrsim 10^{21}$ cm^{-2}, which is about one order of magnitude higher than the typical column density for the halo of an isolated galaxy ($n_{200}R_{200} \lesssim 10^{20}$ cm^{-2}). Also, density sensitive lines from excited ions (e.g. O IV*) seem to be common in AGN outflows (Finn et al., 2014). These lines trace the gas with a density $\gtrsim 10^2$ cm^{-3}, at least 10^5 greater than galaxy halo densities.

The Mg X absorption line equivalent width from a typical galaxy halo would be 20 mÅ in the rest frame (40 mÅ at $z = 1$), which is detectable in a continuum with a S/N > 20. In this paper, we report on such a detection in the sightline toward LBQS 1435-0134, which contains Mg X, Ne VIII, O VI and a number of other highly ionized

ions. We introduce the object and our data reduction methods in Section 2.2. Section 2.3 presents the results of absorption systems along this sightline, and the modeling of the Mg X system is in Section 4.1. We discuss the origin and the implication of this absorption system in Section 5.7.

2.2 Objects and methodology

We carried out a blind search for Mg X doublets using archived COS far-ultraviolet (FUV) spectra in the Mikulski Archive for Space Telescopes (MAST). The Mg X doublet occurs at 609.8 and 624.9 Å, so it is only visible when the redshift is larger than 0.92 in the common COS G130M grating settings with shortest wavelength of 1170 Å. The highest search redshift is limited by the QSO redshift. Here, we avoid a 5000 km s^{-1} velocity region around the QSO redshift to account for intrinsic absorption. Thus, we set the redshift threshold for our selected sample to $z > 1$ with the minimum search upper limit of 0.97 to ensure a search space of $\Delta z \geq 0.05$ for each source.

In this search, we employed the Bayesian Blocks method to characterize the spectra to help us to find absorption features, and several Mg X doublets have been discovered. However, most of them are too strong to be associated with galaxy halos, and also have matched density sensitive lines, which should originate from AGN winds. After excluding these AGN outflow absorption systems, we found one absorption system in LBQS 1435-0134 with Mg X and several absorption features from Ne and O. Also, LBQS 1435-0134 is the only object with a sufficiently high S/N ratio > 20, while other objects are $\lesssim 10$.

2.2.1 LBQS 1435-0134

LBQS 1435-0134 was discovered in the optical survey the Large Bright Quasar Survey (LBQS; Hewett et al. 1995). Subsequently, the NRAO VLA Sky Survey

(NVSS) showed that it is a radio loud QSO with a flux density of 52.7 ± 1.7 mJy at 1.4 GHz (Condon et al., 1998), and with a redshift of 1.310790, as measured in the Sloan Digital Sky Survey (SDSS; Hewett & Wild 2010). The high S/N ratio UV spectra were obtained by COS and the Space Telescope Imaging Spectrograph (STIS) on *HST* in the FUV and the near-ultraviolet (NUV) bands, and the total exposures are 56 ksec and 21 ksec for COS/FUV and STIS/MAMA, respectively.

The COS observations were acquired on 2010 August 8 to 22 as a part of *HST* program 11741 (PI: Tripp). To achieve the full wavelength coverage of COS/FUV ($1150 - 1800$ Å), two different central wavelengths were used for the two medium resolution gratings (G130M and G160M). For G130M, the central wavelengths 1309 Å and 1327 Å were employed to fill the gap between two detector segments, while for G160M, they were 1600 Å and 1623 Å. The total exposures of G130M and G160M gratings were 22 ksec and 34 ksec, respectively, and the times were divided into even parts for two central wavelengths. This configuration of split positions reduces the impact of the fixed pattern noise ($2\% - 3\%$ uncertainty throughout the spectrum), which makes the weak line more reliable (Savage et al., 2011b). The STIS spectra were obtained on 2015 June 1 to 2 in *HST* program 13846 (PI: Tripp). Only one grating (E230M) with a slit of $0.2' \times 0.2'$ and one central wavelength (2415 Å) were employed, and the total exposure time was 21 ksec.

We mainly focused on COS/FUV spectra because of the higher S/N ratio, while STIS spectra were only employed to match the O VI doublet and the Lyman series. Thus, the following search method was only applied to COS data.

2.2.2 The COS Spectral Reduction

The archived *x1d* files from MAST are coadded using routines from the COS team (*coadd_x1d.pro*), introduced in Danforth et al. (2010). Exposures from G130M and G160M are coadded together and resampled in 6 raw pixels ($\approx 0.06 - 0.07$ Å),

which produces a spectral resolution of $\approx$ 20000. During this coadd process, strong galactic lines (e.g. Si II $\lambda\lambda$ 1260.4) are employed to align exposures. However, this alignment cannot eliminate possible instrumental shifts (Tumlinson et al., 2013). This instrumental shift is caused by the geometric distortion and wavelength solutions of COS, which could be up to 20 km s^{-1} in coadded spectra. For the comparison between two wavelength positions, the instrumental shift could be around 30 km s^{-1}, which must be considered in the following profile fitting.

The coadded spectra are characterized using the Bayesian Blocks algorithm to prepare for the absorption feature search and the line identification. Bayesian Blocks was developed to study the time variability in high energy astrophysics, such as gamma-ray bursts, but is applicable to any one-dimensional data set, even if it is discontinuous (Scargle, 1998; Scargle et al., 2013). To use this algorithm in the spectrum cases, we employed the equivalent count, defined as the square of the S/N ratio for each pixel, for each resolution element as the input of Bayesian Blocks. As a non-parametric method, this algorithm represents the spectrum as a series of wavelength intervals, generally unequal in length (blocks), within which the flux is modeled as a constant. These blocks are extracted based on the change points (the beginning or the end points), which is determined by well-tested statistical measures, thus the end result is a spectrum represented by a set of step functions. A reduction example is given in Fig. 2.1.

With the output from the Bayesian Blocks algorithm, absorption lines can be extracted by analyzing the structure of "Bayesian blocks". Absorption blocks are defined as blocks that are local nadirs and shorter than 30 bins in coadded spectra ($\approx$ 1.8 Å for G130M and $\approx$ 2.2 Å for G160M). This width ($\approx$ 2 Å) corresponds to a maximum velocity width $\approx$ 400 km s^{-1}, which matches most of lines and excludes the continuum. These absorption blocks are regarded as the center for absorption lines. The blocks adjacent to an absorption block have three possibilities, the continuum,

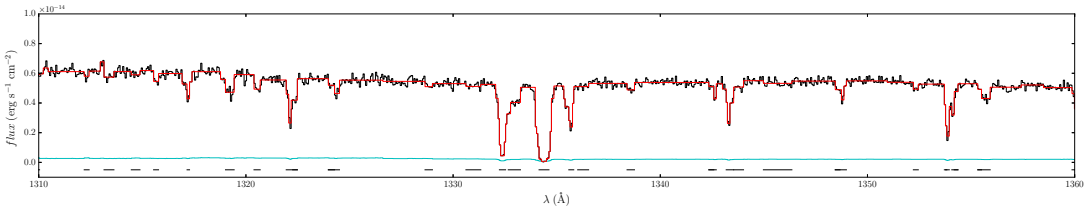

Figure 2.1: This shows an example of the Bayesian Blocks algorithm and the line determination. The black and cyan lines are the rebinned fluxes and their errors from *coadd_x1d.pro*, while the red line is the result of Bayesian Blocks. Adopted absorption lines are shown as black boxes along the bottom.

the wings of this line or a blended line, and the latter two are also absorption features. One adjacent block will be considered as an extension of the absorption block, if it is not a peak and the difference compared to the higher block next to it is larger than 5% (smaller ones are more likely to be the variation of continuum). Applying Bayesian Blocks to spectra with a S/N of ≈ 20, one cannot distinguish absorption with depth of $\lesssim 0.05$ unless the length of the block is larger than 20 resolution elements, which is uncommon. An absorption feature contains an absorption block and its successive extended blocks. Whether these extended blocks are wings or blended lines depends on the symmetry of absorption features, since the wings of a line should be symmetrical. For each absorption feature, we have a central wavelength of the absorption block and two wing widths, which are defined as the distances between the central wavelength and boundaries. If a significant asymmetry is found, this absorption feature will be divided into two absorption lines, where the criterion is that the difference between two wing widths is larger than 0.1 Å (2 bins or 30 km s^{-1}, which is the typical b value of a line). This method can identify the case of two blended lines with enough separation, which is also shown in Fig. 2.1.

The use of the Bayesian Blocks algorithm is a significant advantage in our line search methods. This algorithm can identify potential absorption features without determining the local continuum, which avoids the difficulty of assuming a continuum

shape in a complex spectrum. Also, this algorithm provides a uniform criterion for line detection, which is controlled by a prior parameter. This parameter is a prior guess for the number of change points, which can be regarded as an indicator of the detection significance. Here, this parameter is fixed to 4 in our program, approximately equivalent to 4σ. However, our program is also limited by the S/N ratio of spectra, which means weak lines will not be identified, and complex lines will not be adequately decomposed.

2.2.3 The Identification of Absorption Systems

An absorption system should contain several related ions, so we employed a line template match method to find possible systems. Two templates have been considered in this work, one for the high ionization state including two doublets (Mg X and Ne VIII) and lines from oxygen (O IV and O V) and neon (Ne IV, Ne V and Ne VI). Another template is for low ionization metal lines and galactic lines including strong metal lines within $\lambda \sim 1000 - 1700$ Å, which are common in UV spectra (Werk et al., 2013; Burchett et al., 2015). These two templates do not overlap since the higher one is $\sim 600 - 800$ Å, while the lower one is $\lambda \sim 1000 - 1700$ Å.

To carry out the line match, one line is considered as the reference line, which must exist in an absorption system. We choose the hydrogen Lyman series lines (mainly Lyα and Lyβ for different redshift regions) and Ne VIII $\lambda\lambda$770.409 for the two line templates, respectively, since these choices can cover almost all of the redshift region. After a reference line is fixed, the wavelength ratio between two lines is used to judge whether another line is matched. The observed wavelength ratio is a range since observed lines have widths, which are derived from Bayesian Blocks, so if the exact ratio is in this range, two lines are matched. With the most matched lines, a redshift will be marked as a possible absorption system, and the identified lines in this system are excluded from the observed line list. This process is iterated to find

all possible absorber systems with more than three spectral lines. Here, three lines is the minimum for possible high ionization state systems: the stronger Mg X line, the stronger Ne VIII line, and one intermediate line (e.g. O V or O IV).

Using this method, false absorption systems can occur by chance because of the large number of lines in each spectrum. The possibility to match a random line is around 1/6, assuming there are 300 lines of width 0.3 Å in one spectrum, which means the line coverage is 100 Å out of the total wavelength coverage of 650 Å. Thus, a three line criterion could have around 100 false absorption systems by chance, while for systems with five lines, there are only around 10 false systems. To reduce the number of false systems, we bring in additional information, such as the relative line strengths (f values and abundances) that could physically exist. Among the possible absorption systems, the one at $z = 1.1912$ in LBQS 1435-0134 with 15 lines is confirmed, and we will introduce this system in Section 2.3.

2.2.4 Absorption Line Measurements

To obtain line measurements, local continua are obtained by spline fitting in segments of width $\sim 1100 - 3000$ km s^{-1}, located about the line center. Typically, two sides with width ≈ 300 km s^{-1} are used to do the continuum fitting and to normalize the flux, which ensures that the central ≈ 500 km s^{-1} is left for the line. The wavelength range chosen for continua can be changed by hand if necessary (e.g. when multiple lines appear in one segment, the connection region between two lines will also be included in continuum). With spectra that are normalized by the continuum, the Voigt profile convolved with the COS line spread function (LSF) is used to extract the column density and the b value for the absorption lines in COS/FUV spectra. The fitting is based on the minimum χ^2 method which is realized using the Levenberg-Marquardt optimization algorithm.

During the fitting, we assumed that each absorption system only has one com-

ponent, so if one absorption system has multiple components, it will be divided into several systems with different redshifts (e.g. the high ionization system in LBQS 1435-0134 has been divided in 1.1910 and 1.1912 components). Although we fixed a redshift for each system, velocity shifts were still varied in our fitting because of the uncertainty of redshifts and instrumental shifts (Tumlinson et al., 2013). Thus, for each component, three parameters were varied, including the velocity shift v, the velocity factor b value and the column density N. For ions in the Mg X system, all three parameters are used to fit the profile. If one ion has multiple lines (e.g. the doublet from Mg X), these lines will be fit simultaneously with the same parameters. For contaminating lines from other absorption systems, we fixed its shape properties (b and N), if they could be obtained by fitting other lines from the same ions. Otherwise, all three parameters are varied to fit a line when a contaminating line is unidentified or there is no way to constrain b and N (e.g. the only line from C III). For example, the O IV $\lambda\lambda$608.5 Å line of the high ionization system is blended with three Lyman series lines and one O IV line from other systems. These H I lines are fixed, since there are other Lyman lines in this absorption system, while the contaminating O IV is varied because other O IV lines in this system are out of the COS wavelength coverage.

For lines in STIS spectra, besides the profile fitting, we used the apparent optical depth method (AODM; Savage & Sembach 1991) and the curve of growth method (COG) to measure the column density because of the low S/N ratio. For LBQS 1435-0134 with a 21 ksec exposure, the S/N ratio of the STIS spectrum is only ~ 6 per resolution element, so profile fitting might not work well. However, with the sharp LSF, the AODM should work well for STIS spectra. Both AODM and COG are employed together to determine the consistency of results.

2.3 LBQS 1435-0134

2.3.1 Absorption Systems

Nineteen absorption systems have been identified in the LBQS 1435-0134 spectra using our method. All of these absorption systems are identified using the strategy stated in Section 2.2, and eighteen systems are based on the low ionization line template, while the only one at $z = 1.1912$ is from the high ionization line template. More than 250 lines (including blended lines) have been identified, which do not include isolated Lyα systems. A full summary of the lines are beyond the scope of this paper and will be reported elsewhere.

2.3.2 The Mg X System

For the high ionization absorption system at $z = 1.1912$, there are 17 lines from 11 ions in the wavelength coverage. Fourteen lines lie in the COS spectrum and three lines lie in the STIS spectrum. Two lines from O IV $\lambda\lambda$ 553.329 Å and 554.076 Å are blended with galactic Lyα absorption and the geocoronal hydrogen emission, which is not distinguishable. Using the profile fitting method stated in Section 2.2, we fit all lines in the COS spectrum except for the two O IV lines. The fitted lines are shown in Fig. 2.2 and Fig. 2.3 for high ionization lines and other low or intermediate ionization lines, respectively. The results of the column density and the b value are summarized in Table 2.1. The velocity shifts given in the table are aligned to $z = 1.1912$ with a typical separation of $110 - 140$ km s^{-1} between the two components. We note that the our single component fitting on Mg X may not represent the true structure of this ion, which would only be revealed by higher S/N data. According to the position and the width of the Mg X doublet, we suggest that this ion has a similar shape of Ne VIII. We also tried a two component model to the Mg X doublet, which yielded a total column density of $\log N = 13.95^{+0.21}_{-0.20}$. This column density is consistent with the

single component model because this line is in the low optical depth regime, where the column is nearly independent of the line shape.

Mg X is the crucial ion in our study, but the lines from it are weak because of the low abundance and the small maximum ionization fraction ($\approx 22\%$). As shown in Fig 2.2, the depth of the stronger Mg X line is $\approx 10\%$, while the weaker line is $\approx 5\%$. To determine the significance of the doublets from Mg X, we fit these two lines with and without Mg X. Between the two fittings, the change of χ^2 is 43.0 from 225.2 to 268.2, which can be separated into 28.7 (from 126.6 to 155.3) for the stronger line and 14.3 (from 98.6 to 112.9) for the weaker line. Considering the change of the degree of freedom (dof) is 3, the total significance of the doublets is 5.8 σ, with 4.6 σ for the stronger line and 2.8 σ for the weaker line. Using the same method, Ne VIII shows a total significance larger than 6.5 σ, which confirms its existence. We also calculate the significance level of each line using the method described in Keeney et al. (2012), and the results are consistent with the χ^2 method, showing 4.6σ, 2.7σ and 6.8σ for the Mg X doublet lines and the strong Ne VIII line, with EW of 38.6 ± 7.0 mÅ, 22.8 ± 7.0 mÅ and 82.4 ± 11.8 mÅ, respectively. The weaker Ne VIII line is blended with a galactic Ni II line $\lambda\lambda$1709.600 Å, so the equivalent width is poorly constrained.

In the STIS spectrum, both the O VI doublet and Lyα are matched at the expected positions. For the O VI doublet, the stronger line is blended with another line, which should be the galactic Fe II $\lambda\lambda$2260.079 line. The weaker line is used to obtain the line strength, showing $\log N = 14.49 \pm 0.06$ in AODM and 14.50 ± 0.10 in COG (equivalent width, EW $= 295 \pm 33$ mÅ; $b \approx 20$ km s^{-1}, which is consistent with Ne VI and O V). In the profile fitting, we obtain a total O VI column density of $\log N = 14.57 \pm 0.03$, which may be affected by the galactic Fe II. For the Lyman series, only Lyα has been detected, so just one line is used, showing $\log N = 13.93 \pm 0.04$ using the AODM approach. With the COG approach, since the b value affects the EW significantly in

Table 2.1: Profile fitting results of the Mg X system toward LBQS 1435-0134

Ion	v km s^{-1}	b km s^{-1}	log$N$ cm^{-2}	v km s^{-1}	b km s^{-1}	log$N$ cm^{-2}	log$N_{\rm tot}$ cm^{-2}
Mg X[a]				9.2 ± 28.0	68.5 ± 20.3	13.89 ± 0.10	13.89 ± 0.10
Ne VIII	-104.7 ± 16.7	20.1 ± 11.5	13.64 ± 0.17	33.1 ± 23.1	29.9 ± 16.6	13.67 ± 0.17	13.96 ± 0.17
Ne VI	-78.4 ± 15.8	26.4 ± 10.5	13.98 ± 0.12	57.0 ± 29.5	25.3 ± 19.6	13.68 ± 0.24	14.16 ± 0.16
Ne V[a]				-15.2[b]	46.8 ± 9.2	13.92 ± 0.06	13.92 ± 0.06
Ne IV	-124.4[b]	45.3 ± 38.4	13.44 ± 0.26	3.6[b]	14.6 ± 12.1	13.29 ± 0.24	13.67 ± 0.25
O VI	-93.0 ± 2.7	15.7 ± 1.6	14.39 ± 0.03	10.8 ± 3.0	17.2 ± 2.1	14.10 ± 0.04	14.57 ± 0.03
O V	-104.8 ± 3.5	18.2 ± 2.0	14.07 ± 0.04	4.8 ± 4.4	22.2 ± 2.3	13.98 ± 0.04	14.33 ± 0.04
O IV	-97.5 ± 14.9	27.9 ± 7.8	14.17 ± 0.12	6.4 ± 12.9	21.0 ± 6.1	14.03 ± 0.15	14.41 ± 0.13
O III[a]				-22.8 ± 35.8	52.2 ± 24.7	13.45 ± 0.15	13.45 ± 0.15
N IV	-120.0 ± 24.5	22.7 ± 19.2	12.68 ± 0.22	-7.4 ± 50.1	9.0 ± 23.6	12.23 ± 0.53	$12.81^{+0.32}_{-0.28}$
H I	-87.8 ± 13.8	35.5 ± 6.8	13.85 ± 0.09	28.3 ± 39.9	33.2 ± 17.3	13.30 ± 0.31	13.97 ± 0.13

[a] For these three ions, we only fit them using one component model, since we cannot distinguish two components resulted by the low S/N ratio.

[b] For Ne V and Ne IV, we fixed v to limit the error bar. The fixed v is the best fitting value when it is varied.

the saturated region, we assume the b value is $\approx 30 - 40$ km s^{-1} because of the total velocity width of ≈ 160 km s^{-1}. Thus, the derived column density is log$N$ = 13.99 ± 0.13 cm^{-2} for an EW = 607 ± 45 mÅ in COG. The profile fitting of Lyα shows a consistent column density of log$N = 13.97 \pm 0.13$. This column density is also consistent with the constraint of the weak Lyβ line. The expected equivalent width of Lyβ is ≈ 141 mÅ, which is consistent with the measured equivalent width of 146 ± 54 mÅ, a detection slight below 3σ. For these two ions, we adopt the values from AODM in the following analysis.

After measuring lines from ground levels, we also examined the spectra for the presence of density sensitive lines from excited levels (e.g. O IV* and O V*) in the COS spectrum. A fairly strong line shows up at the position of O V* $\lambda\lambda$ 759.442. However, we rule out the identification of this line as redshifted O V* $\lambda\lambda$ 759.442 for three reasons. First, this line is also identified as O VI $\lambda\lambda$ 1031.912 at $z = 0.6127$ and this doublet can be fitted well without an additional line. Secondly, O V* has two strong lines ($\lambda\lambda$ 759.442 and $\lambda\lambda$ 760.446) with similar f values (0.1913 and 0.1432) and similar low excited levels (10.16 and 10.21 eV with critical density of $\sim 10^5$ cm^{-3}), however, no second line occurs at the expected position. Thus, the absence of another O V* line does not support the existence of density sensitive lines. Also, the O IV* line is absent. O IV has a similar column density to O V in this system and O IV* lines require a much smaller excited energy (0.05 eV) requiring a lower critical density ($\sim 10^3$ cm^{-3}). For these three reasons, no density sensitive line has been detected in this high ionization state system.

2.4 Model

For the analysis of the Mg X system, two models, the photoionization model and the collisional ionization model, are considered to model the ionization states in the gas. Here, we only show the details in the application of ionization models, and

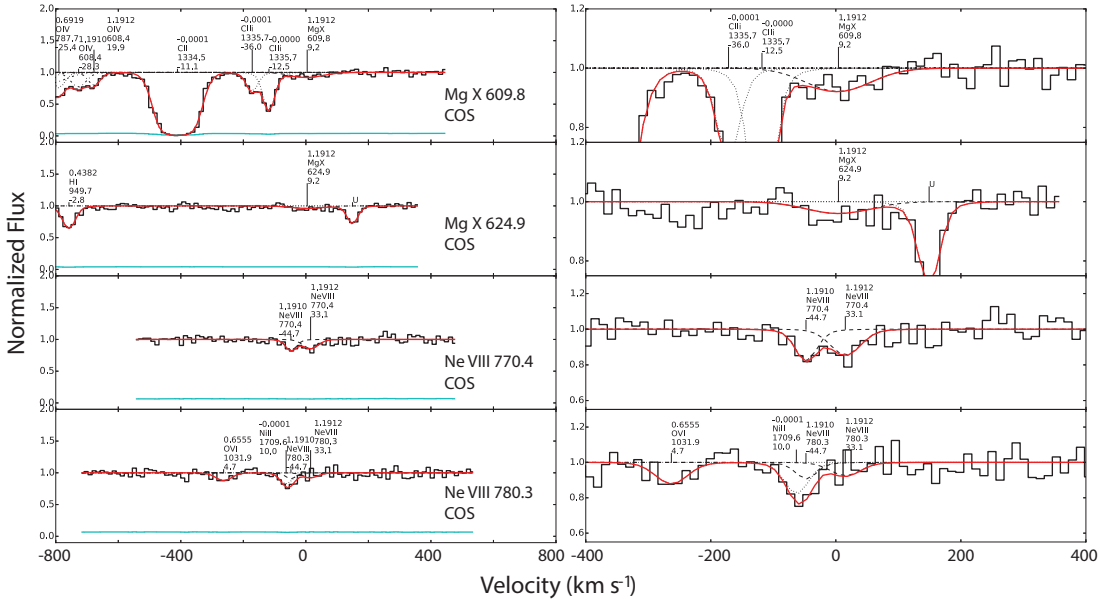

Figure 2.2: Lines due to high ionization species (i.e. Mg X and Ne VIII) and their zoom-in plots are plotted on the right. The data are the solid black lines and the models are red, while dashed, dotted and dash-dot lines indicate lines in the Mg X system and related lines (see the text for details). Every absorption line is marked with its redshift, ion, rest wavelength and velocity shift, while the marker 'U' designates unknown lines.

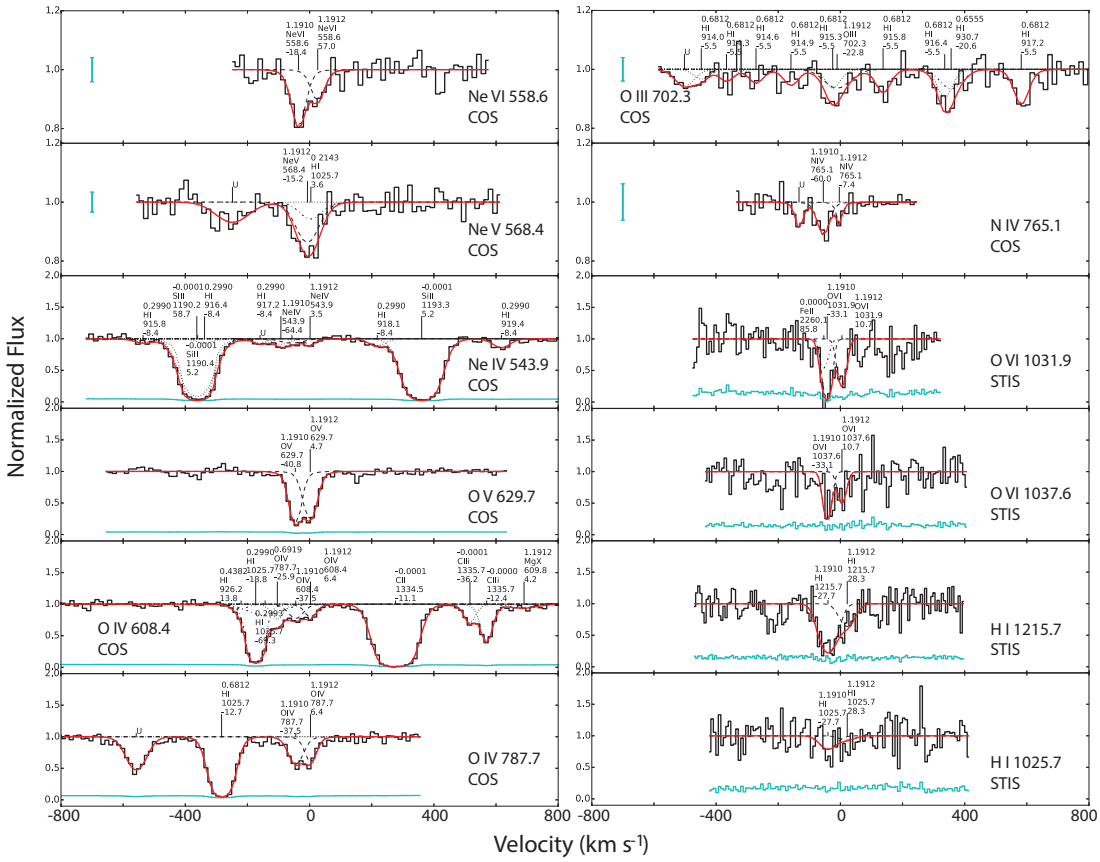

Figure 2.3: Other lines in the $z = 1.1912$ system are shown except for the two O IV blended with non-redshifted H I features. Symbols in this figure are the same as in Fig. 2.2, except for Lyβ, where the red line is the projected shape of Lyα. In the zoom-in plots, characteristic errorbars are given as cyan markers.

the nature of this gas will be discussed in Section 8.11. Also, the combination of the photoionization and the collisional ionization model is beyond the scope of this paper, so we deal with these two models separately.

2.4.1 The Photoionization Model

We employed the photoionization code CLOUDY (version 13.03; Ferland et al. 1998), which can calculate the column density for each ion with the input radiation field and the absorption gas. The input radiation field is the HM05 in CLOUDY, which is the cumulative background radiation field from AGN as calculated by Haardt & Madau (1996) and updated by Haardt & Madau (2005 private communication to CLOUDY). This integrated radiation field is believed to be redshift dependent and uniform at a given redshift. Here, we fixed the redshift to 1.19, and assumed the absorption system is plane-parallel to simplify the calculation. When carrying out the simulation, we fixed the neutral hydrogen column density to the observed value as the boundary condition, and varied the density to achieve different ionization parameters $U = n_\gamma/n_{\rm H}$, where n_γ is the photon density with energies higher than 13.6 eV and $n_{\rm H}$ is the hydrogen density.

In Fig. 2.4, we show two models for the metallicity of $[Z/X] = -0.5$ and $[Z/X] = 0$, where $[Z/X] = \log(Z/X) - \log(Z/X)_\odot$, while the solar metallicity is from Asplund et al. (2009). In these two plots, the column density dependence on the ionization parameter are plotted for all detected ions except for H I, which is fixed to $10^{13.93}$ cm^{-2}, and the observed column densities with 2σ error bars, shown as bold lines for each ion. We note that the lower observed limits are still higher than the peak of Ne V and O IV in the $[Z/X] = -0.5$ model, which is odd since these two ions do not have similar ionizational potentials. This is mainly because of the small H I column density ($\log N = 13.93$) compared to the COS-Halo sample ($\gtrsim 15$; Werk et al. 2014). The standard approach of fixing this problem is to raise the metallicity

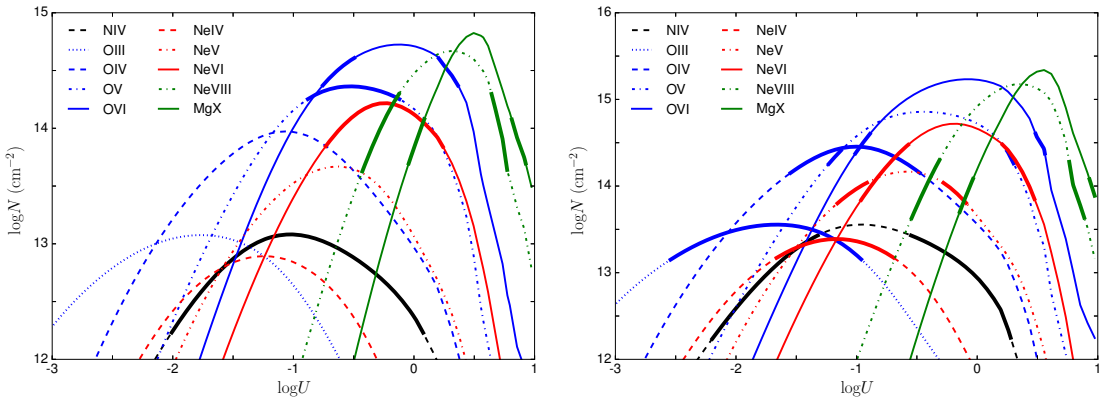

Figure 2.4: The left panel shows the photoionization model with $[Z/X] = -0.5$, while the right panel is $[Z/X] = 0$. The bold solid lines indicate the observational measurements with 2σ error bars.

to obtain detectable metal lines, so we show the one solar metallicity model.

In the one solar metallicity model, there is no single ionization parameter that reproduces all the observed ions. If we consider a two-components model, intermediate ions through Ne VI admit to a solution at $\log U \approx -1.3 \pm 0.3$, which corresponds to a hydrogen density of $10^{-3.5}$ cm^{-3}, a mean temperature of 2.3×10^4 K, and a path length of 1.3 kpc. A second component is required for the two higher ionization species of Ne VIII and Mg X, where a solution is found at $\log U \approx 0.9$. This component corresponds to a density of $10^{-5.7}$ cm^{-3}, a mean temperature of 1.5×10^6 K, and a path length of 1.1×10^3 Mpc. This unreasonably large path length is a result of requiring the high ionization state also to produce the total observed H I column density, which should be fixed. However, using the current data, there is no way to divide the observed H I column density into two parts for the low and high states, respectively. We also consider the case where the observed H I from the high state is at its minimum to reproduce the observed Mg X and Ne VIII. In this case, the solution should be around the peak of the Mg X and Ne VIII, and show an ionization parameter of $\log U \approx 0.5$, which corresponds to a hydrogen column density of $\sim 10^{19.5}$ cm^{-2}, a density of $\sim 10^{-5.5}$ cm^{-3}, and a path length of ~ 3 Mpc. This path length is still

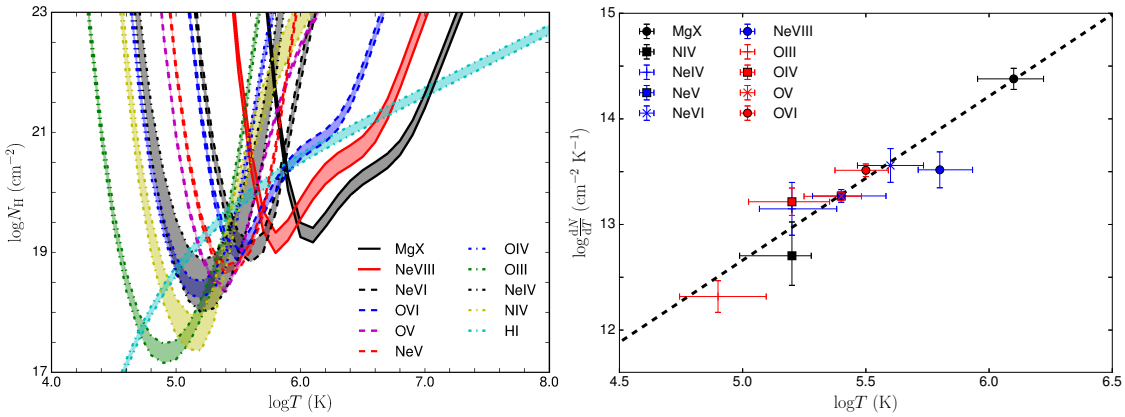

Figure 2.5: The left panel is the $T - N$ diagram for the collisional ionization equilibrium model. For each ion, the band indicates the possible region for its column density. The right panel shows the fitting results of the power law model. The dashed line shows the temperature dependence of the hydrogen column density. For each ion, the temperature is the peak temperature of the ionization fraction, and the error bar is the full width of the half maximum, while the gradient of the column density is the modified gradient of hydrogen $\frac{{\rm d}N_{\rm H,ion}}{{\rm d}T} = \frac{{\rm d}N_{\rm H,model}}{{\rm d}T} \times N_{\rm ion,observed}/N_{\rm ion,model}$.

about three orders of magnitude larger than the lower ionization state solution. This size difference indicates that they are not part of the same cloud but would represent different phases. Whether such phases are reasonable are explored in Section 8.11 after we excluding the possibility of AGN outflow.

2.4.2 The Collisional Ionization Model

We consider the collisional ionization model for the Mg X gas because of the difficulty of reproducing Mg X and Ne VIII in the photoionization model. Here, we assume collisional ionization equilibrium (CIE) for this Mg X gas, using the calculations of Bryans et al. (2006). The temperature-hydrogen column density ($T - N$) diagram for observed ions is given in Fig. 2.5. The width of the band for each ion takes into account the uncertainties in the column densities. The relative abundance of metals are set to the solar abundance and the metallicity of $[Z/X] = -0.5$.

The single temperature model assumes ions originate from the same gas with a

uniform temperature and a given column density, and one may expect that these ions go across a single point in the $T-N$ diagram. We find that not all of the ions can be reproduced by one single temperature model. If only considering Mg X and Ne VIII, they can be modeled by a gas with a temperature of $10^{6.00\pm0.04}$ K and a hydrogen column density of $10^{19.67\pm0.16}$ cm^{-3}. However, Ne VI and O VI cannot be reproduced with these parameters, so a multiple temperature medium is required even only for the high ionization state.

As shown in Fig. 2.5, multiple intermediate ionization species occur near a temperature of $10^{5.5}$ K and a hydrogen column density of $10^{19.1}$ cm^{-2}, suggesting that a two-temperature fit might work. A best-fit for a two temperature model yields the parameters $\log N_1 = 18.60 \pm 0.07$ at $\log T_1 = 5.33 \pm 0.02$ and $\log N_2 = 20.34 \pm 0.09$ at $\log T_2 = 5.89 \pm 0.01$. However, this is not an acceptable fit as $\chi^2 = 19.4(7\ \mathrm{dof})$, with a significant fraction of the χ^2 coming from Ne VIII and Ne V. This deviation can not be mitigated by adjusting the relative abundance of neon, since the observed Ne VIII column density is much lower than the prediction, while Ne V is opposite. Thus, we reject this two temperature model.

The next level of complexity is a three temperature model, which is more successful. The best fitting parameters are $\log N_1 = 18.48 \pm 0.14$ at $\log T_1 = 5.27 \pm 0.04$, $\log N_2 = 19.00 \pm 0.21$ at $\log T_2 = 5.59 \pm 0.07$ and $\log N_3 = 20.06 \pm 0.16$ at $\log T_3 = 5.94 \pm 0.03$. The resulting χ^2 is 5.5 and the dof is 5, an acceptable fit.

This three temperature model has six free parameters for eleven data points, so we also consider a power-law model with only four free parameters. In this model, we adopt a power law between the temperature and the column density $\log(\mathrm{d}N/\mathrm{d}T) = a + B\log T$. Along with parameters a and B, there are the lower and upper limits of temperature (T_{down} and T_{up}). Best-fit results show that $a = 4.3 \pm 2.2$, $B = 1.55 \pm 0.41$, $T_{\mathrm{down}} = 10^{4.39\pm0.13}$ K and $T_{\mathrm{up}} = 10^{6.04\pm0.05}$ K with $\chi^2 = 3.3(7)$, which is an acceptable fit. As shown in Fig. 2.5 and Table 2.2, the high ionization gas is well modeled by

Table 2.2: Model Comparison of the Mg X System

Ion	$\log N_{\rm adopted}$	$\log N_{2T}$	$\log N_{3T}$	$\log N_{\rm pl}$
Mg X	13.89 ± 0.10	13.78	13.93	13.88
Ne VIII	13.96 ± 0.17	14.95	14.51	14.35
Ne VI	14.16 ± 0.16	13.72	14.17	14.19
O VI	14.49 ± 0.06	14.48	14.46	14.41
Ne V	13.92 ± 0.06	13.66	13.97	13.93
O V	14.33 ± 0.04	14.47	14.32	14.34
Ne IV	13.67 ± 0.25	13.69	13.73	13.49
O IV	14.41 ± 0.13	14.39	14.43	14.17
N IV	$12.81^{+0.32}_{-0.28}$	13.06	13.33	13.08
O III	13.45 ± 0.15	13.16	13.42	13.64
H I	13.93 ± 0.04	13.91	13.72	13.93

a power law model with the maximum temperature larger than 10^6 K and the total hydrogen column density $\approx 8.2 \times 10^{19} (0.3 Z_\odot / Z)$ cm^{-2}.

2.5 Discussion

We have examined an absorption system at $z = 1.1912$ in the sightline toward LBQS 1435-0134 with high ionization species (i.e. Mg X and Ne VIII) and several intermediate or low ionization species including O VI and H I. We consider whether the observed absorption system is likely produced by the extended hot halo of a galaxy and if the gas, especially the Ne VIII and Mg X ions, is collisionally ionized or photoionized.

2.5.1 An Intrinsic AGN Outflow?

Before modeling the high ionization state system, we consider whether the Mg X is due to the AGN outflow. As introduced in Section 2.1, previous observations show that Mg X could be common in the intrinsic absorption of AGN rather than absorption by the hot halo of a foreground galaxy. A hot gaseous galaxy halo cannot be confirmed before its host galaxy is discovered, however, with the current observation

and the guidance from previous studies, it is possible to show that absorption by a hot halo is the more likely explanation.

Some AGNs can have very high velocity outflows (up to $\sim$ 0.2 c), while the velocity widths can be quite narrow ($\sim$ 100 km s^{-1}), which may be mistaken as intervening absorption systems (Misawa et al., 2007). These high velocity outflows sometimes can be distinguished from intervening systems, if they show absorption line variability, partial covering, or a density sensitive line from excited states (Teng et al., 2013; Muzahid et al., 2013; Finn et al., 2014; Muzahid et al., 2016b). It is believed that absorption systems with high velocities relative to the AGN are due to the wind originating from the disk, which implies that the variability should be common among the AGN intrinsic absorption; this variability has been observed (Teng et al., 2013; Muzahid et al., 2016b). The signature of partial covering is that the absorption line is saturated but not black. The phenomenon indicates the length scale of the gas is comparable to the disk of an AGN ($\sim$ 10 pc; Sulentic et al. 2000), and it is about four order of magnitude lower than the virial radius of galaxies (several hundreds kpc). The existence of absorption from excited states indicates large densities ($\gtrsim 10^2$ cm^{-3} for O IV*), that would not occur in the galaxy halo (several orders of magnitude larger than n_{200}). Thus, these diagnostics can be employed to confirm AGN outflows, although there can still be intrinsic AGN absorption systems that do not have these features.

Phenomenologically, we want to compare this Mg X system to the observed Mg X AGN outflows, so we give a brief summary for the current results on Mg X AGN outflows. There are nine Mg X outflows in five AGN reported in the literature (Muzahid et al., 2012b, 2013; Finn et al., 2014). Eight of nine absorption systems have relatively large Mg X column densities ($\gtrsim 10^{14.7}$ cm^{-2}), which indicates large total column densities of $\gtrsim 10^{21}$ cm^{-2}. However, with the common existence of O IV* lines (four of five objects), the typical path length is several parsecs, which

is consistent with the partial covering model (Arav et al. 2013; Finn et al. 2014; we checked the O IV* for PG 1206+459 and PG 1338+416). Also, these outflows can be modeled by the multi-phase photoionized gas models (Arav et al., 2013). The Mg X system in LBQS 1435-0134 seems to be significantly different from these Mg X AGN outflows with the smaller column density and the lower density. Thus, although we cannot exclude the possibility of AGN outflow completely, this Mg X system is unlikely to be an AGN outflow.

2.5.2 Photoionization or Collisional Ionization?

For intervening absorption systems, previous studies show that a photoionization model with $\log U \sim -5$ to -1 can be used for the low ionization species, while the origin of the higher ionization species is more complicated. About half of O VI and all of Ne VIII intervening systems are difficult to be reproduced in the photoionization model, which indicates they should be collisionally ionized in the high temperature medium (Thom & Chen, 2008a; Narayanan et al., 2012; Werk et al., 2014). Here, we will show that Mg X is also a tracer for high temperature medium (even higher than 10^6 K).

As stated in Section 2.4.1, there should be two components in the one solar metallicity model to account for intermediate and high ionization species in the photoionization model. The component for intermediate and low species has a ionization parameter of $\log U \approx -1.3$. With this ionization parameter, the required density ($10^{-3.5}$ cm^{-3}) and the total column density (10^{18} cm^{-2}) are consistent with the COS-Halo sample (densities of 10^{-1} to 10^{-4} cm^{-3} and hydrogen column densities of 10^{17} to 10^{20} cm^{-2}; Werk et al. 2014). The path length of 1.3 kpc indicates this component could be a cool cloud in the halo. However, the high ionization state with $\log U \sim 0.9$ has a path length of 1100 Mpc. This extremely large path length leads to a line broadening due to Hubble flow that is about half the speed of light, which is opposite

to the observed narrow line ($\lesssim 100$ km s^{-1}). Even if we consider the modification of the H I column density, the low limit of the ionization parameter is 0.5, which results a density of 3×10^{-6} cm^{-3} (more than one order of magnitude lower than n_{200}), a path length of ≈ 3 Mpc and a Hubble flow of 200 km s^{-1} (twice of the observed value). Therefore, the photoionization solution for the intermediate and low species seems to be plausible, while the one for the high ionization species is unreasonable.

The collisional ionization model is required to model the high ionization species Mg X and Ne VIII. As shown in Fig. 2.5, the possible single temperature solution is around the temperature of $10^{6.0}$ K, which indicates the existence of the hot gas. With the corresponding total column density of $\sim 10^{19.9}$ cm^{-2}, the density of this absorption gas can not be lower than 2.9×10^{-5} cm^{-3} to avoid the path length larger than 1 Mpc, which will result into an unreasonable width due to the Hubble flow. Then, we adopt the density of 5×10^{-5} cm^{-3} (n_{200}) which leads to a thermal pressure of 50 K cm^{-3}.

It is of interest to show whether the intermediate and low ionization gas can be in pressure equilibrium with this hot gas in the photoionization model or the collisional ionization model. In the photoionization model, for the intermediate ionization state species, the predicted temperature is 2.3×10^4 K, and the density is 3.1×10^{-4} cm^{-3}, which implies a pressure of 7 K cm^{-3}. This pressure is one order of magnitude lower than the hot gas inferred from the collisional ionization model, which indicates the possible photoionized gas cannot be in pressure equilibrium with the hot gas. In the collisional ionization model, the variation of the temperature is about one order of magnitude, so to make the gas have uniform pressure, the density should also have a variation of one order of magnitude. With the lower limit of 2.9×10^{-5} cm^{-3}, the density could be up to 1.6×10^{-3} cm^{-3}. Therefore, we suggest that even for the intermediate and low ionization gas, the photoionization is unlikely to be the only origin of the ionization species due to the difficulty to build the pressure balance.

For the collisional ionization model, the Doppler b value can constrain the nature of the gas to analyze the turbulence or other broadening mechanisms. In the power law model, we assume that for each ion except for H I, the temperature is approximately given by the peak of the ionization fraction, which also accounts for most of the column density of that ion. Because of the lower limit of the temperature, approximately 80% of H I is in the temperature region between $10^{4.3}$ to $10^{5.7}$ K, so we adopt the temperature of $\log T \approx 5.0$ as the typical temperature. Based on these temperature constraints, thermal limits of b values for metal ions are constrained to be in the range $20 - 30$ km s^{-1}, while it is 40 km s^{-1} for H I. For ions that can be resolved into two components, this range is consistent with b values shown in Table 2.1, while O VI and H I are consistent with the assumption we used to measure the column density. This consistency indicates that most of ions are in a quiescent state without significant turbulence or convection.

2.5.3 Interaction Layers or A Hot Halo?

There are two possibilities for the intervening absorption due to foreground galaxies – the interaction layer or the hot halo. The interaction layer is the interface between a cool cloud ($\sim 10^3$ K) and the surrounding hot gas ($\sim 10^6$ K) in the halo (Kwak & Shelton, 2010). In this mixing interface, multiple intermediate ions can be produced, such as O VI, O V and Si IV. Based on our modeling results, we may distinguish these two origins for the Mg X system.

Previous works on intervening Ne VIII systems argued that high ionization state ions may also be produced in this interaction layer because of their relatively lower temperature $\log T \sim 5.6-5.7$ (Narayanan et al., 2011; Savage et al., 2011a; Narayanan et al., 2012). Here, they used the single temperature model to reproduce Ne VIII and O VI. However, the assumption required in this model is not substantiated. To apply the single temperature model, it is assumed that Ne VIII and O VI are from the same

gas and both collisionally ionized. Nevertheless, previous studies on intervening O VI surveys show that it could be either collisionally ionized or photoionized (Tripp et al., 2008; Thom & Chen, 2008a), which means using O VI to constrain the collisionally ionization model could result in an incorrect result. Even if O VI is collisionally ionized, recent studies on the Milky Way hot halo show that the hydrogen column density required to reproduce O VI is about one order of magnitude lower than the one derived from O VII (a higher temperature medium), which implies O VI is not cospatial with the higher temperature gas (Hodges-Kluck et al., 2016b). With an ionizational potential of 207.3 eV, Ne VIII traces a higher temperature gas, which is not cospatial with the O VI gas, so the combination of Ne VIII and O VI will result in a lower temperature. Mg X has a peak ionization fraction at $10^{6.1}$ K and has a full width of half maximum of 7.9×10^5 K. Therefore, this ion occurs at the virial temperature of a $L \sim 0.2 - 2\ L^*$ galaxy, which is also the temperature of the hot medium in interaction layer models. Thus, we suggest the gas traced by Mg X and Ne VIII is the hot halo rather than the interaction layer.

Another consideration is the intermediate ionization species column density in the interaction layer model. Currently, there are two theoretical models focusing on the interaction layer, the turbulence mixing layer model and the conductively evaporating model (Kwak & Shelton, 2010; Gnat et al., 2010; Kwak et al., 2015). The turbulence mixing layer model predicts 10^{13} to 10^{14} cm^{-2} O VI for one cloud, which means one expects around 10 clouds to reproduce the observed O VI column density. However, the expected number of cool cloud in one sightline is about 2, which can be estimated by the coverage rate ($\approx$ 90%) in the COS-Halo's sample assuming the Poisson distribution (Werk et al., 2014). The conductively evaporating model even predicts a lower O VI column density ($10^{12.5}$ cm^{-2} per layer) than the turbulence mixing layer model, which results in a larger gap between the expected cool cloud number and the required one. Therefore, this significant gap also suggests

that it is unlikely for all of the observed O VI column density to be due to interaction layers. Also, current mixing layer calculations do not include the columns of Ne VIII or Mg X, which makes it still a question that whether interaction layers can produce detectable high ionization species.

One more consideration is on the Doppler b values of metal lines, which reflect the dynamical information of the gas. As stated in Section 8.11, the gas is quiescent, showing the b value at the thermal velocity limit, which is opposite to the expectation of interaction layer models (Gnat et al., 2010; Kwak et al., 2015). In either turbulence mixing layer model or conductively evaporating model, turbulence or convection is inevitable because of the low efficiency of radiation and thermal conduction due to the low density. The turbulence velocity is about 100 km s^{-1} (Kwak & Shelton, 2010), so small b values at thermal limits ($\sim 20 - 40$ km s^{-2}) imply a volume-filled quiescent halo rather an active interaction layer. Also, small b values in our case are not unique for high ionization states in observations, which have been confirmed to be associated with galaxies. Narayanan et al. (2011) and Meiring et al. (2013) showed both O VI and Ne VIII in PKS 0405-123 and PG 1148+549 have small b values around $20 - 30$ km s^{-1}. Based on these three reasons, we suggest that the majority of the observed gas (dominating the velocity) cannot be due to interaction layers, and a hot but quiescent component should exist.

2.5.4 Implications for the Hot Halo

Based on the discussion in the former three sections, we suggest that the newly discovered high ionization gas likely originates from a volume-filled hot gaseous halo. Compared to other high ionization intervening gas (traced by Ne VIII), this Mg X system has a similar total column density of $\lesssim 10^{20}$ cm^2, but a larger temperature than the previous studies ($\gtrsim 10^6$ K; Narayanan et al. 2012).

The mass of a hot gaseous halo is related to the mass of the galaxy, which also

defines the virial temperature of the system. Theoretically, it is believed that the massive galaxy can host a hot halo at their virial temperature because of their large gravitational potential and the long cooling timescale, while the virialized gaseous halo of a low mass galaxy will not be formed due to the rapid radiative cooling (Kereš et al., 2009). The virialized hot gaseous halo ($\gtrsim 10^6$ K) results in the hot accretion mode, which means the hot gas in the inner 50 kpc radiatively cools and falls onto the galaxy. For temperatures below 5×10^5 K, nearly the entire shock-heated halo cools in less than a Hubble time, so a significant hot halo does not form, with the accreting gas being cold (Kereš et al., 2009). The only hot halo candidate ($T > 10^6$ K) is in HE 0153-4520 reported by Savage et al. (2011b), based on the presence of a Lyα absorption line with a Doppler b value of 140 km s^{-1}. However, without high ionization metal lines to confirm this suggestion, it remains possible that the broad width is due to multiple blended H I components, since it is common that the intervening systems show multiple components. The case becomes ambiguous when several weak features (only evident in the wings of the lines) blend with a strong line, because one cannot determine uniquely whether these broadened wings are from a single component.

As discussed in Section 2.4.2, a multi-temperature medium is required to model all ions in the Mg X system, and the presence of Mg X in our sample raises the upper limit of the temperature up to 10^6 K), compared with the cases with only O VI and Ne VIII ($\sim 10^{5.7}$ K). Adopting the power law model, the total hydrogen column density is 8.2×10^{19} cm^{-2} at 0.3 solar metallicity, and the index is 1.55 ± 0.41, which indicates the higher temperature gas contains most of the mass. Quantitatively, the gas associated with Mg X and Ne VIII ($5.7 < \log T \lesssim 6.0$) has a column density of 7.1×10^{19} cm^{-2}, while the gas corresponded to Ne VI and O VI ($5.5 < \log T < 5.7$) is 7.6×10^{18} cm^{-2}. This multi-phase medium is similar to the hot halo of the Milky Way, where the O VI gas is one order of magnitude lower than the O VII and O VIII

(similar temperature region to Ne VIII) gas (Hodges-Kluck et al., 2016b). Specifically, the currently observed O VII has EW around 15 mÅ, which corresponds to a column density of 5.2×10^{15} cm^{-2} (Nicastro et al., 2002; Rasmussen et al., 2003). Assuming an average ionization fraction of 50% and 0.3 solar metallicity, the total column density is of 5.3×10^{19} cm^{-2}.

Based on our fitting results, the variation of the temperature is 1.65 dex, and the characteristic temperature is approximately $10^{5.93}$ K, which means a half of the hydrogen column density is higher than this temperature. While the hydrogen column density distribution appears to have a peak around Ne VIII and Mg X, there is no information for temperatures above $\sim 10^{6.3}$ K. This shortcoming could be removed when sufficiently sensitive X-ray spectrographs can detect ions such as O VIII.

The total column density of this absorption system is $\sim 8.2\times10^{19}(0.3Z_{\odot}/Z)$ cm^{-2}, which could be used to constrain its host. Here, we show estimations of the total column density for three possible hosts (galaxy, galaxy group and galaxy cluster). We assume that the typical halo radii (R_{200}) of these three objects are 250 kpc, 1 Mpc and 3 Mpc, and the mean density is n_{200} (5×10^{-5} cm^{-3}). Based on these assumptions, the expected total column densities ($n_{200}R_{200}$) are about 3.9×10^{19}, 1.5×10^{20} and 4.6×10^{20} cm^{-2}, respectively. Thus, the column density of the hot gas seems to be reasonable for a galaxy hot halo. For Milky Way like galaxies, we show a detailed model in Fig. 2.6. In this model, we employ a β-model, where density goes as $r^{-3/2}$ and assume the baryon mass in 250 kpc (50% or 100% of the total baryons). In this plot, it is shown that $n_{200}R_{200}$ is a good indicator for the total column density, and the radial dependence of the column density shows that our absorption system correspond to a projected distance $\sim 80 - 170$ kpc.

With the power law index of 1.55, it is of interest to consider whether the temperature dependence is due to the local mixture of multiple phase gases or the large scale radial structure of the galaxy halo. Thus, we try to reproduce the power law

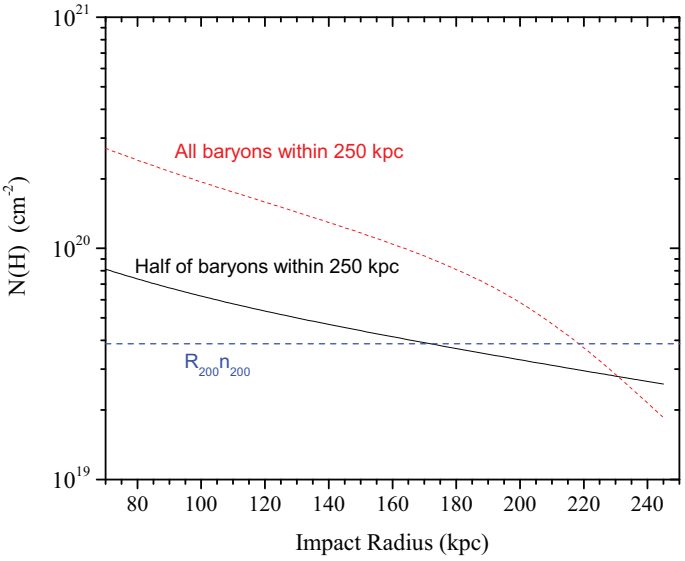

Figure 2.6: For A Milky Way type galaxy, the dotted red line is a model where all the baryons lie within $r = 250$ kpc, while the black line has half of the baryons within 250 kpc (R_{200}). The dashed blue line shows the typical column density $R_{200}n_{200}$.

model in the frame of the galaxy halo. For the radial distribution of the density, we use a modified $\beta-$model described in Miller & Bregman (2015). They show that β is 0.50 ± 0.03 for the Milky Way, which indicates $n \propto r^{-3/2}$. For the radial distribution of the temperature, we use the result from Baldi et al. (2012) for the outer region of galaxy clusters, where the temperature varies as $T \propto r^{-\alpha}$ with α of 0.6 to 1.5. If we assume this law is the same in galaxies or galaxy groups, the relationship between the column density and the temperature is

$$\frac{\mathrm{d}N}{\mathrm{d}T} \propto T^{\frac{3\beta-1}{\alpha}-1}, \tag{2.1}$$

so the power index is $\lesssim 0$, while our fitting shows a power law of

$$\frac{\mathrm{d}N}{\mathrm{d}T} = 10^{4.4\pm2.2-[Z/X]}T^{1.55\pm0.41}, \tag{2.2}$$

where T is in the range $10^{4.39\pm0.13}$ to $10^{6.04\pm0.05}$ K. The difference between the power

law index indicates the empirical model is unlikely to be as steep as our observation. This inconsistency shows that the global radial variation does not reproduce the observed ion species.

The temperature dependence of the column density may be accounted for by the local mixture of multiple phase gases, which have several origins, such as an accretion flow or stellar feedback. The accretion flow can generate cool clouds in the halo, while the stellar feedback can not inject cool clouds to large radii ($\gtrsim$ 100 kpc). The involvement of low temperature gas will lead to the mixture with the hot halo, then, the intermediate state can be generated in interaction layers. Therefore, the column density distribution may be divided into three parts – the cool gas, the interaction layer and the hot halo.

CHAPTER III

An X-Ray- and SZ-bright Diffuse Source toward M31: A Local Hot Bridge

3.1 Introduction

As the best-studied galaxy, the Milky Way (MW) is found to suffer from the missing baryon problem. In the past decade, multi-wavelength observations revealed that the multi-phase medium within the virial radius of the MW could only account for $\approx 10^{11}\ M_{\odot}$ of baryons (Anderson & Bregman, 2010; Gupta et al., 2012; Miller & Bregman, 2015; Zheng et al., 2019a; Qu et al., 2020). Considering the MW halo mass of $1 - 2 \times 10^{12}\ M_{\odot}$ (Xue et al., 2008), about half of the expected baryons are still missing from observations (adopting the cosmic baryonic fraction of 0.158; Planck Collaboration et al. 2016a). One possible solution to this missing baryon problem is that baryons are beyond the virialized halo of the MW.

It is well known that the MW is embedded in the local group (LG), which is dominated by two member galaxies with similar masses: the MW and the Andromeda galaxy (M31; Einasto & Lynden-Bell 1982). The halo mass of the LG is found to be $\log M \approx 12.26 - 12.83$ and hosts a hot gas-dominated multi-phase medium by matching the local environment (e.g., satellite galaxies) with simulations (Li & White, 2008; Nuza et al., 2014). Observationally, cool-warm clouds ($\log T \approx 4 - 5$)

are detected towards both M31 and anti-M31 directions by detecting the ultraviolet (UV) and H I high velocity clouds (Bouma et al., 2019). However, these cool-warm gases only contribute to a small fraction of the total gas mass, and it is still an open question as to the properties of the major gaseous medium associated with the LG.

Observations of X-ray and Sunyaev-Zeldovich (SZ) effect are two effective means to detect the hotter gas than the UV-tracing gas (Bregman, 2007). X-ray ions O VII and O VIII are the two most common high ionization state ions in the Universe, and trace gases at $\log T = 5.5$ to 6.8. The SZ signal is sensitive to all hot gas (electron; $\log T > 6$). Previous studies show that the hot gas covering the entire sky is mainly Galactic rather than from the LG (Bregman & Lloyd-Davies, 2007), which is determined by the spatial distribution of the O VII absorption equivalent width. Previous efforts to search for the LG hot gas associated led to upper limits by considering the X-ray emission (*ASCA*, *Einstein*, and *ROSAT*) and SZ signals (*COBE* and *Planck*; e.g., Suto et al. 1996; Pildis & McGaugh 1996; Banday & Górski 1996; Sidher et al. 1999; Rasmussen & Pedersen 2001; Rubin & Loeb 2014).

In this paper, we analyze the X-ray data (i.e., O VII and O VIII line measurements obtained by *XMM-Newton*) and the SZ y signal (extracted from *WMAP* and *Planck* maps) toward the M31 direction. We discover a $r \approx 20^\circ$ diffuse hot gas feature toward M31, which is confirmed by both X-ray emission and SZ y signals. This diffuse hot gas is likely to be a Local Hot Bridge connecting the MW and M31, which accounts for a significant baryonic mass. The adopted data are mainly from Henley & Shelton (2012, hereafter, HS12; O VII and O VIII line measurements) and Qu et al. (2020, in preparation; SZ extraction). The sample and data reduction are briefly introduced in Section 2. The origins of this feature and physical implications are discussed in Section 3, where we develop a toy model of the Local Hot Bridge, and discuss observational limitations and caveats. We summarize key results in Section 4.

3.2 Data and Reduction

In the following analyses, we adopt the distance to M31 of $D_{\rm M31} = 750$ kpc (Riess et al., 2012), and assume that the projected center of the diffuse hot gas is at M31 (l, $b = 121.17°$, $-21.57°$). Although the real center is unknown, the commonly used barycenter of LG (l, $b = 147°$, $-25°$; Einasto & Lynden-Bell 1982) is not favored by both X-ray line measurements and SZ y signals.

3.2.1 The O VII and O VIII Emission Measurements

The adopted O VII and O VIII emission line measurements are originally extracted by HS12. Here, we only briefly describe the criteria for the subset of data used in our study and refer readers to the original paper for the construction of the sample. Using *XMM-Newton* archival data, HS12 selected all observations with good time longer than 5 ks (not affected by Solar flares). They constructed two samples – a Solar wind charge exchange (SWCX) clean sample of 1868 sight lines (determined by the Solar wind proton flux); and a low extra-galactic emission sample of 1003 sight lines with an additional constraint on the X-ray flux at $2-5$ keV. The SWCX could introduce non-astrophysical O VII and O VIII emissions, which is problematic when extracting the all-sky diffuse emission. Therefore, a low Solar wind proton flux is crucial to have a clean sample with low SWCX contamination. The X-ray flux at $2-5$ keV is mainly a criterion to constrain the contamination due to background AGNs. Using the SWCX-clean and low-background sample, Miller & Bregman (2015, hereafter MB15) applied an additional filter, which cross-matches the *XMM-Newton* field (a field of view of 0.5°) with known strong X-ray sources (e.g., *ROSAT* catalogs and galaxy clusters; Voges et al. 1999; Piffaretti et al. 2011) to lower possible contamination. This additional filtering leads to a sub-sample of 649 sight lines.

These 649 sight lines only have 9 sight lines in the $r = 25°$ circle around M31. To use more observations, we also include another 25 sight lines from the original

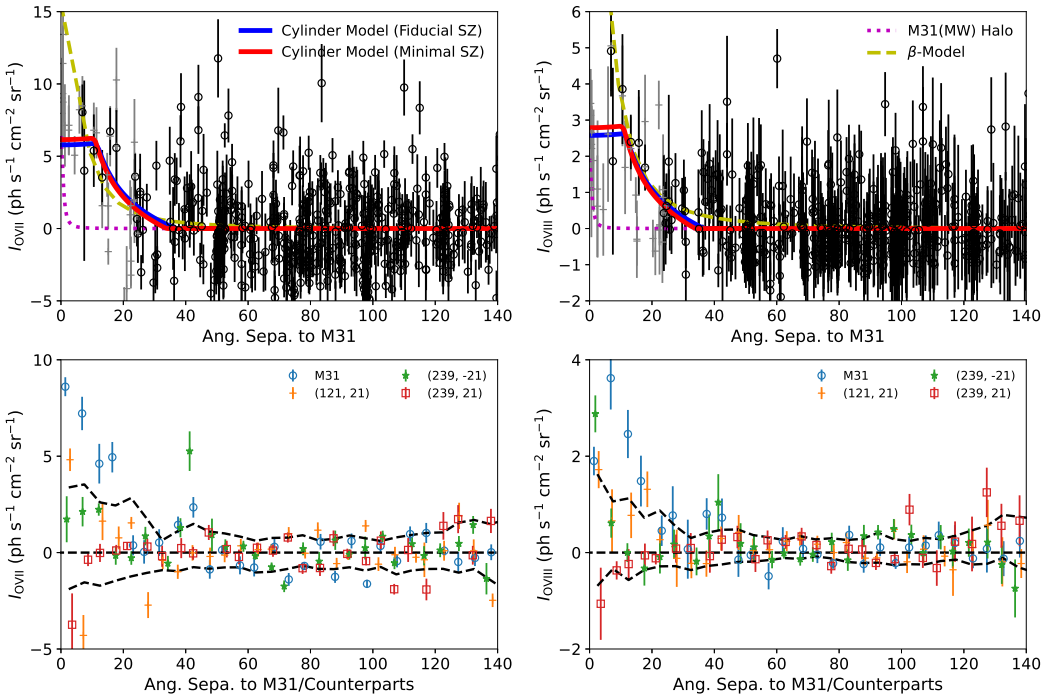

Figure 3.1: The upper two panels show the X-ray emission line measurements (corrected for the MW model) for O VII (left) and O VIII (right). The black circles are adopted from MB15, while the grey crosses are from HS12 (the 1868 sight line sample), which may have more contamination. For both samples, we masked out the region within 60° around the Galactic center, and the measurements with large uncertainties (> 3 L.U. for O VII and > 2 L.U. for O VIII). The yellow dashed lines are a projected β-model based on the input model from the SZ extraction, which has a core of 8°. This model systematically overestimates the strengths of O VII, O VIII emission measurements and SZ y. The magenta dotted lines are a projected MW-like halo at the distance of M31. The blue and red solid lines are the Bridge (cylinder) model connecting the MW and M31 for fiducial SZ and minimal SZ, which are shown in the Fig. 3.3. The lower panels show the radial profile (5° bins) of O VII and O VIII Galactic-symmetric regions of M31 ($l = 121.17°$ or $238.83°$, $b = \pm 21.57°$). In these two plots, sight lines have the same weights in the HS12 and the MB15 samples. The black dashed lines show the 1σ uncertainty of the radial profile of random sight lines with fixed $b = \pm 25°$. The signals toward M31 are higher than the other three regions and random sight lines, which indicates it is not a systematical feature associated with the Galactic disk.

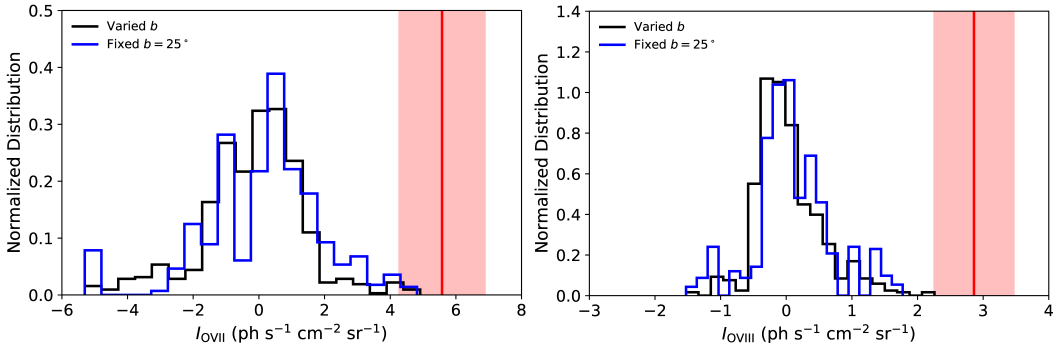

Figure 3.2: The simulation of the significance of O VII and O VIII. we compare the M31 O VII and O VIII measurements to the strength distribution of random sight lines (within 20°) over the entire sky (black) and with fixed latitudes at $b = \pm 25°$ (blue). These tests leads to significances of 3.6σ (3.0σ for fixed b) and 5.6σ (4.8σ) for O VII and O VIII measurements, respectively.

sample (1868 sight lines) of HS12, which are within $r = 25°$ around M31, and have small uncertainties ($<$ 3 L.U. for O VII and $<$ 2 L.U. for O VIII; L.U. has units of ph^{-1} cm^{-2} s^{-1} sr^{-1}). The low uncertainty criterion is also applied to the MB15 sample. We note that 7/25 sight lines are in the M31 disk, which might affect the O VII and O VIII extractions because of the thermal component in M31 disk. These additional sight lines from HS12 may have larger contamination compared to the subset used in MB15. Therefore, in the following modeling, we will lower the significance of these additional sight lines.

We examine the emission around M31 by subtracting the MW contribution, since the all-sky O VII and O VIII emission are dominated by the Galactic hot halo (Henley & Shelton, 2013). Here, we adopt the Li & Bregman (2017) model (model No. 9 in Table 1; hereafter LB17; Fig. 5 in LB17), which considered a β-model $n(r) = n_0(1+(r/r_{\rm c})^2)^{-3/2\beta}$ and an exponential disk ($n(r_{\rm XY}, z) = \exp(-r_{\rm XY}/r_0 - z/z_0)$) with radiative transfer. For this Galactic model, we adopt the same assumptions as LB17 to correct the hydrogen absorption and the contribution due to the Local Bubble (LB).

The O VII and O VIII line measurement residuals show a north-south asymmetry,

which is commonly seen for multi-wavelength observations (e.g., the warm gas; Qu et al. 2019). The O VII emission is systematically higher in the northern hemisphere than the southern hemisphere, while the O VIII measurements show the opposite trend. The difference between the two hemispheres is about $10 - 20\%$. To better model the MW emission (649 sight line sample), we use two normalization factors to reduce the median values of the residuals to zero for the northern and southern hemispheres, respectively.

In Fig. 3.1, we show the residuals projected around M31. It is clear that both O VII and O VIII emission measurements show enhancements in addition to the Galactic emission. This enhancement shows a plateau shape within $\theta_0 \approx 15^\circ$ of M31, and decays to the zero beyond $\theta_1 \approx 30^\circ$. The extra sight lines from HS12 are consistent with the MB15 sample for the O VII. The O VIII emission measurements shows 3 additional sight lines from HS12 are slightly lower (≈ 1 L.U.) than the plateau of the MB15 sample within 10°.

The X-ray emitting region around M31 has an angular diameter of 40°. Within $r = 20^\circ$, the O VII enhancement (Galactic emission subtracted) has a mean value of 5.6 ± 1.3 L.U., which is about the same level as the all-sky Galactic O VII emission ($\approx 5 - 6$ L.U. for the MB15 sample). The O VIII enhancement is about 2.8 ± 0.6 L.U. within $r = 20^\circ$, which is higher than the Galactic O VIII emission (≈ 1.3 L.U.). Using the additional sight lines from HS12, the mean values are 5.5 ± 0.5 L.U. and 1.8 ± 0.3 L.U. for O VII and O VIII (excluding the central 2° to avoid the M31 halo or disk contribution). The final detection significance is given in Section 3.2 by a Markov chain Monte Carlo (MCMC) model, which is slightly lower (4.8σ and 4.5σ) because we lower the weights of additional sight lines in the HS12 sample.

There are two caveats for this extraction, because the LB17 model only models the large scale variation of the Galactic emission, and is dominated by the hot halo of a β-model. First, some X-ray studies suggest that the Galactic emission is dominated by a

disk component (Nakashima et al., 2018; Kaaret et al., 2020). If the disk component is not correctly accounted for in the LB17 model, it is possible that a variation over Galactic latitudes (higher at low latitudes) leads to the observed feature around M31 because of the low latitude of M31. In Fig. 3.1, we plot the radial profiles of both O VII and O VIII measurements for the Galactic-symmetrical regions of M31 ($l = 121.17^\circ$ or 238.83°, and $b = \pm 21.57$). The signal toward M31 is higher than other directions, which disfavors the possibility that the observed feature around M31 is due to unaccounted large-scale variations (i.e., the disk component).

To further investigate this possibility, we also extract 300 random sight lines over all Galactic longitudes, but with limited Galactic latitudes ($b = \pm 25^\circ$) to represent the disk variation at similar latitudes of M31. The 1σ radial profile uncertainty is plotted in the lower panels of Fig. 3.1. It is clear that only the M31 direction shows a significant enhancement within 20° away from M31. We also note that the mean residuals of O VII and O VIII emission are slightly positive around M31 ($0.1 - 0.2$ L. U.), which may be evidence for the disk component enhancement. However, the significance of this enhancement is about 0.5σ and 0.8σ for O VII and O VIII, respectively, which is likely to be random variation. Also, even if this enhancement is real, it only affects the measurement of the X-ray enhancement around M31 by $2 - 10\%$, and should not affect the detection of the M31 enhancement. However, it may influence the derivation of the mass and the metallicity (see discussions in Section 3.4).

Second, the auto-correlation suggests there are remained features $< 20^\circ$ in the residuals of O VII and O VIII measurements. We simulate random sight lines to test whether the feature around M31 is due to the random variation of all-sky Galactic emission rather than a disk variation. We extract 1000 random sight lines over the entire sky, and calculate the median of residuals within 20° for each sight line. We mask out the 30° region around M31 to avoid a contribution from the M31 feature

to null tests. None of these random sight lines has a similar strength of the feature seen toward M31. Based on this test (Fig. 3.2), the significance is 3.6σ and 5.6σ for O VII and O VIII, respectively. For the simulation of limited latitudes ($b = \pm 25^\circ$), the extracted significance is reduced to 3.0σ and 4.8σ for O VII and O VIII. We note that O VII is more affected by features in the disk (e.g., supernova remnants), leading to larger residuals and a somewhat lower significance.

3.2.2 The SZ y Extraction

The adopted SZ data in this work will be described in Qu et al. (2020, in preparation) as a part of the all-sky large-scale SZ signal. Here, we briefly describe the data reduction. We combine the nine-year *WMAP* (Bennett et al., 2013) and the *Planck* data release 3 (PR3) single frequency maps (Planck Collaboration et al., 2020) to extract the SZ signal. A low-pass filter is applied to extract large-scale features (FWHM $> 5^\circ$). To avoid the dust contamination, we masked out 40% of the highest intensity dust region around the sky (determined in the *Planck* 353 GHz map), and the PCCS catalog for point sources (Planck Collaboration et al., 2016b). We also exclude the region around the ecliptic plane ($\pm 10^\circ$), because the Zodiacal dust contribution is not fully removed in the PR3 maps, showing significant zodiacal contamination of the SZ y (Qu et al. 2020, in preparation). After these exclusions, 22% of the sky remains. Toward M31 there are useful SZ signals from the half of $b \lesssim -20^\circ$, mainly due to Galactic dust exclusion regions.

We use the internal linear combination (ILC) method to extract large scale features. The standard ILC method minimizes the variance of the extracted SZ map, which could introduce bias reducing the SZ signal strength (more details in Eriksen et al. 2004; Delabrouille et al. 2009). Here, we use the ILC to do the model fitting, which has an input model for the large scale features. We minimize the variance of the SZ residual maps (i.e., the difference between the extracted SZ map and the

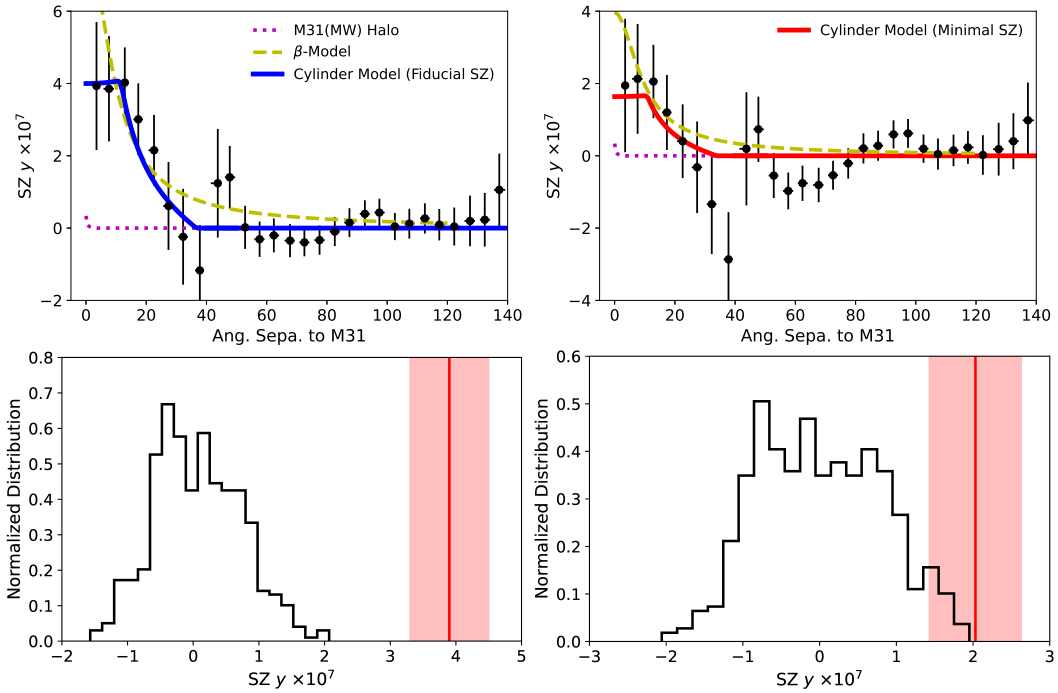

Figure 3.3: The upper two panels show the fiducial SZ extraction (left) and the minimal SZ extraction (right), while different models have the same colors as Fig. 3.1. For the SZ extraction, the data points are binned in 5° bins. In the fiducial SZ extraction, we include all four components (i.e., the MW, M31, the local Universe, and the cosmic SZ) in the extraction, which may overestimate the SZ strength. The feature at 45° in the fiducial extraction is a random variation with a significance of 1.8σ, which is a result of the small area left after our heavy masking of the Galactic disk, the ecliptic plane, and point sources. By disabling the model of M31 and the MW, we extract the minimal SZ strength (see the text for details). The β-model is scaled down by a factor of 2 in the minimal SZ plot. The lowers panels show random sight line tests for the two SZ extractions, which leads to significance of 5.9σ and 2.5σ.

input model) instead of the extracted SZ map (the standard ILC). Therefore, this is a model-dependent extraction of the SZ signal, and we vary the input model to minimize the variance of the residual map. Then, the SZ extraction and model fitting are performed simultaneously.

Our fiducial input model includes four large scale features: the foreground MW SZ, the feature around M31, the local Universe SZ (e.g., the Virgo cluster), and the cosmic SZ background (i.e., the integration over all redshifts). The MW foreground SZ is decomposed into two components: a Gaussian disk; and a spherical β-model halo. The feature around M31 is modeled as a cored power-law ($y(\theta) = y_0(1 + (\theta/\theta_c)^2)^{-\alpha}$), where θ is the angular distance from the center of M31, and with a fixed core radius of $\theta_c = 8^\circ$ (100 kpc at M31). The local Universe SZ is constructed based on the low-z galaxy group and cluster catalog from Lim et al. (2017, $\log M_{\rm halo} > 13$). For each halo, the total SZ Y is calculated by using the mass-SZ y scaling relationship from Pratt & Bregman (2020, extrapolated from $\log M$ =13.25 to 13), and the universal pressure profile is adopted from Arnaud et al. (2010). The cosmic SZ is modeled as a constant over the entire sky since the large scale variations are included in the local Universe SZ component. Using the MCMC model, we constrain the parameters in these components. Our fitting results suggested that these four components are significant ($> 5\sigma$). In this paper, we focus on the feature around M31, while more results on other components will be discussed in Qu et al. (2020, in preparation).

The final M31 features are extracted from the M31 model along with the total residual (the total model subtracted from the extracted SZ map). We extract the radial profile in bins of 5° in Fig. 3.3, where the input model is also plotted. A cored power-law model over-predicts the SZ signal for $\theta \lesssim 15^\circ$, but the residual could correct this tendency. The final extracted SZ shows a significant plateau at $y \approx 4 \times 10^{-7}$ within $\approx 15^\circ$. We refer to this extraction as the fiducial SZ y signal, which is preferred.

The model-dependent extraction of signals may have biases that overestimate the signal, so we test whether one could see similar signals without the input model. In Fig. 3.3, we also show the case in which only the local Universe and the cosmic SZ components are included in the extraction, which leaves out the MW and M31 components. This extraction shows a similar plateau shape, but the strength is about half of the fiducial extraction ($y \approx 2 \times 10^{-7}$). However, the background around M31 shows large scale structures, which are corrected in the fiducial extraction. This extraction leads to the minimal SZ signal, because the ILC method has a bias to reduce the signal (Delabrouille et al., 2009). The ILC bias is the systematic cancelling of the SZ signal due to empirical correlation between the SZ signal and random noise or astrophysical signals (e.g., the dust and the point sources). According to Delabrouille et al. (2009), we estimate the ILC bias for our extraction is about 5×10^{-8}, which is considerable relative to the total SZ signal.

The uncertainty of the SZ extraction has two origins, the model uncertainty obtained from the MCMC model, and the residual variation (including measurement uncertainties and contaminations). Using the MCMC chain, the model uncertainty is extracted, which is less than 10^{-8} around M31, so the final uncertainty is dominated by the residual variation. We calculate the global standard deviation over the entire sky (except for the region around M31 within 30°), and scaled it by a $-1/2$ power law with the number of independent spherical harmonic modes in each angular bin. For the entire sky, there are 1466 independent modes for FWHM $> 5°$, and 328 modes left after the masking. Then, we can use the number of pixels to calculate the equivalent number of modes in each bin, and subsequently, the uncertainty. This uncertainty leads to a reduced $\chi^2 = 0.81$ for regions $> 40°$ from M31, which are expected to have no features.

We use two means to determine the significance of the SZ extraction. The direct calculation is the integration of the radial profiles within 20°, which gives a signifi-

cance of 6.6σ and 3.3σ for fiducial and minimal extractions, respectively. In another estimation, we simulate 1000 random sight lines over the entire sky, and extract the median SZ within 20° around these sight lines. For these sight lines, we require that there should be more than 1000 pixels (pixel size of $\approx 0.5°$) within the 20° region (affected by the mask), since the 20° region around M31 has 1244 pixels, and a small number of pixels leads to a larger uncertainty. Based on the SZ distribution of simulated sight lines (Fig. 3.3), we determine that the median SZ signal around M31 is 5.9σ away from the random distribution for the fiducial extraction, and 2.5σ for the minimal extraction. The simulation significances are slightly smaller than the local significance, which indicates that there are still unaccounted features in the sky (e.g., small-scale Galactic features or contamination).

3.3 Physical Conditions of the Hot Gas

3.3.1 A β-Model Halo?

We rule out this feature to be the M31 hot halo for two reasons. First, one needs a core radius of 200 kpc to explain the plateau of 15°, which would be quite unusual for a galaxy group (typical values of tens of kpc). Second, using the SZ signal, one could estimate the total mass at a given temperature. For M31 (an MW-like galaxy), the halo temperature is about $2-3\times10^6$ K. Then, one could estimate the mass of such a SZ feature to be

$$M_{\rm SZ} \approx 2.5\times10^{12} M_\odot \frac{{\rm SZ}y_0}{4\times10^{-7}} \frac{2.5\times10^6}{T({\rm K})} (\frac{D({\rm kpc})}{750})^2, \tag{3.1}$$

where ${\rm SZ}y_0$ is the SZ strength of the plateau, D is the distance of the hot gas, and T is the temperature. Such a massive hot medium exceeds the cosmic baryonic fraction ($\Omega_{b,0}/\Omega_{m,0} = 0.158$; Planck Collaboration et al. 2016a). The halo mass of the local group is $\log M = 12.72$ (12.26 to 12.83; $5-95\%$; Li & White 2008), and the expected

total baryonic mass is about 8.3 $(2.9 - 10.7) \times 10^{11}\ M_{\odot}$. A mass of $2.5 \times 10^{12} M_{\odot}$ is too large by a factor of $3 - 10$ to be physically plausible.

If this β-model halo is between M31 and MW (400 kpc to MW), the required core radius is about 100 kpc, which is larger than generally seen in galaxy groups but not unreasonably so (Mulchaey, 2000). The estimated mass will be about $8.8 \times 10^{11}\ M_{\odot}$. However, a $\beta = 0.5$ model (typical values of galaxy groups) suggests a long tail to larger angles (Fig. 3.3). Using current data, the SZ signal does not favor a long tail, while the existence of this long tail cannot be distinguished by the O VII and O VIII emission measurements (Fig. 3.1). A varied β extraction leads to $\beta > 1$, which is not found for the β-model of galaxies or galaxy groups (Osmond & Ponman, 2004). Therefore, we do not favor this explanation either, but this is not a completely unphysical model.

3.3.2 A Galactic Source?

We consider whether the detected diffuse feature belongs to Galactic structures (e.g., Case B and C in Fig. 3.4). We derive the scaling relationships between physical parameters with the distance under the observational constraints. Here, we assume that the hot diffuse structure has a length of L_0 and a radius of R_0. Then, the two ratios of L_0/D and R_0/D are determined by θ_0 and θ_1.The temperature is a constant that is determined by the O VII/O VIII ratio. Two other constraints nTL_0 and $Zn^2\Lambda L_0$ are also constant, determined by the SZ and the O VII or O VIII emission. At a distance of D_{10} (in units of 10 kpc), the scaling relations (with the fiducial SZ

value) will be

$$
\begin{aligned}
L_0 &\approx 9.7 D_{10} \text{ kpc} \\
R_0 &\approx 3.2 D_{10} \text{ kpc} \\
n &\approx 5.0 D_{10}^{-1} \times 10^{-2} \text{ cm}^{-3} \\
Z &\approx 2.4 D_{10} \times 10^{-3} Z_{\odot}
\end{aligned}
$$

$$
\begin{aligned}
M &\approx 4.4 D_{10}^2 \times 10^8 M_{\odot} \\
L_{\rm OVII+OVIII} &\approx 9.2 D_{10}^2 \times 10^{36} \text{ erg s}^{-1} \\
L_{\rm X} &\approx 3.0 D_{10} \times 10^{40} \text{ erg s}^{-1} \\
I_{\rm X} &\approx 6.2 D_{10}^{-1} \times 10^{37} \text{ erg s}^{-1} \text{ kpc}^{-2} \text{ sr}^{-1}. \qquad (3.2)
\end{aligned}
$$

$L_{\rm OVII+OVIII}$ is the total luminosity of O VII and O VIII, and $L_{\rm X}$ and $I_{\rm X}$ are the X-ray bolometric luminosity and the X-ray surface brightness. To convert $L_{\rm OVII+OVIII}$ to $L_{\rm X}$, we adopt the APEC model (Smith et al., 2001). This conversion factor is proportional to the inverse of the metallicity, because when $Z \lesssim 0.01$, the X-ray emissivity is dominated by bremsstrahlung emission rather than metal lines.

This feature cannot be too close to the Sun (e.g., $D < 10$ kpc), or it would have been discovered by all-sky X-ray surveys (e.g., *ROSAT*; Snowden et al. 1997) because of the high surface brightness ($I_{\rm X}$). As a comparison, the unabsorbed Galactic X-ray emission is about $3 - 4 \times 10^{35}$ erg s^{-1} kpc^{-2} sr^{-1}. Also, the mass of this feature will be larger than 4×10^6 $M_{\odot}$ at $D > 1$ kpc, which is unlikely to be a feature in the disk.

We also suggest that this hot gas structure cannot be in the MW halo (≈ 100 kpc) because of the resulting high pressure. In the MW halo, the typical ambient gas pressure is about $n_{200} T_{\rm vir} \approx 100$ K cm^{-3}, where n_{200} is 200 times the critical matter density, and $T_{\rm vir}$ is the virial temperature. If the detected hot gas structure is about

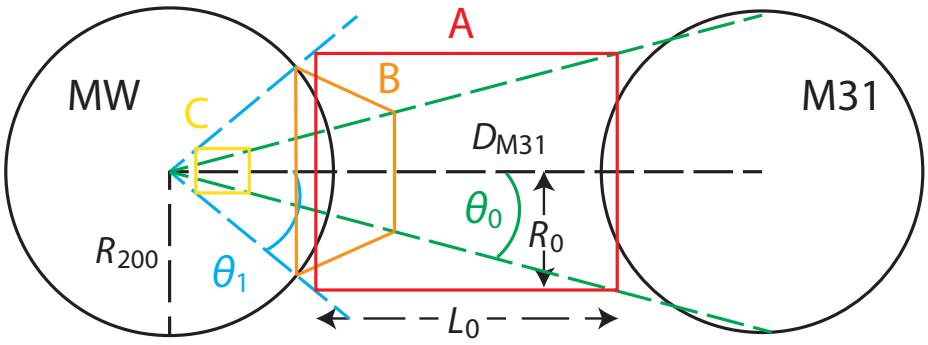

Figure 3.4: An illustration of the geometry of the Local Bridge. The plateau feature indicates two characteristic angels: the ending angle of the plateau (θ_0) and the angle beyond which the emission is zero (θ_1). Case A is the fitting model described in Section 3.3. Cases B and C are discussed in section 3.2.

100 kpc away from the Sun, the hot gas pressure will be about 1.1×10^4 K cm^{-3}, two orders of magnitude greater than expectations. Therefore, it is very unlikely to be a structure in the MW halo.

3.3.3 The Local Hot Bridge Connecting MW and M31 – A Single-Phase Toy Model

The plateau of the SZ signal inspires a toy model of a hot bridge connecting the MW and M31. As suggested by simulations (e.g., Nuza et al. 2014), a hot bridge occurs between the MW and M31 after $z < 1$, although these two galaxies have not yet entered each others virial radius (Nuza et al., 2014). Here, we use the simplest assumption to model the observation – a single temperature, uniformly distributed medium filling in a cylinder between the MW and M31 (Fig. 3.4). The direction of this cylinder is toward M31, and the barycenter is the middle point along the sight line (375 kpc). The length and radius of the cylinder are L_0 and R_0, respectively.

It is well known that the CGM is typically multi-phase (Tumlinson et al. 2017 and references therein). However, a multi-phase medium model cannot be constrained without direct observations of cool or warm gas associated with the bridge. In sec-

Table 3.1: Properties of the Local Hot Bridge

	Fiducial SZ	Minimal SZ
$I_{\rm OVII,0}$ (L.U.)	$5.7^{+1.3}_{-1.2}$	$6.0^{+1.4}_{-1.3}$
$I_{\rm OVIII,0}$ (L.U.)	$2.5^{+0.6}_{-0.5}$	$2.8^{+0.7}_{-0.6}$
SZy_0	$3.9 \pm 0.8 \times 10^{-7}$	$1.62^{+0.9}_{-1.0} \times 10^{-7}$
L_0 (kpc)	430 ± 150	420 ± 150
D_0 (kpc)	120 ± 20	110 ± 20
$\log n_{\rm H}({\rm cm}^{-1})$	$-2.91^{+0.17}_{-0.14}$	$-3.29^{+0.26}_{-0.45}$
$\log T({\rm K})$	6.35 ± 0.03	6.35 ± 0.03
$\log M_{\rm hot}(M_\odot)$	11.74 ± 0.11	$11.28^{+0.22}_{-0.42}$
$\log M_{\rm oxy}(M_\odot)$	7.68 ± 0.15	$8.08^{+0.46}_{-0.25}$
$L_{\rm OVII}$ (erg s^{-1})	$8.9^{+2.2}_{-2.1} \times 10^{39}$	$8.3^{+2.2}_{-2.0} \times 10^{39}$
$L_{\rm OVIII}$ (erg s^{-1})	$4.5 \pm 1.0 \times 10^{39}$	$4.2^{+1.4}_{-1.2} \times 10^{39}$
$L_{\rm X}{}^a$ (erg s^{-1})	$1.1 \pm 0.3 \times 10^{42}$	$2.6 \pm 0.8 \times 10^{41}$
$\log Z/Z_\odot$	-2.0 ± 0.2	$-1.2^{+0.9}_{-0.4}$

Note: all parameters in this table are based on the single phase assumption, the correction due to the multi-phase medium is in Section 3.4.2.
[a] adopting the APEC model to convert the line emissivity to the bolometric luminosity.

tion 3.4, we discuss the limitation (bias) introduced by the single-phase assumption, together with the observational limitations.

The strength of O VII and O VIII emission measurements or the SZ y signal is proportional to the path length in the cylinder. There are two characteristic angles for this bridge model: the opening angle at the M31 side, $\tan\theta_0 = R_0/(D_{\rm M31}/2 + L_0/2)$, and the opening angle at the MW side, $\tan\theta_1 = R_0/(D_{\rm M31}/2 - L_0/2)$. Based on these two angles, the path length in the cylinder could be divided into three regimes:

$$\begin{aligned} L_{\rm Cyl} &= L_0/\cos\theta,\ 0 < \theta < \theta_0, \\ &= R_0/\sin\theta - D_{\rm min}/\cos\theta,\ \theta_0 \le \theta < \theta_1, \\ &= 0,\ \theta_1 \le \theta, \end{aligned} \tag{3.3}$$

where $D_{\rm min}$ is $D_{\rm M31}/2 - L_0/2$.

Within the cylinder, the gas is assumed to be well mixed, with the same density,

temperature, and metallicity. For the O VII and O VIII emission, we use the AtomDB data set to extract the emissivity at different temperatures (Foster et al., 2012). A factor of 0.58 is used to correct the solar oxygen abundance difference, 8.5×10^{-4} in AtomDB (Anders & Grevesse, 1989), and we use 4.9×10^{-4} from Asplund et al. (2009).

The M31 hot halo may also contribute to the observed X-ray and SZ signals. Here, we assume that M31 hosts a MW-like hot halo (the LB17 model) at 750 kpc. The contributions due to such a hot halo are important within about $1^\circ - 2^\circ$ around M31 (Fig. 3.1 and Fig. 3.3). In practice, we subtract the contribution due to this MW-like hot halo from observed signals, before the modeling of the cylindrical hot bridge.

For the fitting, we expect that points within 25° significantly contribute to the model constraints. The MB15 sample has 9 sight lines, the SZ radial profile has 5 bins, while the HS12 sample has additional 24 sight lines. As stated in Section 2, the additional sight lines in HS12 may suffer from more contamination than MB15, so we lower their weights by a factor of 10 in the fitting. Then, the HS12 sample has about $2-3$ equivalent sight lines, which has slightly lower contributions to the model fitting than the MB15 sample and the SZ signal. We also have an additional uncertainty for O VII of 1.5 L.U., because the O VII is more clumpy, showing small scale variations (MB15, LB17). The total likelihood is

$$\ln p = -\frac{1}{2}(\sum \chi^2_{\rm MB15} + \sum \chi^2_{\rm SZ} + \frac{1}{10}\sum \chi^2_{\rm HS12}). \tag{3.4}$$

The MCMC model is calculated with *emcee* (Foreman-Mackey et al., 2013), and the results are shown in Fig. 3.5 and Fig. 3.6 for fiducial SZ and minimal SZ extractions, respectively. The physical parameters are summarized in Table 3.1.

The cylinder model suggests the length of this structure is about 400 kpc, which is sufficient to connect the dark matter halo of the MW and M31 (250 kpc for each

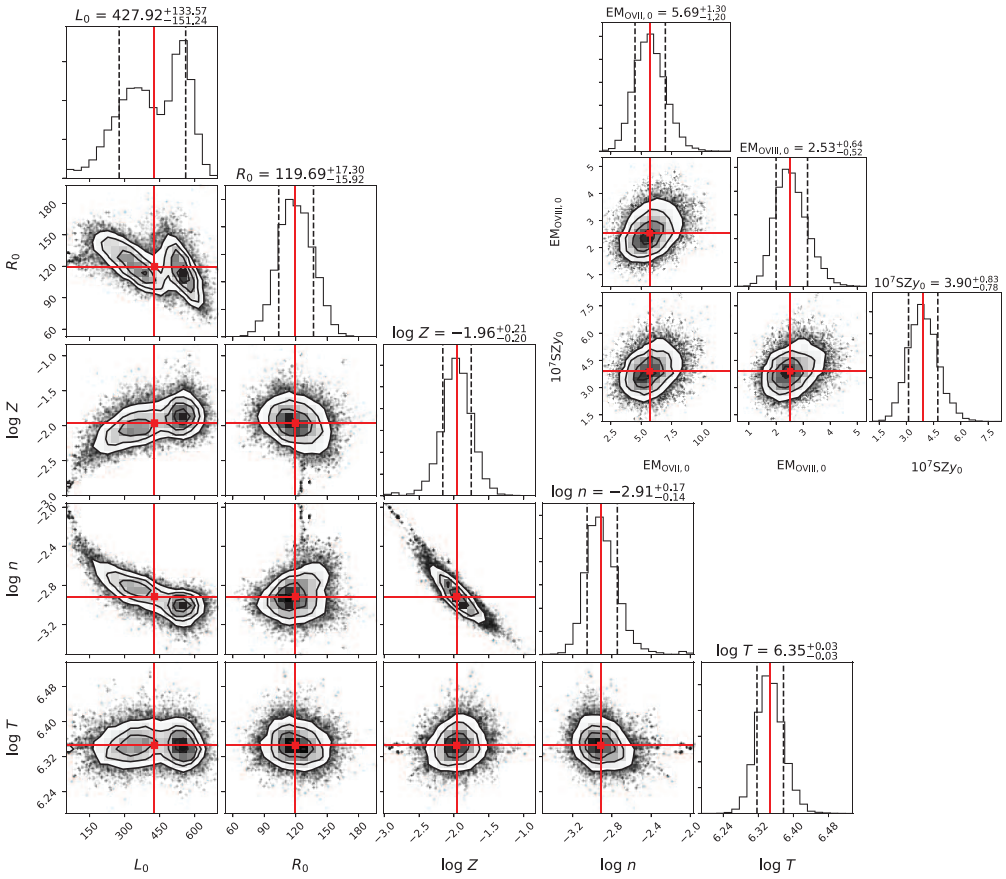

Figure 3.5: The posterior distribution of the toy model for the fiducial SZ extraction. The lower left corner plot is the input physical parameters of the length (L_0), the radius (R_0) of the cylinder, the number density ($\log n$), the metallicity ($\log Z$), and the temperature ($\log T$). The upper right plot shows the phenomenological parameters derived from the model: the strength of the plateau for O VII and O VIII emission measurements and the SZ y strength.

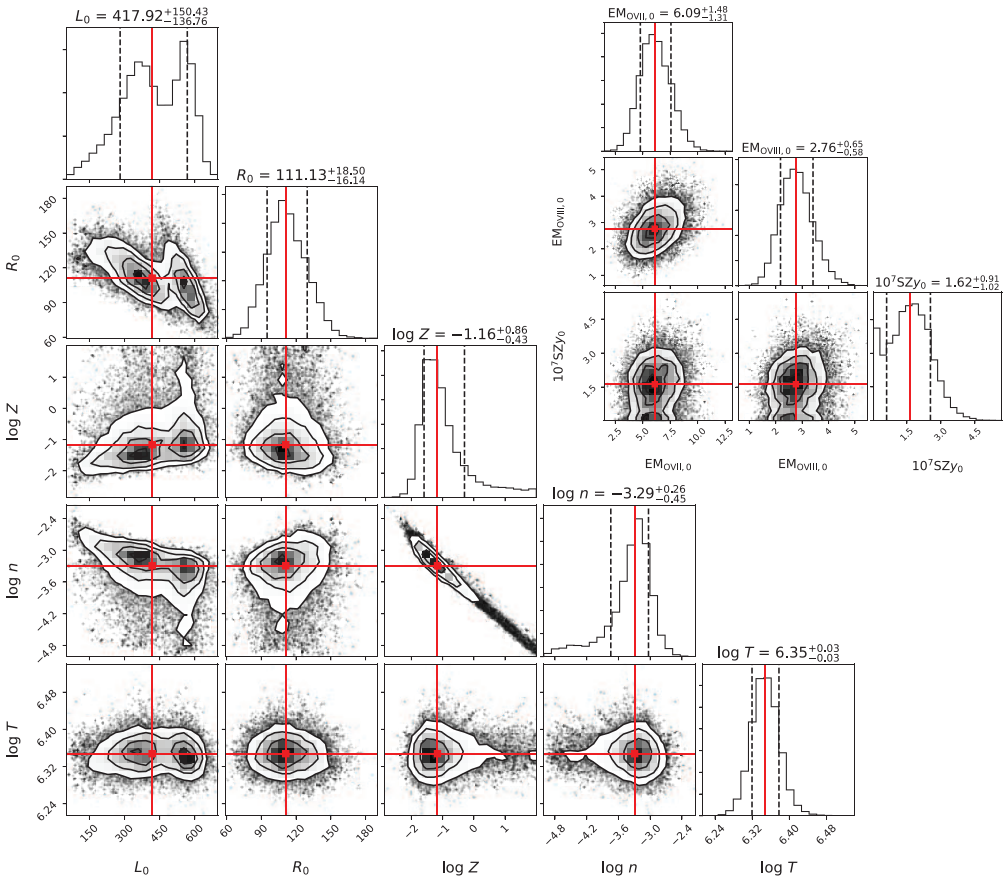

Figure 3.6: Same as Fig. 3.5, but for the minimal SZ extraction.

galaxy). Therefore, it is consistent with the assumption that the observed hot diffuse feature is a Local Hot Bridge connecting the MW and M31. It is of interest to note that a γ-ray excess is also detected projected at $\approx 4^\circ - 15^\circ$ away from M31 (Karwin et al., 2019).

For the fiducial SZ model, the estimated hot gas mass is $\log M(M_\odot) = 11.74 \pm 0.11$, while the minimal SZ model has a mass of $\log M(M_\odot) = 11.28^{+0.22}_{-0.42}$. With a LG halo mass of $\log M = 12.72$, the associated baryon mass is about $\log M = 11.92$ (Li & White, 2008; Planck Collaboration et al., 2018). Then, the Local Bridge structure contributes about 66% of the baryon mass (23% in the minimal model). As a comparison, we estimate the baryon masses in the MW and M31. The MW has a stellar mass of $\log M = 10.71 \pm 0.09$ (Licquia & Newman, 2015), a hot gas CGM of $\log M = 10.5 - 11$ (Gupta et al. 2012; MB15; LB17; Faerman et al. 2017, 2020), and a warm gas CGM of $\log M \lesssim 10$ (Zheng et al., 2019a; Qu & Bregman, 2019). M31 has a stellar mass about twice the MW of $\log M \approx 11$ (Tamm et al., 2012), but a similar halo mass of $\log M \approx 12 - 12.3$ (Kafle et al., 2018). The hot component of the M31 CGM is still unknown, but should be comparable to the MW because of the similar halo mass. The cool-warm CGM in the M31 halo has mass of $\log M \approx 10.6$ (Lehner et al., 2020). Therefore, the baryons within the MW and M31 halos account for $\log M = 11.3 - 11.6$ $(24 - 48\%)$.

We estimate the total oxygen masses are $\log M_{\rm oxy} = 7.68 \pm 0.15$ and $8.08^{+0.46}_{-0.25}$ for fiducial and minimal SZ models, respectively. According to Peeples et al. (2014), the total oxygen generated in a MW-like galaxy is $\log M_{\rm oxy} = 8.7$, and about $20 - 40\%$ of oxygen ($\log M_{\rm oxy} = 8.0 - 8.3$) is missing within the virial radius. Then, the total missing oxygen is about $\log M_{\rm oxy} = 8.3 - 8.6$, saying M31 is also a MW-like galaxy. The metals in the Local Bridge also considerably account for the LG missed metals $(10 - 80\%)$. We note that with a lower SZ strength, the oxygen mass will be higher.

The total O VII and O VIII luminosity is about $1.3 \pm 0.3 \times 10^{40}$ erg s^{-1}. Adopting

the APEC conversion factors (Smith et al., 2001), the bolometric X-ray luminosity is 1.1×10^{42} erg s^{-1} (fiducial SZ extraction) and 2.6×10^{41} erg s^{-1} (minimal SZ extraction), which are comparable to poor galaxy groups (Osmond & Ponman, 2004; O'Sullivan et al., 2014). A typical galaxy absorption toward M31 of 5×10^{20} cm^{-2} leads to an observed luminosity of $\approx 5 - 6 \times 10^{38}$ erg s^{-1} the $0.2 - 5$ keV band for the fiducial SZ extraction and $\approx 1 - 2 \times 10^{38}$ erg s^{-1} for the minimal SZ extraction.

3.3.4 Caveats and Preferred Parameters

As shown by current observations, there is an enhancement around the M31 direction, but the measurement and physical interpretation involve several uncertainties mainly due to observational limitations. Here, we summarize these observation limitations and uncertainties, and raise the caveats. With these limitations, we also discuss the preferred physical properties.

3.3.4.1 X-ray and SZ Measurement Uncertainties

In Section 2.1, we suggested that the enhancement around the M31 direction is unlikely due to a random variation at 6.6σ, or a Galactic disk variation at 5.7σ. However, it is still possible that the MW has contributions to the M31 enhancement. To have a large-scale ($\approx 20^\circ$) enhancement, the feature is likely to be close to the Sun, so the LB is a possible source for the MW variation. The LB model used in Section 2.1 is from MB15 (the same as LB17), which uses the path length derived based on Na I absorption survey of nearby stars (Lallement et al., 2003). In the MB15 model, the LB has a mean contribution to the observed O VII measurements of 0.83 L.U. with a 1σ uncertainty of 0.17 L.U., while the contribution to O VIII is negligible. Toward M31 within 20°, the LB model suggest a relatively low OVII contribution of 0.72 L.U.. Considering the variation of the LB contributions, the O VII measurement may be reduced by ≈ 0.2 L.U., which is $< 5\%$ of the O VII enhancement (5.7 L.U.).

The scatter of 20° features is 1.5 L.U. for O VII and 0.5 L.U. for O VIII (Fig. 3.1). It may affect the enhancement measurements at a similar level, which is uncertain due to the limitation of current data (i.e., more sight lines could reduce the statistical uncertainty). We are conducting a M31 hot halo study (Huang et al. in prep.), which will increase the number of sight lines around M31 within 10° (more than 30 sight lines), and improve the current situation.

The uncertainty of the SZ observation is mainly the possible overestimation of the fiducial extraction and the underestimation of the minimal extraction as stated in Section 2.2. An SZ signal of $y \approx 4 \times 10^{-7}$ in the fiducial extraction is about an upper limit of the SZ signal, while the lower limit is $y \approx 2 \times 10^{-7}$ extracted in the minimal model. Although it is possible that the real SZ signal is undetectable ($< 2 \times 10^{-7}$) because of the 2.5σ detection in the minimal extraction, the well-behaved radial profiles suggest a more physical reason rather than random variation for both extractions.

One common issue is the coverage of the feature for both SZ and X-ray signals. There is only a half of area with signals ($b \lesssim -20°$), so it is not guaranteed that the upper and the lower halves have similar signals. In an extreme case, the upper half of $b \gtrsim -20°$ does not have any enhancement. This possibility reduces the angular coverage of the observed features, but will not affect the derived temperature, density, and path length. However, it will affect the mass estimation as discussed in Section 3.4.3.

3.3.4.2 Corrections due to the Multi-Phase Medium

Although we assume a single-phase model in the toy model, the bridge structure could be multi-phase. Lehner et al. (2020) show the covering factor of strong absorption of the UV ion O VI ($\log N > 14.6$) has a tentative peak at 20° (Fig. 11 in their paper), which might indicate a transition from the hot gas to the lower-temperature

gas (i.e., multi-phase medium). However, the cool-warm gas contribution associated with the hot bridge is unknown to the observed UV absorption systems. Therefore, the temperature distribution of the multi-phase medium is also unknown. We adopt a steady-state cooling assumption ($M \sim T/\Lambda$; roughly a power law with a slope of -1.5; Qu & Bregman 2018b) for the warm-hot gas ($\log T > 5$) to investigate the acceptable temperature region. The O VII, O VIII, and SZ measurement is only sensitive to the high-temperature region, so we fix the lower temperature bound to $\log T = 6$. The maximum temperature cannot be much higher than $\log T = 6.6$, otherwise, it predicts less O VII than O VIII, while the observed ratio is about 2.

The multi-phase assumption could significantly reduce the baryon mass and raise the metallicity. The total mass is proportional to Y/T (i.e., electron column density and physical area), so a higher mean temperature gives a lower baryon mass. At $\log T = 6.3-6.4$, O VII and O VIII are at about their emissivity peaks. If more mass is in the hot phase not contributing to O VII and O VIII emission measurements, a higher metallicity is needed to match the observations. With a high-temperature end of $\log T = 6.6$, the total baryon mass will be reduced by 30%, and the metallicity will be raised by 80% for both fiducial and minimal SZ models.

In the single-phase models, the derived hot gas masses are about 5.5×10^{11} $M_\odot$ and 1.9×10^{11} $M_\odot$ for the fiducial and minimal SZ extraction, respectively (Table 3.1). Considering the multi-phase correction, the masses are reduced to 4.2×10^{11} $M_\odot$ and 1.4×10^{11} $M_\odot$. Also, the metallicity will be raised to ≈ 0.02 $Z_\odot$ (fiducial) and 0.12 $Z_\odot$ (minimal). Although this bias (always higher mass and lower metallicity in the single-phase modeling) is within the uncertainty ($\approx 1\sigma$), this trade between single-phase and the multi-phase assumptions could play an important role, when accounting for baryons or metals in the hot phase ($\log T > 6$).

3.3.4.3 Mass and Density and Metallicity

The modeling based on current data suggests a mass of $1.4 - 4.2 \times 10^{11}\ M_{\odot}$ for the hot bridge. However, as discussed in Section 3.4.1, the current data has some uncertainties, so here we provide a set of estimations for the lower limit of the hot gas mass. First, we ignore the SZ signal, which has a higher systematical uncertainty due to the extraction method. As shown in Fig. 3.5 and Fig. 3.6, the density (proportional to the mass and SZ y signal) and the metallicity are negatively correlated. Theoretically, there is a solid upper limit of the metallicity of the hot bridge at the Solar metallicity. Thus, assuming the Solar metallicity, a solid lower limit of the mass is $> 2 \times 10^{10}\ M_{\odot}$ (considering O VII and O VIII measurement uncertainties), while the preferred mass lower limit is $\approx 8 \times 10^{10}\ M_{\odot}$ (with the preferred line measurements) in the multi-phase model.

We also consider the uncertainty of the O VII and O VIII measurements by reducing the strength by a factor of 2 (i.e., $\approx 2\sigma$ of the random variation for both ions). Then, the mass lower limit is reduced to $6 \times 10^{10}\ M_{\odot}$. Because the current coverage of X-ray and SZ measurements is only the lower half ($b < -20°$), the lower limit can be reduced by another factor of 2 (i.e., only the lower half has the bridge structure). Finally, the lower limit of the bridge mass is about $3 - 4 \times 10^{10}\ M_{\odot}$, so it is still a massive baryonic component in the LG.

The upper limit of the hot gas mass is from the fiducial single-phase model (i.e., $5 - 6 \times 10^{11}\ M_{\odot}$). Then, the possible range of the mass is between $3 \times 10^{10}\ M_{\odot}$ and $6 \times 10^{11}\ M_{\odot}$, while it is likely to be higher than $7 \times 10^{10}\ M_{\odot}$ (9% of the LG baryons). For a mass of $7 \times 10^{10}\ M_{\odot}$, the conclusion still holds that the X-ray and SZ enhancement is unlikely to be the M31 hot halo. If the enhancement is around M31 at 750 kpc, the mass will be increased to $2.8 \times 10^{11}\ M_{\odot}$ (a factor of 4), which still breaks the M31 baryonic constraint: a total baryon mass of $1.6 - 3.2 \times 10^{11}\ M_{\odot}$ (Kafle et al., 2018), $\approx 1 \times 10^{11}\ M_{\odot}$ in the disk (Tamm et al., 2012), and a massive

cool-warm CGM of $> 4 \times 10^{10}$ $M_\odot$ (Lehner et al., 2020).

The upper limit of the Solar metallicity also reduces the 1σ upper limit of the oxygen mass from 3.4×10^8 $M_\odot$ to 2.1×10^8 $M_\odot$. Then, the contribution to the missing metals is reduced from 80% to 50% in the LG.

The density is proportional to the mass with the same geometry (cylindrical bridge), which is not sensitive to the O VII, O VIII, and SZ y strengths. Applying a similar estimation as the mass, the range of the density is about 2×10^{-4} to 10^{-3} cm^{-3}. This density is similar to the measured hot gas density of $1.2 \pm 0.9 \times 10^{-3}$ cm^{-3} of the bridge in the galaxy group HCG 16 (a spiral rich galaxy group; O'Sullivan et al. 2014).

With the multi-phase correction, the preferred metallicity is about 0.02 to 0.12 $Z_\odot$, which is consistent with the X-ray measurements of the HCG 16 intra-group medium (O'Sullivan et al., 2014). Here we suggest that it is also possible to be higher (even higher than the Solar metallicity) in the minimal SZ model considering the uncertainty of the y measurement. The relatively low metallicity implies an intra-group medium origin of the local hot bridge, because the CGM of the MW is expected to have a higher metallicity ($\gtrsim 0.3$ $Z_\odot$; Bregman et al. 2018).

3.4 Conclusion

The diffuse hot gas feature projected around M31 is detected in both X-ray emission lines (O VII and O VIII) and SZ y signals with a total significance of 7σ (4.8σ of O VII, 4.5σ of O VIII, and $> 2.5\sigma$ of SZ). We rule out the possibilities that this feature is the hot halo around M31, otherwise it exceeds the cosmic baryon fraction. This hot gas feature cannot be in the MW halo, due to its excessively high thermal pressure (~ 100 times the ambient hot halo), or in the MW disk (too X-ray bright). A preferred explanation is that this hot gas feature is a structure between the MW and M31. A cylinder model suggests that the length of this structure is about 400

kpc with a radius of 120 kpc. Therefore, it is a Local Hot Bridge connecting the hot halos of the MW and M31. This bridge structure has a temperature of $\approx 2.2 \times 10^6$ K, a density of $2 \times 10^{-4} - 10^{-3}$ cm^{-3}, and a metallicity $\approx 0.02 - 0.12 Z_{\odot}$. Such a hot bridge contributes about $\approx 10 - 50\%$ ($\approx 0.8 - 4.2 \times 10^{11}\ M_{\odot}$) of the total baryons in the LG, and $\approx 10 - 50\%$ of the LG missing metals (i.e., oxygen, $\approx 0.4 - 2.0 \times 10^8\ M_{\odot}$).

CHAPTER IV

The Warm Gaseous Disk and the Anisotropic Circumgalactic Medium of the Milky Way

4.1 Introduction

The gaseous baryons in galaxies can be found in both gaseous disks (the interstellar medium; Dickey & Lockman 1990) and gaseous halos (the circumgalactic medium; CGM; Putman et al. 2012; Tumlinson et al. 2017). The gaseous disks are roughly cospatial with the galaxy stellar disks, whereas the CGM are surrounding the stellar disks. H I 21 cm line surveys or ultraviolet (UV) observations reveal that the gaseous disks can extend beyond the stellar disks (up to $30-50$ kpc along the major axis) with masses from $10^7\ M_\odot$ to $\lesssim 10^{10}\ M_\odot$ for low-redshift galaxies ($z \lesssim 0.2$; Oosterloo et al. 2007; Bregman et al. 2018). With statistical assembly of Quasar-galaxy pairs in UV absorption lines, the CGM can be detected out to large radii (> 150 kpc) and contribute a large amount of baryonic materials ($\gtrsim 10^{10}\ M_\odot$) for galaxies at $z \lesssim 0.5$ (Stocke et al., 2013; Werk et al., 2014; Lehner et al., 2015; Keeney et al., 2017).

The existence of these gaseous components is important for galaxy evolution by mediating both accretion and feedback processes (Mo et al., 2010). For $L \gtrsim L^*$ galaxies, the CGM is normally volume-filled by warm-hot gas ($\log T \approx 5-7$) together with discrete cool gas clouds ($\log T \approx 4-5$), which is mainly shock-heated by gas

accreted from the intergalactic medium (IGM) and altered by feedback processes from host galaxies (Cen & Ostriker, 2006). The existence of the CGM could prevent direct accretion from the IGM; instead, it provides cooling materials from itself by thermal or gravitational instabilities (Kereš et al., 2009). These cooling flows from the CGM supplement the gaseous disk, and sustain the star formation activities in the stellar disk (Lehner & Howk, 2011; Li et al., 2014; Borthakur et al., 2015; Qu & Bregman, 2018b). In turn, the stellar and active galactic nuclei (AGN) feedback could enrich the CGM by ejecting gas, energy, and metals (Borthakur et al., 2013; Fielding et al., 2017b; Oppenheimer et al., 2018).

The warm ($\log\ T \approx 5$) gas is of special importance, since it is at transitional temperatures (the peak of the radiative cooling curve). In this temperature range, the gas could be the interaction layer between the cool gas and the warm-hot gas. These interactions are mostly associated with galactic feedback (e.g., outflows) or gas accretion onto the disk (e.g., accretion shocks). Therefore, the distribution of the warm gas is crucial to investigate these fundamental processes. Observationally, the warm gas distribution could be divided into two components: the warm gas disk and the warm CGM. The warm gas disk has been studied for both other galaxies (Boettcher et al., 2016; Zheng et al., 2017; Qu et al., 2019) and the Milky Way (MW; Howk et al. 2002; Finkbeiner 2003; Savage et al. 2003; Wakker et al. 2012). For other galaxies, the warm gas disk is detected in various observations. Direct imaging on nearby edge-on galaxies has detected the warm gas disk at radii of $\approx 1 - 10$ kpc in X-ray band, UV band, or nebula emission lines (Rand et al., 2008; Li & Wang, 2013; Boettcher et al., 2016; Hodges-Kluck et al., 2016a). However, for the warm CGM, these observations are limited at larger radii (> 50 kpc) due to the current instrument limitations and the low surface brightness of the diffuse ionized gas. An alternative is to use UV absorption lines against the continua of background AGN/stellar objects to detect gas with column densities as low as $\approx$

10^{12} cm^{-2} (Tumlinson et al. 2017 and reference therein). The warm gas is traced by intermediate-high ionization state UV ions, such as Al III, Si IV, C IV, and O VI (Stocke et al., 2013; Werk et al., 2014; Johnson et al., 2015; Lehner et al., 2015; Zheng et al., 2017; Qu et al., 2019). However, extragalactic absorption-line studies are all limited by the sample of available sightlines for individual galaxies.

The MW is a unique target to study the warm gas distribution with hundreds of sightlines over the sky mapping both the disk and the CGM (Savage et al., 1997; Howk et al., 2002; Wakker et al., 2003; Savage & Wakker, 2009; Lehner & Howk, 2011; Lehner et al., 2012; Wakker et al., 2012; Fox et al., 2014, 2015; Bordoloi et al., 2017b; Karim et al., 2018). Previous studies indicated that the warm gas could be discrete kpc-size clouds, which can be detected as intermediate-velocity clouds (IVCs) or high-velocity clouds (HVCs; Sembach et al. 2003; Wakker et al. 2003; Fox et al. 2004; Shull et al. 2009; Wakker et al. 2012; Werk et al. 2019). At large scales, the warm gas distribution in the MW was modeled as a plane-parallel slab with only one dimensional (1-D) variation over the vertical direction (perpendicular to the disk) as an exponential function of $n(z) = n_0 \exp(-|z|/z_0)$, where z_0 is the scale height (Savage & Wakker 2009 and references therein; hereafter SW09). The scale height of the warm gas disk is measured using column densities against UV-bright stars at different z-heights and AGNs. In this model, the stellar sightlines are used to estimate the ion density at the mid-plane of the disk. Combining with the sightlines toward AGNs (determining the maximum projected column density), the scale heights of the plane-parallel slab model are obtained for various ions, where no CGM component is considered. However, more recent observations reveal the CGM also contributes to the column densities of the intermediate-high ionization state ion measured in the AGN sightlines (Werk et al., 2014; Johnson et al., 2015; Lehner et al., 2015; Stocke et al., 2017; Zahedy et al., 2019). As pointed out by Zheng et al. (2019a, hereafter Zheng19), the MW CGM contributes to a significant amount of column

density to the Si IV absorption lines measured with 132 AGN sightlines obtained by the Cosmic Origins Spectrograph (COS; Green et al. 2012) on the *Hubble Space Telescope* (*HST*). They demonstrated that the warm gas in the MW, as observed with all-sky AGN sightlines, should be modeled with a two-component model (i.e., a disk component and a CGM component). In their two-component model, the disk component follows the 1-D plane-parallel slab model as SW09 adopted, and the halo component is modeled as a uniform global background.

This paper is built upon the two-component model of Zheng19 to develop a disk-CGM model that accounts for both the radial and vertical density profiles of the disk. This model is applied to Si IV and O VI, which are typical ions tracing the transitional temperature gas (Savage et al., 1997; Wakker et al., 2012). In Section 2, we summarize the data used in this study, which includes column density measurements from MW stellar sightlines by SW09, and from all-sky AGN sightlines by Savage et al. (2003, hereafter Savage03) and Zheng19. We introduce our model in Section 3, and show that the inclusion of the disk radial profile can alleviate the disagreement between the plane-parallel slab model based on the stellar sample (SW09) and the two-component model based on the AGN sample (Zheng19). The anisotropic CGM model is also introduced in Section 3, showing that the MW is likely to have a warm CGM with anisotropic column density distribution. In Section 4, we discuss the implication of this work on the warm gas disk (Section 4.2), the warm CGM of the MW (Section 4.3), and the north-south asymmetry of the MW warm gas absorption features (Section 4.4). The key results are summarized in Section 5.

4.2 Data

At the temperature of $\approx 10^5$ K, the transitional gas can be traced by intermediate-high ionization state ions, such as Si IV with ionization potential of 33.5 - 45.1 eV, C IV (47.9 - 64.5 eV), N V (77.5 - 97.9 eV), or O VI (113.9 - 138.1 eV). These ions

are detectable in absorption against the continua of background UV-bright stars or AGNs. For observations of the MW warm gas disk and CGM, the stellar sightlines are normally at low Galactic laitutdes ($|b| \lesssim 5°$; SW09), whereas the AGNs are at high Galactic latitudes ($|b| \gtrsim 30°$; Savage03; Zheng19). The stellar sightlines are employed to measure the mid-plane density of the disk, while the AGN sightlines can trace the large-scale variation of the disk (e.g., scale height of the disk) and the CGM. Therefore, these two samples are equally important to constrain both the gaseous disk shape and the CGM contribution. We only consider the ions that have high $S/N \gtrsim 15$ samples for both disk stars and AGNs of sample sizes $\mathcal{N} \gtrsim 100$.

Based on this criterion, Si IV and O VI are the two ions, which have both stellar sightlines from SW09 and AGN sightlines from Savage03 and Zheng19. In this study, we do not consider C IV, since the current largest AGN sample ($\mathcal{N} \approx 30 - 40$) from Wakker et al. (2012) does not have sufficient sightlines to obtain a good fitting result. All of the used three samples (Savage03; SW09; Zheng19) have similar velocity ranges ($|v| \lesssim 100$ km s^{-1}) for the measurement of the column density, so we only study the low-intermediate velocity gas of the MW (without HVCs $|v| \gtrsim 100$ km s^{-1}). Zheng et al. (2015) showed that a significant amount of the CGM is at low-intermediate velocities using a MW-mass hydrodynamic simulation (Joung et al., 2012), so we expect that we could detect both the warm gas disk and CGM using these samples.

For the stellar sample, SW09 summarized the *FUSE*, *IUE*, and *Copernicus* sightlines toward the 109 MW stars, 25 AGNs, and 6 LMC/SMC stars with good measurements ($\sigma_N < 0.4$ dex) or limits of Si IV and O VI. This sample is mainly based on the Galactic O VI surveys, such as Bowen et al. (2008) for low-latitude disk stars and Zsargó et al. (2003) for halo stars. Compared to the Bowen et al. (2008) sample, SW09 excluded sightlines with large uncertainties of O VI and other transitional ions (e.g., C IV, Si IV; Savage et al. 2001). The excluded sightlines are mainly stellar sightlines within 1 kpc. Since SW09 also included sightlines toward halo stars at

Table 4.1: The Si IV and O VI Samples

Ion	$\mathcal{N}_{\rm star}$[a]			$\mathcal{N}_{\rm AGN}$[a]			σ_p[b]	Ref.
Si IV	49	13	13		...		0.30	SW09
		...		119	11	0	0.13	Zheng19
O VI	73	0	4		...		0.23	SW09
		...		93	0	8	0.15	Savage03

[a] These two columns are the number of sightlines from the stellar or AGN sample, respectively. In each column, three numbers are for sightlines with column density measurements, lower limits, and upper limits, respectively.
[b] σ_p is the patchiness parameter (defined in Section 3.2), which represents the intrinsic scatter of the column density measurements in each sample. The patchiness parameter is derived to reduce the reduced χ^2 value to 1 for each sample individually.

$|z| > 1$ kpc, this sample is better to constrain the scale height of the disk component. We exclude sightlines that might be contaminated by foreground H II regions as marked out by SW09. Besides the Galactic stellar sample, SW09 also included 6 stars in LMC/SMC, which are not used in our analyses. This is because one needs to assume the radial density profile of the MW CGM to model the ion column densities from stars at the distance of $50-60$ kpc, which is highly uncertain. Therefore, we do not implement this variation in our model, and omit the sightlines toward LMC/SMC stars. The final stellar sample used in our analyses is composed of 77 sightlines, 75 of which have good column density ($\log N$) measurements or limits for Si IV, and all of them have good $\log N$ values or limits for O VI (Table 5.1).

For the AGN sample, we adopt two data sets. We make use of the Si IV measurements from the COS-GAL sample (Zheng19), which is based on the Hubble Spectroscopic Legacy Archive (Peeples et al., 2017). Moreover, we retrieve the O VI measurements from the *FUSE* observations analyzed by Savage03. We do not include the AGN sample in SW09, since it has a large overlap with the Zheng19 sample (18/25) and the Savage03 sample (22/25). The final AGN sample includes 130 sightlines for Si IV and 101 sightlines for O VI (Table 5.1).

4.3 Models and Results

4.3.1 Previous Models

Previously, the warm gas disk (e.g., traced by Si IV and O VI) of the MW is modeled as an 1-D plane-parallel slab model (Jenkins 1978; Bowen et al. 2008; SW09). The model only has one dimensional variation: the density distribution of the warm gas over the disk height z as an exponential function of $n(z) = n_0 \exp(-|z|/z_0)$, where n_0 is the ion density at the mid-plane and z_0 is the scale height. The current stellar sightlines are normally close to the Sun with a distance of $d \lesssim 2$ kpc, which implies that the average ion densities traced by these sightlines do not vary significantly at large scales. Therefore, the stellar sightlines mainly determine the average density of the mid-plane around the solar system ($n_\odot$). For the AGN sightlines, both the disk and the CGM are detected to show the large-scale variation. Based on AGN sightlines, one could obtain the maximum projected column density along the z-direction ($N \sin|b|$) for the disk component, since in the plane-parallel slab model, the CGM contribution is ignored. Combining these two measurements, the scale height z_0 in the plane-parallel slab model is derived as $N \sin|b|/n_\odot$ around the solar neighborhood.

This model works well for the sample dominated by stellar sightlines, such as SW09, which has ≈ 100 stellar sightlines and ≈ 20 AGN sightlines. However, this model might have two problems with more and more AGN sightlines obtained by *HST*/COS. First, for sightlines toward AGNs, the contribution from the MW CGM is not considered, which has been shown as an important component for low redshift galaxies ($z \lesssim 0.5$; e.g., Stocke et al. 2013; Werk et al. 2014; Johnson et al. 2015). Second, the AGN sightlines could trace the large scale variation of the disk in both the vertical and radial directions, so the plane-parallel slab model might lead to divergence from the observations.

The first problem is partially solved in Zheng19 by introducing an isotropic CGM component ($N_{\rm CGM}$) into the plane-parallel slab model; their model is referred as the two-component disk-CGM model hereafter. They applied the two-component disk-CGM model to fit the Si IV column density distribution measured along 130 AGN sightlines across the Galactic sky, and found a significant contribution of the MW CGM of $\log N_{\rm CGM} \approx 13.53$. The Zheng19 analyses provide the first statistical evidence that the MW hosts an extended warm CGM. However, in this model, the disk component ($\log N_{\rm disk} = 12.1$) is different from SW09 ($\log N_{\rm disk} = 13.4$) by more than one order of magnitude. Therefore, there is still a huge gap between the model dominated by stellar sightlines (the plane-parallel slab model; SW09) and the model dominated by AGN sightlines (the two-component disk-CGM model; Zheng19). In the following, we introduce a 2-D disk-CGM model with a disk radial profile that alleviates the tension between the flat-slab model by SW09 and the two-component disk-CGM model by Zheng19 in studying the warm gas in the MW.

4.3.2 The 2-D Disk-CGM Model

We improve the previous models by introducing a two-dimension (2-D) disk into the two-component disk-CGM model of Zheng19. In this model, we consider the number density distribution of the disk component, which is a 2-D distribution ($n_{\rm disk}(r, z)$) depending on the radius (r) from the Galactic center (GC), and the z-height above and below the Galactic plane. For a given sightline at a given distance (l, b, and d), we can calculate the column density contribution from the disk by integrating the 2-D density distribution of the disk component. For the CGM component, we first consider a constant CGM column density over all directions (isotropic $N_{\rm CGM}$; the same as Zheng19). This CGM component is only applied to the AGN sightlines, while the disk component is calculated for both stellar and AGN sightlines.

For a given sightline, the model predicted column densities are

$$\begin{aligned} N(l,b,d) &= N_{\rm disk}(l,b,d) \text{ for stars,} \\ N(l,b) &= N_{\rm disk}(l,b,d_{\rm max}) + N_{\rm CGM} \text{ for AGNs,} \end{aligned} \tag{4.1}$$

where $d_{\rm max}$ is the maximum distance for the disk component, which is set to be the virial radius of the MW halo ($R_{\rm vir} = 250$ kpc).

Here, we emphasize that the decomposition of the disk and the CGM component is phenomenological, since we assume the stellar sightlines do not trace any CGM gas. This is limited by the current sample, which does not have sightlines in the MW halo that trace the radial profile of the MW CGM at large radii, so we cannot calculate the CGM contribution to the column density measurements in stellar sightlines. However, this assumption is also reasonable with the current sample. For stellar sightlines, most stars are close to the disk mid-plane center $|z| \lesssim 3$ kpc, which are marginally affected by the CGM component. There are only three stars have $|z| > 3$ kpc, leading a tiny effect on the fitting results.

For the 2-D disk component, the radial and vertical profiles are assumed to be independent from each other, so the ion number density distribution in the disk is

$$n(r,z) = n_0 f_r(r) f_z(z), \tag{4.2}$$

where $f_r(r)$ and $f_z(z)$ are the profile functions in the radial and vertical directions. For $f_z(z)$, we adopt the same exponential profile, $f_z(z) = \exp(-|z|/z_0)$, as the plane-parallel slab model (SW09). We also assume the radial profile to be exponential as $f_r(r) = \exp(-r/r_0)$, where r_0 is the scale length. Both of the radial and vertical exponential profiles are empirical as inferred from the H I disk and the stellar disk (Kalberla & Dedes, 2008; Bovy & Rix, 2013). It is possible that the warm gas disk follows a different density distribution, since the warm gas disk is more extensive

and affected by Galactic feedback. Therefore, in our following analyses, we also consider the Gaussian function $f(x) = \exp(-(x/x_0)^2)$ for both $f_r(r)$ and $f_z(z)$ to test whether the shape of the warm gas disk can be distinguished from the observations. In total, there are four phenomenological models for our disk density profiles, named as $\mathrm{R_E Z_E}$ (exponential radial and vertical profiles), $\mathrm{R_G Z_E}$ (Gaussian radial profile and exponential vertical profile), $\mathrm{R_E Z_G}$ (Exponential radial profile and Gaussian vertical profile), and $\mathrm{R_G Z_G}$ (Gaussian radial and vertical profiles). In these models, the solar system is placed at $r_\odot = 8.5$ kpc (Ghez et al., 2008) and $z_\odot = 0$ kpc.

We apply these models to the column density measurements of Si IV and O VI (Savage03; SW09; Zheng19), and obtain the best parameters using the minimum χ^2 estimation. In our fittings, we include the lower or upper limits of $\log N_{\mathrm{SiIV}}$ and $\log N_{\mathrm{OVI}}$ values, which are typically not considered in previous modelings (e.g., SW09). For these limits, we only calculated the χ^2 value when it is opposite to the limits, i.e., higher than the upper limit and lower than the lower limit; otherwise, the χ^2 value is fixed to 1 for these limits. The uncertainties of the sightlines are one-sided uncertainty, which we set according to the intrinsic scatters (i.e., the patchiness parameter derived later; Table 5.1). Therefore, the uncertainty of limits in the stellar sample is set as 0.3 dex, while the AGN sample is set as 0.1 dex.

Previous studies show that the intrinsic column density scatters of the disk and the CGM are the major contributors of the deviation in the fitting (i.e., Bowen et al. 2008; SW09; Zheng19). The intrinsic scatter is modeled as the patchiness parameter (σ_{p}), which is an additional uncertainty attached to the measurement uncertainty as $\sigma_{\mathrm{f}}^2 = \sigma_{\mathrm{p}}^2 + \sigma_{\mathrm{m}}^2$. σ_{f} is the final adopted uncertainty in model fittings, and σ_{m} is the measurement uncertainty. There are two methods to implement patchiness parameters. The first method is varying the patchiness parameter to obtain the reduced $\chi^2 = 1$, which is adopted in SW09 (and reference herein). The second method is to implement the patchiness uncertainty into the Bayesian model as introduced in

Zheng19. These two methods obtain similar results, and we adopt the first method in our analyses. The calculated $\sigma_{\rm p}$ values are shown in Table 5.1, which leads to reduced χ^2 of $0.95-1.05$ due to the significant figures. In SW09, the patchiness parameters of Si IV and O VI are 0.266 and 0.233, respectively. The larger patchiness parameters (0.30 and 0.23) in Table 5.1 are mainly due to the inclusion of upper or lower limits in our fittings, and the exclusion of AGN sightlines, which normally have smaller scatters. For the AGN samples, the previously $\sigma_{\rm p}$ are 0.18 and 0.25 for Si IV and O VI, respectively (Savage03; Zheng19), which are larger than our values in Table 5.1 (0.13 and 0.15). The reduction of the patchiness parameter indicates that the radial distribution of the disk affects the AGN sample more significantly.

The fitting results are summarized in Table 4.2. Overall, the exponential function leads to smaller scale lengths or scale heights than the Gaussian function, because the exponential function has a slower decay with the same characteristic length. With the isotropic CGM, the $\rm R_G Z_E$ model (indicating Gaussian function for the radial profile and exponential function for the vertical profile) is preferred with the significance of $\lesssim 2\sigma$ (inferred from the difference of total $\chi^2 \lesssim 4$). Similarly, the anisotropic CGM models show that no specific model is preferred, which will be described and discussed in detail in Section 3.3. Therefore, we suggest that the current stellar and AGN samples cannot distinguish the density profiles (exponential or Gaussian) of the warm gas disk, and we set the $\rm R_E Z_E$ model as the fiducial model.

Table 4.2: The Disk and CGM model for Si IV and O VI

Model	$\log n_0$ (cm^{-3})	r_0 kpc	z_0 kpc	$\log N_{\rm mp}^{\rm CGM}$ (cm^{-2})	$\log N_{\rm nd}^{\rm CGM}$ (cm^{-2})	red. χ^2 (dof)	$\log n_{\odot}^{\rm disk}$ (cm^{-3})	$\log n_{\odot} z_0$ (cm^{-2})	$\log M_{\rm disk}$ ($M_{\odot}$)
(1)	(2)	(3)	(4)	(5)	(6)	(7)	(8)	(9)	(10)
The 2-D disk-CGM models with isotropic CGM of Si IV									
$\mathrm{R_E Z_E}$	-7.82 ± 0.24	4.3 ± 1.2	2.5 ± 0.6	13.18 ± 0.12		1.232 (201)	-8.68	13.21	3.78
$\mathrm{R_G Z_E}$	-8.21 ± 0.16	8.3 ± 1.5	2.8 ± 0.7	13.14 ± 0.15		1.182 (201)	-8.67	13.26	3.70
$\mathrm{R_E Z_G}$	-7.74 ± 0.23	3.7 ± 0.9	3.3 ± 0.6	13.16 ± 0.11		1.267 (201)	-8.73	13.22	3.80
$\mathrm{R_G Z_G}$	-8.21 ± 0.15	7.4 ± 1.1	3.5 ± 0.7	13.12 ± 0.14		1.202 (201)	-8.78	13.26	3.66
The 2-D disk-CGM models with isotropic CGM of O VI									
$\mathrm{R_E Z_E}$	-7.19 ± 0.20	5.7 ± 1.8	2.3 ± 0.6	13.98 ± 0.14		1.210 (174)	-7.84	14.02	4.39
$\mathrm{R_G Z_E}$	-7.51 ± 0.13	9.8 ± 1.9	2.6 ± 0.7	13.93 ± 0.18		1.196 (174)	-7.83	14.08	4.29
$\mathrm{R_E Z_G}$	-7.18 ± 0.20	5.4 ± 1.6	2.4 ± 0.5	14.03 ± 0.09		1.240 (174)	-7.86	13.95	4.31
$\mathrm{R_G Z_G}$	-7.50 ± 0.12	8.8 ± 1.4	2.7 ± 0.6	13.98 ± 0.12		1.222 (174)	-7.90	14.01	4.16
The 2-D disk-CGM models with anisotropic CGM of Si IV									
$\mathrm{R_E Z_E}$	-7.93 ± 0.20	5.2 ± 1.4	2.6 ± 0.6	12.62 ± 0.40	13.32 ± 0.08	1.128 (200)	-8.64	13.27	3.86
$\mathrm{R_G Z_E}$	-8.25 ± 0.14	9.2 ± 1.6	2.7 ± 0.7	12.67 ± 0.44	13.28 ± 0.10	1.106 (200)	-8.62	13.29	3.74
$\mathrm{R_E Z_G}$	-7.89 ± 0.19	4.6 ± 1.0	3.4 ± 0.6	12.46 ± 0.45	13.32 ± 0.07	1.138 (200)	-8.69	13.28	3.86
$\mathrm{R_G Z_G}$	-8.27 ± 0.12	8.4 ± 1.2	3.5 ± 0.7	12.48 ± 0.52	13.28 ± 0.08	1.105 (200)	-8.72	13.31	3.70
The 2-D disk-CGM models with anisotropic CGM of O VI									
$\mathrm{R_E Z_E}$	-7.35 ± 0.15	8.0 ± 2.5	2.6 ± 0.6	13.21 ± 0.58	14.19 ± 0.08	1.104 (173)	-7.82	14.08	4.55
$\mathrm{R_G Z_E}$	-7.60 ± 0.09	12.2 ± 2.4	2.7 ± 0.6	13.18 ± 0.66	14.16 ± 0.10	1.108 (173)	-7.81	14.11	4.40
$\mathrm{R_E Z_G}$	-7.33 ± 0.15	7.2 ± 2.2	2.9 ± 0.5	13.21 ± 0.50	14.22 ± 0.07	1.121 (173)	-7.84	14.05	4.49
$\mathrm{R_G Z_G}$	-7.59 ± 0.09	10.7 ± 1.8	3.0 ± 0.6	13.18 ± 0.57	14.19 ± 0.08	1.119 (173)	-7.84	14.08	4.28

Notes: Column 1) The model name: R and Z denote radial and vertical directions; E and G denote exponential and Gaussian profiles. Column 2) The density at the GC. Column 3) The scale length. Column 4) The scale height. Column 5) The CGM column density along the disk mid-plane ('mp'). For isotropic CGM model, this value is the same as the CGM column density perpendicular to the disk. Column 6) The CGM column density perpendicular to the disk ('nd' denotes the normal line). Column 7) The reduced χ^2 and the degree of freedom. Column 8) The ion density at the solar system. Column 9) The disk column density toward $b = 90^{\circ}$ at the solar system. Column 10) The disk mass of ions.

All of our four models show that both the disk and the CGM components contribute significantly to the observed column densities in AGN sightlines. Using $n_0 z_0$ as the characteristic column density of the disk, the disk component is comparable to the CGM component for both Si IV and O VI (Table 4.2). Previously, the plane-parallel slab model shows that the disk component has Si IV column density ranging from $\log N = \log n_0 z_0 = 13.36$ to 13.56, and O VI from $\log N$ =14.12 to 14.28 (SW09). These values are all larger than our values of $13.21 - 13.26$ (Si IV) and $13.95 - 14.08$ (O VI). The lower values of our disk component are because we take into account the contribution of the MW CGM to ion column density measurements toward AGN sightlines, whereas the plane-parallel slab model assumes no contribution from the CGM. Our fitting results show that the CGM components are $13.12 - 13.17$ (Si IV) and $13.91 - 14.02$ (O VI). These values are comparable with the Si IV and O VI column densities measured from transverse AGN sightlines at $R \approx 100$ kpc ($\approx 0.5 R_{\rm vir}$) for low redshift L^* galaxies ($z \approx 0.5$; Werk et al. 2013; Savage et al. 2014; Johnson et al. 2015). Although the sightlines through the MW CGM have a different geometry from sightlines for external galaxies, this consistency indicates a decreasing column density dependence on the radius of a power law with a slope of about -1 (Werk et al., 2013).

For the disk component, although we cannot distinguish between the exponential and Gaussian profiles, the scale height (z_0) and the scale length (r_0) can be determined. In the fiducial model ($\rm R_E Z_E$), the scale heights are 2.6 ± 0.6 kpc and 2.4 ± 0.6 kpc for Si IV and O VI, respectively. The scale lengths are 4.2 ± 1.2 kpc and 5.6 ± 1.7 for Si IV and O VI, respectively. The scale lengths are first measured in this work for the MW warm gas disk.

The radial profile of the disk component is important to solve the divergence between the plane-parallel slab model (SW09) and the two-component disk-CGM model (Zheng19), which have different relative contributions between disk and CGM compo-

nents. In Fig. 4.1, we predict the projected column density distribution ($\log N \sin|b|$) as a function of $|z|$-height and Galactic latitude (b) using the $R_E Z_E$ model with isotropic CGM with best-fit parameters in Table 4.2.

Before introducing the plots, we define the observed scale height, which is an observable for the warm gas analysis. This parameter is defined as $N \sin|b|/n_\odot$, where $N \sin|b|$ is the projected column density observed from the Sun, and $n_\odot$ is the mid-plane ion density around the Sun. The observed scale height could be estimated as the z-height of the turnover point in the projected column density function of z-height. For example, in the left panel of Fig. 4.1, the observed scale height is about $|z_{\rm obs}| \approx 0.03$ kpc at $|b| = 0.1°$, while it is $|z_{\rm obs}| \approx 1$ kpc at $|b| = 5°$. This is different from the scale height z_0 defined in Equation (4.2), which is a constant over the entire sky. The scale height z_0 could be calculated as $N_{\rm r,nd}/n_{\rm r,mp}$, where $N_{\rm r,nd}$ and $n_{\rm r,mp}$ are the column density toward $b = 90°$ (the normal direction of the disk) and the mid-plane density at any given radius of r.

The difference between the scale height (z_0) and the observed scale height ($z_{\rm obs}$) is mainly due to the radial density distribution of the disk component. Using two AGN sightlines as an example, one sightline is toward $b = 90°$, while another sightline is toward the anti-Galactic center (anti-GC; $l = 180°$) direction with any Galactic latitudes. Considering the calculations of the scale height and the observed scale height, the mid-plane densities are the same, since both of densities are around the Sun. However, the projected column densities of the disk component are different: the term $N_{r_\odot,\rm nd}$ is always larger than $N \sin|b|$ at different b. This is a result of the disk radial distribution, since $N \sin|b|$ could be approximated as $N_{r_\odot,\rm nd} \exp(-(r - r_\odot)/r_0)$, where r is always larger than $r_\odot$ for anti-GC sightlines. Therefore, we expected that the observed scale height is always lower than the real scale height for anti-GC sightlines. Also, since a low b leads to a small $\tan b$ value, the low latitude sightlines need a longer path length to reach the same height. Then, the effect of the disk radial

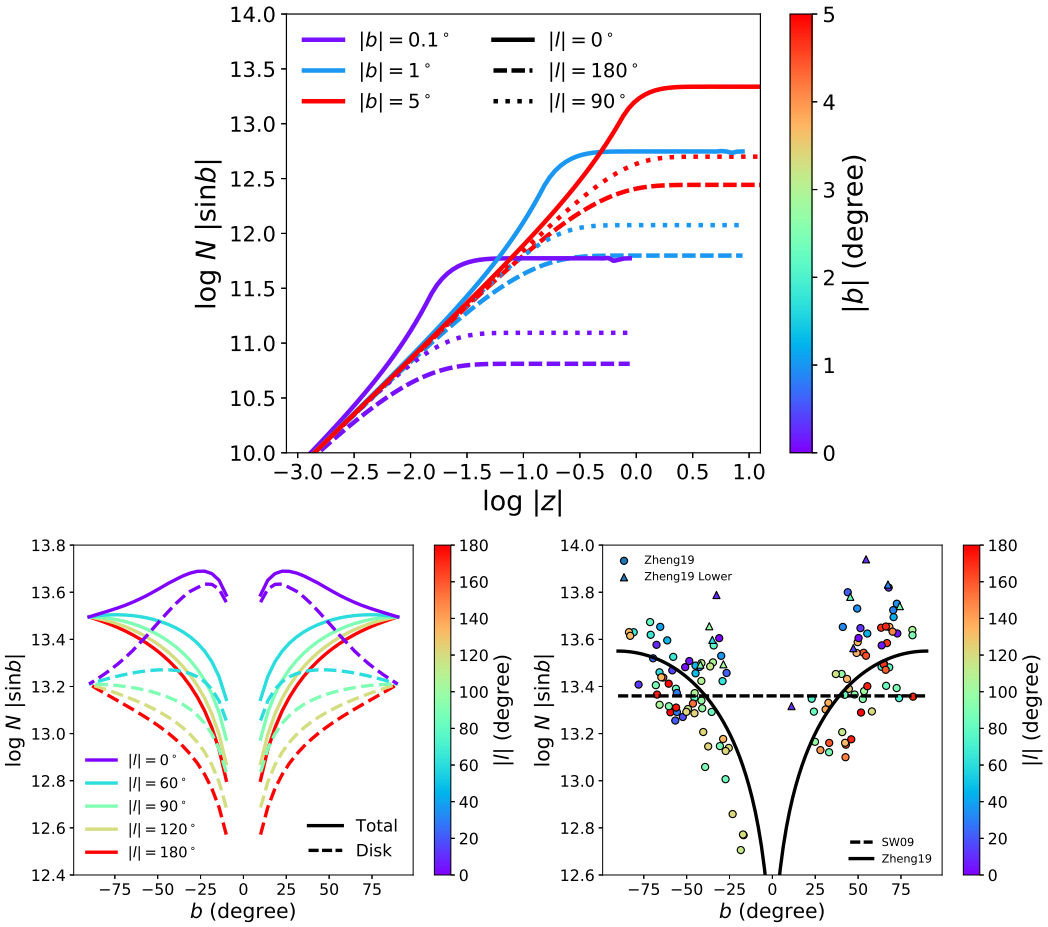

Figure 4.1: The prediction $\log N \sin|b|$ using $\mathrm{R_E Z_E}$ model with the isotropic CGM. The model parameters are adopted for Si IV (first row of Table 4.2). *Left panel*: the predicted relationship between $\log N \sin|b|$ and $\log|z|$ for stellar sightlines at $|b| < 5°$ with contribution only from the disk component. Lower latitudes and larger longitudes lead to lower projected column densities ($N \sin|b|$), hence lower observed scale heights ($N \sin|b|/n_\odot$; see the definition in the text), which is proportional to the projected column density. *Middle panel*: the predicted relationship between $\log N \sin|b|$ and $\log|b|$ for AGN sightlines at $|b| \gtrsim 30°$. The dashed lines are the disk component, while the solid lines are the total model. Sightlines around the anti-GC show rapid decrease of the projected column densities with lower latitudes due to the disk radial variation. *Right panel*: the plane-parallel slab model (SW09; the dashed line) and the two-component disk-CGM model (Zheng19; the solid line). In these two models, $\log N \sin|b|$ only has dependence on Galactic latitude, since these two models only have 1-D disk with a density profile over the height-$|z|$.

distribution is more significant for low latitude sightlines, and lower projected column densities are expected for these sightlines (the left panel in Fig. 4.1).

The sightlines toward the GC ($l = 0°$) is more complex, since the disk radial distribution leads to higher density around the GC. However, the stellar sightlines are mainly at low latitudes $|b| \lesssim 5°$. In our fiducial $R_E Z_E$ model, the scale heights of both Si IV and O VI are higher than 2 kpc. Using this scale height and a Galactic latitude of 5°, one expects a radius difference of $z_0/\tan|b| > 20$ kpc to reach the scale height of the disk. With this radius difference, the final effect on the observed scale height will be a competition between the high-density gas around the GC and the low-density gas at large radii. Our numerical calculation shows that it is possible to have larger observed scale heights around the GC direction (the left panel in Fig. 4.1). Therefore, the sightlines around the GC direction have higher projected column densities than those toward anti-GC directions due to the high-density gas at the GC. Since the solar system is at $r_\odot = 8.5$ kpc, this difference is most significant around $|z| = 8.5\tan|b|$ kpc, which is ≈ 0.7 kpc for $|b| = 5°$.

In the middle panel of Fig. 4.1, we show the predicted projected column density for the AGN samples using the fiducial $R_E Z_E$ model. Our model predicts that the projected column density has a dependence on both Galactic latitude and Galactic longitude, while the previous models only have dependence on Galactic latitude (SW09 and Zheng19; the right panel of Fig. 4.1). The $\log N$ dependence on both l and b is due to the radial profile of the disk component, so it is similar to the case in the disk-only model (the left panel of Fig. 4.1), but for higher Galactic latitudes ($|b| > 30°$). The projected column densities are generally higher toward the GC direction than the anti-GC direction, and all the values converge at $|b| = 90°$. The anti-GC sightlines show a more significant dependence on the Galactic latitude $|b|$ (decreasing rapidly), which is due to the radial profile in our model. The Zheng19 model also reproduces this feature, but in a different way. The Galactic latitude dependence in

the Zheng19 model is due to the term of $N_{\rm CGM} \sin|b|$, and do not have dependence on the Galactic longitude, so this model does not reproduce the feature that the GC sightlines have higher column density than the anti-GC sightlines (also see Fig. 5 in Zheng19, and Fig. 7 in Wakker et al. 2012).

4.3.3 The Anisotropy of the CGM Component

In the previous section, we adopt the isotropic CGM assumption from Zheng19. However, this isotropic CGM profile over the entire sky may not best represent the gas density distribution in the CGM. For example, Bordoloi et al. (2011) found that the absorption features are stronger along the minor axis using Mg II absorption lines for external galaxies (also see Lan & Mo 2018). Besides the absorption strength, Martin et al. (2019) found that the non-detections of Mg II are mainly along the minor axis (perpendicular to the disk), which indicates a lower detection rate along the minor axis. Therefore, we consider the azimuthal variation of CGM in our 2-D disk-CGM model of the MW.

For the MW, the azimuthal variation of external galaxies is equivalent to a variation of the CGM column densities as a function of Galactic latitude. We refine our 2-D disk-CGM model by changing CGM density from an isotropic distribution to an anisotropic distribution with a dependence on Galactic latitude. In this model, we define two characteristic CGM column densities: the column density along the disk ($N_{\rm mp}$; denoting the mid-plane) and the column density perpendicular to the disk ($N_{\rm nd}$; denoting the normal direction of the disk). These two directions are similar to the major and minor axis directions for external galaxies. For simplicity, we assume that the CGM column density depends on Galactic latitude b as an elliptical function:

$$\log N_{\rm CGM}(b) = \sqrt{\log^2 N_{\rm mp} \cos^2 b + \log^2 N_{\rm nd} \sin^2 b}, \tag{4.3}$$

where $N_{\rm mp}$ and $N_{\rm nd}$ are free parameters in our model. For AGN sightlines, the term $N_{\rm CGM}$ in Equation 2 has a dependence on Galactic latitude ($N_{\rm CGM}(b)$). In this model, we assume the variation of the CGM column density is in the logarithmic scale rather than in the linear scale, i.e., $N_{\rm CGM}(b) = (N_{\rm mp}^2 \cos^2 b + N_{\rm nd}^2 \sin^2 b)^{1/2}$. In the linear scale variation model, if $N_{\rm nd}$ is much larger than $N_{\rm mp}$ (e.g., a factor of > 3), the CGM column density will be dominated by $N_{\rm nd} \sin b$, and $N_{\rm mp}$ cannot affect the fitting results. Therefore, the linear scale variation model does not have the ability to trace the large amplitude CGM variation (i.e., $|\log N_{\rm nd} - \log N_{\rm mp}| > 0.5$ dex).

The χ^2 fitting results show that the anisotropic CGM model is significantly better than the isotropic CGM model (Table 4.2). The total χ^2 values are reduced by $15.6 - 26.4$ and $15.7 - 21.2$ for Si IV and O VI, respectively. The mean values of the χ^2 difference are 20.8 and 18.5, which lead to a 4.6σ and 4.3σ significance considering the degree of freedom (dof) is reduced by 1. According to the fitting, the CGM column density is higher along the normal direction of the MW disk ($N_{\rm nd}$) than the direction along the disk ($N_{\rm mp}$) by $0.6 - 0.9$ dex and ≈ 1.0 dex for Si IV and O VI, respectively. The differences between $N_{\rm nd}$ and $N_{\rm mp}$ are consistent for different disk density profiles (exponential or Gaussian). This consistency indicates the CGM anisotropy is a real feature rather than an artificial feature due to the choice of the disk density profiles. Therefore, we suggest that the anisotropic model is preferred at least at a level of 4.0σ for both Si IV and O VI distributions. Combining these two ions together, the significance is about 6.3σ. However, this result does not imply the CGM has an elliptical geometry, and it is even unknown whether this feature is completely due to the CGM, which will be discussed in Section 4.3.

Adopting the anisotropic CGM model does not affect the disk parameters significantly, but one interesting difference is the larger scale length. This is the result of the smaller CGM column density at low Galactic latitudes. In the isotropic CGM model, the CGM column density is dominated by the AGN sample at high Galactic latitudes.

This isotropic column density ($\approx N_{\rm nd}$) is higher than the real column density at low Galactic latitudes ($N_{\rm mp}$), and suppresses the extension of the disk component along the radial direction. In the fiducial $R_E Z_E$ disk model with an anisotropic CGM, the scale lengths are 5.3 ± 1.4 kpc and 7.8 ± 2.4 for Si IV and O VI, respectively. These numbers indicate that the warm gas disk is more extensive than the stellar disk (≈ 2 kpc; Bovy & Rix 2013) and the H I disk (≈ 3.5 kpc; Kalberla & Dedes 2008) at about 2σ.

Column density predictions by the preferred models ($R_E Z_E$ disk with anisotropic CGM) are compared to the observations in Fig. 4.2, Fig. 4.3, and Fig. 4.4 for Si IV and O VI, respectively. We plot the stellar samples in the top panels, which generally follow the model ($R_E Z_E$ disk with isotropic CGM; Fig. 4.1) described in Section 3.2. Different from the plane-parallel slab model (SW09), we predict the maximum projected column density has a dependence on Galactic latitude due to the radial profile of the disk (Section 3.2). However, the difference between low and high Galactic latitude sightlines does not show up for the observed scale heights, since there are no high-$|z|$ stellar sightlines at low latitude ($|b| \lesssim 3°$), which are expected to follow the purple lines in the top left panels. The observations show the longitude dependence of the projected column density, since the sightlines toward the anti-GC generally have lower projected column density than the sightlines toward the GC.

The middle panels show the global variation of the total column densities predicted for AGN sightlines. It is of interests to find that the predicted global minimum among the AGN sightlines occurs around $|b| = 30° - 50°$ around the anti-GC, which is the combination of the disk variation and the anisotropic CGM. The disk component has the minimum around the polar regions ($|b| \approx 90°$), where has the shortest path length, while the anisotropic CGM component in our model has the minimum along the disk radial direction ($|b| = 0°$). Then, considering these two effects together, the minimum of the total column density will be around $|b| \approx 45°$. Observationally, this feature

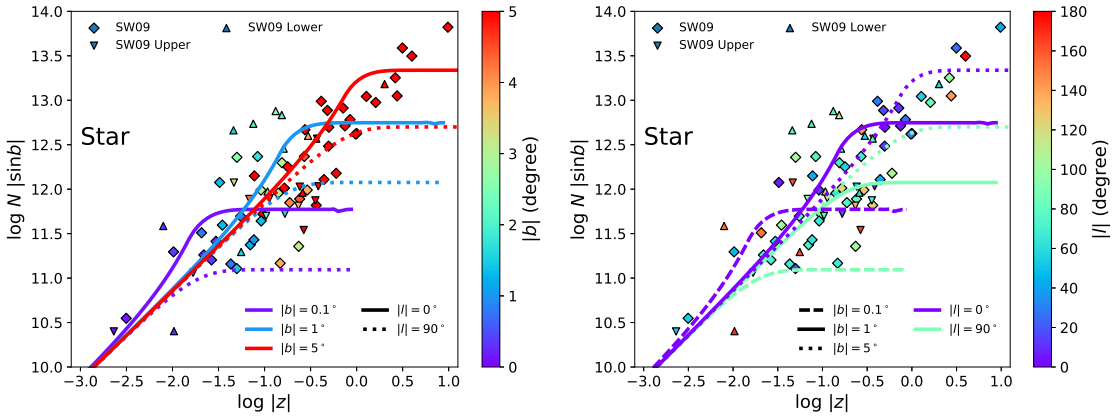

Figure 4.2: The comparison between 2-D disk-CGM model predictions and observations for Si IV (the stellar sample). Two plots are color-coded in Galactic latitude ($|b|$; left) and Galactic longitude ($|l|$; right), respectively. Lower $|b|$ sightlines have lower projected column densities since these sightlines are more affected by the disk radial distribution (need longer path length to reach the same height). Sightlines toward the GC have higher projected column densities due to the high ion density around the GC.

was found by Wakker et al. (2012), showing an O VI deficit region at $l = 70 - 280°$, $b = -60$ to $-10°$. This deficit is more clear in the southern hemisphere, since the southern hemisphere has systematically lower column densities.

The projected column density of the AGN samples is plotted in the lower panels of Fig. 4.2 and Fig. 4.4. The northern hemisphere sightlines have systematically higher column densities than the southern hemisphere by $0.1 - 0.2$ dex. The origin of this north-south asymmetry is beyond the scope of this paper, but we discuss it phenomenologically in Section 4.4. Here, we do not consider this north-south column density asymmetry in our modeling. The predicted tendency stated in Section 3.2 matches with the observations, which show the anti-GC sightlines have lower projected column densities.

We find that the anisotropic model can better reproduce the large $\log N$ variation at lower Galactic latitudes for two reasons (Fig. 4.2 and Fig. 4.4). First, the variation of the projected column density at low latitudes is mainly caused by the

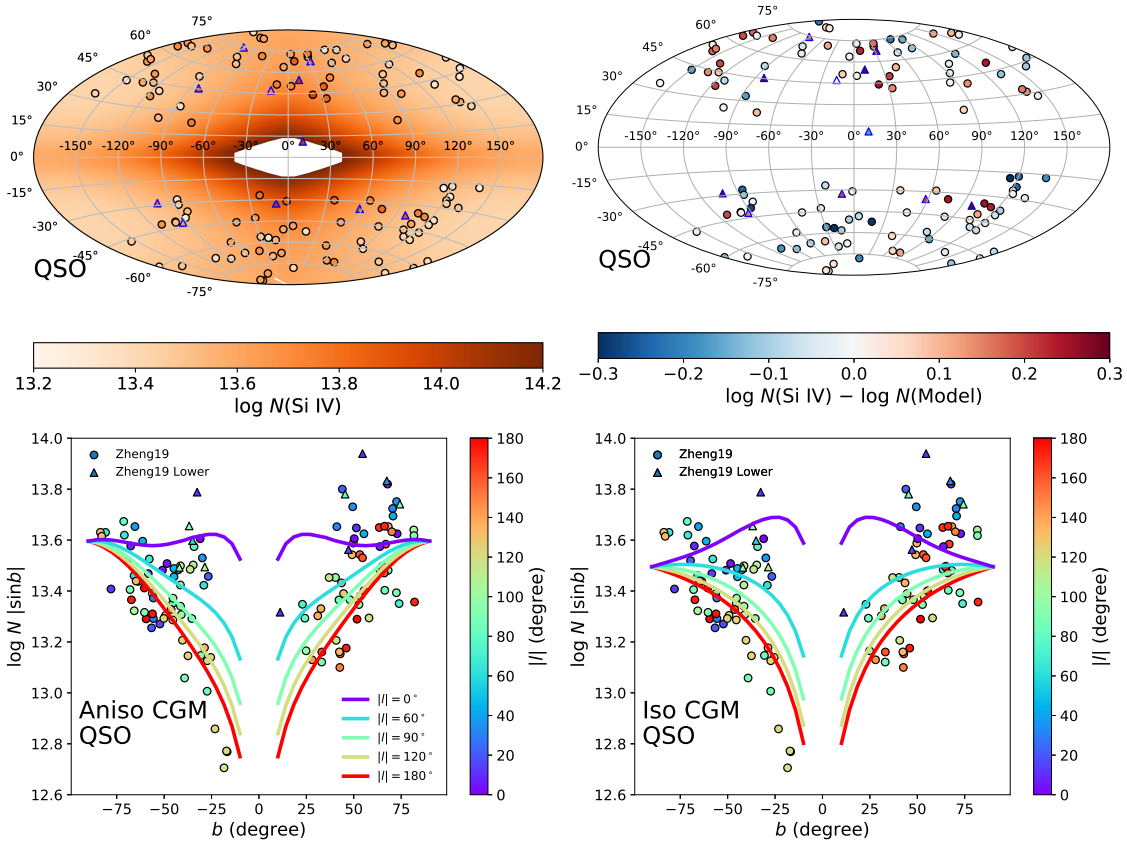

Figure 4.3: The comparison between 2-D disk-CGM model predictions and observations for Si IV (the AGN sample). *Upper panels*: the global variation of total column densities for the AGN sample plotted in the Aitoff projection (the left panel). In the left panel, the white diamond-like region at the GC ($l = 0°$ and $b = 0°$) has column densities of $\log N > 14.2$, so it is left as a blank region. The model predicts that the minimum column density for AGN sightlines occurs around Galactic latitudes of $30° - 50°$, which is a result of the competition between the disk component (the minimum at $b = 90°$) and the CGM component (the minimum at $b = 0°$). The right panel is the residual of $\log N$(Observation) $-$ log N(Model), which mainly shows the north-south asymmetry (discussed in Section 4.4). *Lower panels*: the comparison between anisotropic CGM model (left panel) and the isotropic CGM model (right panel). The anisotropic CGM model is 4.6σ better than the isotropic CGM model by reducing the total χ^2 of 20.8. The anisotropic CGM model reproduces the sharp decreasing of the projected column density at low Galactic latitudes better for sightlines toward the anti-GC ($|l| = 180°$; also see Fig. 4.4).

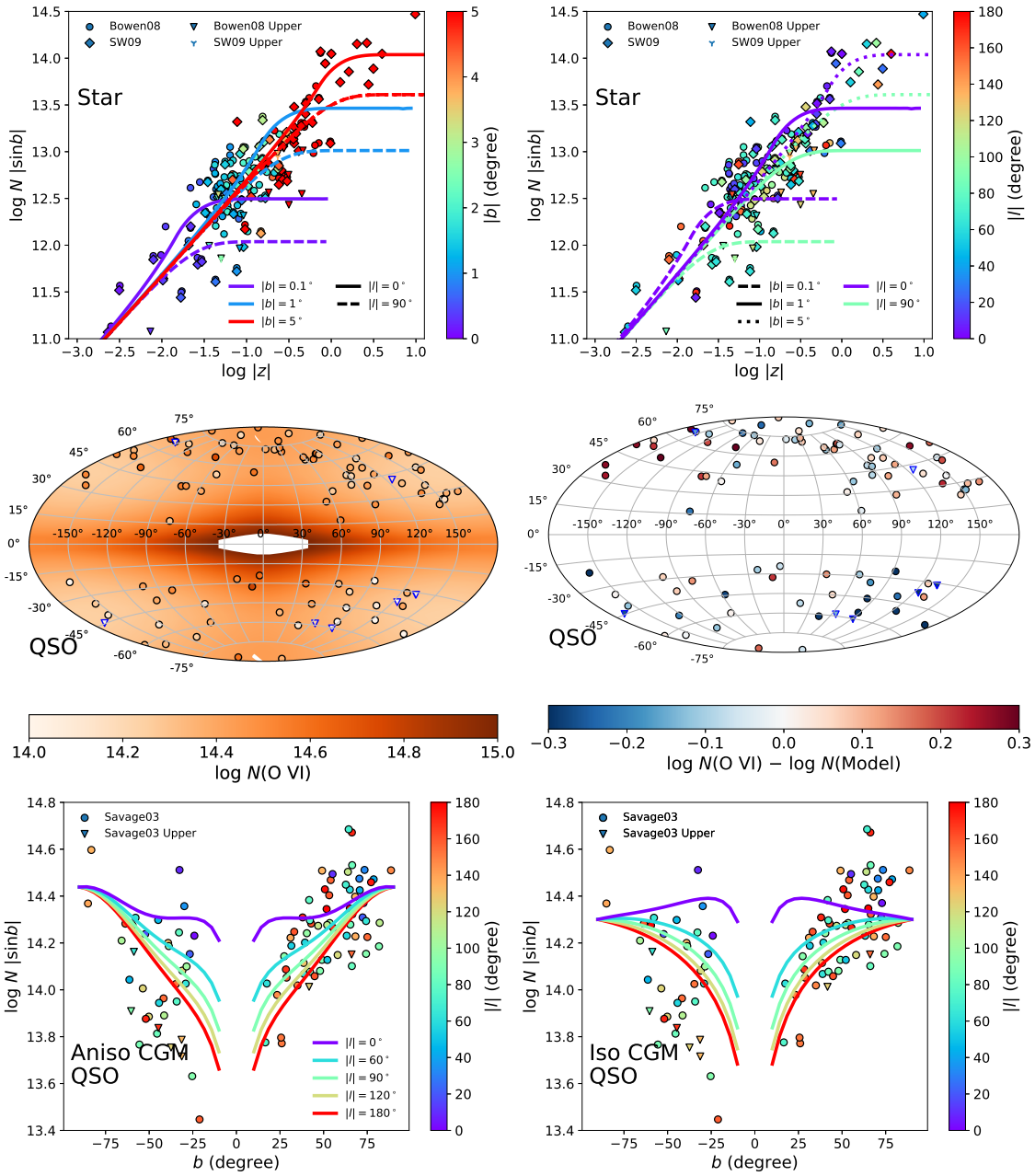

Figure 4.4: The comparison between model predictions and observations for O VI. Each panels are the same as Fig. 4.2 and 4.3. For the top panels, we also plot the Bowen et al. (2008) sample, which is not included in the fitting. For O VI, the anisotropic CGM model is 4.3σ better by reducing the total χ^2 of 18.5.

radial variation of the disk. The low column density along the disk radial direction ($\log N_{\rm mp}$) allows a more extended disk, which increases the column density variation at low Galactic latitudes, since this variation is due to the variation of the disk (the middle panel of Fig. 4.1). Second, the variation of the CGM column density leads to a steeper decrease of the projected column density at low latitudes around the anti-GC. Since the CGM column density is higher at $b = 90°$, the total column density is also increased at high latitudes.

In all, we prefer the $R_E Z_E$ model with anisotropic CGM profile to other models (Fig. 4.5). We examine the Si IV column density residuals to evaluate the performance of the plane-parallel slab model (SW09; left column), the two-component disk-CGM model (Zheng19; middle column), and our preferred model (right column). The plane-parallel slab model (SW09) fits the stellar sample well, which does not have unaccounted features in the residual (i.e., flat residuals over Galactic longitude), although there is a large scatter. However, there are significant unaccounted structures in the residuals for the AGN sample (low residuals at low Galactic latitudes), although the intrinsic scatter is less than the stellar sample. The two-component disk-CGM model (Zheng19) has comparable residuals to our 2-D disk-CGM model for the AGN sample, but the residuals show a peak around $l = 0°$. Also, this model predicts a disk component of $\log N = 12.1$, which is about one order of magnitude lower than SW09 and this work ($\log N \approx 13.3$). The two-component disk-CGM model does not have distance constraints, so the $\log N$ measurement from stellar sightlines cannot be reproduced in this model (Zheng19). Our new model could reproduce the column density measurements from both the stellar and the AGN sightlines equally well without unaccounted features in the residuals.

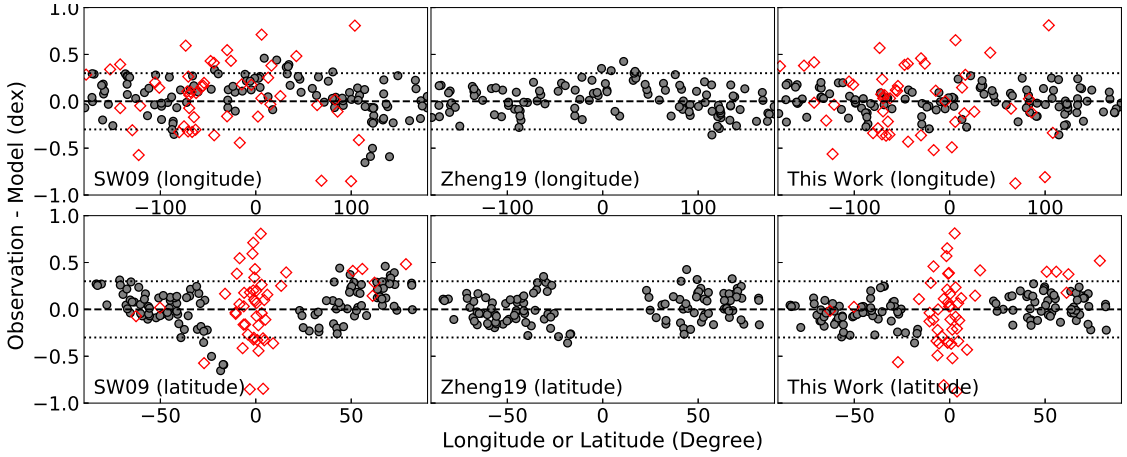

Figure 4.5: The comparison of the Si IV residuals between three models: the plane-parallel model (SW09; *left panels*), the two-component disk-CGM model (Zheng19; *middle panels*), and the 2-D disk-CGM model (this work; *right panels*). The filled gray circles are the residuals of the AGN sample, while the open red diamonds are the stellar sightlines. Here, we only plot measurements without upper or lower limits. The dotted lines are at levels of ± 0.3 dex. The SW09 model are comparable to the 2-D disk model for the stellar sample (flat residuals but large scatters), while the Zheng19 model cannot reproduce the stellar sample. For the AGN sample, both SW09 and Zheng19 models show hints for unaccounted features, such as the peak around $l = 0°$.

4.4 Discussion

4.4.1 The Comparison with Zheng19

Using the archival data (Savage03; SW09; Zheng19), we build a 2-D disk-CGM model to fit the Si IV and O VI column density measurements for warm gas moving at $|v| \lesssim 100\,\mathrm{km\ s^{-1}}$ from both the AGN and stellar sightlines simultaneously. Previously, the plane-parallel slab model is commonly used to study the MW disk (Jenkins 1978; Bowen et al. 2008; SW09). However, the plane-parallel slab model cannot explain a mismatch between the AGN and stellar sample as noted and discussed in Zheng19, which is due to the lack of CGM component in the plane-parallel slab model. Zheng19 introduced an additional isotropic CGM component to the plane-parallel slab model to account for the CGM contribution in the AGN sightlines. Here, we mainly compare our 2-D disk-CGM model with the two-component disk-CGM model with 1-D disk (Zheng19).

For the model setting, the major difference is the inclusion of the disk radial distribution in our 2-D disk-CGM model (Section 3.2), while a minor difference is an improvement from the isotropic CGM model to the Galactic latitude-dependent CGM model (Section 3.3). In Zheng19, the disk component is still the 1-D plane-parallel slab model, which leads to a lower disk component. This is because the plane-parallel slab model has a constant projected column density of AGN over different Galactic latitudes. Therefore, the low Galactic latitude sightlines with low projected column densities (Fig. 4.2 and Fig. 4.4) lead to a low value of the disk component in the two-component disk-CGM model (Zheng19). For the CGM component, we find that the column density distribution of MW CGM is likely to be a function of Galactic latitude instead of an isotropic one (Section 3.3). Since the AGN samples are mostly around the high latitude ($|b| \gtrsim 30^\circ$), this CGM modification lead to a significant difference ($\approx 0.7 - 1.0$ dex for both Si IV and O VI) at low Galactic latitudes between our

models and the two-component disk-CGM model (Zheng19).

Another difference is the adopted statistical method, where we used the χ^2 optimization, while Zheng19 used the Bayesian frame. Assuming the Gaussian distribution for the measurement uncertainty and the uniform prior, these two methods are equivalent in the sense to obtain the minimum of χ^2 or the maximum of likelihood. Besides the method to obtain the fitting results, another difference in the statistical method is the choice of the likelihood or the uncertainty distribution. Zheng19 assumed the column density uncertainty follows a normal distribution (the linear scale) rather than a lognormal distribution, while the latter distribution is adopted in our models. Although the real distribution of the uncertainty is unknown, the lognormal distribution is more used for the data with a large variation (e.g., one order of magnitude). It is worth to notice that these two distributions are similar to each other when the uncertainty is small (≈ 0.02 for most sightlines in Zheng19).

Zheng19 also used the block bootstrapping to account for the possible unknown large scale structures. From the residual map in Fig. 4.2 and Fig. 4.4, we noticed the north-south asymmetry, which is the most prominent variation over the entire sky. This feature is addressed and discussed phenomenologically in Section 4.4. In section 4.5, we introduce several blocking tests for large scale structures, which show consistent results with the unblocked fitting.

Another minor difference is that we obtain the patchiness parameter by reducing the reduced χ^2 to 1, while Zheng19 implemented the patchiness parameter in the Bayesian frame. Again, Zheng19 assumed a normal distribution rather than a lognormal distribution for this intrinsic scatter. Therefore, their patchiness parameter estimate is $N_{\rm p} = 1.4 \times 10^{13}$ in the linear scale. We convert it into the logarithmic scale by $\log_{10} e \times \frac{N_{\rm p}}{N_{\rm SiIV}} \approx 0.179$, where $N_{\rm SiIV}$ is the mean column density of the AGN sample of Si IV. This value is larger than the one in our models (0.13 dex; Table 5.1), and we suggest that this difference is mainly due to the inclusion of the disk radial

profile to better account for the column density scatters as seen in the AGN data.

4.4.2 The Warm Gas Disk

The warm gas at $(1-5)\times10^5$ K is important for gas assembly and recycling in a galaxy due to their high cooling rates and short lifetimes ($\approx$ 10 Myr; Oppenheimer & Schaye 2013). Theoretically, this gas normally trace the interaction layer between cool and hot gases, and the cooling from hotter mediums (Gnat et al., 2010; Kwak et al., 2015). These phenomena are usually associated with galactic outflows (feedback processes), infall gas (gas accretion), and interactions between the disk and the CGM (McQuinn & Werk, 2018; Qu & Bregman, 2018b). Therefore, one could obtain unique insights into the disk and the CGM formation by observing the warm gas.

The scale height is a key property of the warm gas disk, since it indicates how extensive the disk is, which is a test for the ionization mechanism and the gas origin (Bowen et al. 2008; SW09; Wakker et al. 2012). For example, the scale height should be larger for ions with higher ionization potentials under collisional ionization equilibrium (CIE). However, as shown in SW09, the O VI disk ($z_0 = 2.6 \pm 0.5$ kpc) has slightly lower scale height than both Si IV ($3.2^{+1.0}_{-0.6}$ kpc) and C IV ($3.6^{+1.0}_{-0.8}$ kpc) in the SW09 model. This phenomenon might indicate that the Galactic Si IV and O VI are produced under different ionization mechanisms (SW09).

However, as stated in Section 3.2, we find that the Si IV scale height is reduced from $3.2^{+1.0}_{-0.6}$ kpc (SW09) to 2.6 ± 0.6 kpc (the R_EZ_E model with the anisotropic CGM). The O VI scale height (2.6 ± 0.6 kpc) is similar to SW09 (2.6 ± 0.5 kpc). Therefore, our models do not support that Si IV and O VI have different scale heights. The different behaviors between Si IV and O VI scale heights are because of: the inclusion of the disk radial profile and the anisotropic CGM component, the different samples, and the exclusion of AGN sightlines around the north Galactic polar region in SW09.

Besides the scale heights, we find that the scale lengths are also similar between

Si IV and O VI within 1σ. Therefore, we consider whether both of the ions follow the same density profile distributions of the disk component. A joint fitting model is applied to Si IV and O VI samples simultaneously, where we tie the parameters of the O VI model to the Si IV model, including the scale length (r_0), the scale height (z_0), and the CGM difference between two axes ($\Delta \log N^{\rm CGM}$). In the model where the three parameters are all tied (Table 4.3), the difference of total χ^2 is 3.51 compared to the best model with all parameters are free (the models in Table 4.2). Because the best model has a 3 more dof, it is 1σ better than the most limited model, so the best model is not a significantly better model. We also tie these three parameters in turn to check which is the most dominant factor in the χ^2 difference. We find that tying the scale length leads to the highest χ^2, but the difference is still insignificant. Therefore, we prefer the most limited model with all three parameters tied, and suggest that there is no significant difference of the density profile between Si IV and O VI adopting the new models.

Our model measures the scale length of the warm gas disk of the MW for the first time. We can further estimate the total mass of the warm gas disk of the MW. First, we obtain the total number of ions ($\mathcal{N}^{\rm disk}_{\rm total}$; for Si IV or O VI) within the warm gas disk by integrating the ion number density over the radial and vertical directions:

$$\mathcal{N}^{\rm disk}_{\rm total} = n_0 \int_0^{R_{\rm vir}} {\rm d}r \exp(-\frac{r}{r_0}) \int_{-R_{\rm vir}}^{R_{\rm vir}} {\rm d}z \exp(-\frac{|z|}{z_0}). \tag{4.4}$$

Then, we calculate the masses of Si IV and O VI ions in the warm gas disk for different models (Table 4.2 and Table 4.3). For each ion, various models lead to similar ion masses within 0.3 dex. Summarizing our results, we obtain the mass of Si IV is $\log(M/M_\odot) = 3.8 \pm 0.1$, while the O VI mass is $\log(M/M_\odot) = 4.4 \pm 0.2$.

Table 4.3: The Joint Fitting Results of Si IV and O VI

Ion	$\log n_0$ (cm^{-3})	r_0 kpc	z_0 kpc	$\Delta \log N^{\mathrm{CGM}}$ [a] dex (cm^{-2})	$\log N_{\mathrm{nd}}^{\mathrm{CGM}}$ (cm^{-2})	red. χ^2 (dof)	$\log n_{\odot}^{\mathrm{disk}}$ (cm^{-3})	$\log n_{\odot}^{\mathrm{disk}} z_0$ (cm^{-2})	$\log M_{\mathrm{disk}}$ ($M_{\odot}$)
Si IV	-8.02 ± 0.12	6.1 ± 1.2	2.6 ± 0.4	0.82 ± 0.32	13.32 ± 0.07	1.126 (376)	-8.63	13.28	3.91
O VI	-7.22 ± 0.12	...	...	...	14.17 ± 0.08	...	-7.83	14.08	4.46
Si IV	-8.04 ± 0.13	6.1 ± 1.2	2.9 ± 0.5	0.86 ± 0.43	13.30 ± 0.08	1.123 (374)	-8.64	13.30	3.93
O VI	-7.21 ± 0.12	...	2.3 ± 0.5	0.74 ± 0.32	14.20 ± 0.08	...	-7.81	14.04	4.42
Si IV	-7.92 ± 0.16	5.2 ± 1.2	2.6 ± 0.4	0.69 ± 0.32	13.32 ± 0.07	1.117 (374)	-8.64	13.26	3.86
O VI	-7.36 ± 0.13	8.0 ± 2.3	...	0.99 ± 0.49	14.19 ± 0.08	...	-7.82	14.08	4.56
Si IV	-7.96 ± 0.16	5.5 ± 1.2	2.7 ± 0.5	0.81 ± 0.32	13.32 ± 0.08	1.118 (374)	-8.63	13.29	3.89
O VI	-7.32 ± 0.15	7.5 ± 2.1	2.4 ± 0.5	...	14.18 ± 0.08	...	-7.82	14.06	4.50

Notes: Every two lines are one model, since these are joint models for both Si IV and O VI. The blank parameters of O VI are tied to Si IV.

[a] $\Delta \log N^{\mathrm{CGM}} = \log N_{\mathrm{nd}}^{\mathrm{CGM}} - \log N_{\mathrm{mp}}^{\mathrm{CGM}}$. Positive values indicate that the CGM column density is higher in the direction perpendicular to the disk $\log N_{\mathrm{nd}}^{\mathrm{CGM}}$ than the radial direction ($\log N_{\mathrm{mp}}^{\mathrm{CGM}}$).

To obtain the total mass of the Si IV or O VI-bearing gases, we assume the warm gas has the solar metallicity, and adopt log(Si/H) and log(O/H) solar abundance values from Asplund et al. (2009). Also, we assume the average ionization fraction of 0.2 and 0.1 for Si IV and O VI, respectively (about half of the maximum in CIE or PIE to represent the average ionization fraction; Gnat & Sternberg 2007; Oppenheimer & Schaye 2013). Then, the expected total number of hydrogen atoms is $\mathcal{N}_{\rm H} = \mathcal{N}^{\rm disk}_{\rm total}/f/a$, where f is the ionization fraction of Si IV or O VI, and a is the abundance of silicon or oxygen. Taking the helium mass into account, the total mass of the warm gas disk is $1.3\mathcal{N}_{\rm H}m_{\rm H}$, where $m_{\rm H}$ is the hydrogen atom mass. Finally, the derived total masses of the warm gas disk based on Si IV and O VI are

$$\log(M_{\rm H}/M_\odot)^{\rm disk}_{\rm SiIV} = (7.6 \pm 0.1) - \log\frac{f_{\rm SiIV}}{0.2} - \log\frac{Z}{Z_\odot},$$
$$\log(M_{\rm H}/M_\odot)^{\rm disk}_{\rm OVI} = (7.6 \pm 0.2) - \log\frac{f_{\rm OVI}}{0.1} - \log\frac{Z}{Z_\odot}, \quad (4.5)$$

which are similar to each other.

The similarities of shapes and masses between Si IV and O VI disks indicate that these two ions might trace the same gases. However, it does not mean that these two ions are cospatial, since the ion ratio (Si IV/O VI) shows large scatters (≈ 0.5 dex; SW09). Si IV and O VI occupy the same space at large-scale (Galactic scale) due to the similarities of the disk shapes, but these two ion-bearing gases are clumpy to be non-cospatial at small-scale (single cloud size; kpc size; Werk et al. 2019). The Si IV gas is more clumpy than O VI because it has larger intrinsic scatters (the patchiness parameter; Table 5.1). The same shapes of the Si IV and the O VI disk profiles from our models indicate that the warm gas disk cannot be in equilibrium. If these ions are in photoionization equilibrium, the Si IV gas should have a larger scale height, while the thermal-supported collisional disk predicts the opposite behavior.

A possible explanation of the same scale heights for Si IV and O VI is that these

ions are produced by feedback processes (e.g., the Galactic fountain; Bregman 1980; Melso et al. 2019). In the Galactic fountain, the gas could be IVCs, which are separate clouds (Wakker et al., 2008; Shull et al., 2009; Werk et al., 2019). Then, the Si IV gas is close to the core of H I, while the O VI gas is likely to be the envelope, since Si IV has a lower excitation potential. The scale heights of these two ions are both set by the ejection due to Galactic feedback. It is also explained that the Si IV gas is more clumpy than the O VI gas, since as an envelope, the O VI gas should have a larger volume filling factor.

As a comparison to the neutral gas, the H I disk has a total mass of $7.1 \times 10^9\ M_\odot$, a scale height of 0.15 kpc, and a scale length of 3.25 kpc within 30 kpc (Kalberla & Dedes, 2008; Nakanishi & Sofue, 2016). Besides the thin H I disk component, there is also a more extensive H I disk with a scale height of $1.6^{+0.6}_{-0.4}$ kpc, which contains a mass of $3.2^{+1.0}_{-0.9} \times 10^8\ M_\odot$ (named as the H I halo in Marasco & Fraternali 2011). The warm gaseous disk has a larger scale height than the thick H I disk, while the mass is about one order of magnitude lower.

4.4.3 The Anisotropic CGM

As stated in Section 3.2, the preferred CGM component in our model is anisotropic with a dependence on Galactic latitude. The joint fitting of Si IV and O VI shows that there is an enhancement of $\Delta \log N = 0.82 \pm 0.32$ for the column density perpendicular to the disk compared to the direction along the disk. It is worth noticing that although the component is named as "CGM", it does not mean that this enhancement of the column density is completely due to the CGM of the MW. This column density enhancement could be due to the enriched CGM of the MW or the interaction layer between the disk and the CGM (e.g., interface layers around low-intermediate velocity clouds).

In the first scenario, the CGM above the disk is enriched by feedback processes

from the disk which ejected (and recycled) materials/metals into the CGM. Also, the escaping ionizing fluxes are more intense in the z-direction, which could lead to higher ionization states (Si IV and O VI) by photoionization. Another possibility is that there is an interaction layer between the disk and the halo gas above the disk, such as the Galactic fountain (Bregman, 1980), which can be observed as low-intermediate velocity clouds (Wakker et al., 2008; Werk et al., 2019). If this component cannot be included in the disk component in our modeling, then it has to be attributed to the anisotropic "CGM" component, which might be the case here. Although these two possibilities are both associated with the feedback processes, the difference is the location of the gases, which could affect the estimation of the mass of the MW warm CGM. However, current observations cannot determine the location of these gases. Hereafter, we assume it is the enriched CGM scenario.

To estimate the mass of the warm CGM, we calculate the the average CGM column density over the entire sky, which is $\frac{1}{2}\int_{-\pi/2}^{\pi/2} \mathrm{d}b N_{\mathrm{CGM}}(b)\cos b$. The average CGM column densities are $\log N = 12.84$ and $\log N = 13.70$ for Si IV and O VI, respectively. The maximum radius of the CGM is fixed as the virial radius of the MW (250 kpc). The total ion mass is $\log(M/M_\odot) = (5.6 \pm 0.2) + 2\log(R_{\mathrm{max}}/250\ \mathrm{kpc})$ assuming the uniform density distribution for Si IV, and $\log(M/M_\odot) = (6.3 \pm 0.2) + 2\log(R_{\mathrm{max}}/250\ \mathrm{kpc})$ for O VI, where R_{max} is the maximum radius of the CGM. The metallicity of the MW CGM is assumed to be 0.5 $Z_\odot$ (Bregman et al., 2018), and the average ionization fraction is about the half of the peak from CIE or PIE (similar to the disk calculation in Section 4.2). Then, the Si IV and O VI-bearing gases have

masses of

$$\begin{aligned}
\log(M_{\rm H}/M_\odot)^{\rm CGM}_{\rm SiIV} &= (9.8\pm0.2) - \log\frac{f_{\rm SiIV}}{0.2} - \log\frac{Z}{0.5Z_\odot}, \\
&\quad +2\log\frac{R_{\rm max}}{250{\rm kpc}}, \\
\log(M_{\rm H}/M_\odot)^{\rm CGM}_{\rm OVI} &= (9.8\pm0.2) - \log\frac{f_{\rm OVI}}{0.1} - \log\frac{Z}{0.5Z_\odot}, \\
&\quad +2\log\frac{R_{\rm max}}{250{\rm kpc}}. \qquad (4.6)
\end{aligned}$$

Different from the disk component, we cannot constrain whether Si IV and O VI have similar shapes for the CGM, but if we assume they follow the same density profile, the masses are the same for these two ions. If one wants to estimate the mass for the interaction-layer scenario, one could use $\log N = 12.50$ and $\log N = 13.36$ instead in the mass estimation, which is a difference of ≈ 0.34 dex.

The mass of the CGM has a dependence on the radial profile of the density. Although the radial profile of the warm gas cannot be determined using current observations for the MW, we show the effect of this variation as the following. For simplicity, we assume a β-model of $n(r) = n_0 r^{-3\beta}$ (a power law model), which is empirical for the MW hot gas (Li & Bregman, 2017) and warm gas in external galaxies (Werk et al., 2013; Johnson et al., 2015). Then, the new CGM mass is

$$\frac{M_\beta}{M_{\rm u}} = \frac{1-3\beta}{1-\beta}\frac{R_{\rm max}-R_{\rm min}}{R^3_{\rm max}-R^3_{\rm min}}\frac{R^{3-3\beta}_{\rm max}-R^{3-3\beta}_{\rm min}}{R^{1-3\beta}_{\rm max}-R^{1-3\beta}_{\rm min}}, \qquad (4.7)$$

where M_β is the mass in the β-model, while $M_{\rm u}$ is the mass in the uniform density model (Equation 5). $R_{\rm max}$ and $R_{\rm min}$ are the maximum and the minimum radii. With a boundary of 10 kpc and 250 kpc, the $M_\beta/M_{\rm u}$ ratio is 0.24 with $\beta = 1/2$ (the theoretical hydrostatic equilibrium solution; Mo et al. 2010), which is a correction of -0.6 dex for Equation 6. Generally, a larger β leads to a smaller mass of the CGM. Varying β from 1/3 to 2/3, the mass ratio varies from 0.45 to 0.12, and the mass is

always lower than the uniform model. Therefore, we suggest that the mass in the Equation 6 is the upper limit if the radial profiles of Si IV and O VI are decreasing at larger radii with the same assumptions of the abundance and the ionization fraction. The suggested mass region is $\log(M/M_{\odot}) \approx 8.9-9.5$ with a correction of $-\log\frac{Z}{0.5Z_{\odot}}$.

The mass of the HVCs are not included in the previous discussion, since the Savage03 and Zheng19 samples only measured absorption features at low and intermediate velocities ($|v| \lesssim 100$ km s^{-1}). One of the major contributor of the HVCs is the Magellanic Systems (MS), which has a total mass of $\log(M/M_{\odot}) \approx 9.3$ for atomic and warm-ionized gases: $\approx 4.9\times10^{8}$ $M_{\odot}$ in H I; $\approx 1.0\times10^{9}$ $M_{\odot}$ in the warm gas in MS; and $\approx 5.5\times10^{8}$ $M_{\odot}$ in the envelope of the MS (Brüns et al., 2005; Fox et al., 2014). Besides the Magellanic systems, other HVCs have a total H I mass of 2.6×10^{7} $M_{\odot}$ (Wakker, 2004; Putman et al., 2012). Assuming other HVCs have a similar the H I/total warm gas ratio of MS (1:4), the total mass of other HVCs is about 1×10^{8} $M_{\odot}$ (Lehner et al., 2012). Then, the total HVC mass in the MW is $\log(M/M_{\odot}) \approx 9.4$, which is comparable to the derived mass of low- and intermediate-velocity gas in this paper. Therefore, the total mass of the warm-ionized gaseous halo is about $\log(M/M_{\odot}) \approx 9.5-9.8$ for the all velocity range.

This derived mass is consistent with the mass of $\log(M/M_{\odot}) \gtrsim 9.3$ reported in Zheng19, which only used the Si IV AGN sample to estimate the CGM column density of the MW. Our estimation of the warm CGM mass is comparable to the Andromeda galaxy, which has a total mass of $\log(M/M_{\odot}) \approx 9.1-\log(Z/Z_{\odot})$ for the warm gas (up to C IV; Lehner et al. 2015). The warm CGM mass of the MW is consistent with some L^{*} galaxy samples at redshifts of $z \lesssim 0.2$ with $\log(M/M_{\odot}) \approx 9.5-10.4$ (Stocke et al., 2013), while there are also samples showing significant differences of L^{*} galaxies at $z \approx 0.2$ (e.g., COS-Halos), which obtained a mass of $\log(M/M_{\odot}) \approx 10.8-11.0$ (Werk et al., 2014; Prochaska et al., 2017). However, significantly different masses are derived with different models using the same COS-Halos data, such as $\log(M/M_{\odot}) \approx 10.1$

(Stern et al., 2016; Bregman et al., 2018). These uncertainties suggest that the mass estimation of CGM is model-depended, but the local L^*galaxies (i.e., the MW and the Andromeda) do not favor a warm CGM with a mass comparable to the stellar mass.

4.4.4 Comments on the North-South Asymmetry

As shown in Fig. 4.2 and Fig. 4.4, there is a significant north-south (NS) asymmetry for the observed scale height of AGN samples, which indicates the asymmetry of the warm gas distribution. This asymmetry is similar to the NS asymmetry of the Galactic X-ray background, which shows more soft X-ray emission in the northern hemisphere (Snowden et al., 1997). The physical origin of this asymmetry is unclear, and beyond the scope of this paper. However, it is of interest to determine the origin of the warm gas asymmetry phenomenologically (i.e., the disk or the CGM).

Based on previous results, we assume Si IV and O VI have the same behaviors for both the disk and the CGM: the scale length, the scale height, and the CGM difference between two axes. Considering the NS asymmetry, there are three possible variations between two hemispheres: the scale height of the disk; the disk normalization density; and the CGM column density. Here, we ignore the possible difference of the scale length, which is fixed to the same for both hemispheres. Then, this model can have different scale heights and different disk density normalizations between the north and south disks, and different azimuthal CGM column densities (Table 4.4). The total χ^2 difference is 35.1, which is 5.3σ with a dof difference of 3. The fitting reveals that the differences of the disk density normalizations and the CGM column density normalizations are close to zero, within the uncertainty. The largest variation is due to the difference in the scale heights.

Table 4.4: The Fitting Results of the North-South Asymmetry

Ion	$\log n_0$ [a] (cm^{-3})	$\Delta \log n_0^{\mathrm{NS}}$ [b] (cm^{-3})	r_0 kpc	z_0^{N} kpc	z_0^{S} kpc	$\Delta \log N^{\mathrm{CGM}}$ dex (cm^{-2})	$\log N_{\mathrm{nd}}^{\mathrm{CGM}}$ [a] (cm^{-2})	$\Delta \log N_{\mathrm{CGM}}^{\mathrm{NS}}$ [b] (cm^{-2})	red. χ^2 (dof)
Si IV	-8.01 ± 0.12	0.06 ± 0.05	6.0 ± 1.1	3.4 ± 0.6	2.5 ± 0.4	0.92 ± 0.46	13.21 ± 0.14	-0.09 ± 0.15	1.034 (373)
O VI	-7.20 ± 0.12	...	...	...	...	...	13.96 ± 0.16	...	...
Si IV	-7.97 ± 0.12	0.14 ± 0.02	6.0 ± 1.0	2.9 ± 0.4	...	0.98 ± 0.46	13.26 ± 0.08	...	1.045 (375)
O VI	-7.17 ± 0.11	...	...	...	...	...	14.06 ± 0.11	...	...
Si IV	-8.03 ± 0.12	...	5.9 ± 1.1	3.5 ± 0.5	2.3 ± 0.4	0.83 ± 0.41	13.26 ± 0.08	...	1.039 (375)
O VI	-7.23 ± 0.12	...	...	...	...	...	14.04 ± 0.11	...	...
Si IV	-7.95 ± 0.13	...	5.2 ± 1.0	2.5 ± 0.4	...	0.56 ± 0.20	13.40 ± 0.06	0.29 ± 0.09	1.063 (375)
O VI	-7.18 ± 0.12	...	...	...	...	...	14.25 ± 0.06	...	...

Notes: Every two lines are one model, since these are joint models for both Si IV and O VI. The blank parameters of O VI are tied to Si IV.

[a] The disk density and the CGM column density are for the northern hemisphere.

[b] For the difference between two hemispheres, the positive value indicates that the northern hemisphere is higher than the southern hemisphere.

Quantitatively, we vary these parameters individually to determine the dominant factor (Table 4.4). The fitting results show that the scale height is the dominant parameter rather than the disk normalization or the CGM normalization with the smallest reduced χ^2. Only varying the scale height, this model is 0.8σ worse compared to the "best" model (with all parameters free) by $\Delta\chi^2 = 1.78$ and the dof difference of 2. Similarly, the disk normalization model is 1.5σ away from the "best" model. Although the scale height model is preferred, it is not a large statistical difference between these two models with varied disk shapes. Compared to models where the disk is varied, the model with CGM-only differences is less preferred since it is 2.9σ away from the "best" model.

In the different scale height models, the northern and the southern hemispheres have scale heights of 3.5 ± 0.5 kpc and 2.3 ± 0.4 kpc, respectively. The difference of the scale heights is about 1.2 kpc, which is at about 2σ. As shown in Fig. 4.6, a larger scale height leads to a larger scatter at low latitudes, which is favored by the observations. In this model, the variation of the model parameters does not affect the mass estimation in Section 4.2 and 4.3, which are all within 1σ. Therefore, we do not report new values for the masses of both the disk and the CGM.

4.4.5 The Possible Non-Uniform Structures

It is well known that the warm gas disk and CGM of the MW both have lots of structures, e.g., the Fermi Bubbles (FBs), HVCs, and the Local Bubble. These structures may have a non-uniform contribution to the measured column density of warm gases, which is opposite to our assumption that the density profile of the warm gas can be modeled by smooth functions. Therefore, we adopt the blocking method to test whether these possible non-uniform structures affect our fittings; a similar method has also been used by Zheng19 to study the underlying gaseous structures in the MW halo. For the blocking, we mean to block some part of the sky to obtain

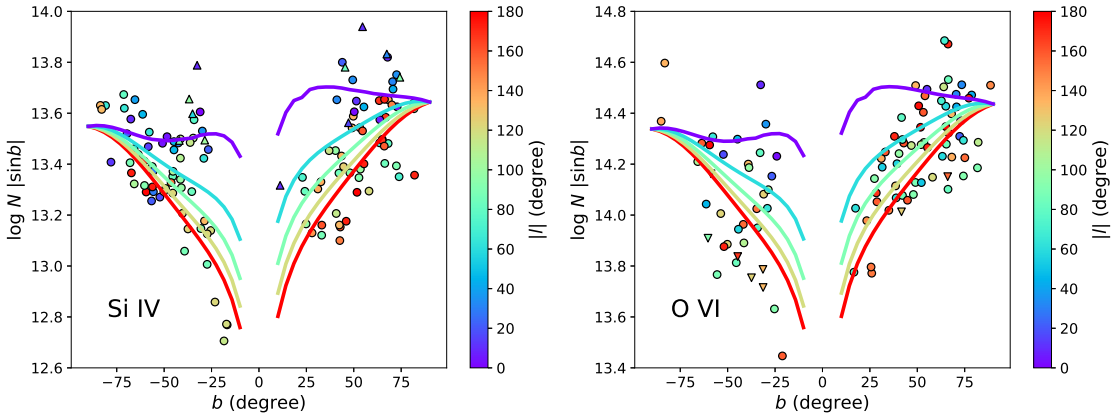

Figure 4.6: The varied scale height model to account for the north-south asymmetry. The data and model are color encoded in the same way as Fig. 4.2 and Fig. 4.4.

a new set of sample and fitting result. The (non-)consistency between blocked and unblocked fitting results show the hints for the effect of the possible structures in the blocked region.

First, we consider a known structure – the FBs. Bordoloi et al. (2017b) and Karim et al. (2018) showed the enhancement of HVCs due to the FBs (both the northern and southern bubbles), which are not included in our modeling. Therefore, we block the sky region of $-60° < b < 60°$ and $-30° < l < 30°$ to avoid the AGN sightlines (17 for Si IV and 5 for O VI) througth the FB. The stellar sightlines are not masked out since none of the stars are distant enough to be in the FB. The fitting results are $R_0 = 5.5 \pm 1.1$ kpc, $z_0 = 2.9 \pm 0.5$ kpc, and the CGM difference of 0.80 ± 0.34 dex. This solution is within 0.5σ from the fiducial model (Table 4.3). The mass estimates of the warm gas are all within uncertain of 0.2 dex for both the disk and the CGM. Therefore, we suggest that the FBs do not contribute to the low-intermediate velocity warm gas significantly, although detailed studies on the FBs show evidence for the enhancement of HVCs (Bordoloi et al., 2017b; Karim et al., 2018).

Then, we consider possible unknown large scale structures, such as the possible

connection with HVCs and IVCs (Sembach et al., 2003). Zheng19 used the block bootstrapping to study it, while we consider this in a simple way. Following Zheng19, the sky is divided into eight regions with $90^\circ \times 90^\circ$ based on the latitude and the longitude. Each region is blocked out in turn, so we have eight new samples with about 7/8 sightlines of the fiducial sample. We applied the joint model to these new samples. The fittings of the blocked sample lead to the parameter region of $R_0 \approx 5.2 - 7.4$ kpc, $z_0 \approx 2.2 - 3.0$ kpc, and $\Delta \log N^{\rm CGM} \approx 0.63 - 1.23$. These results are all within uncertainty (1σ) of the fiducial model, which indicates that there are no significant contributions from the unknown structures, and our assumption of the smooth profiles is roughly hold at large-scale.

4.5 Summary

We develop a 2-D disk-CGM model for the MW absorption line samples of Si IV and O VI. The radial density profile of the disk is introduced to determine if it alleviates the tension between the stellar sample and the AGN sample, where a thick warm disk is supported by the stellar sample (SW09), but not by the two-component disk-CGM model of the AGN sample (Zheng19). More details can be found in Section 4.1 for the difference between the new model and the previous studies (e.g., SW09; Zheng19). Adopting the new model, we obtain the scale heights and the scale lengths for the warm gas disk traced by Si IV and O VI, and estimate the masses in both the gaseous disk and the gaseous halo. Here, we summarize our results:

1. For the MW, the preferred warm gas distribution has a 2-D disk component ($\rm R_E Z_E$) with exponential radial and vertical profiles ($n(r,z) = n_0 \exp(-|z|/z_0)$ $\exp(-r/r_0)$) and an anisotropic CGM component (depending on Galactic latitude). The joint fitting of Si IV and O VI shows that these two ions could be modeled by the same density profile, which has a scale length of $r_0 = 6.1 \pm 1.2$

kpc and a scale height of $z_0 = 2.6 \pm 0.4$ kpc. The same shape of Si IV and O VI might indicate that these two ions are physically associated with each other despite a significant difference in their ionization potentials. This scale length is larger than the H I disk ($\approx 3-4$ kpc) and the stellar disk (≈ 2 kpc). In SW09, O VI was found to have a lower scale height than Si IV, which was suggested as an evidence for different ionization mechanisms between Si IV and O VI. However, our fitting shows that there is no significant difference between the Si IV and the O VI scale heights, but this does not mean that these two ions are cospatial.

2. From our best-fit model (the $R_E Z_E$ disk and anisotropic CGM), the total mass of the warm gas disk ($\log T \approx 5$) is about $\log(M/M_\odot)_{\rm SiIV} = (7.6 \pm 0.2) - \log \frac{Z}{Z_\odot}$.

3. The CGM component in our model makes a comparable contribution of the column density as the warm gas disk. Our modeling indicates that it has a higher column density in the direction perpendicular to the disk than the direction along the disk at $> 4\sigma$ levels for both Si IV and O VI. Combining these two ions, the difference is 0.82 ± 0.32 dex at about 6.3σ between the vertical and radial directions. However, some of this difference may be due to an interaction layer close to the disk, which we attribute to the CGM.

4. The mass of the low-intermediate velocity ($|v| \lesssim 100$ km s^{-1}) warm ($\log T \approx 5$) gas in the CGM is estimated to be $\log(M/M_\odot) \approx 9.8 \pm 0.2$ with a uniform density distribution and a metallicity of 0.5 $Z_\odot$. When we adopt a β-model (power law; $n(r) = n_0 r^{-3\beta}$) to approximate the density profile to 250 kpc, the total mass will be reduced to $\log(M/M_\odot) \approx 9.5$ ($\beta = 1/3$), $\log(M/M_\odot) \approx 9.2$ ($\beta = 1/2$), and $\log(M/M_\odot) \approx 8.9$ ($\beta = 2/3$). Then, the total mass of the warm CGM is estimated to be $\log(M/M_\odot) = 9.5 - 9.8$ for the MW, combining with the HVC mass of $\log(M/M_\odot) = 9.4$ for the MW.

5. The projected column density ($\log N \sin|b|$) of AGN indicates a significant north-south asymmetry. Our models suggest that this asymmetry is more likely due to an asymmetric disk rather than an asymmetric CGM at about 2σ. For the asymmetric disk, the variation of the density or the scale height cannot be distinguished, but the model with varying scale heights shows a smaller reduced χ^2 (at $\approx 0.7\sigma$). The northern and the southern hemispheres have scale heights of 3.5 ± 0.5 kpc and 2.3 ± 0.4 kpc, respectively.

CHAPTER V

The Warm Gas in the MW: A Kinematical Model

5.1 Introduction

As part of the galaxy baryon cycle, the multi-phase gas exists in both the gaseous disk (interstellar medium; ISM; Dickey & Lockman 1990; Cox 2005) and the gaseous halo (circumgalactic medium; CGM; Putman et al. 2012; Tumlinson et al. 2017). The gaseous disk is roughly cospatial with the stellar disk and provides fuels for current star formation. The existence of the gaseous halo not only supplies the gaseous disk for continuous star formation but also gathers the feedback materials from stellar evolution. The gas exchange between the gaseous disk and the gaseous halo involves fundamental processes in galaxy formation and evolution: the gas assembly and the galactic feedback, which are still highly uncertain.

The warm-hot gas ($\log T \approx 5$) in galaxies is a unique tracer for accretion and feedback processes, because it is at the peak of the radiative cooling curve, which leads to short cooling timescale ($\log \tau \lesssim 10$ Myr; e.g., Oppenheimer & Schaye 2013; Gnat 2017). The existence of this gas is unstable, so it needs to be refreshed by accretion (e.g., accretion shocks McQuinn & Werk 2018; Qu & Bregman 2018b; Stern et al. 2018) and feedback processes (e.g., galactic fountain and galactic wind; Shapiro & Field 1976; Bregman 1980; Thompson et al. 2016).

The warm-hot gas is commonly observed in both external galaxies and the Milky

Way (MW). For external galaxies, the extended warm-hot gas is detected in multi-wavelength emissions (Howk & Savage, 2000; Rand et al., 2008; Li et al., 2014; Hodges-Kluck et al., 2016b; Boettcher et al., 2016). The detection approaches utilizing warm gas emission has a limitation of low emissivity at large radii ($\gtrsim 20$ kpc). However, the low-density warm-hot gas at large radii could be detected as absorption lines against the continua of background AGN/stellar objects (Stocke et al., 2013; Werk et al., 2013; Lehner et al., 2015; Johnson et al., 2015; Bowen et al., 2016; Tumlinson et al., 2017; Burchett et al., 2019). For the warm-hot gas, the most popular intermediate-to-high ionization state ions are in the UV band, such as Si IV, C IV, and O VI, with a limiting column density of $\log N \approx 13$ at $S/N = 10$. The major limitation of the absorption line studies is that the bright background UV targets (AGN or UV-bright star for local galaxies) are rare to have a large sample (more than 10 sight lines) for individual galaxies (Lehner et al., 2015; Bowen et al., 2016; Zheng et al., 2017; Qu et al., 2019).

The only exception is the MW, which has hundreds of sight lines toward AGN and stars within the MW halo observed in past decades (Jenkins, 1978; Cowie et al., 1979; Bruhweiler et al., 1980; Savage & de Boer, 1981; de Boer & Savage, 1983; de Kool & de Jong, 1985; Sembach & Savage, 1992; Sembach et al., 1994; Shull & Slavin, 1994; Sembach et al., 1997; Savage et al., 2001, 2003; Sembach et al., 2003; Fox et al., 2004; Bowen et al., 2008; Savage & Wakker, 2009; Lehner & Howk, 2011; Wakker et al., 2012; Fox et al., 2014, 2015; Bordoloi et al., 2017b; Karim et al., 2018; Werk et al., 2019; Zheng et al., 2019a). These studies suggested that the MW has a thick warm gas disk close to the stellar disk (e.g., Savage & Wakker 2009) and a massive warm gas halo (e.g., Zheng et al. 2019a). However, the radial density distribution of the warm gas is still poorly known, because the column density integrated over the sight line cannot determine the density distribution directly.

Here, we propose a new method to extract the density distribution by considering

warm gas kinematics. The basis of this method is that, given a bulk velocity field, different radial density distributions will lead to significantly different absorption line shapes. This is because gas close to the Sun will have small projected velocities, while distant gas will have large velocity shifts. Then, different velocities (in the absorption line shape) could be converted to distances of the gas. Combining with column densities (amount of gas) at different velocities, the density distribution of the warm gas could be derived.

The issue for this method is that the kinematics of the MW warm gas is not completely understood, although it is important to understand the Galaxy evolution (i.e., the continuous star formation; Lehner & Howk 2011). Previous studies suggested that the warm gas in the MW shows signatures from both galaxy rotation (Wakker et al., 2012) and gas inflow ($-100 \lesssim v_{\rm LSR} \lesssim 0$ km s^{-1}; Lehner & Howk 2011; Zheng et al. 2019a). This is consistent with both the H I disk (and the H I halo; Dickey & Lockman 1990; Marasco & Fraternali 2011) measured from 21 cm line mapping, and hot gas traced by X-ray absorption features (Hodges-Kluck et al., 2016b). For both H I and X-ray observations, kinematical models have been applied to reproduce the observed features (e.g., line centroids or line widths), and extract kinematics information. The H I halo (up to z height $\approx 2-3$ kpc) are co-rotating with disk with a rotation velocity of $v_{\rm rot} = 220$ km s^{-1} and a vertical velocity gradient (disk-halo lagging) of $\mathrm{d}v_{\rm rot}/\mathrm{d}z = -15 \pm 4$ km s^{-1} kpc^{-1} (Marasco & Fraternali, 2011). Also, the H I halo has a significant inflow with a velocity along the radial direction of 30^{+7}_{-5} km s^{-1} and a vertical velocity of 20^{+5}_{-7} km s^{-1}. Similarly, the hot halo is also co-rotating with the disk at $v_{\rm rot} = 183 \pm 41$ km s^{-1}, while the hot halo does not have detected inflow, outflow, or lagging features due to the limitation of the X-ray instrument (Hodges-Kluck et al., 2016b).

However, no such kinematical model has been applied to reproduce the warm gas absorption features. Previous studies only modeled the (column) density distribution

without kinematics, hence the density distribution at large radii cannot be obtained (Savage & Wakker 2009; Zheng et al. 2019a; Qu & Bregman 2019; hereafter QB19). To make up this gap, we build up a kinematical model, which contains free parameters for both the warm gas density distribution, the gas kinematics (e.g., rotation, inflow. or outflow), and the gas properties (e.g., the broadening velocity). In this kinematical model, the absorption features are predicted to exist in the velocity range of ≈ -200 to 200 km s^{-1}, which is mainly determined by galaxy rotation. To constrain this kinematical model, we extract a Si IV differential column density line shape sample based on the *Hubble Space Telescope*/Cosmic Origins Spectrograph (*HST*/COS; Green et al. 2012) archival data, and obtain the best parameters to optimize the likelihood of reproducing all Si IV line shapes.

In this paper, Section 5.2 summarizes the employed sight lines (mainly extracted from the *Hubble* Spectroscopic Legacy Archive; HSLA; Peeples et al. 2017) and introduces the data reduction of individual sight lines. In Section 5.3, we introduce the previous models of the MW warm gas (column) density distribution (no kinematics in models), which is the basis of the new kinematical model in this work. In the new model, we assume that the warm gases are clouds or layers rather than a continuous distribution, and assumptions of the cloud-like feature are introduced in Section 5.4. The kinematical models are described in Section 5.5, which includes the density distribution (Section 5.5.1), the kinematics (Section 5.5.2), calculation of the differential column density line shape (Section 5.5.3), and the Bayesian model to optimize parameters (Section 5.5.4). Section 5.6 describes the fitting results from the kinematical model, where we extract the warm gas density distribution, the rotation velocity, the radial velocity, and properties of single warm gas clouds. We discuss the results in Section 5.7, such as the origin of the warm gas, the implications of kinematics, and the warm gas mass and accretion rate. We summarize key conclusions in Section 5.8.

5.2 Sample and Data Reduction

We consider both the stellar sample and the AGN sample in our analyses. The CGM at large radii is only detected against the AGN continuum ($r \gtrsim 10$ kpc; r is the distance to the Galactic center; GC), and the large scale variation of the disk is also dominated by the AGN sight lines (QB19). Due to the high sensitivity, the *HST*/COS obtains hundreds of AGN sight lines, which could be employed to extract absorption line shapes at high signal-to-noise ratios ($S/N > 10$). Using the line shape, one could extract both the MW gas density distribution and kinematics (details in Section 5). The stellar sample is employed to better constrain the midplane gas properties (hence the disk properties).

In this study, we focus on the intermediate ionization state ion Si IV, which has doublet lines at 1393.8 Å and 1402.8 Å. The doublet could be used to exclude contamination and check saturation. Therefore, Si IV is a good choice to extract the differential column density line shape. C IV is another important ion of interests, which has doublet lines at 1548.2 Å and 1550.8 Å. With a higher element abundance, the C IV absorption column density are typically ≈ 0.5 dex stronger than the Si IV column density, which helps to extract weak features. However, the stronger absorption leads to more serious saturation issues for C IV at the peak of the differential column density line profile (about the half of sight lines have flattened peaks due to saturation). The flattened peaks will significantly affect the model constraints on the gas distribution (i.e., the higher peak around $v = 0$ km s^{-1} means more gas close to the Solar system). The method is beyond the scope of this paper to extract the column density line profile from the modestly saturated lines, so we do not analyze C IV in this paper.

We construct the Si IV line shape sample for AGN sight lines based on the HST Spectroscopic Legacy Archive (HSLA; Peeples et al. 2017). For the stellar sight lines, we only use the column density measurements (without line shapes) for Si IV in the

literature (Savage et al., 2001; Savage & Wakker, 2009; Lehner & Howk, 2011), which is extracted using observations obtained by the *International Ultraviolet Explorer* (*IUE*) and *HST*/Space Telescope Imaging Spectrograph (*HST*/STIS). There are 186 AGN sight lines with differential column density line profiles and 88 stellar sight lines with column density measurements.

5.2.1 Stellar sight lines

The Si IV stellar samples are adopted from Savage & Wakker (2009) and Lehner et al. (2011). Savage & Wakker (2009) mainly summarized column density measurements from *IUE* observations (Savage et al., 2001). The Savage & Wakker (2009) sample includes five transitional ions (Al III, Si III, Si IV, C IV, and O VI) for 109 MW stellar sight lines, 6 Large Magellanic Clouds/Small Magellanic Clouds (LMC/SMC) stellar sight lines, and 25 AGN sight lines. In our analysis, we only use the MW stellar sightlines, since COS gives a better AGN sample. These *IUE* observations have typical spectral resolutions of ≈ 20 km s^{-1} and $S/N \gtrsim 5$. The Lehner et al. (2011) sample is composed of the *HST*/STIS observations, which typically have higher S/N than the IUE sample, so we adopted STIS measurements for overlapping sight lines. There are 14 sight lines observed by both *IUE* and STIS, among which 12 sight lines are consistent within 2σ. Two sight lines have lower limits in the *IUE* sample, while the STIS sample has measurements lower than these lower limits. This indicates that the *IUE* observation may overestimate some continuum levels, which is limited by the S/N.

To test the possible systematic uncertainty of the *IUE* sample, we built two models in the fitting process (Section 5.6). One model uses the combination of both *IUE* and STIS samples, while another one only uses the STIS sample. These two samples give similar results (within 1σ), which indicates that the IUE sample is consistent with the STIS sample (more details in Section 8.3). Therefore, we still use the combination of

IUE and STIS samples for following analyses.

Savage & Wakker (2009) showed that H II regions have a significant contribution to the Si IV column density, so we omit the sight lines that have known foreground H II regions. The final sample has 65 Si IV column density measurements, 11 lower limits and 12 upper limits, among which 27 are from STIS.

We do not use the COS archival stellar sight lines in the following analyses. To constrain the midplane gas properties, we need sight lines that have suitable distances ($\approx 1-10$ kpc) and low Galactic latitude ($b \lesssim 20°$). However, there are few useful sight lines in the COS archival data. The COS instrument was used to obtain spectra in hundreds of stellar sight lines, with 354 of them having $S/N > 10$, but most sight lines do not have suitable distances. More than two-thirds of these stellar targets are nearby white dwarfs with distances of $\lesssim 0.1$ kpc. These sight lines mostly have non-detection for Si IV due to small path-lengths. Among the remaining ≈ 100 targets, about half are LMC/SMC targets (Roman-Duval et al., 2019), similar to the AGN (the column densities are sensitive to gas within ≈ 50 kpc), but affected by the LMC/SMC ISM (at $v \approx 200-300$ km s^{-1}). There are 8 stellar sight lines in M33 (Zheng et al., 2017), which have the same role as AGN sight lines nearby.

The remaining sight lines (≈ 50) have distances of $\approx 1-10$ kpc. However, about half of these targets have strong stellar features (i.e., strong stellar winds, emission lines, and structured continua), which make the extraction of absorption features unreliable. Finally, there are only ≈ 20 sight lines close to the disk and with well-behaved continua. These targets are mainly UV-bright stars in globular clusters (i.e., blue horizontal branch stars; Werk et al. 2019) at high b and $|z|$-height (above or below the disk), which is opposite to our purpose to constrain the midplane density of Si IV. Therefore, the archival COS data cannot improve our fitting significantly, and we do not include the line shapes from COS for stellar sight lines in this study.

5.2.2 AGN sight lines

For AGN sight lines, we limit the sample to $S/N > 10$, which is higher than the threshold of the stellar sample ($S/N \gtrsim 5$). This is because the line shapes in the AGN sample is required to constrain the kinematical model, while for the stellar sample, we only use the column density measurements. Si IV features normally have a velocity width of ≈ 100 km s^{-1} (≈ 6 resolution elements for both *IUE* and COS; the STIS sample has a higher resolution, but the *IUE* sample is dominant). Therefore, the uncertainty of line shape (per resolution element) for AGN sight lines at $S/N = 10$ should be comparable to the total uncertainty of the integrated column density for the stellar sample at $S/N = 5$.

We extract the line shape sample based on the HSLA database, which provides a uniformly-reduced scientific-level database (Peeples et al., 2017). As a quick summary, the HSLA database archives all of the COS public data, extracts one-dimension spectra for individual exposures, and coadds all exposures for one target to generate the final coadded spectrum. The output spectra have wavelength bins of 9.97×10^{-3} Å for the grating G130M and 12.23×10^{-3} Å for the grating G160M. Based on the first data release of the HSLA, Zheng et al. (2019a) constructed the COS-GAL sample, an AGN sample for the MW absorption features, which includes Si IV column density and line centroid measurements within $|v_{\rm LSR}| \leq 100$ km s^{-1}. Here, we construct an updated Si IV sample for three reasons. First, the HSLA database has the second release, which includes hundreds of new AGN sight lines, which also contains tens of $S/N > 10$ sight lines. Second, Zheng et al. (2019a) employed an arbitrary velocity criterion of 100 km s^{-1} to truncate the measurements, which excludes some wings of high-velocity clouds (HVCs), which could affect our model constraints. Third, we need to combine the two lines of the Si IV doublet to reduce the noise for the differential column density line shape.

Si IV has the doublet at 1400 Å, so we focus on the G130M spectrum that covers

the wavelength range of $1100-1450$ Å. In the second data release of the HSLA, there are 802 AGN sight lines, among which 402 sight lines have spectra using the grating G130M.

Our construction of the Si IV line shape sample has two parts. In the first part, we determine the continuum near 1393 Å and 1402 Å in a 5.6 Å interval (-600 km s^{-1} to 600 km s^{-1}), and select the sight lines with $S/N > 10$ per resolution element (6 original pixels). To determine the continuum, we use an iteration method, which masks out absorption features. First, we mask out pixels lower than the mean value of the flux by 1.5 times the error and obtain the initial guess of the continuum using the spline fitting for each interval. The factor of 1.5 is used to avoid the absorption features that might affect the fitting of the continuum. With the initial continuum, we mask out the pixels with flux lower than this continuum by 1.5 error and estimate the new continuum. This step is iterated until the continuum converges, which means the masked out region is the same for two successive continuum fittings. With the final continuum, the S/N values are calculated for the two intervals of 1393 Å and 1402 Å. Normally, these two regions have similar S/N values, except that an AGN broad emission line occurs in the Si IV region. We select all sight lines with $S/N > 10$ for either interval (1393 Å or 1402 Å). The 186 selected sight lines are summarized in Table 5.1, and there are 9 sight lines with relatively low $S/N < 10$ for one interval. Because we will combine two lines to obtain the final differential column density line shape, the combined S/N is always higher than 10.

In the second part, we combine the differential column density line shape and calculate the integrated column density. The line shape is calculated based on the apparent optical depth method (AODM; Savage & Sembach 1991), which converts the absorption depth into the apparent optical depth, hence the differential column

density $N(v)$ of the velocity (v):

$$N(v) = \frac{m_{\rm e}c}{\pi e^2 f \lambda} \ln \frac{I_0(v)}{I_{\rm obs}(v)}, \tag{5.1}$$

where $I_0(v)$ and $I_{\rm obs}(v)$ are the continuum flux and the observed flux. To reduce the uncertainty per data point in the line shape, the spectra are rebinned by 3 pixels (half of the resolution element; 6.4 km s^{-1}). Then the differential column densities are calculated for both strong and weak lines. By comparing the shapes of the strong line and weak line, we mask out the contamination regions in either line. We mainly calculate the line shape in the velocity range of -300 km s^{-1} to 300 km s^{-1}, which is the velocity region that could be accounted for in our model (Section 5.5) and continua of about 100 km s^{-1} in both sides. The coadded regions could be varied if necessary to include HVCs with extremely high velocities of $|v| > 300$ km s^{-1}. Fig. 5.1 shows two examples of the sight lines toward PG 1553+113 and Mrk 1392. The coadded column density is calculated using column density errors as weights, then the uncertainty of the coadded column density is $1/(1/\sigma^2_{N_{\rm s}} + 1/\sigma^2_{N_{\rm w}})^{1/2}$, where "s" and "w" denote the strong and the weak lines.

Because we will model the line shape, it is not necessary to decompose the absorption features into individual components for the following analyses. However, for the common use for the community, we decompose the components based on separated peaks (Table 5.1). These components can be divided into two classes roughly based on the line centroids ($v_{\rm c}$): the MW disk with low-velocity CGM ($v_{\rm c} \lesssim 150$ km s^{-1}) and HVC ($v_{\rm c} \gtrsim 150$ km s^{-1}). Using the coadded line shape, the total column density and line centroid for each component are calculated by integrals:

$$\begin{aligned} N &= \textstyle\int_{v_{\rm min}}^{v_{\rm max}} N(v) {\rm d}v \\ v_{\rm c} &= \textstyle\int_{v_{\rm min}}^{v_{\rm max}} N(v) v {\rm d}v / \int_{v_{\rm min}}^{v_{\rm max}} N(v) {\rm d}v, \end{aligned} \tag{5.2}$$

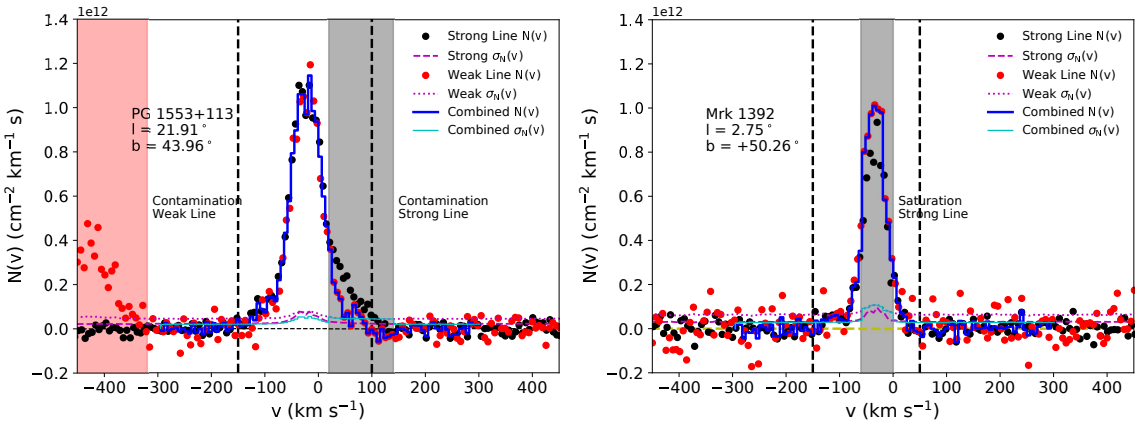

Figure 5.1: Two example sight lines of PG 1553+113 (left panel) and Mrk 1392 (right panel) showing combination of the Si IV doublet to obtain the column density line shape (the blue line). The black and red dots are the apparent column density of the strong (1393.8 Å) and the weak (1402.8 Å) lines, respectively. The shadowed regions are blocked out in the combination of the doublet due to contamination or saturation.

where $v_{\rm min}$ and $v_{\rm max}$ are the minimum and maximum velocity for each component. The column densities and line centroids for individual components are summarized in Table 5.1, and plotted in Fig. 5.2. The HSLA spectrum is in the heliocentric frame, so the reported velocities are also in the heliocentric frame. We do not convert this velocity into the LSR frame, and the motion of the Solar system is modeled in the kinematical model (Section 5.5.2).

There are three special issues need to note for the data reduction:

1. *Wrong continuum.* Most ($> 70\%$) of the sight lines use the continua generated in the first part of our method, using the automatically iterative method. However, the automatic continuum may deviate from the true continuum significantly, due to the AGN broad emission line (i.e., sharp features), and high S/N (i.e., the continuum fitting progress catching the wing of absorption features). Therefore, we inspect every automatic continuum fit, and do the continuum fitting by hand when necessary, where we select the continuum regions by hand and apply the spline fitting.

Table 5.1: The Column Density Measurements of the Selected Si IV Sample

Sightline	l	b	S/N	S/N	$v_{\rm min}$	$v_{\rm max}$	$\log N$	$\sigma_{\log N}$	$v_{\rm c}$	$\sigma_{v_{\rm c}}$
	deg.	deg.	Strong	Weak	km s^{-1}	km s^{-1}	dex	dex	km s^{-1}	km s^{-1}
(1)	(2)	(3)	(4)	(5)	(6)	(7)	(8)	(9)	(10)	(11)
Mrk 1392	2.8	50.3	24	23	−150	50	13.75	0.02	−37.1	1.2
LQAC 209+017 004	2.9	71.8	25	25	−140	30	13.70	0.01	−42.8	1.4
PG 1352+183	4.4	72.9	37	39	−180	60	13.65	0.01	−45.0	1.1
RBS 1768	4.5	−48.5	20	20	−220	−60	13.17	0.03	−141.7	3.4
					−60	120	13.58	0.02	29.7	1.6
LQAC 350-034 001	5.5	−69.4	17	18	−130	−70	12.68	0.07	−102.2	2.6
					−70	50	13.23	0.03	−15.7	2.3

Columns: (1) Target name; (2) Galactic longitude; (3) Galactic latitude; (4) S/N of the strong line continuum; (5) S/N of the weak line continuum; (6) Lower bound of absorption component; (7) Upper bound of absorption component; (8) Total column density of a component; (9) Column density uncertainty; (10) Line centroid of a component; (11) Line centroid uncertainty. The entire version of this table is in the publication version (https://iopscience.iop.org/article/10.3847/1538-4357/ab774e).

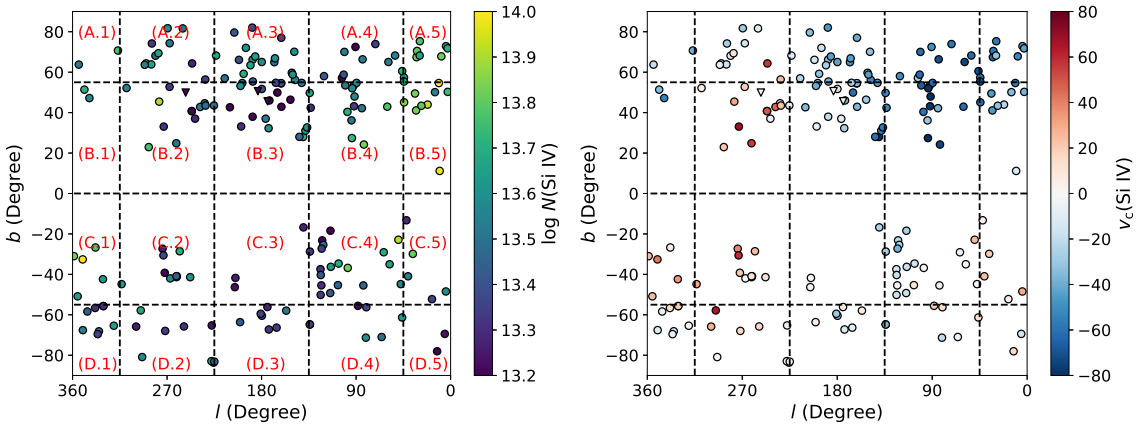

Figure 5.2: The column density (left panel) and the line centroid (right panel) of the MW Si IV line shape sample. The entire sky is divided into 20 regions based on the Galactic longitude and Galactic latitude grids. For each region, we stack the column density line shape to obtain an average line shape in Fig. 5.8.

2. *Saturation of the strong line.* Due to the higher oscillator f factor, the strong line of the Si IV doublet is twice stronger than the weak line, which might be affected by saturation. The saturation is shown as the feature that the weak line has a higher AODM column density than the strong line. However, the higher column density of the weak line does not necessarily mean saturation occurred, because it can also be due to contamination in the weak line. Therefore, we use Voigt fitting to test whether the weak line and the strong line are matched (i.e., two lines can be modeled by one Voigt model). If the two lines are matched, we need to check whether the weak line is significantly affected by saturation. We suggest that the weak line is not significantly affected by saturation if the AODM column density of the weak line is within 2σ of the summation of the fitting components. Then, we use the peak of the weak line column density shape as the peak of the combined line shape instead of the combination of both the strong and weak lines (Mrk 1392 in Fig. 5.1). In practice, all of the saturation features are weak saturation features, where we could extract the peak shape of the column density line shape from the weak line, although the strong line is partially saturated.

3. *Badly blended features.* If the two lines of the doublet are both blended with contamination lines, the true line shape cannot be extracted using the AODM approach. There are 12 sight lines with the badly blended features, and we omit these sight lines from our sample (not in Table 5.1).

One additional issue is name consistency. The HSLA archive uses the target name in the *HST* proposals, among which some are nonstandard, and can be challenging to follow. Therefore, we check the database SIMBad to extract more formal target names. AGN are normally first detected in radio, optical, and X-ray surveys, so we choose names from these surveys. Because this work is in the UV band, we prefer the UV name first (e.g., the Mrk survey), then the optical, X-ray, and radio names, The high-frequency surveys are HE, Mrk, PG, and RBS, as shown in Table 5.1.

5.3 Previous Models without kinematics

For the MW warm gas, various models have been proposed to explain the measured column density in both stellar and AGN sight lines (Savage & Wakker 2009; QB19; Zheng et al. 2019a). In Fig. 5.3, the comparison between these three models are shown, and the observation data are from Table 5.1. The detailed comparisons between these models are in Zheng et al. (2019a) and QB19. Here we just describe these models briefly.

Based on the stellar dominated sample (≈ 100 stellar sight lines and ≈ 20 AGN sight lines), a thick warm gas disk is suggested (Savage & Wakker, 2009). Previous studies employed a plane-parallel slab model, where $n(z) = n_0 \exp(-|z|/z_0)$, and z_0 is the scale height. For the intermediate to high ionization state ions (e.g., Si IV, C IV, and O VI), the scale heights are about $2 - 4$ kpc (Savage et al., 2003; Bowen et al., 2008; Savage & Wakker, 2009). This is a model with a one-dimensional (1D) variation over the z height (above or below the disk), and the expected column density has a dependence of the column density on Galactic latitude ($N_{\rm slab}(b) = N_{\rm slab,0}/\sin b$)

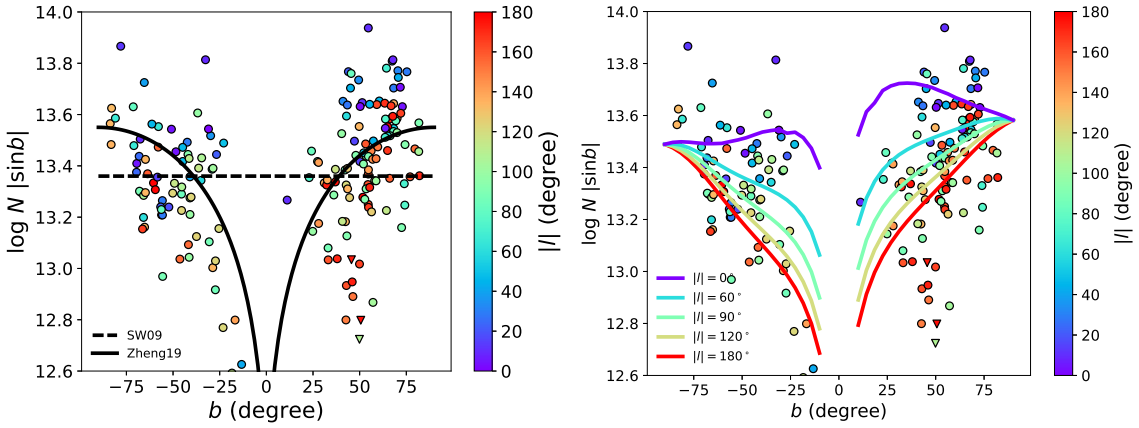

Figure 5.3: Three previous models are compared to the new line shape sample: the Savage & Wakker (2009) model (left panel), the Zheng et al. (2019a) model (left panel), and the QB19 model (right panel). The circles are the measurements of column densities, while triangles are upper limits. The Savage & Wakker (2009) model and the Zheng et al. (2019a) model are the original ones in literature, while the QB19 model is the new one fitted to the new sample, which is consistent with the original model in QB19. With the new sample, it is more clear that the projected Si IV column density has dependences on both Galactic longitude and Galactic latitude, which implies the necessity of the 2D disk-CGM model.

for AGN sightlines, showing $\log N_{\rm slab,0} = 13.36$ for Si IV (Savage & Wakker, 2009). However, Zheng et al. (2019a) found the expectation in the slab disk model shows conflicts with their AGN sample (the COS-GAL Si IV sample). At low Galactic latitudes, AGN sight lines have lower column density than the prediction of the slab disk model. To solve this problem, Zheng et al. (2019a) proposed a two-component model, which contains both the 1D slab disk and an isotropic CGM component. Applying this model to the AGN sample, they obtained a massive CGM model ($\log N_{\rm CGM} \approx 13.5$) with a relatively small disk ($\log N_{\rm slab,0} \approx 12.11$). This solution improves the fitting on the AGN sample (Fig. 5.3), however, it is inconsistent with the thick disk supported by the stellar sample. Therefore, there is tension between the slab disk model (dominated by the stellar sample) and the two-component disk-CGM model (determined by the AGN sample).

To relieve the tension between these two models, QB19 proposed the two-dimensional

(2D) disk-CGM model by introducing the radial profile of the disk into the two-component disk-CGM model. Instead of the 1D variation of the disk $n(z) = n_0 \exp(-|z|/z_0)$, the 2D disk has a density distribution given by $n(z) = n_0 \exp(-|z|/z_0) \exp(-|r_{\rm XY}|/r_0)$, where $r_{\rm XY}$ is the radius in the Galactic XY plane (the disk midplane) and r_0 is the scale length. Compared to the previous two models, the column density not only depends on Galactic latitude but also Galactic longitude (i.e., sight lines toward the GC $|l| = 0$ have higher measured column densities; Fig. 5.3). Based on the 2D disk-CGM model, QB19 suggested that the stellar sample and the AGN sample are not mutually incompatible, but can be fit with one model.

We applied the QB19 model to the new AGN sample (Table 5.1) and the Savage & Wakker (2009) stellar sample (the same one used in QB19). The AGN sample only uses components within $|v_{\rm c}| < 150$ km s^{-1}, which could be modeled by our kinematical model (Section 5.5). The fitting suggested similar results as QB19 (notations taken from QB19, and QB19 values in brackets): the disk scale length $r_0 = 6.62 \pm 0.86$ kpc (5.9 ± 1.1 kpc); the disk scale height in northern hemisphere $z_0^{\rm N} = 3.86 \pm 0.89$ kpc (3.5 ± 0.5 kpc); the disk scale height in northern hemisphere $z_0^{\rm N} = 3.43 \pm 0.61$ kpc (2.3 ± 0.4 kpc); the CGM component perpendicular to the disk direction $\log N_{\rm nd}^{\rm CGM} = 12.96 \pm 0.31$ (13.26 ± 0.08); the CGM component along the disk direction $\log N_{\rm mp}^{\rm CGM} = 10.70 \pm 1.90$ (12.43 ± 0.42). This similarity of the fitting results suggests that the absorption column densities between 100 km s^{-1} $< |{\rm v}| \lesssim 150$ km s^{-1} have a minor effect on the large scale structure in the column density-only model. In the following analyses, we will introduce the kinematics into the 2D disk-CGM model and adopt conclusions from QB19 as the basis of the fiducial model. Namely, we assume the north-south difference is mainly due to the scale height of the disk and will fix the midplane disk density and CGM density to be the same for the northern and southern hemispheres (details in Section 5.6.1).

5.4 The Cloud Path-Length Density

The observations of the MW absorption features reveal that the warm gaseous components are clumpy rather than smoothly and uniformly distributed in the gaseous disk and halo (Savage et al., 1997, 2003; Lehner et al., 2003; Wakker et al., 2003; Zsargó et al., 2003; Bowen et al., 2008; Savage & Wakker, 2009; Wakker et al., 2012; Zheng et al., 2019a). The clumpy nature of the warm gas could be modeled by the patchiness parameter method. The patchiness parameter is an additional uncertainty to lower the reduced χ to 1, when one wants to compare the observation with the model (Savage & Wakker 2009 and reference therein). For intermediate-to-high ionization state ions (e.g., Si IV, C IV, and O VI), the typical values of the patchiness parameter are about $0.2 - 0.4$ dex for stellar-dominated samples, and $0.1 - 0.2$ dex for AGN-dominated samples.

This intrinsic scatter could have physical meanings. To account for the intrinsic scatter, we assume the cloud nature of the warm gas, which is suggested by simulations (Kwak & Shelton, 2010; Shelton & Kwak, 2018; Hummels et al., 2019; Ji et al., 2019a; Liang & Remming, 2020). In our modeling, the warm gas is assumed to be separated clouds with a typical column density of $\log N_{\rm sg}$ ("sg" denotes single). Along a given sight line (l, b, d), the predicted number of clouds in the model is the $\mathcal{N}_{\rm c}$, which is an integral of the path-length density of clouds (X). Then, the predicted column density is $N_{\rm sg}\mathcal{N}_{\rm c}$. Because the number of clouds $\mathcal{N}_{\rm c}$ follows the Poisson distribution, the number of clouds has an intrinsic uncertainty of $\mathcal{N}_{\rm c}^{1/2}$, hence the column density uncertainty is $N_{\rm sg}\mathcal{N}_{\rm c}^{1/2}$. Then, the uncertainty due to the number of cloud variation is $\mathcal{N}_{\rm c}^{-1/2}\log_{10} e$ dex.

If this uncertainty is caught by the patchiness parameter, one could use the patchiness parameter to estimate the typical column density for the warm gas. In Section 5.3, we applied the QB19 model to the new AGN sample, and obtain a set of new parameters. Using the new parameters, we estimate the patchiness parameters (fit-

ting the residuals with a Gaussian function) are 0.162 dex for the AGN sample and 0.360 dex for the stellar measurements. For the AGN sample, $\sigma_{\mathcal{N}_c}/\mathcal{N}_c = \sigma_N/N = 0.162/\log_{10} e = \mathcal{N}_c^{-1/2}$, then we know the average number of clouds is $\mathcal{N}_c \approx 7.2$. The median column density of the AGN sample is $\log N = 13.53$, then the estimated typical column density of single cloud is $\log N_{sg} = 12.67$. Similarly, the average number of clouds is $\mathcal{N}_c \approx 1.5$ for the stellar sample, and the typical column density of single cloud is $\log N_{sg} = 13.00$ (with a median stellar sample column density of $\log N = 13.15$).

The typical column density of a single cloud of the stellar sample is much larger than the AGN sample by a factor of $0.3 - 0.4$ dex. This difference has two interpretations on whether this difference is real. First, if this difference is real, then there is a physical difference between the gas on the warm gas disk and the gas beyond the disk (i.e., CGM), which indicates the warm cloud in the CGM has a smaller typical column density than the disk. This might be caused by the pressure difference in the disk (high pressure; $\approx 10^3$ K cm^{-2}) and in the CGM (low pressure; $\approx 1-10^2$ K cm^{-2}). Assuming that clouds in the disk and the CGM have a similar total mass and temperature (determined by ionization state), the column density has a dependence on the pressure as $N \propto P^{2/3}$, which leads to lower typical column density in the CGM.

Another possibility for the physical difference is that the ISM might be more structured than the CGM, which is affected by stellar activity, such as from spiral arms. Based on O VI observations, Bowen et al. (2008) suggested that the scatter of the O VI column density does not depend on the distance, which indicates that the scatter caused by the ISM structures dominates the statistical scatter due to a number of clouds. In this case, the column density of a cloud should be a distribution rather than a fixed column density. Here, we emphasize that it is also unclear whether the CGM could be approximated by a fixed column density, so the cloud model of the warm gas is still an assumption. However, it is certain that there are significant

differences between the stellar sample (for disk) and the AGN sample (mainly for the CGM).

Second, the difference between the disk and the CGM clouds may not be real, because there are several other observational uncertainties for the stellar sample. For example, the distance to a star may have significant uncertainties. The reported distance uncertainties in Savage & Wakker (2009) are about ≈ 0.1 dex. The distances in the Savage & Wakker (2009) sample are from Bowen et al. (2008), which are mainly spectroscopic distances (i.e., obtaining absolute magnitude based on the spectral type and estimating the distance by comparing with apparent magnitude; see their Appendix B for more details). We believe that this is the best way to obtain a large uniformly-reduced distance sample, but the uncertainty of this method can be large (Shull & Danforth, 2019), which contributes to the difference between the stellar sample and the AGN sample. Also, the stellar continua sometimes contain intrinsic features (e.g., stellar winds, and absorption close to the star). Especially in the relatively low S/N (≈ 5) spectrum, the stellar features may be difficult to identify, which could introduce additional uncertainty in the column density measurements of interstellar absorption. This explanation is supported by the result that the additional patchiness parameter of the stellar sample is sightly reduced when we only use the STIS sample (Section 8.3). However, the STIS-only fitting model still has a none-zero additional patchiness parameter ($\sigma_{\rm p} = 0.15 \pm 0.09$). This may be due to the systematic uncertainty of the STIS sample, but it is highly likely that the ISM is physically different from the CGM.

The reason for the difference between ISM and CGM is beyond the scope of this paper, since the structure of the ISM is a huge topic. Here we just introduce an additional patchiness parameter to the stellar sample ($\sigma_{\rm p}$). This patchiness parameter may be due to the stellar intrinsic features, or physical difference between the warm gas in the disk and the CGM gas. Then, the cloud assumption is only applicable

to the CGM observation to model the intrinsic scatter, which cannot be applied to ISM, because the additional patchiness parameter $\sigma_{\rm p}$ significantly affects the scatter of column density measurements in stellar sight lines (Section 8.3).

In the following analyses, we use the path-length density (X) and $\log N_{\rm sg}$ for a single cloud to replace the density distribution. This implementation of the density formulation not only predicts the total column density, but also predicts model uncertainty for each sight line due to the variation of the total number of clouds along the sight line ($\mathcal{N}_{\rm c}$). For the AGN sample, the model uncertainty will be used to reproduce the intrinsic scatter (previously, the patchiness parameter). For the stellar sight line, the predicted column density uncertainty will be combined with the additional patchiness parameter (more details in Section 5.5.3).

5.5 The 2D disk-CGM Model with kinematics

In addition to the QB19 model, we consider the kinematics in the new model, which includes two major parts: the ion density distribution and the bulk velocity field. The density distribution is divided into two components as the disk and the CGM phenomenologically (Section 5.5.1). Here, we note that this decomposition does not imply that these two components are physically de-associated with each other. Instead, the combination of both components is to approximate the real warm gas distribution. For the velocity field, there are also two components, the rotation velocity and the radial velocity (Section 5.5.2). With all of these assumptions, we calculate the differential column density distribution to compare with the observed column density line shape sample (Section 5.5.3). The Bayesian framework employed to estimate the best parameters is introduced in Section 5.5.4.

The assumptions and implementation of this model are described in the following subsections, while the varied parameters in the kinematical model are summarized in Table 5.2.

Table 5.2: Parameters in the Kinematical Model

Syms	Description
$X_0^{\rm disk}$ [a]	The path-length density of clouds for the disk component at the GC.
r_0 & $\alpha_{\rm rxy}$	The scale length and the index parameter of the disk density distribution along the radial direction: $n(r_{\rm XY}) = \exp(-(r_{\rm XY}/r_0)^{\alpha_{\rm rxy}})$.
z_0 [a] & $\alpha_{\rm z}$	The scale height and the index parameter of the disk density distribution along the z direction: $n(z) = \exp(-(z/z_0)^{\alpha_{\rm z}})$.
$R_{\rm disk}$ [a]	The size of the disk without radial velocities, in the units of the scale height or scale length.
$\sigma_{\rm p}$	The additional patchiness parameter for the stellar sample.
$X_0^{\rm mp}$ [a]	The path-length density of cloud for the CGM component at the core region along the midplane of the disk.
$X_0^{\rm nd}$ [a]	The path-length density of cloud for the CGM component at the core region along the normal direction of the disk.
$r_{\rm c}$	The core radius of the β-model for the CGM component.
β	The slope in the β-model for the CGM density distribution.
$v_{\rm rot}$	The rotation velocity on the flat part of the rotation curve in the midplane.
$v_{\rm rad,10}$ [a]	The radial velocity at 10 kpc assuming constant accretion $\dot{M}$.
$v_{\rm abs}$	The intrinsic broadening velocity of the Si IV absorption, $= 0.707\ b$ factor.
$v_{\rm rand}$	The random motion of the cloud along the sight line direction.
$N_{\rm sg}$	The Si IV column density of single cloud.

[a] For these parameters, they may have NS asymmetry. Then, "N" or "S" denote values for the northern or southern hemispheres, respectively.

5.5.1 The Density Model

Before introducing the Si IV density distribution for both disk and CGM components, we note that the model has the origin at the Galactic center (GC) rather than the Solar system. Therefore, we need to convert a given position in the Galactic coordinate system (l, b, and d) to the Galactic XYZ coordinates (x, y, and z; Fig. 5.4):

$$\begin{aligned} x &= 8.5 \text{ kpc} - d\cos l\cos b, \\ y &= -d\sin l\cos b, \\ z &= d\sin b. \end{aligned} \tag{5.3}$$

Here, we assume the Solar system is at $r_\odot = 8.5$ kpc (Ghez et al., 2008). The coordinates x and y are in the disk midplane, while z is the height above or below the disk midplane. Then, the distance to the GC (r), the XY plane distance to the GC ($r_{\rm XY}$), and the corresponding spherical angles (ϕ and θ; Fig. 5.4) are

$$\begin{aligned} r &= (x^2+y^2+z^2)^{1/2}, \\ r_{\rm XY} &= (x^2+y^2)^{1/2}, \\ \sin\phi &= \frac{y}{r_{\rm XY}},\ \cos\phi = \frac{x}{r_{\rm XY}},\ \sin\theta = \frac{z}{r}. \end{aligned} \tag{5.4}$$

These parameters will be used in the definition of the ion density distribution and the velocity field.

Following the QB19 model, the total cloud path length density is the summation of the disk and the CGM components. The total cloud path length density is

$$X(l,b,q) = X^{\rm disk}(r_{\rm XY},z) + X^{\rm CGM}(r,\theta), \tag{5.5}$$

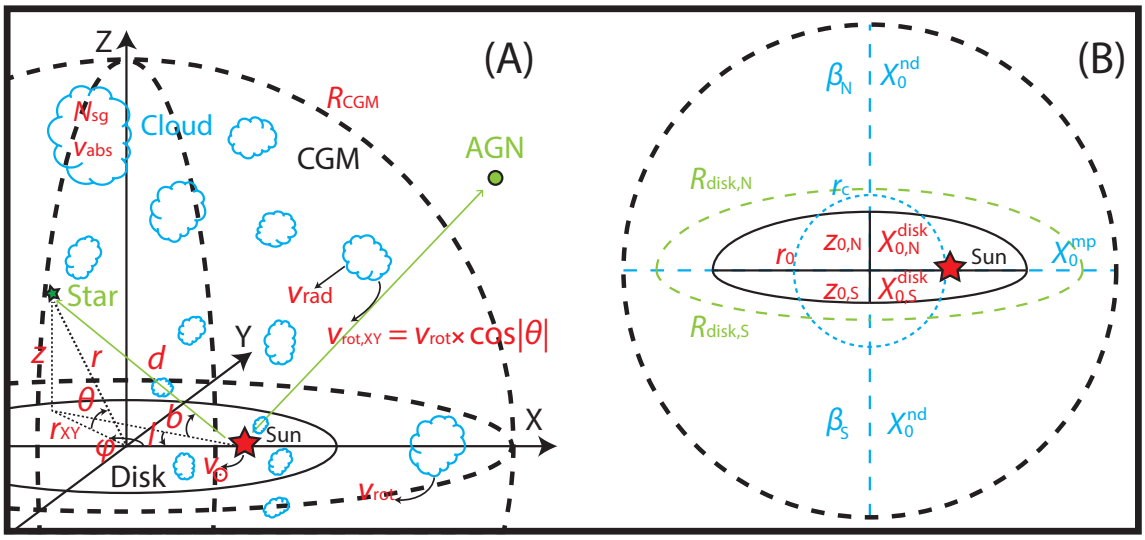

Figure 5.4: An illustration of the kinematical model (not scaled). Left panel: the coordinate parameters (x, y, z, ϕ, and θ) and parameters to describe the velocity field ($v_{\rm rot}$, $v_{\rm rad}$, and $v_\odot$). Right panel: the parameters that describe the ion density distribution: the disk component (r_0, z_0, and $X_0^{\rm disk}$) and the CGM component ($r_{\rm c}$, β, $X_0^{\rm mp}$, and $X_0^{\rm nd}$).

where $X^{\rm disk}$ and $X^{\rm CGM}$ are the path density of clouds for the disk and the CGM components, respectively.

The disk density distribution is 2D ($r_{\rm XY}$ and z) and axial symmetric with the axis as the disk normal line through the GC. The 2D disk density distribution includes both radial ($r_{\rm XY}$) and vertical (z) profiles, which are independent between each other. Empirically, both radial and vertical profiles are exponential. Then, the cloud path length density of the disk component has a format of:

$$X^{\rm disk}(r_{\rm XY}, z) = X_0^{\rm disk} \exp(-\frac{|r_{\rm XY}|}{r_0}) \exp(-\frac{|z|}{z_0}), \tag{5.6}$$

where $X^{\rm disk}$ is the path-length density for the disk component, and r_0 and z_0 are the scale length and the scale height of the disk. As discussed in QB19, the radial and vertical profiles might have other formats (e.g., the Gaussian function). Therefore,

we parameterize this variation by introducing two index parameters ($\alpha_{\rm rxy}$ and $\alpha_{\rm z}$):

$$X^{\rm disk}(r_{\rm XY}, z) = X_0^{\rm disk} \exp(-(\frac{|r_{\rm XY}|}{r_0})^{\alpha_{\rm rxy}} - (\frac{|z|}{z_0})^{\alpha_{\rm z}}). \tag{5.7}$$

Larger $\alpha_{\rm rxy}$ or $\alpha_{\rm z}$ values lead to sharper edges of the ion distribution for the radial or the z-height directions. If $\alpha_{\rm rxy}$ or $\alpha_{\rm z}$ are 1, the density distributions are exponential, while if $\alpha_{\rm rxy}$ or $\alpha_{\rm z}$ are 2, the density distributions are Gaussian.

Previously, the CGM component is modeled as the column density distribution (isotropic in Zheng et al. 2019a or dependent on Galactic latitude in QB19) rather the density distribution. This is the limitation of models that only consider the integrated column density (without line shape; i.e., kinematics) sample. In the new kinematical model, we could constrain the CGM density distribution with the velocity field. Here, we assume the β-model for the CGM density distribution, which is commonly adopted in X-ray investigations to study the quasi-hydrostatic equilibrium hot gas for both the MW and external galaxies (Bogdán et al., 2013a; Miller & Bregman, 2013; Li & Bregman, 2017; Li et al., 2017a, 2018a).

$$X^{\rm CGM}(r, \theta) = X_0^{\rm CGM}(\theta) \times (1 + (\frac{r}{r_{\rm c}})^2)^{-3\beta/2}, \tag{5.8}$$

where $X_0^{\rm CGM}(\theta)$ is the core density, $r_{\rm c}$ is the core radius, and -3β is about the power law index at large radii. $X_0^{\rm CGM}(\theta)$ has a dependence on θ, which accounts for the anisotropy of the MW CGM as introduced in QB19.

QB19 found that the MW warm CGM column density distribution (traced by both Si IV and O VI) is anisotropic, which is not a constant column density over the entire sky. This is also found in external galaxies for the cool gas ($\approx 10^3$ K; traced by Mg II and Fe II) in the CGM (Bordoloi et al., 2011; Lan & Mo, 2018; Martin et al., 2019). These studies showed that the Mg II or Fe II column density depends on the azimuthal angle (the projected angle related to the minor axis). In QB19, we

considered this variation by assuming a column density distribution as a function of Galactic latitude. Here, we improve on this assumption by introducing a dependence on θ ($X_0^{\rm CGM}(\theta)$) instead of Galactic latitude b, where θ is the angle measured from the midplane with the origin at the GC (see the cartoon in Fig. 5.4):

$$\log X_0^{\rm CGM}(\theta) = \log X_0^{\rm mp} \cos^2\theta + \log X_0^{\rm nd} \sin^2\theta, \tag{5.9}$$

where $X_0^{\rm mp}$ is the cloud path-length density along the radial direction in the disk midplane ("mp"), and $X_0^{\rm nd}$ is the cloud path-length density along the z direction (the normal direction; "nd") perpendicular to the disk. This is similar to the format in QB19 ($\log N_{\rm CGM}(b) = \sqrt{\log^2 N_{\rm mp} \cos^2 b + \log^2 N_{\rm nd} \sin^2 b}$). Here, we omit the square root in the new function, because $\log X$ could be negative, while $\log N \approx 12 - 13$ is always positive. These two formats show similar variations (with differences $<$ 10%) when the difference of $\log N$ or $\log X$ in two directions are within $1 - 2$ (i.e., $|\log X_{\rm mp} - \log X_{\rm nd}| < 2$ or $|\log N_{\rm mp} - \log N_{\rm nd}| < 2$).

The β-model converges to the power law model at large radii ($r >> r_{\rm c}$). Typically, the $r_{\rm c}$ of external galaxies are not resolved by current X-ray instrument, so it is $\lesssim 10$ kpc (Bogdán et al., 2013b; Li et al., 2018a). For the MW, $r_{\rm c}$ is measured to be 2.5 ± 0.2 kpc using O VII and O VIII X-ray emission lines (Li & Bregman, 2017). However, in our Si IV absorption line study, this parameter cannot be constrained, because few sightlines pass through the GC at distances < 2.5 kpc. Therefore, we fix $r_{\rm c}$ to 2.5 kpc in the following analyses, which will not affect the power-law approximation at large radii.

The β-model should have a maximum radius ($R_{\rm max}$), because the total number of ions does not converge when $\beta < 0.7$, which is pretty likely ($\beta = 0.5$ for hot gas in the MW; Li & Bregman 2017). Here, $R_{\rm max}$ is fixed to 250 kpc (about the virial radius of the MW). Our model is not sensitive to this parameter as discussed in Section 5.6.3.

5.5.2 The Velocity field

The bulk velocity field has two major contributors: the Galactic rotation and the radial motion (outflow or inflow). For a given position (r, θ, and ϕ; Fig. 5.4), the total velocity is the combination of both rotation and radial velocities:

$$\vec{v}_{\rm bulk}(r,\theta,\phi) = \vec{v}_{\rm rot}(r,\theta,\phi) + \vec{v}_{\rm rad}(r,\theta,\phi). \tag{5.10}$$

The rotation velocity is approximated by a linear part ($r_{\rm XY} \leq 0.5$ kpc) and a flat part ($r_{\rm XY} > 0.5$ kpc; Kalberla & Dedes 2008). At the midplane, the velocity of the flat part is a free parameter in our model ($v_{\rm rot}$):

$$\begin{aligned} v_{\rm rot}(r_{\rm XY}) &= (r_{\rm XY}/0.5\ {\rm kpc})v_{\rm rot},\ r_{\rm XY} \leq 0.5\ {\rm kpc} \\ &= v_{\rm rot},\ r_{\rm XY} > 0.5\ {\rm kpc}. \end{aligned} \tag{5.11}$$

When it is above (the northern hemisphere) or below (the southern hemisphere) the midplane, we consider a rotating cylinder (i.e., no z-component velocity). Then the value of rotation velocity is

$$v_{\rm rot}(r,\theta) = v_{\rm rot}(r_{\rm XY})\cos\theta, \tag{5.12}$$

and the three-dimensional (3D) rotation velocity vector is

$$\vec{v}_{\rm rot}(r,\theta,\phi) = (-\sin\phi, \cos\phi, 0)\cdot v_{\rm rot}(r,\theta). \tag{5.13}$$

The radial velocity is introduced to account for the possible inflow or outflow of the warm gas. The warm gas disk is expected to have no radial velocity, which is similar to the H I disk (Marasco & Fraternali, 2011). Therefore, we assume that there is a boundary for the radial velocity, and the boundary follows the shape of the

isodensity line of the disk component (as stated in Section 5.5.1):

$$(\frac{|r_{\rm XY}|}{r_0})^{\alpha_{\rm rxy}} + (\frac{|z|}{z_0})^{\alpha_{\rm z}} = R_{\rm disk}, \tag{5.14}$$

where $R_{\rm disk}$ is a dimensionless parameter to describe the size the disk without the radial velocity. At this boundary the cloud path density of the disk component is a constant of $X_0^{\rm disk}\exp(-R_{\rm disk})$.

We assume that the radial velocity is spherically symmetric, so it only has a dependence on the distance to the GC (r). For the radial velocity dependence on the radius, we assume a constant accretion/outflow rate at different radii for the CGM.

$$4\pi r^2 v_{\rm rad}(r) N_{\rm sg} X^{\rm CGM}(r) = \dot{M} = const., \tag{5.15}$$

where $N_{\rm sg}X^{\rm CGM}(r)$ is equivalent to the ion density of the CGM component, and $\dot{M}$ is the mass loading rate (outflow) or the accretion rate (inflow) of the CGM component. For simplicity, we use the radial velocity at 10 kpc as the characteristic radial velocity. Then, the radial velocity dependence on the radius is

$$v_{\rm rad}(r) = \frac{10^2 X^{\rm CGM}(10)}{r^2 X^{\rm CGM}(r)} v_{\rm rad,10}, \tag{5.16}$$

where $v_{\rm rad,10}$ is the free parameter in our model (Table 5.2). Positive value of $v_{\rm rad,10}$ indicates outflow, while negative $v_{\rm rad,10}$ means gas accretion. Then, the 3D radial velocity is

$$\vec{v}_{\rm rad}(r,\theta,\phi) = (\frac{x}{r},\frac{y}{r},\frac{z}{r})\cdot v_{\rm rad}(r). \tag{5.17}$$

Because the calculated velocity of the line shape sample is in the heliocentric frame, we need to consider the Solar motion in the velocity calculation. We have two ways to include the Solar motion. One is fixing the Solar motion to $\vec{v}_\odot = (-9,-232,7)$ km s^{-1} (Delhaye, 1965), while another choice is varying the velocities of the Solar motion as

free parameters. Based on our tests, the Si IV sample is insufficient to constrain the Solar motion, because of the sample size and the complicated variation of the warm gas distributions and kinematics (affected by stellar activity). Therefore, we fix the Solar motion as $(-9, -232, 7)$ km s^{-1} in the fiducial motion in Section 5.6.1. The warm gas velocity relative to the Solar motion is:

$$\vec{v}_{\rm bulk,rel} = \vec{v}_{\rm rot} + \vec{v}_{\rm rad} - \vec{v}_{\odot}.$$

Finally, the projected velocity is (because we define the Galactic radial velocity in Section 5.5.2, we use the "projected velocity" to represent the normal radial velocity):

$$v_{\rm proj}(l, b, q) = \vec{v}_{\rm bulk,rel}(l, b, q) \cdot \vec{\mathbf{n}}, \tag{5.18}$$

where $\vec{\mathbf{n}} = (-\cos l \cos b, -\sin l \cos b, \sin b)$ is the direction vector toward l and b.

In addition to the bulk velocity field, a single cloud may have a random motion. For this variation, we assume the random motion follows a normal distribution with a mean value of 0 km s^{-1} and a standard deviation of $v_{\rm rand}$, which is a free parameter in our model (Table 5.2). The inclusion of $v_{\rm rand}$ in the kinematical model is described in Section 5.5.3 and Section 5.5.4.

5.5.3 The Model Prediction

Based on the assumptions of the density distribution and the bulk velocity field, we could predict the observed column density (stellar) and differential column density line shape (AGN) for each sight line. As stated in Section 5.4, we also consider the associated model uncertainty due to the number variation of clouds in each sight line.

For each stellar sight line (l, b, and d), we calculate the total number of clouds ($\mathcal{N}_{\rm c}$) by integrating X (the cloud path length density) over the path length to the target. Then, the predicted column density of stellar sight line is expected to be

$N_{\rm st} = \mathcal{N}_{\rm c} N_{\rm sg}$, where $N_{\rm sg}$ is the column density for individual clouds. To consider the model uncertainty, we assume the distribution of the cloud number follows a Poisson distribution. Therefore, the cloud number uncertainty is $\mathcal{N}_{\rm c}^{1/2}$, and the model uncertainty of the column density is $\sigma_N = \mathcal{N}_{\rm c}^{1/2} N_{\rm sg}$ in the linear scale. In the logarithm scale, the model uncertainty is $\sigma_N = \mathcal{N}_{\rm c}^{1/2} \log_{10} e$ dex. Besides the model-predicted uncertainty, the stellar sample also suffers from an additional uncertainty (patchiness parameter; $\sigma_{\rm p}$) as discussed in Section 5.4. Then, the total uncertainty of one stellar sight line is $\sigma_{\rm st}^2 = \sigma_N^2 + \sigma_{\rm p}^2$.

For the AGN sample, we need to consider the line shape by introducing the velocity field (Section 5.5.2). For each AGN sight line (l, b), there are five steps to obtain the model prediction of the line shape. (1) We calculate the max path length ($d_{\rm max}$) within the MW halo ($R_{\rm max} = 250$ kpc), which is the distance between the Sun and the maximum radius of the sphere along a sight line (l and b). (2) The entire path length is divided into bins with a width of $\Delta q = 0.1$ kpc. Because the cloud path length density at 250 kpc is extremely low, we ignore that the last bin that may not be 0.1 kpc. (3) For one bin at a distance of q, we calculate the cloud path-length density ($X(l, b, q)$) in the bin using Eq. (5.5) and the corresponding projected (observed radial) velocity $v_{\rm proj}(l, b, q)$ using Eq. (5.18). Then, the cloud number in the path length bin is $\Delta\mathcal{N}_{\rm c}(l, b, q) = X(l, b, q)\Delta q$. This indicates that there are $\Delta\mathcal{N}_{\rm c}$ clouds at the projected velocity of $v_{\rm proj}$. (4) After the calculation of all path length bins, we rebin the cloud number based on the projected velocity. The adopted projected velocity bin is the observed velocity bin for each AGN sight line. Therefore, we could know the cloud number in each observed velocity bin ($\mathcal{N}_{\rm c}(v)$). (5) The cloud number in each velocity bin is converted to the column density ($N_{\rm c}(v) = (\mathcal{N}_{\rm c}(v) N_{\rm sg})$.

Similar to the stellar sample, we also calculate the corresponding model uncertainty for the line shape. For each bin, the uncertainty of the cloud number is $\mathcal{N}_{\rm c}(v)^{1/2}$, based on the Poisson statistic assumption. Then, the naive column density uncer-

tainty is $\mathcal{N}_{\rm c}(v)^{1/2}N_{\rm sg}$ for individual velocity bins.

However, there is one issue when applying this naive column density uncertainty to the column density line shape. By varying $\log N_{\rm sg}$, we expect to capture the intrinsic scatter of the integrated column density as stated in Section 5.4. Nevertheless, this $\log N_{\rm sg}$ value for the integrated column density overestimates the uncertainty in each bin of the column density line shape.

Here, we use the χ^2 framework to show the basic idea, although we implement the Bayesian frame in the following analyses (Section 5.5.4). For one sight line, the total observed column density is N, the model column density is M, and the model uncertainty is E. With a suitable $\log N_{\rm sg}$, one could always obtain a reduced $\chi^2 = (N - M)^2/E^2 = 1$. The situation is different for the line shape calculation. Assuming there are m bins for the spectrum, each bin has an average column density of N/m, a model column density of M/m, and a model uncertainty of $E/m^{1/2}$, based on the Poisson statistics. Then, for each bin in the spectrum, the corresponding $\chi^2 = 1/m$, which is unacceptable, although the adopted $\log N_{\rm sg}$ makes the total column density sample have reduced $\chi^2 = 1$. We make the model self consistent by using the line width (in number of spectral bins) to reduce the naive model uncertainty for each bin (i.e., $\mathcal{N}_{\rm c}(v)^{1/2}N_{\rm sg}/m^{1/2}$). Here, for each sight line the value of m is not the number of bins for the entire spectrum, because the spectrum also contains the continuum, which should not contribute to m. Finally, the value of m is fixed to be the number of spectral bins that have model column densities $> 10^{10}$ cm^{-2} (much lower than the detection limits in our sample). Using this criterion, we exclude the continuum region, which would lower the significance of the model.

By now, the model column density and the uncertainty are both intrinsic values, which have not been affected by several broadening processes (e.g., thermal or turbulence broadening). These broadening processes cannot be distinguished from observations, so we introduce the absorption broadening velocity $v_{\rm abs}$ to model them

together. Using $v_{\rm abs}$, we generate a Gaussian kernel and convolve this kernel to the intrinsic column density model and uncertainty. The convolved model and uncertainty are the model for AGN sight lines, considering the density distribution and the bulk velocity field.

As introduced in Section 5.5.2, warm gas clouds could also have random motions besides the bulk velocity. To determine the random motion component, we extract the power spectrum from the cross-correlation of the convolved model (without the random motion) and the observation for every sight line. Then, the peak position of the power spectrum corresponds to the required velocity shift ($v_{\rm shift}$) to account for the random motion. We show two examples (3C 57 and HE 2259-5524) in Fig. 5.5, where the input model is the preferred model in Section 5.6.1. The bulk velocity model of 3C 57 shows a similar shape as the observed line shape, but the line centroid is shifted. The bulk velocity model with a velocity shift of -19.2 km s^{-1} reproduces the line shape better, which is the final model to compare with the data. For HE 2259-5524, the line shape is not reproduced as well as 3C 57, but the velocity shift also shows up by the peak of the column density line shape. Here, we emphasize that the velocity shift is part of the kinematical model to obtain the final model-predicted line shape for AGN sight lines as well as the ion density distribution and the bulk velocity field.

Finally, for the stellar sample, we have the model predicted column density and the total uncertainty of the column density (the combination of both the model uncertainty and the stellar patchiness parameter). For each AGN sight line, we have the predicted column density line shape, associated uncertainty line shape, and the velocity shift for the random motion.

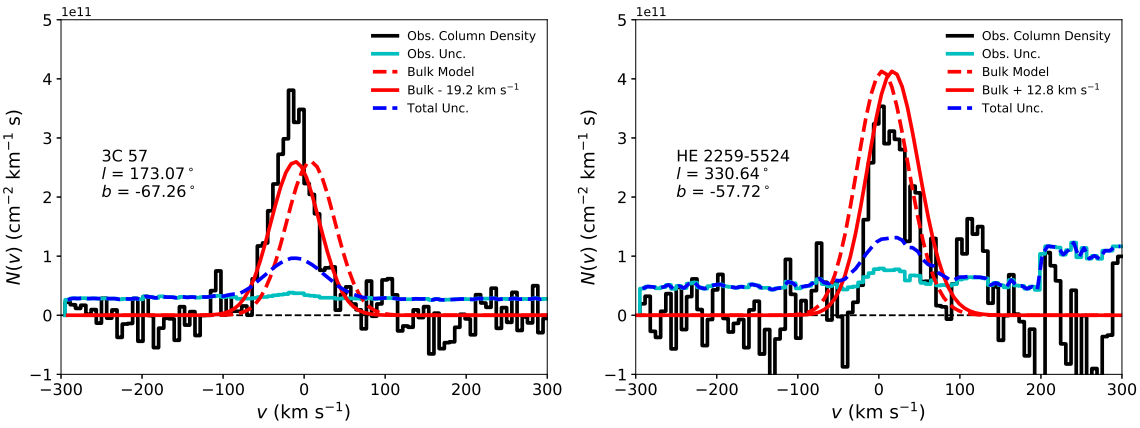

Figure 5.5: Two examples sight lines of 3C 57 (left) and HE 2259-5524 (right) showing the velocity shift along the sight line direction. The red dashed lines are the predicted column density line shape without the random motion (i.e., only with the bulk velocity field). The red solid lines are the model considering the random motion along the sight line direction determined from the power spectrum of the cross-correlation. The blue dashed lines are the total uncertainty combining both the observation uncertainty (cyan lines) and the model uncertainty.

5.5.4 The Bayesian Analysis

We use the Bayesian framework (together with the Markov Chain Monte Carlo method; MCMC) to compare the model prediction and the observation sample and obtain the best parameters of the kinematical model (Zheng et al., 2019a). Compared to the χ^2 minimization method, the Bayesian method could obtain the entire posterior distribution rather than the most likely parameter (with the minimum χ^2). The posterior distribution is necessary when there are unconstrained parameters in the model, which is the case here (Section 5.6.1). The MCMC simulation is run by using the *emcee* package (Foreman-Mackey et al., 2013).

In the Bayesian approach, we need to optimize the likelihood function ($p_{\rm tot}(\theta|D)$), where D and θ are the observation data and the model parameters, respectively. The total likelihood function contains two major parts for both stellar ($p_{\rm st}$) and AGN

($p_{\rm AGN}$) samples:

$$p_{\rm tot}(\theta|D) = p_{\rm st}(\theta|D) \times p_{\rm AGN}(\theta|D).$$

Based on Bayes' theorem, the likelihood depends on

$$p(\theta|D) = \frac{p(D|\theta)p(\theta)}{p(D)},$$

where $p(D|\theta)$ is the possibility for a model with parameters of θ to reproduce the data D, $p(\theta)$ is the prior knowledge for the parameters, and $p(D)$ is the possibility to have the observation data. In our implementation of the Bayesian simulation, $p(\theta)$ is assumed to be uniform in the given parameter space, so it is a constant. The boundary of the parameter space is determined to allow each parameter to have sufficient variation (except for parameters only have limits) as shown in Fig. 5.6. $p(D)$ is a complex term, but this term is the same for all model, so it can be ignored in practice. Finally, $p(D|\theta)$ is determined by comparing the model prediction and the observation. In the following analyses, $\ln p$ stands for $\ln p(D|\theta)$ or $\ln p(\theta|D)$. The difference between these two values is constant, which does not affect the results.

The stellar sample only provides a column density, so the likelihood function only has one term for the total column density. Following Zheng et al. (2019a), the logarithmic value of the column density likelihood (for the stellar sample in our work) is

$$\ln p{\rm st} = -\sum_{k=1}^{75}(\ln \sigma_{{\rm t},k} + \frac{1}{2}\frac{(\log N_k - \log N_{{\rm m},k})^2}{\sigma_{{\rm t},k}^2}), \tag{5.19}$$

where $\sigma_{{\rm t},k}^2 = \sigma_{\log N,k}^2 + \sigma_{\log N_{\rm m},k}^2 + \sigma_{\rm p}^2$ is the total uncertainty of the k-th stellar sight line, and m denotes for the model prediction. N_k is the k-th observed column density, while $N_{{\rm m},k}$ and $\sigma_{\log N_{\rm m},k}$ are the model predicted column density and uncertainty.

For the AGN sight line, there are three components for the total likelihood ($p_{\rm AGN}$):

the line shape ($p_{\rm ls}$), the random motion along the sight line ($p_{\rm rand}$), and the total column density ($p_{\rm cd}$):

$$\ln p_{\rm AGN} = \sum_{k=1}^{186} (\ln p_{{\rm ls},k} + \ln p_{{\rm rand},k} + \ln p_{{\rm cd},k}). \tag{5.20}$$

The total likelihood of the AGN sample is the summation for the 186 sight lines. For each sight line, the first term is the line shape, where we compare the model-predicted line shape (Section 5.5.3) and the observed column density line shape (Section 5.2). We note that the model prediction includes the velocity shift along the sight line ($v_{\rm shift}$). Then for each bin, we could calculate the likelihood, and the total likelihood is the summation of the logarithmic likelihoods of individual bins:

$$\ln p_{\rm ls} = -\frac{1}{m'} \sum_{j=1}^{m} (\ln \sigma_{{\rm t},j} + \frac{1}{2} \frac{(N_j - N_{{\rm m},j})^2}{\sigma_{{\rm t},j}^2}), \tag{5.21}$$

where $\sigma_{{\rm t},j}^2 = \sigma_{N,j}^2 + \sigma_{N_{\rm m},j}^2$, m is the total number of bins in the spectrum, and j denotes the j-th bin in the column density line shape. Compared to Eq. (19), there are three differences. First, the calculation here is in the linear scale, while Eq. (19) is in the logarithm scale. This is because the total column density is always a large number ($\log N \gtrsim 12$), and the distribution is better approximated by a lognormal distribution. However, the differential column density in each bin of the line shape could be negative (continuum region or low significance features), which is also included in the modeling. For these bins, the logarithm scale is not appropriate, so we use a linear scale. Second, $\sigma_{{\rm t},k}$ does not have an additional patchiness parameter as discussed in Section 5.4. Third, we normalize the total logarithm likelihood by a factor of $1/m'$, where m' is defined as the number of bins with observed column density $> 10^{10}$ cm^{-2} rather than the total number of bins in the entire spectrum. Similar to the χ^2 arguments, each bin in the line shape has a reduced $\chi^2 = 1$, then AGN sight lines have m times more weights than stellar sight lines if no normalization is

applied. By adopting this normalization, all sight lines (both stellar and AGN) have similar weights. Here, we use m' instead of m to do the normalization because the continuum region in the line shape is constant for different models, which will not affect the fitting results. The choice of 10^{10} cm^{-2} criterion is to exclude the continuum region that dilutes the model significance.

The second term ($\ln p_{\rm rand}$) is the likelihood for the velocity shift ($v_{\rm shift}$) along the AGN sight line. We assume that $v_{\rm shift}$ follows a normal distribution with a mean of zero and a standard deviation of $v_{\rm rand}$:

$$\ln p_{\rm rand} = -\ln v_{\rm rand} - \frac{1}{2}\frac{v_{\rm shift}^2}{v_{\rm rand}^2}. \tag{5.22}$$

The last term ($\ln p_{\rm cd}$) is for the total column density derivation for AGN sight lines. This term is similar to the stellar sample, but without the patchiness parameter:

$$\ln p_{\rm cd} = -\ln \sigma_{\rm t} - \frac{1}{2}\frac{(\log N - \log N_{\rm m})^2}{\sigma_{\rm t}^2}, \tag{5.23}$$

where $\sigma_{\rm t}^2 = \sigma_{\log N}^2 + \sigma_{\log N_{\rm m}}^2$ is the total uncertainty of the column density. These two terms ($\ln p_{\rm rand}$ and $\ln p_{\rm cd}$) do not need the normalization as the line shape term ($\ln p_{\rm ls}$), because these two terms should be applied to each pixel (e.g., every pixel should be moved by $v_{\rm shift}$; Fig. 5.5). Therefore, the calculation is already normalized.

5.6 Fitting Results and Implications

5.6.1 Overview of the Fiducial Model

In Section 5.5, we introduce the basic assumptions of the kinematical model. In practice, there are additional improvements that could be considered, such as the NS asymmetry. There is a systematic NS asymmetry for the Si IV and O VI column density distribution for northern and southern hemisphere (measured in the AGN

sample; Savage et al. 2003; Zheng et al. 2019a). Based on the column density-only sample (and model), QB19 suggested that this NS asymmetry is mainly caused by the difference of the exponential disk density distribution in two hemispheres (i.e., the scale height). In this subsection, we introduce the our fiducial model and tests that we used to finalize it, while a more detailed discussion are on the fitting results (Section 8.3), the density distribution (Section 5.6.3), the gas kinematics (Section 5.6.4), and the gas properties (Section 5.6.5).

With the new kinematical model, we can learn more about the variation for the NS asymmetry: the ion density distribution, the warm gas kinematics, and the gas properties. For the density distribution, the disk component has five possible variations: the disk normalization (the GC density; $\log X_0^{\rm disk}$); the scale length (r_0); the scale height (z_0); and two index parameter for disk expansion ($\alpha_{\rm rxy}$ and $\alpha_{\rm z}$). The CGM component has another four parameters: the CGM normalization (the density at the core; $\log X_{\rm mp}$ and $\log X_{\rm nd}$), the core radius ($r_{\rm c}$), and the β factor.

QB19 excluded the NS variation of the disk normalization and the CGM normalization based on tests, so we adopt this conclusion in the kinematical model. QB19 suggested the scale length is the same, and we adopt this assumption for two reasons. First, the scale length is related to the stellar disk, which is supposed to be the same for both hemispheres. Also, the difference of the scale length is at low Galactic latitude, but there are very few AGN sight lines at low Galactic latitude ($|b| < 20$; 4/186) to distinguish it. We assume that $\alpha_{\rm rxy}$ of both hemispheres are the same for similar reasons. For the CGM component, the core radius of the β-model is fixed to 2.5 kpc (obtained from the X-ray emission modeling), because the warm gas absorption line sample cannot be used to measure the gas within $\lesssim 2$ kpc of the GC. Finally, there are only three parameters left: the scale height, the $\alpha_{\rm z}$ index parameter and the β factor. As stated in Section 5.5.1, we are using two components (disk and CGM, with different profiles) to approximate the real warm gas distribution. Then, the index

parameters and β are degenerate with each other. As will shown in Section 5.6.3, α_z and β both determine the gas slope at $20-50$ kpc along the z-direction, so we only keep the NS variation for one of these parameters. Here we choose β in following modelings. In our test, the only varying the β leads to a difference of ≈ 5 for the Bayesian information criterion (BIC; moderately significant), so we retain this in the fiducial model. Adding variation of α_z does not improve the model (BIC < 2).

For the kinematics, the rotation velocity is assumed to be the same for both hemispheres, because the midplane velocity should be continuous. The radial velocity is found to be different between two hemispheres because the same radial velocity model leads to a BIC difference of > 10 (very significant). Therefore, the NS asymmetric radial velocity is included in the fiducial model. Additionally, we also consider the radial velocity boundary difference for both hemispheres ($R_{\rm disk}$). This parameter mainly determines the amount of gas with a significant radial velocity, while the radial velocity determines the velocity shift of the gas.

The gas property may be different in both hemispheres, such as the column density per cloud, the absorption width, and the random velocity of absorption features along the sight line. Based on our test, these parameters are roughly same with BIC $\lesssim 3$, which indicates that the model with more parameters (NS asymmetry for these parameters) is not a better model than the simple model (with the same parameter for both hemispheres). For the absorption broadening velocity, the variation among individual sight lines is larger than the difference between the two hemispheres. Therefore, our model only obtains the average broadening velocity. The random velocity of absorption features shows smaller scale variation, rather the NS asymmetry, as discussed in Section 5.6.5. Therefore, we do not include the NS asymmetry for these three parameters.

Finally, the fiducial model has 19 parameters (Fig. 5.6 and Table 5.2).

5.6.2 Fitting Results

For the MCMC fitting to our Bayesian model, the parameter space is sampled with 100 walkers and each walker has 20000 steps to fully thermalize the posterior distribution. As stated in Section 5.2.1, we fit the fiducial model with two different sets of observation samples. The preferred fitting model uses both *IUE* and STIS stellar sample, while another model only uses the STIS sample. The COS AGN sample is the same for these two fitting models. The fitting results are consistent between two models within 1σ uncertainty (expect for the additional patchiness parameter of the stellar sample). Typically, the STIS-only model has larger uncertainties for some parameters (e.g., cloud number density of the disk component), because fewer stellar sight lines are considered in this model. The patchiness parameter of the stellar sample is slightly smaller for the STIS-only model (0.15 ± 0.09) compared to the combined-sample model ($0.19^{+0.07}_{-0.10}$). This indicates that the IUE sample has a larger systematic uncertainty, but this uncertainty is modeled by the patchiness parameter, which does not affect other parameters significantly. Therefore, we suggest that there is no physical difference between these two models. In the following analyses, we only discuss the results from the combined-sample model.

The fitting results are presented in Fig. 5.6, where most parameters are constrained, except for four of them. The 1 σ limits for these four unconstrained parameters are the disk boundary for the radial velocity in the south $R_{\rm disk,S} > 3.4$, the radial velocity in the south $v_{\rm rad,S} < -12$ km s^{-1}, the CGM component in the midplane $\log X_0^{\rm mp} < -2.1$) and the CGM component cloud path-length density perpendicular to the disk ($\log X_0^{\rm nd} < -4.2$).

These unconstrained parameters ($R_{\rm disk,S}$, $v_{\rm rad,S}$, $\log X_0^{\rm mp}$, and $\log X_0^{\rm nd}$) has two physical implications. First, there is an insufficient number of absorbing clouds in the southern hemisphere at $10 - 20$ kpc, which are needed to determine the radial velocity. This also leads to the unconstrained radial velocity and boundary (Section

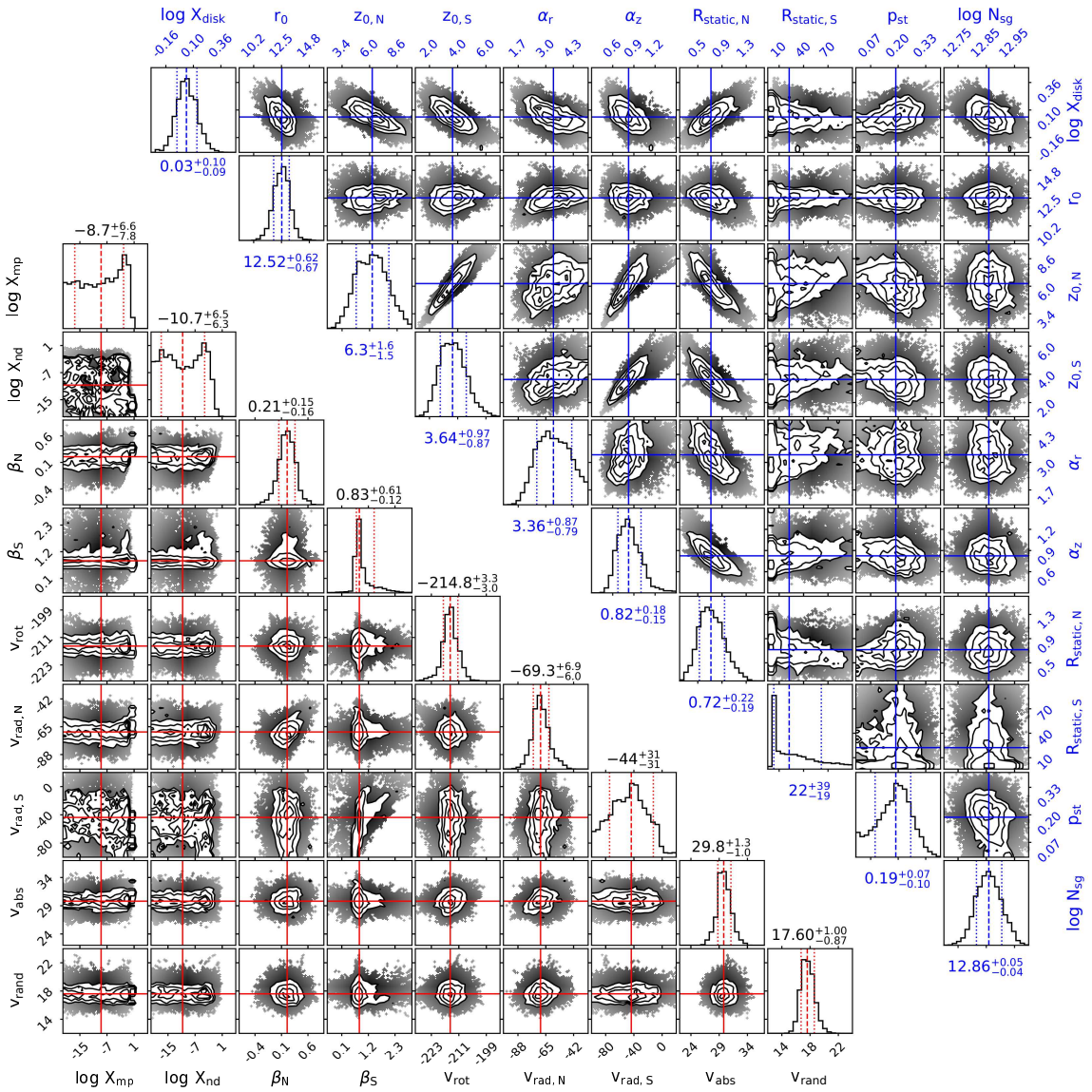

Figure 5.6: The posterior distribution of the parameters in the fiducial model. In this model, the NS asymmetry are modeled by four parameters: the disk scale height (z_0), the boundary of the radial velocity ($R_{\rm disk}$), the β factor, and the radial velocity ($v_{\rm rad,10}$). Most parameters are constrained, except for 4/19 parameters: the boundary of the radial velocity in the southern hemisphere ($R_{\rm disk,S} > 3.4$), the radial velocity in the southern hemisphere ($v_{\rm rad,10,S} < -12$ km s^{-1}), the CGM core density ($\log X_0^{\rm mp} < -2.1$ and $\log X_0^{\rm nd} < -4.2$).

5.6.4). This is consistent with the large β value in the south, which confirms less gas at large radii (excluding the LMC/SMC). Second, the upper limits of the CGM component path-length densities suggest that the gas distribution is dominated by the disk component (Section 5.6.3). We note that the disk component defined in Section 5.5.1 is more extended in the z-direction than the previously adopted exponential disk (e.g., Savage & Wakker 2009). The implication of all parameters is described and discussed in details in following subsections on various topics: the warm gas distribution, the warm gas kinematics, and the warm gas property. Here, we compare the model prediction to the observation.

In Fig. 5.7, we plot the column density distribution and the model predictions for both the stellar sample and the AGN sample. The behaviors of the models are similar to the observations and the QB19 model (details are described in QB19). We find that sight lines with high Galactic latitudes ($|b|$) and small Galactic longitudes ($|l|$) have higher projected column density ($\log N \sin|b|$) for stellar sight lines at the same z heights. For the AGN sample, the kinematical model captures the feature that the projected column density is higher for sight lines toward the GC ($|l| = 0°$) compared to the anti-GC ($|l| = 180°$) direction. For sight lines toward the anti-GC, the projected column density shows a rapid decrease toward low Galactic latitudes. Then, the inclusion of the kinematics in the model does not break the self-consistency with the previous column density-only model (QB19; more comparisons are in Section 5.7.1).

To test the role of the warm gas kinematics, we compare the stacked line shapes based on the AGN sample and the model predictions. The kinematical model predicts that the line shape has a dependence on Galactic longitude and Galactic latitude. Therefore, we divide the entire sky into 20 regions, which roughly have a similar number of sight lines (~ 10) in each region. Galactic longitude have grids of $0° - 45°$, $45° - 135°$, $135° - 225°$, $225° - 315°$, and $315° - 360°$, while the Galactic latitude

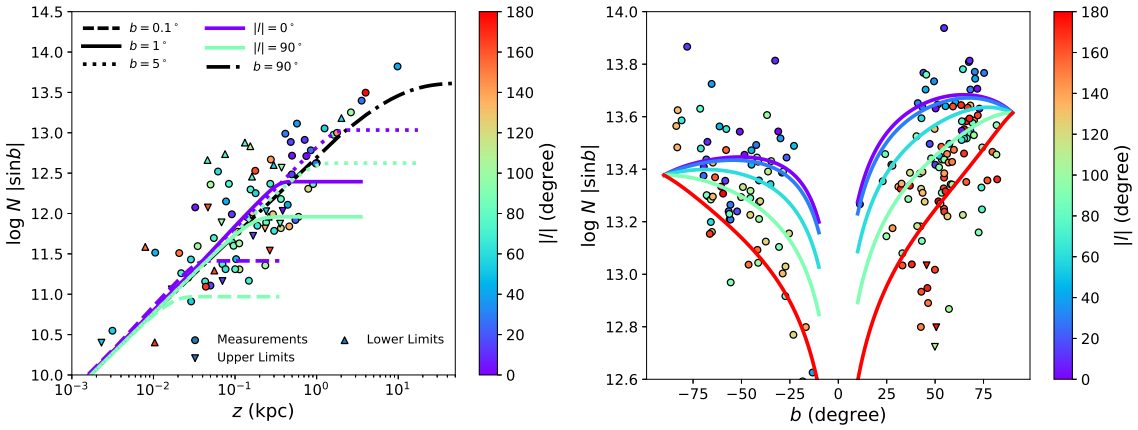

Figure 5.7: The comparison between the fiducial model and the observed column density of the stellar sample (left) and the AGN sample (right). The behavior of the kinematical model is similar to the QB19 because we use the 2D disk-CGM model as the basis of the kinematical model. In the left panel, we only plot the model of the northern hemisphere for simplicity. The southern hemisphere model is slightly lower than the northern hemisphere due to the NS asymmetry.

grids are $-90°$ to $-55°$, $-55°$ to $0°$, $0°$ to $55°$, and $55°$ to $90°$ (grids in Fig. 5.2). In each region, we stack the differential column density line shape by obtaining the mean value for all sight lines as shown in Fig. 5.8, where we also plot the fiducial model. The fiducial model reproduces the major absorption features around -150 to 150 km s^{-1} including some intermediate-velocity clouds (IVCs) and HVCs in specific regions (e.g., sight lines in region B.4 have HVCs at < -100 km s^{-1}).

However, there are still some HVC features are not accounted for in the kinematical model, such as negative HVCs at ≈ -300 to -150 km s^{-1} in regions C.4, C.5, D.4, and D.5, and the positive HVC at ≈ 300 km s^{-1} in region C.2. The negative HVCs could be a population of clouds associated with the Local Group (LG; Bouma et al. 2019), while the positive HVCs are likely to be associated with the LMC/SMC (discussed further in Section 5.7.3.3.

For individual sight lines, the difference between the model predictions and the observed total column density are shown in Fig. 5.9. Broadly, these residuals of

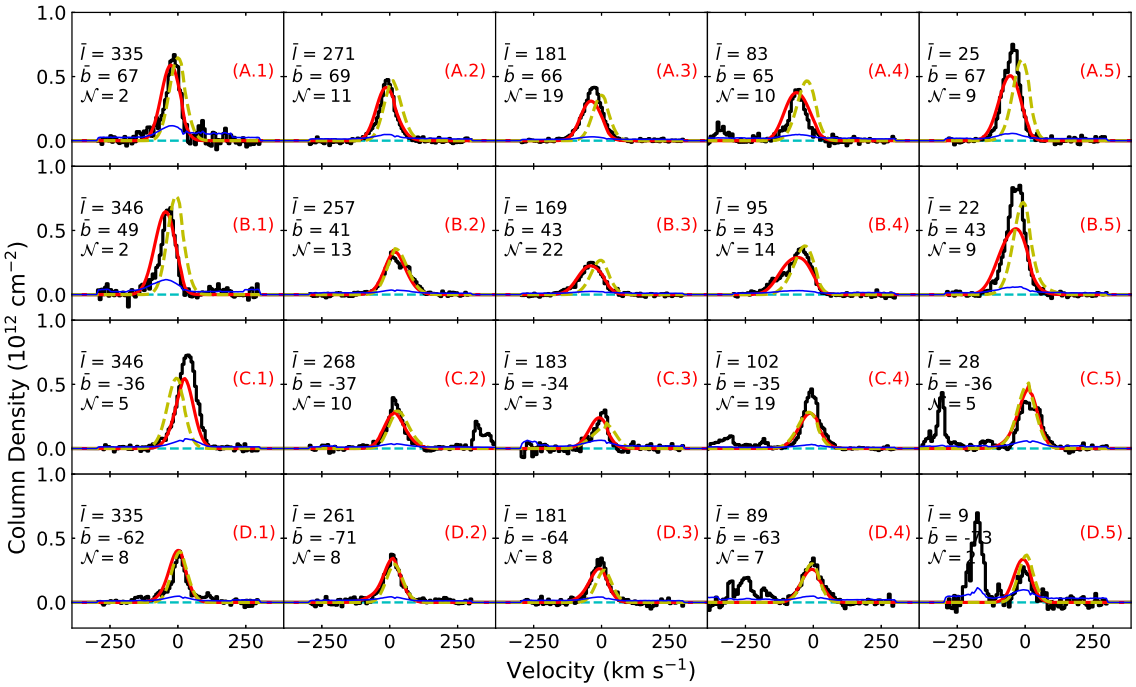

Figure 5.8: The comparison between the stacked line shape of observation and the kinematical model prediction: the sky is divided into 20 regions (the grids in Fig. 5.2). The observed line shapes (black lines) are consistent with the model predictions (red lines) within the uncertainty (blue lines) for most regions. The dashed yellow lines are the model without the radial velocity component (other parameters are the same as the fiducial model). In the northern hemisphere, the yellow lines have systematically positive shifts compared to the observation and the fiducial model, which is the evidence of systematic inflow. The southern hemisphere does not show these systematic shifts, although the region C.1 shows an outflow feature (positive shifts). In some regions (e.g., B.5), the absorption broadening velocity is smaller than the average broadening velocity in the fiducial model, which leads to broader features. Some regions show features that cannot be accounted for by the kinematical model, which is suggested to have other origins: C.2 might be affected the MS (Fox et al., 2014), while C.4 and nearby regions might be an HVC population associated with the LG (Bouma et al., 2019).

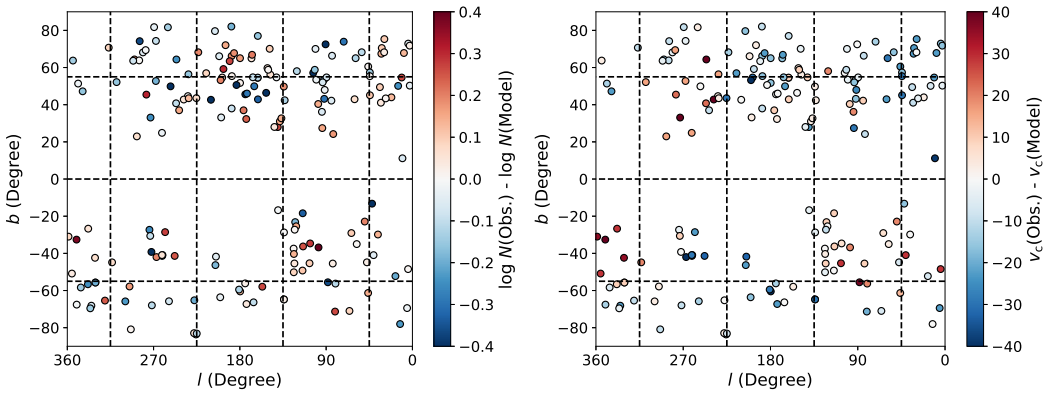

Figure 5.9: The column density residual (left), the velocity shift (right) maps. For the column density residuals, both hemispheres show average values about the zero, which shows no large scale differences ($\gtrsim 90°$). However, at small scale ($\approx 20°$), the column density residual shows clustering (e.g., the positive structure around $l = 180°$ and $b = 60°$). Similarly, the velocity shift also shows the small scale structure, but the kinematical structure ($\approx 50°$) is larger than the column density variation. These qualitative results are confirmed in more accurate estimation in Fig. 5.12.

column density are uniformly distributed over the entire sky at the large scale but shows some clustering (coherence) on scales of $\approx 20°$ (with similar enhancements or deficits). There is no significant connection between the column density enhancement or deficit and the known HVCs or IVCs detected in H I. The velocity shifts of individual sight lines (Fig. 5.9 right panels) also show clustering, but on a larger scale than the column density variation (more details are discussed in Section 5.6.5). The positive and negative shifts occur over the entire sky, which suggests that the bulk velocity field included in the kinematical model is the first-order approximation of the velocity of absorption features.

5.6.3 The Gas Distribution

In the fiducial model, the cloud path-length density of the warm gas clouds is about 1.3 ± 0.2 per kpc at the GC, while it is 0.6 ± 0.1 per kpc at the Solar neighborhood. For the Solar neighborhood, this path-length density is consistent with the nearby

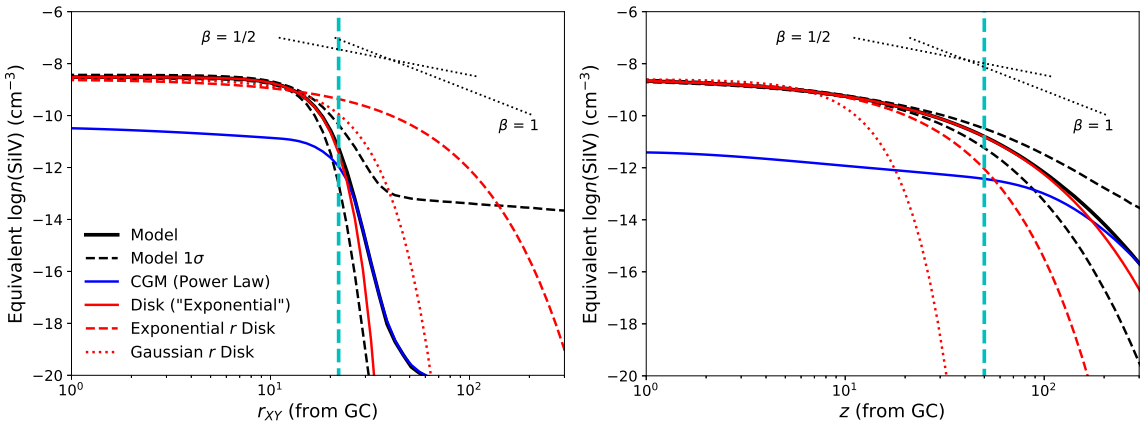

Figure 5.10: The equivalent Si IV density distribution along the radial (left) and the z (right) directions. The vertical cyan dashed lines indicate the limiting radius ($20-50$ kpc), which is set by the limiting column density. In the fiducial model, the radial direction density distribution (the red solid line) shows a sharp decay at about $10-20$ kpc compared to the exponential function (the red dashed line) and the Gaussian function (the red dotted line). Oppositely, the z direction density distribution is more extended than the exponential function. The difference between the two directions suggest that the MW warm gas traced by Si IV is affected by feedback processes originated from the disk.

($d \lesssim 0.2$ kpc) WD stellar sample, where no ISM Si IV has been detected. The path-length cloud densities set upper limits of the cloud size of about 0.8 kpc at the GC and 1.5 kpc at the Solar neighborhood. If individual clouds have sizes much larger than 1.5 kpc, the warm gas traced by Si IV will be smoothly continuous rather than the cloud-like variation (i.e., the intrinsic scatter traced by the patchiness parameter). It is not clear whether there is a real difference between the GC and the Solar neighborhood, but some differences are expected because the GC has higher pressure for the warm gas, where could lead to smaller cloud sizes. This constraint for the warm gas is consistent with our more accurate estimation of cloud size in Section 5.6.5 (1.3 kpc).

We calculate the equivalent density profile (the cloud path-length density times the column density per cloud; $XN_{\rm sg}$) for every single point in the MCMC chain and obtain the median and the 1 σ uncertainty (Fig. 5.10). For both density distributions, the outskirts suffer from large uncertainties. Here, we set the observation limits

as $\approx 10^{-11}$ cm^{-3}, which is the ratio of the limiting column density (10^{12} cm^{-2}) and the typical path length of ($30 - 50$ kpc). Then, we suggest that the warm gas density distribution are well constrained within the limiting radius (although the model extend to 250 kpc): $\approx$ 20 kpc in the $r_{\rm XY}$ direction and $\approx$ 50 kpc in the z-direction.

The majority of gas contributing to the column density is within 20 kpc to the GC. Quantitatively, we calculate the average distance of the warm gas with weights as the column density ($\int nr\mathrm{d}r / \int n\mathrm{d}r$). In $r_{\rm XY}$ and z-directions, the distance are 20 and 13 kpc, respectively. With the origin at the Sun, we could calculate the average observed gas distance. Then, the average distance of the observed absorbing gas has distances of 3 kpc ($r_{\rm XY}$), 5 kpc (z in the south), and 9 kpc (z in the north). Therefore, we suggest that the observed Si IV features can be considered at $\approx$ 5 kpc, and we use this value as a typical distance to estimate the cloud physical size in Section 5.6.5.

There is a significant difference between the $r_{\rm XY}$ and z directions, where the density distribution along the z-direction is more extended than the $r_{\rm XY}$-direction. For the z-direction density distribution, the CGM component begins to take over at about 100 kpc, although it is a minor contributor to the column density, so the statistical constraints are poor. Within the distance range of $10 - 100$ kpc, the approximated power law slope is about -1.5 to -2 ($\beta \approx 0.5 - 0.7$). The $r_{\rm XY}$ density distribution has a much sharper edge than the z-direction density distribution at about $10 - 20$ kpc, which is about the size of the stellar disk.

The difference of the Si IV density distributions between the $r_{\rm XY}$ and z-directions indicates that the warm gas distribution traced by Si IV depends on the disk orientation. This could be explained as that the warm gas is more associated with the disk phenomena (i.e., feedback) rather than accretion from the IGM. Theoretically, feedback processes could enrich the warm gas above or below the disk by ejecting gas and metals or providing more ionizing photons to photo-ionize Si IV. The gas above

and below the disk is more affected by Galactic feedback than the disk radial direction. Therefore, it is expected that the gas dominated by feedback follows a disk-like shape, while accretion leads to more spherical geometry (e.g., Stern et al. 2019). The origin of the warm gas is discussed further in Section 5.7.3.

5.6.4 The Gas kinematics

In the kinematical model, we consider the first-order approximation of the bulk velocity field as the combination of the rotation velocity and the radial velocity. Here we mainly consider the kinematics of the major absorption features (with centroids at ≈ 0 km s^{-1}), but these features are not necessary to be low velocity (e.g., in some sky regions, the features could extend to HVCs; $|v| > 100$ km s^{-1}).

The fiducial model suggests that the rotation velocity of the warm gas is about $-214.8^{+3.3}_{-3.0}$ km s^{-1} at the midplane, which is comparable to the H I disk (and halo; ≈ -220 km s^{-1}Kalberla & Dedes 2008) and the stellar disk (≈ -200 km s^{-1}; Huang et al. 2016). This measured rotation velocity in the kinematical model has a dependence on the Solar motion, especially the Y-component, which is fixed to -232 km s^{-1} in the fiducial model. Physically, the line shapes of the Si IV absorption features in the AGN sight lines suggests that the rotation velocity of warm gas is about $15 - 20$ km s^{-1} smaller than the Solar rotation velocity.

Above or below the midplane, the rotation velocity is found to have a velocity gradient (i.e., lagging). In the kinematical model, we do not employ the linear format of the lagging, which could reverse the rotation direction at $z \approx 20 - 30$ kpc, if the lagging is ≈ 10 km s^{-1} kpc^{-1}. However, absorption line investigations on external galaxies shows that the CGM is co-rotating (the same rotation direction) with the disk (Martin et al., 2019). By adopting $v_{\rm rot}(r, \theta) = v_{\rm rot} \cos\theta$, we assume a cosine function for the velocity lagging, which never break the co-rotation between the CGM and the disk. In this assumption, an equivalent linear velocity gradient is $\mathrm{d}|v|/\mathrm{d}|z| \approx$

-8 km s^{-1} kpc^{-1} within $|z| = 10$ kpc around the Solar system.

The radial velocity is found to behave differently in the northern and southern hemispheres. The northern hemisphere has a radial inflow velocity of $-69.3^{+6.9}_{-6.0}$ km s^{-1} at 10 kpc, while the radial velocity in the southern hemisphere is not well constrained, with $v_{\rm rad,N} < -12$ km s^{-1}.

In the northern hemisphere, the kinematical model assumes that radial velocity depends on the radius (Eq. 16), which is approximated as $v_{\rm rad} \propto r^{3\beta-2}$. The β factor is $0.21^{+0.15}_{-0.16}$, which indicates that the accretion velocity is larger in the inner region of the northern hemisphere. The accretion velocity is $30 - 200$ km s^{-1} between 30 kpc and the boundary of the accretion. The boundary for the radial velocity ($R_{\rm disk}$) is given by the boundary surface:

$$(\frac{r_{\rm XY}}{12.35 \text{ kpc}})^{\alpha_{r_{\rm XY}}} + (\frac{z}{4.9 \text{ kpc}})^{\alpha_z} = 0.72^{+0.22}_{-0.19}. \quad (5.24)$$

We show this boundary for the northern hemisphere in Fig. 5.11. Because most column densities are from the warm gas within $30-50$ kpc, the accretion velocity is also dominated by the behavior in this region; the radial velocity beyond 50 kpc is unconstrained. Because the radial format of the radial velocity is a model assumption, we do not suggest that the radial velocity is necessary to be the $r^{3\beta-2}$ format. However, it is concluded that the inner region has higher radial velocities, because the constant radial velocity model (beyond the boundary) is significantly worse (ΔBIC > 6)

For the southern hemisphere, both the radial velocity ($v_{\rm rad} < -12$ km s^{-1}) and the boundary of the radial velocity ($R_{\rm disk} > 3.4$) are unconstrained. The boundary and the radial velocity are degenerate to some degree for the southern hemisphere. Ideally, the radial velocity determines the velocity shift of the gas beyond the boundary, while the boundary position determines the amount of gas that is shifted. Thus, the total column density away from the peak of the rotation-only model is roughly proportional

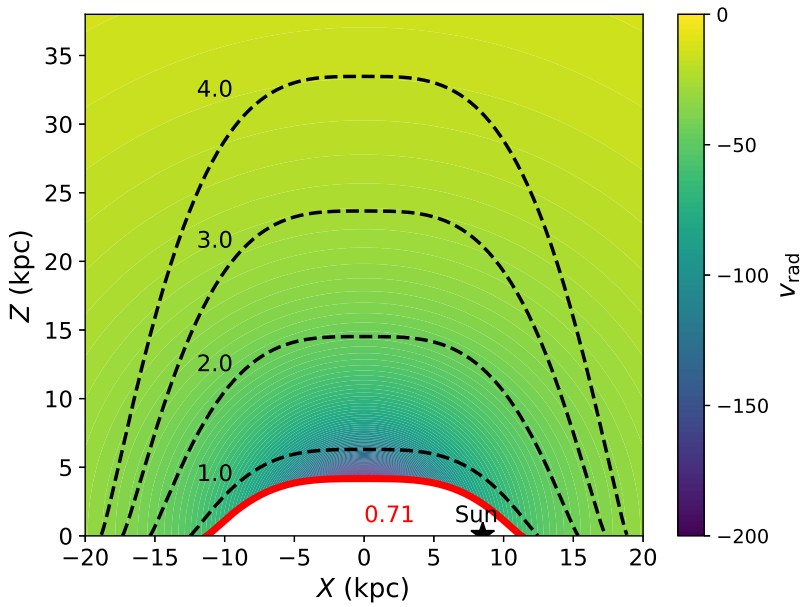

Figure 5.11: The boundary of the radial velocity in the northern hemisphere. The thick red solid line is the boundary of the radial velocity, below which there is no radial velocity. This line follows the isodensity contour of the disk component of $(r_{XY}/r_0)^{\alpha_{rxy}} + (|z|/z_0)^{\alpha_z} = 0.72$. The black dashed lines are also isodensity contours at different levels. Because the majority of absorbing gas is within $20 - 50$ kpc, the majority of radial velocity is about $30 - 200$ km s^{-1} in the northern hemisphere.

to the gas beyond the boundary times the velocity shift. The absorption features in the southern hemisphere do not show shifted column densities that would constrain both the radial velocity and the boundary.

To show the effect of the radial velocity, we plot the model without radial motions for both northern and southern hemispheres (other parameters are the same as the fiducial model) in Fig. 5.8. All regions in the northern hemisphere show line shapes (for both the observation and the fiducial model) with negative shifts compared to the model without the radial velocity. These negative shifts indicate that there is accretion in the northern hemisphere. For the southern hemisphere, the models with/without radial velocity and the observation do not have a significant differences in the line centroids for most sky regions. However, the region C.1 shows the outflow

feature as a positive shift to the model. In this sky region, 4/5 of sight lines pass through the Fermi Bubble (FB), so expansion of the FB might be responsible for this feature. This outflow feature is for the majority of the warm gas (e.g., the disk) in this direction, so it is different from individual HVCs as detected in Karim et al. (2018). As a comparison, there is no sight line passing through the FB in regions C.5 and B.1. The region B.5 has 5/9 sight lines passing through the FB, but this region does not show significant outflow for the absorption features around 0 km s^{-1}, although HVCs associated with the FB are detected in Bordoloi et al. (2017b).

The velocity shifts ($v_{\rm shift}$) of individual sight lines are shown in Fig. 5.9, which is introduced to account for the random motion of warm gas cloud along sight lines. The random motion is not completely random, because there is clustering in both hemispheres. In the northern hemisphere, random velocities are reduced in four regions roughly with centers at (270°, 40°), (180°, 55°), (135°, 40°), (45°, 55°). In the southern hemisphere, these clustering regions have centers at (225°, −55°) and (90°, −40°), and the possible FB feature in C.1. These clustering regions imply that the warm gas has kinematical structures with angular sizes of coherent $40° - 50°$.

We exclude the possibility that these features are artifacts of how the model was constructed. If the radial velocity is not well determined, the northern or the southern hemispheres should show the systematic positive or negative shifts in Fig. 5.9. However, this feature is not evident, as the average shifts in both hemispheres are close to the zero. For the rotation velocity, the most significant features should occur near 270° or 90°, and they should be of opposite sign: 270° negative and 90° positive (this means the fitting rotation velocity $|v_{\rm rot}|$ is larger), or 270° positive and 90° negative (the smaller fitting rotation velocity $|v_{\rm rot}|$). If the rotation velocity is not well determined, both hemispheres should have the same signal at different Galactic latitudes (e.g., both positive or negative shifts at 270°). These features also are not seen in the velocity shift map in Fig. 5.9. Therefore, we suggest that both rotation

and radial velocities are well determined and the clustering patterns are due to local features rather than poor fitting of global features. The physical origins of these features are discussed in Section 5.7.3.

5.6.5 The Gas Properties

In the kinematical model, we assume that the warm gas is cloud/layer-like, which introduces intrinsic scatter for the observed column density. The fiducial model suggests that the column density of single cloud ($\log N_{\rm sg} = 12.86^{-0.04}_{+0.05}$) is slightly larger than the estimation based on the patchiness parameter ($\log N_{\rm sg} = 12.68$; Section 5.4) in the column density-only model (no kinematics). This is because when applying $\log N_{\rm sg}$ to the line shape, it not only accounts for the uncertainty of the column density, but also the uncertainty of the kinematical model.

The absorption broadening velocity is $29.8^{+1.3}_{-1.0}$ km s^{-1}, which is an average of all sight lines (Fig. 5.8). This broadening velocity contains three major contributors: the COS instrumental broadening, the thermal broadening, and the turbulence broadening. The resolution of COS/FUV is 12.8 km s^{-1} at 1400 Å, so the intrinsic broadening due to the warm gas is 26.9 km s^{-1}. This velocity is equivalent to the b-factor of 38 km s^{-1}, and a full width half maximum (FWHM) of 63 km s^{-1}. This result is consistent with the direct measurements of from Wakker et al. (2012), which has an FWHM of 63 ± 11 km s^{-1} for Si IV.

We suggest that the intrinsic broadening (≈ 27 km s^{-1}) is more dominated by turbulent broadening rather than thermal broadening. It is not clear whether the observed Si IV has multiple components in our sample, because the *HST*/COS cannot resolve features with velocity separation $\lesssim 15$ km s^{-1}. However, using higher-resolution STIS spectra ($\Delta v \approx 2$ km s^{-1}), Lehner et al. (2011) detected much narrower Si IV features in sight lines toward disk stars, which set the constraint on the temperature and the thermal broadening of the Si IV gas (≈ 10 km s^{-1}), which is well below the

intrinsic broadening of 27 km s^{-1}.

Another fundamental property of the warm gas cloud is the cloud size. Here we use a similar method to Werk et al. (2019), which proposed the method to estimate the cloud size based on the relationship between the angular distance and the absolute column density difference of AGN-AGN pairs. It is equivalent to extracting the angular power spectrum of the column density variation. When two sight lines are close enough to pass through the same cloud, the absolute difference of the column density is less at a smaller distance. If two sight lines are distant, there is no relation between the two column density measurements in these sight lines, so the absolute column density difference is more random.

We examine column density and velocity variations over the angular separation by using 17205 AGN-AGN pairs extracted from 186 sight lines. First, for each AGN-AGN pair, we extract the angular separation and the absolute difference between the measured (original) column density (left panel of Fig. 5.2). Then, we extract the distribution of the absolute column density difference for every angular distance bin of 3°. For each angular distance bin, the histogram of the absolute column density difference distribution (upper left panel in Fig. 5.12) is approximated by a Gaussian function (i.e., even at a large angular separation, the largest possible difference is also 0). Combing histograms, we found that at small angular distances (purple lines), the peaks of the distributions are higher and the corresponding wings are narrower than the distributions at large angular distance (red lines). This becomes clearer when we extract the 1σ width (68% percentile; $\sigma_{\mathrm{d}N}$) of the absolute column density difference distribution (lower left panel in Fig. 5.12). This value is equivalent to the power spectrum of the column density variation at a given angular separation. The value of $\sigma_{\mathrm{d}N}$ keeps increasing within the angular distance of $\approx 55°$, after where $\sigma_{\mathrm{d}N}$ has a flat part. Within the angular distance of $\approx 55°$, $\sigma_{\mathrm{d}N}$ is significantly smaller, which indicates there are physical correlations between sight lines within this separation. This

is consistent with the conclusion in Werk et al. (2019), who found a tight correlation for halo stars with z-heights of $\approx 3-10$ kpc up to 40°, indicating an angular size of the warm gas of at least 40°.

However, the column density has a global variation due to the disk and the CGM variations (e.g., the minimum of column density in $|b| = 40° - 60°$ and $|l| = 180°$; QB19). This global variation could introduce additional correlations between column densities at large angular separations. Therefore, we try to correct for the global variation by subtracting the fiducial model from the column density measurements. We make similar plots using the column density residuals in the fiducial model (left panel of Fig. 5.9) instead of the original column density. By using the column density residuals, we exclude the global variation of column densities. The result is shown in the middle left panel of Fig. 5.12, which appears similar to the upper left panel. Also, we extract the 1σ width of the column density difference distribution (in the lower left panel of Fig. 5.12), which shows that the correlation of the column density is within $\approx 15°$ (i.e., flat part after 15°). By comparing the non-corrected variation and the model-corrected variation, it is clear that the correlation disappears at angular scales of $\approx 15° - 55°$. This phenomenon means that the moderate scale correlation at $\approx 15° - 55°$ is due to the global variation of the Si IV column density rather than the local variation due to individual clouds. Then, we divide the entire angular separation into three ranges: individual clouds ($\lesssim 15°$), the global variation ($\approx 15° - 55°$; due to the large-scale warm gas distribution), the random variation ($\gtrsim 55°$; no correlation). This does not mean the correlation seen in the Werk et al. (2019) sample is also due to the global variation, because these halo star sight lines have relatively smaller distances and different z-heights, which may affect the column density behaviors.

This two-point correlation of the Si IV gas is consistent with what has been found for HVCs, where a legacy HVC survey was done for the MW using the COS archival data (Richter, 2017). It is found that a strong correlation occurs within $\approx 20°$, and

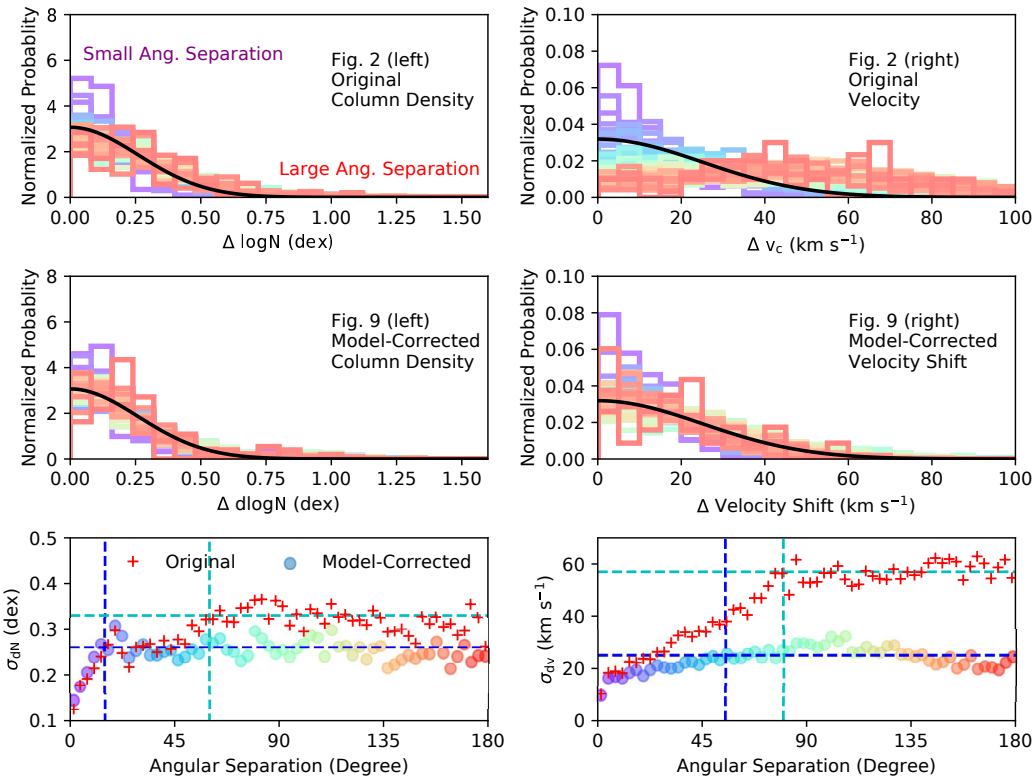

Figure 5.12: Plots to show the the coherence of the column density (left panels) or the velocity variations (right panels) as a function of angular scales. In the top two rows, the distribution of the absolute difference of column density or velocity (see the text for details). These distributions are color-encoded by the angular separation (in 3° bins) from purple (0°) to red (180°; encoded in rainbow colors, see the lower panels for a detailed match). The first row is for the original maps (Fig. 5.2), while the second row is for the model-corrected maps (residual maps; Fig. 5.9). The common feature is that the purple lines (small separation) typically have higher peaks and narrower wings than the red lines (large separation). This indicates that the smaller angular separation leads to a smaller variation of both the column density and the velocity. The 1σ widths of the distribution are plotted in the lower panels: original data (red cross) and model-corrected data (circles colored for increasing angular separation). The flat part of the 1σ dependence on the angular separation means that there is no correlation between two sight lines at this angular separation. Based on both original and residual variations, we divide the angular separation behavior into three parts: the cloud variation (lower than the vertical blue lines), the global variation (between the blue and cyan lines), the random variation (larger than the cyan lines). The cloud size is about 15°, and the global variation is about 55°. The kinematic structure is about 55°, and the global variation goes up to 80°.

a weak correlation is present up to $\approx 70^\circ$ (Richter, 2017). This consistency indicates that rotation and inflow in the northern hemisphere are the two dominant factors for the HVCs, which is the high-velocity tail of the warm gas distribution.

The 15° angular size can be converted into a physical size by adopting a distance. Using the density distribution in Section 5.6.3, the mean distance of the warm gas (weighted for the column density; $\int nz\mathrm{d}z / \int n\mathrm{d}z$ or $\int nr_{\mathrm{XY}}\mathrm{d}r_{\mathrm{XY}} / \int n\mathrm{d}r_{\mathrm{XY}}$) is about 5 kpc from the Solar system. Then, the warm gas cloud size is estimated to be 1.3 kpc. This value is consistent with the estimation based on the cloud path-length density, which has an upper limit of $\lesssim 1.5$ kpc around the Solar system. We can estimate the volume filling factor by combining the physical size of the warm gas and the cloud path-length density. At the Solar neighborhood, the volume-filling factor is about $(1.3\ \mathrm{kpc} \times 0.6\ \mathrm{kpc}^{-1})^3 \approx 50\%$.

These kpc-size structures are also seen in external galaxies. Hα and BVI imaging of NGC 891 indicates that there are $0.1 - 1$ kpc-size diffuse ionized gas features at z-heights of $1-2$ kpc (Howk & Savage, 2000). The Si IV gas has a higher temperature than the gas traced by Hα, so the smaller size of Hα is expected.

Combining the cloud size with the single cloud column density, one can derive a Si IV density of $10^{12.86}\ \mathrm{cm}^{-2}/1.3\ \mathrm{kpc} = 2 \times 10^{-9}\ \mathrm{cm}^{-3}$, which is slightly higher than the average Si IV density around the Solar system. The value $2 \times 10^{-9}\ \mathrm{cm}^{-3}$ is the average Si IV in a warm gas cloud, but it is not necessary for the Si IV density to be uniform in the cloud. The Si IV-bearing gas could be a shell surrounding a cooler core (e.g., H I seen in Hα). Then, we suggest that the estimated volume filling factor (50%) of warm gas is the upper limit, because it is not clear whether the core region is also the warm gas.

For kinematical structures, we also extract the power spectra of the line centroid velocity (right panel of Fig. 5.2) and the model velocity shift (right panel of Fig. 5.9), which allow us to understand the size of the kinematical structures of the MW

warm gas (Fig. 5.12). The difference between the non-corrected and model-corrected angular variation is much more significant than the column density. This is because the kinematics of the gas (i.e., the rotation and the accretion in the northern hemisphere) has more significant global effects (e.g., rotation leads to opposite shifts at $l = 90°$ and 270°). For the kinematical structure, the angular size is 80° without the model correction, while it is reduced to 55° after the model correction. Then, the kinematical structure has a physical size of 4.8 kpc at a distance of 5 kpc. This is larger than the column density structures by a factor of $\approx 3-4$, which indicates that every kinematical structure could contain multiple clouds (Section 5.7.3).

5.7 Discussion

5.7.1 Comparison with the QB2019 Model

In Section 5.3, we introduced three previous models, which are the basis of the kinematical model. The 2D disk-CGM model proposed in QB19 could fit both the stellar and the AGN samples simultaneously, showing a comparable contribution of the disk ($\log N \approx 13.0$) and the CGM component ($\log N \approx 13.2$) for Si IV. This conclusion differs from the new results based on the kinematical model, where we find that the cloud path-length density of the CGM component only has an upper limit. Therefore, the CGM column is much lower than the disk component in the kinematical model. Here, we discuss whether there are physical differences between the QB19 model and the kinematical model. For the comparisons between three previous models, more details can be found in Zheng et al. (2019a) and QB19.

There are three major differences between the kinematical model and the QB19 model: the inclusion of the cloud nature, the density distribution (disk and CGM), and the kinematical constraints. The kinematical model assumes the cloud nature of the warm gas (with the path-length density and the column density of a single cloud;

Section 5.4) instead of the ion density distribution. This method not only predicts the column density of individual sight lines (l, b, and d), but also predicts the intrinsic uncertainty (based on the Poisson noise of the number of clouds). Therefore, the cloud nature of the gas also introduces additional variation to the measured column density, which is similar to the traditional method of the patchiness parameter. However, the patchiness method assumes a constant additional variation to all AGN sight lines, which implies a constant weight on different sight lines. The cloud nature suggests the variation has a dependence on the path length. For AGN sample, the path length is large ($\approx$ 250 kpc), which leads to similar uncertainty for these sight lines. For the stellar sample, the uncertainty variation is large, such as from 0.4 dex to 0.2 dex from 1 kpc to 10 kpc, which is equivalent to having different weights for stellar sight lines. These weights of the stellar sample do not affect the large scale structure in the fitting results (e.g., r_0 and z_0) significantly, because the stellar sample has typically small distances and mainly determine the midplane properties. Therefore, we suggest that the cloud nature mainly determines the column density of individual clouds, and has little effect on the gas distribution due to the weights on the stellar sample.

The density distributions in the kinematical model are similar to the QB19 model, but there are three significant differences. First, the CGM component in QB19 has a column density distribution over l and b that is limited by the ability to constrain the CGM radial density distribution. This method implies an origin at the Solar system, which is impractical. In the kinematical model, the CGM radial density distribution could be extracted based on the kinematics, so we consider the GC as the origin (ϕ and θ in Fig. 5.4). Second, the QB19 CGM model only has a column density distribution, and only applies to AGN sight line predictions, which implies no CGM gas cospatial with the disk. In the kinematical model, we also consider the core region of the CGM, which could affect the stellar sight lines. Third, we introduce the α parameters in the disk model, which is a more detailed way of representing the

disk extension in both direction r and z. This variation could affect the distribution of CGM, i.e., the z-direction density distribution of the disk is more extended, which suppresses the CGM component.

Finally, the most important factor is the kinematics, based on which the distance to the gas could be estimated. In QB19, we extract a density distribution for the disk component, but this is mainly based on the global variation of the AGN sample (and the midplane gas properties determined by the stellar sample). The scale length is constrained by the variation at low Galactic latitude of AGN sight lines. However, the distribution profile was not well constrained in QB19, in which the exponential and Gaussian profiles show similar fitting results. The scale height is the variation over different Galactic latitudes. Similarly, the profile in the z direction was also poorly constrained. Therefore, we suggest that the scale height and scale length in QB19 are not accurately measured parameters from the column density-only sample.

With the bulk velocity field in the kinematical model, we measure the spatial density distribution of the warm gas, from the line shape at different velocities. We find that the most of warm gas (contributing to the MW absorption features) is close to the disk ($\lesssim 20 - 50$ kpc) rather at large radii (i.e., 100 kpc) (Section 5.6.3). For gas close to the disk, we find the modified disk model (with α) adequately models the gas distribution, which sets the upper limit for the CGM. For the CGM at large radii (> 100 kpc), we obtain the upper limit for the average ion density.

5.7.2 The MW Warm Gas Mass and Accretion Rate

With the measured density distribution, we estimate the mass of the warm gas. Combining the density distribution with kinematics, we could also estimate the accretion rate from the warm gaseous halo.

5.7.2.1 Mass

In the kinematical model (Section 5.5), we use two functions to approximate the density distribution of the warm gas: an "exponential" disk (sharp decrease at large radii) and a power-law CGM (slow decrease at large radii). As stated in Section 5.6.3, the disk component dominates the ion density distribution within 50 kpc, and the density distribution has a large uncertainty at > 50 kpc.

To estimate the mass, we first integrate the ion density distribution to obtain the total ion number of Si IV ($\mathcal{N}_{\rm SiIV}$). Then, the total silicon number is $\mathcal{N}_{\rm SiIV}/f$, where f is the ionization fraction, which is assumed to be 0.2 for Si IV (bout half of the maximum in CIE or PIE to represent the average ionization fraction; Gnat & Sternberg 2007; Oppenheimer & Schaye 2013). The hydrogen number is estimated by accounting for the metallicity (assumed to be $Z = 0.5Z_{\odot}$; Bregman et al. 2018) and silicon abundance ($a = 3.24 \times 10^{-5}$; Asplund et al. 2009). Therefore, the total hydrogen number $\mathcal{N}_H = \mathcal{N}_{\rm SiIV}/f/Z/a$. Finally, the total mass is $1.3\mathcal{N}_H m_{\rm H}$, where 1.3 accounts for the helium mass and $m_{\rm H}$ is the mass of the atom hydrogen.

We use two ways to report the masses. First, we calculate the masses based on the disk and the CGM components. To obtain the model-predicted mass (with uncertainty), we not only use the median value of the posterior distribution in Fig. 5.6, but all models in the MCMC chain to estimate the uncertainty of the mass. For the disk component, the mass distributions are shown in Fig. 5.13 for both hemispheres. The northern disk has a mass of $\log M = 7.89^{+0.05}_{-0.04}$, while southern disk is $\log M = 7.66^{+0.06}_{-0.05}$; the total disk component mass is about $\log M = 8.09^{+0.05}_{-0.04}$. These masses could be scaled according to the ionization fraction and the metallicity as $-\log(f/0.2) - \log(Z/0.5Z_{\odot})$. For the CGM component, we could only obtain an upper limit. Within 250 kpc, the 3σ upper limit is $\log M < 9.1$ for the northern hemisphere and 8.0 for the southern hemisphere. Combining the two hemispheres, the total CGM component has a 3σ upper limit mass of $\log M < 9.1$ (excluding the

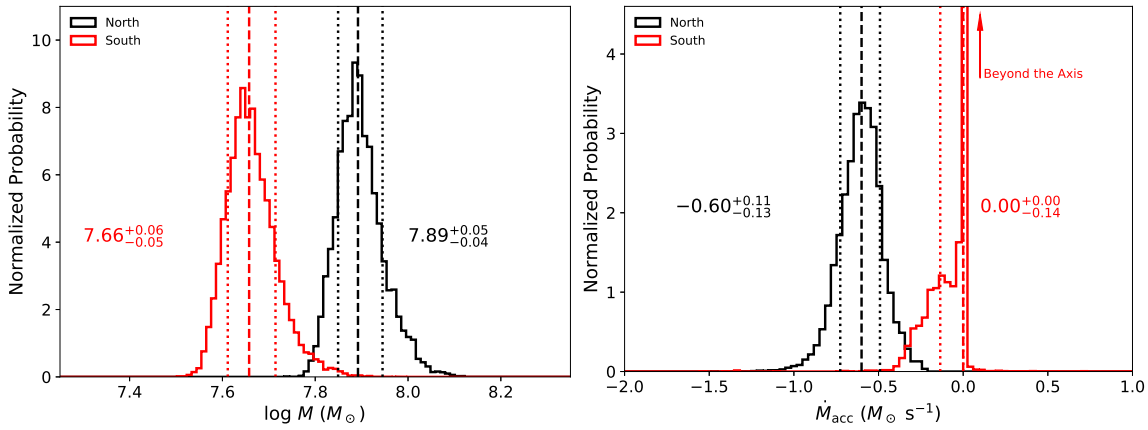

Figure 5.13: The estimations of the warm gas disk mass (left panel) and the accretion rate (right panel). Vertical dashed lines and dotted lines are the median and the 1σ uncertainty. The disk component dominates the mass within 50 kpc, which has a total mass of $\log M = 8.09^{+0.05}_{-0.04}$. The CGM component might dominate the mass upto 250 kpc, which has a 3σ upper limit of $\log M < 9.1$ (no MS contribution). The accretion rate in the southern hemisphere is close to the zero, but has a 3σ upper limit of $-0.4 M_\odot$ s^{-1}.

Magellanic system; MS).

Another approach is to report the total mass within the given radii. As shown in Fig. 5.10, the density distribution of the warm gas are well constrained at 30-50 kpc for both z and r directions. The density distribution of warm gas is dominated by the disk component within 50 kpc, and the total mass is $\log M(r < 50 \text{ kpc}) = 8.09^{+0.05}_{-0.04}$. For warm gas within 250 kpc, although the column density measured from the Sun is dominated by the gas close to the disk, the mass may be dominated by the gas at large radii (> 50 kpc). The mass upper limit, from combining the disk and the CGM component, is $\log M < 9.1$ within 250 kpc at 3 σ(excluding the MS). This is consistent with QB19 that the warm gas in the MW is dominated by the MS, which has a mass of $\log M \approx 9.4$ (Fox et al., 2014).

5.7.2.2 Accretion Rate

With the kinematical model, we determine the accretion velocity (for the northern hemisphere) and obtain the bulk accretion velocity field at different radii. We estimate the accretion rate by combining the density distribution and the radial velocity. As described in Section 5.5, we set a boundary for the radial velocity ($R_{\rm disk}$), within which there is no radial velocity. Here we calculate the total mass accretion rate at this boundary.

At the boundary surface, we integrate the product of the inflow velocity $v_{\rm rad}$ and the equivalent ion density $n = XN_{\rm sg}$:

$$\dot{M} = A \int n(z, r) v_{\rm rad}(r) {\rm d}S, \tag{5.25}$$

where S is the surface area of the boundary, and $A = 1.3 m_{\rm H}/f/Z/a$ is the conversion factor from Si IV ion number to total mass. Similar to the mass estimation, we calculate the accretion rate for every model in the MCMC chain and plot the posterior distribution in Fig. 5.13. For the northern hemisphere, the accretion rate is $-0.60^{+0.11}_{-0.13}\ M_\odot\ {\rm s}^{-1}$. For the southern hemisphere, the accretion rate is estimated to be $0.00^{+0.00}_{-0.14}\ M_\odot\ {\rm s}^{-1}$, and the 3 sigma upper limit of accretion is $-0.4\ M_\odot\ {\rm s}^{-1}$. The distribution of the southern hemisphere accretion rate is not a Gaussian-like distribution, but has a very high peak and a sharp edge at $0.00\ M_\odot\ {\rm s}^{-1}$. Therefore, the preferred accretion rate in the southern hemisphere is $0.00\ M_\odot\ {\rm s}^{-1}$, although the distribution of the accretion rate shows a negative wing. Combining both hemispheres, the total accretion rate is $-0.64^{+0.14}_{-0.17}\ M_\odot\ {\rm s}^{-1}$.

5.7.3 Physical Implications of the kinematical Model

The fitting results of the kinematical model are described in Section 8.3. Here we discuss the implications of the kinematical model, focusing on the warm gas origins

and the warm gas kinematics.

5.7.3.1 Galactic Fountain Origin of the Warm Gas

The warm gas in the MW has four possible origins considering the location where it is formed from the inner region to the outskirts: the ISM on the disk, the ejected material from the disk (feedback), the cooling flow in the MW gaseous halo, and the direct accretion from the IGM. The warm gas density distribution could provide hints to distinguish between these origins. Theoretically, the first two possibilities indicate that the warm gas distribution follows a disk shape (Fielding et al., 2017a), while the accretion from IGM is expected to be more spherical, because no cosmic filament is observed in local galaxies around the MW (Tully et al., 2019).

As introduced in Section 5.6.3, there is a significant difference between the vertical direction (perpendicular to the disk; z) and the radial direction (along the midplane; $r_{\rm XY}$). The warm gas in the z direction is more extended than in the $r_{\rm XY}$ direction, so we suggest that the warm gas distribution is affected by Galactic feedback. This effect is not only for the disk itself, but also extends to $20-50$ kpc, as shown in Fig. 5.10. For the MW, more warm gas above or below the disk implies that the disk feedback processes are important to understand the warm gas formation.

The most direct explanation is that the warm gas is formed by the Galactic wind, where ejected gas could reach the virial radius (and beyond). Galactic winds could produce a large amount of warm gas at $10-100$ kpc in the z direction through radiative cooling (Thompson et al., 2016). Along the disk r-direction, a Galactic wind could not be launched, which leads to less warm gas. This scenario could explain the warm gas distribution observed in the MW. However, one issue remains for the Galactic wind model as the warm gas is mainly accreted (the northern hemisphere) or there is no systematical radial flow (the southern hemisphere). In the Galactic wind model, Galactic wind is mainly outflowing, except for the large mass loading

case (i.e., more ejected hot gas than the star formation rate; Thompson et al. 2016).

An alternative model is the Galactic fountain, where some of the ejected material (typically warm gas) is recycled (accreted) to the disk instead of leaving the galaxy halo with the Galactic wind (Bregman, 1980; Fraternali, 2017; Kim & Ostriker, 2018). In the Galactic fountain scenario, the warm gas fountain is a byproduct of the hot wind, which is formed in the Galactic wind shocks. The kpc-scale numerical simulation suggests that the warm gas in the hot wind has a periodic outflow and inflow cycles with a timescale of ≈ 50 Myr (regulated by stellar activity; Kim & Ostriker 2018). The majority of the outflow and inflow velocity is within -50 to 50 km s^{-1} at any epoch. Then, one could estimate the length scale of the size of the Galactic fountain structure to be ≈ 3 kpc.

The theoretical predictions of Galactic fountains are consistent with our measurements of the MW warm gas. Based on the kinematical model, inflow and outflow features are observed in addition to the bulk velocity field (i.e., rotation and inflow). These inflow and outflow features have a velocity dispersion of ≈ 20 km s^{-1} ($v_{\rm rand}$). This velocity dispersion is the projected value along sight lines, so the 3D dispersion is higher. Assuming the random motion is isotropic, the 3D velocity dispersion is ≈ 35 km s^{-1}, which is consistent with the velocity distribution predicted in Kim & Ostriker (2018).

As stated in Section 5.6.5, the kinematical structure typically has a size of ≈ 5 kpc, which is $3-4$ times the cloud size (1.3 kpc; i.e., column density structures). One kinematical structure could contain multiple clouds. In sub-kpc-scale (≈ 0.1 kpc) numerical simulations, the warm gas is generated in interaction (or mixing) layers between cool gas ($\approx 10^3 - 10^4$ K) and hot gas ($\approx 10^6$ K; Gnat et al. 2010; Kwak & Shelton 2010). Recent simulations predict the Si IV column density per layer is $\log N \approx 11$ (Ji et al., 2019a) or $\log N \approx 12$ (Kwak et al., 2015). For a cloud, the sight line could pass though the mixing layer at least twice for a cool gas core or filament,

so the predicted Si IV column density per cloud is about $\log N = 11.5$ or 12.5. The Ji et al. (2019a) model has a lower number density (10^{-2} cm^{-3}; hence the pressure) for the cool gas than the Kwak et al. (2015) model (10^{-1} cm^{-3}). We suggest that the Ji et al. (2019a) model is more similar to Si IV clouds in the galaxy halo, while the Kwak et al. (2015) model is more appropriate to the galaxy disk. For the MW, the observed Si IV features are mainly due to warm gas in or close to the disk ($\lesssim 20$ kpc), which has the higher pressure, and is more similar to the Kwak et al. (2015) model ($\log N \approx 12.0 - 12.5$).

5.7.3.2 The Origins of the Net Inflow in the Northern Sky

As a significant NS asymmetry, the northern hemisphere has a net accretion flow (also more massive; Section 5.7.2), while the southern hemisphere does not. This net accretion flow is also observed as prominent IVCs and HVCs in the northern hemisphere, which are detected by the H I 21 cm line (Wakker, 2004) and nebular lines such as Hα (Haffner et al., 2001). For the hotter gas ($\log T \approx 6$), current X-ray instruments are not sensitive to this level of accretion. Here, we limit the discussion to the cool and warm gas.

There are two possible origins for the inflow in the northern hemisphere: asymmetric disk activities or accretion histories. We suggest that even though the inflow might be due to the accretion from the IGM, the warm gas is still shaped by feedback processes to account for the density distribution (Section 5.6.3).

For the disk origin, the northern hemisphere inflow might be due to a one-sided hot wind burst. In zoom-in simulations, the hot wind is not necessarily symmetric between the two hemispheres, which could lead to different density distribution and kinematics (Kim & Ostriker, 2018). If the hot wind is temporarily blocked in one side, one only expects the recycled (accreted) gas in the other side. Then, an one-sided gigantic burst in the past might regulate the Galactic fountain, and lead to net

accretion in the northern hemisphere. However, there are three remaining issues for this scenario. First, small Galactic fountain structures are supported by numerical simulations (i.e., ≈ 3 kpc; Kim & Ostriker 2018). This typical size cannot cover the entire northern hemisphere (> 10 kpc at 5 kpc). Second, the timescale of the Galactic fountain cycle is about $\approx 50 - 150$ Myr. Then the burst should happen within the past $\lesssim 1$ Gyr to keep the systematic accretion feature, otherwise the random motion will dominate the kinematics. Third, there is about $M \approx 3 \times 10^7\ M_\odot$ more warm gas in the northern hemisphere, which is comparable with the total mass of the warm gas disk of the MW. It is almost impossible that the disk activities lifted all of the $\log M \approx 7.5$ more warm gas in the north.

Therefore, the inflow in the northern hemisphere should also reflect the accretion history of the MW. There are two possible accretion modes onto the MW, through the sub-halo or the cosmic filament, which cannot be distinguished by our observations. In the sub-halo scenario, the inflow in the northern hemisphere is due to a merger of a dwarf galaxy in the past. The mass of the dwarf galaxy cannot be small, which is limited by the momentum conserved in the gas inflow. Then, this merger may lead to observable features in the MW stellar halo (Deason et al., 2019). Another possibility is that the gas inflow is due to the continuous accretion of the IGM through a cosmic filament in a given direction. The materials accreted from the IGM could cool down within the MW halo, which could lead to significant inflow ($v_{\rm r} \approx 100$ km s^{-1}) close to the disk (Stern et al., 2019).

5.7.3.3 The kinematics of IVC/HVC

The absorption systems of the MW are divided into three classes based on the velocity: absorption features due to the MW disk ($|v_{\rm LSR}| \lesssim 20$ km s^{-1}), IVCs (20 km s^{-1} $\lesssim |{\rm v_{LSR}}| \lesssim$ 90 km s^{-1}), and HVCs (90 km s^{-1} $\gtrsim |{\rm v_{LSR}}|$). As discussed in Wakker (1991), this classification is arbitrary, and it does not consider Galactic

rotation. Therefore, Wakker (1991) introduced the deviation velocity ($v_{\rm DEV}$), which is the velocity difference between the observed line centroids and the predictions in a rotation-only model. Based on the deviation velocity, Wakker (1991) defined IVCs (35 km s^{-1} $<$ $|{\rm v_{DEV}}|$ $<$ 90 km s^{-1}) and HVCs ($|v_{\rm DEV}|$ $>$ 90 km s^{-1}). As summarized in Wakker (2004), prominent H I IVCs with negative velocities show up in the northern hemisphere (e.g., IV-Arch and IV-Spur). Because the deviation velocity excludes the effect of Galactic rotation, the existence of prominent IVCs indicates that the kinematics of IVC cannot be accounted for by a rotation-only model. Similarly, Sembach et al. (2003) found that the velocity distribution of O VI HVCs prefers a static halo (at $|z| > 3$ kpc) rather than a co-rotating halo.

However, as shown in Fig. 5.8, the major absorption features (-150 km s^{-1} $\lesssim$ ${\rm v_{helio}}$ $\lesssim$ 150 km s^{-1} including some IVCs and HVCs) could be reproduced by our fiducial model, which contains both Galactic rotation and inflow. There are three differences between our fiducial kinematical model and the rotation-only model used in Wakker (1991) and Sembach et al. (2003), which lead to the different conclusions whether the IVCs and HVCs could be reproduced in a rotation scenario. First, the velocity lagging is important to understand the velocity of warm gas at high latitudes. A lagging of 10 km s^{-1} kpc^{-1} leads to a velocity difference of -30 km s^{-1} at a vertical height of 3 kpc. After the projection along the sight lines, it is about -20 to -30 km s^{-1} at high Galactic latitudes ($|b| \gtrsim 60^\circ$). Second, our density distribution extends to higher z and larger $r_{\rm XY}$, while previous studies typically assume a boundary of $z = 3$ kpc for the warm gas. A more extended density distribution means a larger lagging effect to account for more negative absorption features. Third, the radial velocity (inflow) is important for the northern hemisphere. This is of special importance for warm gas at $|l| \approx 180^\circ$, which has a negative-velocity HVC. Therefore, we suggest that the MW rotation-inflow halo could explain most IVCs and HVCs seen in the Si IV absorption features.

Besides these MW halo IVCs and HVCs, there are still high-velocity features that cannot be modeled in the fiducial model. In Fig. 5.8, the region C.2 shows a features at about $250-400$ km s^{-1}, while regions C.4, C.5, D.4, and D.5 show unaccounted for features -400 to -100 km s^{-1}. We suggest that these features could be divided into two populations. One is the HVCs associated with the MS (mainly around LMC). For this population, Fox et al. (2014) has a detailed analyses, which is found to contribute a significant amount of the total warm gas mass in the MW halo (Zheng et al. 2019a; QB19). Another population is the gas associated with the LG, which shows extremely high-velocity HVC at $v < -300$ km s^{-1} towards the barycenter of the LG (Richter et al., 2017; Bouma et al., 2019). The LG barycenter is located in the region C.4 in Fig. 5.8, where one sees the unaccounted features. We note that the LG population may not only contain extremely HVCs but also HVCs (even low-velocity features), which might be misidentified as MW warm gas, and lead to additional variance in our kinematical model. To distinguish better between the LG and the MW absorption features, one needs a better understanding of the LG kinematics, which is beyond the scope of this paper. Here we suggest that the unaccounted features around the region C.4 may be associated with the LG.

5.8 Summary and Conclusions

In this paper, we extract the line shape sample of the MW Si IV absorption features using the *HST*/COS archival data, and develop a kinematical model. Using the kinematical model to reproduce the line shape sample, we constrain the ion density distribution of Si IV, the bulk velocity field (i.e., the rotation velocity and the radial velocity), and the warm gas properties (i.e., the broadening velocity). Here, we summarize the key results:

1. In the kinematical model, we approximate the warm gas density distribution

by two components: an exponential-like disk component of $n(r_{\rm XY}, z) = n_0 \exp(-(r_{\rm XY}/r_0)^{\alpha_{r_{\rm XY}}}) \exp(-(|z|/z_0)^{\alpha_z})$ and a β-model CGM component of $n(r) = n_0(1+(r/r_{\rm c})^2)^{-3\beta/2}$. The parameters $\alpha_{r_{\rm XY}}$ of 3.4 ± 0.8 and α_z of 0.8 ± 0.2 indicate that the warm gas distribution is significantly more extended in the z direction (perpendicular to the disk) than the radial direction of the disk (Fig. 5.10). The scale length of the Si IV disk is 12.5 ± 0.6 kpc, which leads to a shape decay of density at the disk edge. Similar to QB19, we note that there is a significant NS asymmetry for the warm gas distribution. The northern hemisphere has a larger scale height ($z_{0,\rm N} = 6.3 \pm 1.5$ kpc) than the southern hemisphere ($z_{0,\rm S} = 3.6^{+1.0}_{-0.9}$ kpc). The CGM component only has upper limits, which indicates that the majority of the observed column density is close to the disk rather than at large radii of > 50 kpc.

2. The warm gas in the MW is co-rotating with the stellar or H I disk at a rotational velocity of -215 ± 3 km s^{-1}. Above and below the disk, there is also rotation velocity gradient (lagging) of ≈ 8 km s^{-1} kpc^{-1} at $z = 3$ kpc, and smaller at higher z heights. This velocity gradient is important for fitting the absorption features at high Galactic latitudes. The radial velocity shows a NS asymmetry as a significant inflow of -69 ± 7 km s^{-1} (at 10 kpc) in the northern hemisphere, while the southern hemisphere does not show a significant net outflow or inflow.

3. The total mass of the disk component is $\log M = 8.09 - \log(Z/0.5Z_\odot)$, which is also the dominant mass contributor in the inner 50 kpc. At larger radii, the total mass of the warm gas in the MW halo might be dominated by the CGM component, which has an upper limit of $\log M < 9.1 - \log(Z/0.5Z_\odot)$ at 3σ (excluding the warm gas associated with the MS). Combining the ion density distribution with the kinematics, we estimate the accretion rate in the northern

hemisphere is $-0.60^{+0.11}_{-0.13}$ $M_\odot$ yr^{-1}. For the southern hemisphere, we set a 3σ upper limit to the accretion of -0.4 $M_\odot$ yr^{-1}.

4. In the kinematical model, we adopt the cloud model rather than continuously smooth density distribution (Section 5.4). Using the cloud model, we determine the average column density of individual clouds of $\log N(\mathrm{SiIV}) \approx 12.6 - 12.8$. By subtracting the model from the observation, we estimate the cloud size by analyzing the angular power spectrum of the column density residual (Fig. 5.9 and Fig. 5.12). The angular size of the cloud is found to be $\approx 15°$, which corresponds to a physical size of 1.3 kpc at 5 kpc (the average distance of the observed column density; Fig. 5.10). Similarly, we determine the size of the kinematical features based on the velocity residuals, showing an angular size of $\approx 55°$ and a physical size of 4.8 kpc at 5 kpc. This indicates that every kinematical structure contains multiple clouds.

5. We suggest that most of the observed features could be explained in the Galactic fountain scenario rather than Galactic winds and continuous accretion from the IGM. First, the warm gas observed in absorption is mainly co-rotating with the stellar disk (with the velocity gradient). Second, the Si IV density distribution shows a significant dependence on the disk-shape (not spherically distributed), which suggests the origin of Si IV is more associated with feedback processes rather than accretion. Third, we see kpc-size variations of the kinematical structures for both northern and southern hemispheres, which contain both inflow and outflow (after excluding the bulk velocity field), which is consistent with recent simulations (Kim & Ostriker, 2018).

6. Based on the kinematical modeling, we find that a considerable amount of IVCs and HVCs could be explained in the scenario of Galactic rotation and inflow in the northern hemisphere. The remaining HVCs in Fig. 5.8 might be associated

with the MS and the LG.

CHAPTER VI

HST/COS Observations of the Warm Ionized Gaseous Halo of NGC 891

6.1 Introduction

The formation of L^* galaxies leads to a hot halo with $T \sim T_{\rm virial}$ and extending to or beyond the virial radius, ($R_{\rm vir}$; White & Rees 1978; Cen & Ostriker 1999; Mo et al. 2010; Sokołowska et al. 2018). The gas density of the hot halo increases inward so that the cooling time falls below the Hubble time at $R \sim 100$ kpc (Thompson et al., 2016; Qu & Bregman, 2018b). As this gas cools, it slowly flows inward and can accrete onto the galaxy, provided that feedback from the galaxy does not completely offset the cooling (Kereš et al., 2005; Nelson et al., 2013).

Feedback, at the level we expect today in spiral galaxies, will expel hot gas from the disk but rarely at velocities great enough to unbind the gas from the galaxy halo, even during starburst events (Veilleux et al., 2005; Fielding et al., 2017a). This feedback creates a galactic fountain of typical height $5 - 10$ kpc above the disk and is seen in X-ray emission studies of edge-on galaxies (e.g., Strickland et al. 2004; Hodges-Kluck & Bregman 2013; Li & Wang 2013). One does not expect a sharp boundary between the galactic fountain and extended hot halo, as particularly hot plumes can rise further and there can be mixing between the two regions (e.g., Fielding

et al. 2017a). Nevertheless, regions close to the disk should be dominated by galactic fountain activities and regions further away by the long-lived hot halo.

Metallicity may offer a diagnostic to distinguish between the extraplanar and halo gas. The metallicity of galactic fountain gas should be about solar (Fox et al., 2015, 2016; Savage et al., 2017), as it flows upward from the disk, although the metallicity may be further enhanced by the supernovae that drive the flow (Scannapieco et al., 2008; Li et al., 2017b). The metallicity of the extended hot halo gas should be lower, as material falling onto galaxies is predicted to have less enrichment (Oppenheimer et al., 2016). This is supported by absorption line observations of extended gas, where the metallicity is typically $0.1 - 0.5 Z_{\odot}$ (Lehner et al., 2013; Wotta et al., 2016; Prochaska et al., 2017).

It is challenging to obtain metallicities near the transition between the galactic fountain and the extended hot halo. For the Milky Way, the intermediate velocity clouds are typically a few kpc above the disk and from ultraviolet (UV) absorption line studies, one finds a typical metallicity of $\approx 0.5 - 1.0 Z_{\odot}$ (Fox et al., 2016; Savage et al., 2017), although there are infalling high velocity clouds at heights of ~ 10 kpc and with metallicities of about $0.3 Z_{\odot}$ (Wakker, 2001; Wakker et al., 2008; Barger et al., 2012; Fox et al., 2018). X-ray emission and absorption studies infer a mean metallicity of about $0.5 Z_{\odot}$ for gas within 50 kpc (Bregman et al., 2018).

Background AGN sightlines through external galaxies rarely pass through the disk, and when this occurs, it is impossible to spatially assign a height to the absorption. The exception to this is for edge-on galaxies, which have been studied in X-ray emission (Strickland et al., 2004; Hodges-Kluck & Bregman, 2013; Li & Wang, 2013) and through dust-scattering halos (Hodges-Kluck & Bregman, 2014; Hodges-Kluck et al., 2016a). The dust-scattering halos indicate a change in the nature of the dust metallicity at $5 - 10$ kpc, suggesting a transition to the extended hot halo. The X-ray emission has the potential to yield the metallicity as a function of height, but

this demands lengthy observations with current instruments. The first observation capable of making this determination, from XMM-Newton observations of NGC 891, is discussed in a separate work (Hodges-Kluck et al., 2017, 2018).

An absorption line study of this transition gas in an edge-on galaxy is possible for NGC 891, where a background AGN (LQAC 035+042 003) projects to 5 kpc above the disk and for the inner part of the galaxy (Bregman et al., 2013). Spectra taken with STIS on *Hubble Space Telescope* (*HST*) revealed absorption lines of Fe II, Mg I and Mg II, with different abundances from subsolar to nearly solar. The limitations of this study are that the lines were not well resolved and the elements probed are subject to depletion onto grains. These shortcomings could be overcome by the Cosmic Origin Spectrograph (COS; Green et al. 2012), which provides high resolution ultraviolet (UV) spectra.

In this paper, we present the analyses of the COS/far-ultraviolet (FUV) spectrum of LQAC 035+042 003, which probes absorption by a number of elements and ionization states, including refractory elements that are not heavily depleted in halo clouds (Savage & Sembach, 1996). Another target (3C 66A) projected along the disk major axis at 108 kpc is also presented, which probes the outer region of the halo. In Section 2, we describe the observation data (UV and H I 21 cm lines), the data reduction method and the column density measurements. The photoionization models are described in Section 3 for all detected systems, leading to the hydrogen density and hence the path length of the absorption structures. We discuss the origin for the detected UV absorption systems in Section 4 and summarize our results in Section 5.

6.2 Observations and Data Analysis

6.2.1 LQAC 035+042 003

6.2.1.1 The QSO

The background QSO located at RA = 02h22m24.4s, DEC = +42°21′38″ (J2000) was discovered as an X-ray source in the *ROSAT* image by Read et al. (1997) and identified as a QSO in a followup optical spectroscopic observation (see details in Bregman et al. 2013). This QSO is projected near the edge-on disk of NGC 891 with an angular separation of 106″, which is 4.7 kpc at the NGC 891 distance of 9.12 Mpc (Tully et al., 2013). The AGN is also projected close to the minor axis of the disk with a separation of 11″ (0.5 kpc; Bregman et al. 2013).

6.2.1.2 The *HST*/COS Spectrum

The *HST*/COS spectra were acquired on 22-24 August 2013 in the FUV band and 22 July 2013 in the near-ultraviolet (NUV) band (*HST* proposal GO 12904; PI: Bregman). The high resolution FUV spectrum ($R \approx 20000$) was obtained with the grating G130M, and the total exposure time is 23.7 ks. The central wavelength in each exposure is 1291 Å, and multiple FP-POS positions are employed to reduce the fixed pattern noise. The low resolution grating G230L was employed for the NUV spectrum ($R \approx 2500$), and the total exposure time is 10.2 ks. Similar to the FUV observations, the NUV exposures have different FP-POS positions at the same central wavelength (2870 Å).

To coadd different exposures, we follow the procedure described in Wakker et al. (2015), for which we give a brief summary here. In each exposure, we calculate the net gross counts using the net rate and the exposure time, which is corrected for the background and the fixed pattern noise. Then, we coadd the total counts from each exposure and divide by the total exposure time at each wavelength to obtain the net

count rate. The final noise is the Poisson noise derived from the total counts, which is found to be better matched with the measured noise of the coadded spectrum Wakker et al. (2015). It is known that COS spectra may have velocity shifts (≈ 20 km s^{-1}) due to the geometric distortion and wavelength solutions from CALCOS. However, in this spectrum, the continuum count rates are too low (most pixels have zero/one gross count in one exposure) to do the cross correlation or to measure line centroids of single lines, which is necessary to correct the wavelength solution of individual exposures. Therefore, we adopt the CALCOS wavelength solutions and do not align different exposures using strong Galactic lines in this stage. The median S/N is 7.5 in the coadded COS/FUV spectrum at $R = 20000$ and 14.4 in the coadded COS/NUV spectrum at $R = 2500$.

The coadded spectrum is binned by three pixels (yielding the bin width of $\Delta\lambda = 0.02991$ Å) for fitting and line identification in NGC 891 (see the Appendix for details for other systems). Twelve ions are detected near the systemic redshift of 528 km s^{-1} (z = 0.001761; de Vaucouleurs et al. 1991): C I (2.1σ), C II, C II*, Fe II, Si II, Si III, Si IV, S II, N I, N V, Ni II, and P II. In addition to the primary absorption system, there is a weaker absorption system at $v = 90 - 100$ km s^{-1} related to the systemic velocity of 528 km s^{-1}, which we refer as a high velocity cloud (HVC). The properties measured from fitting Voigt profiles to these lines are given in Table 6.1, and the best-fit models are shown in Fig. 6.1. For each ion, different lines are fitted simultaneously and the continuum is determined using spline fitting in intervals of $3 - 6$ Å. The Voigt profile model is convolved with the COS line spread function to address the non-Gaussian broadening of COS, and the preferred solution is determined by minimizing the χ^2. Extra one component is added if the χ^2 difference is larger than 10 ($> 2\sigma$ at degrees of freedom of 3).

In the primary absorption features at ≈ 0 km s^{-1}, N I, Fe II, C II, Si II, and Si III show saturated features, which might affect the column density measurements.

Table 6.1: The COS/FUV Absorption Line Measurements

Ion	$\log N$ cm^{-2}	$\sigma_{\log N}$ dex	b km s^{-1}	σ_b	v^a	v_c^g km s^{-1}	σ_v
NGC 891 (LQAC 035+042 003)							
C I	13.76	0.17	23.5	15.7	−34.6	−16.7	10.0
C II	15.8	>	...	...	−25.0	−7.1	2.6
C II*	14.14	0.05	33.3	5.5	−34.2	−16.3	3.6
N I	15.71	0.10	34.1	1.7	−24.0	−6.1	1.3
N V	13.97	0.10	42.8	14.7	−27.3	−9.4	9.4
Mg II[f]	15.5	<	...	...	...	...	...
Si II	14.8	>	...	...	−39.1	−21.2	1.1
Si III	14.7	>	...	...	−50.2	−32.3	5.3
Si IV[b]	13.89	0.08	48.1	8.6	−69.2	−51.3	8.3
Si IV[b]	13.62	0.16	22.4	7.7	−5.4	12.5	4.3
Si IV[b]	12.93	0.31	32.5	29.4	75.8	21.8	
P II	13.76	0.09	25.1	9.6	−4.1	13.8	6.0
S II	15.33	0.02	50.9	3.2	−25.5	−7.6	2.2
Fe II	15.10	0.04	55.1	4.6	−34.1	−16.2	3.2
Ni II	14.19	0.06	53.0	10.4	−36.1	−18.2	6.7
NGC 891 HVC							
C I[c]	13.66	0.23	7.3	14.0	81.4	99.3	5.7
C II	13.97	0.18	10.0	...[d]	107.1	125.0	3.1
N I[f]	13.8	<	...	...	...	...	...
N V	13.47	0.15	19.7	12.8	99.6	117.5	7.1
Si II	13.50	0.08	14.8	2.1	89.4	107.3	1.5
Si III[e]	13.1	>	...	...	89.4	107.3	...
Si IV[f]	12.5	<	...	...	...	...	...
Fe II	13.77	0.18	20.0	...[d]	106.8	124.7	11.0
NGC 891 (3C 66A)							
C II	13.03	0.11	10.0	...[d]	35.0	57.8	4.0
C IV	13.79	0.03	23.2	2.3	31.1	53.9	1.5
Si II[f]	11.9	<	...	...	...	...	...
Si III	12.70	0.05	22.8	4.3	28.2	51.0	2.6
Si IV	12.45	0.10	14.8	7.3	32.4	55.2	4.2

[a] The velocity shift is calculated at $z = 0.001761$, which corresponding to the bulk velocity of NGC 891 (528.3 km s^{-1}).
[b] Si IV has multiple components for the absorption associated with NGC 891.
[c] C I only has one detected line λ1328.8 Å, while another strong line λ1277.2 Å is in the gap between two segments.
[d] For these ions, b factors can not be well constrained, so we fixed them in the fitting at values of $10 - 20$ km s^{-1}.
[e] The HVC Si III is completely blended with the AGN outflow Ne VI, which leads to large uncertainty of the measurements. See text for discussions on this ion.
[f] These ions have the upper limits calculated from the limiting EW at the 2σ level.
[g] The velocity measurements are corrected by aligning the FUV spectra and the H I 21 cm lines (see the text for details).

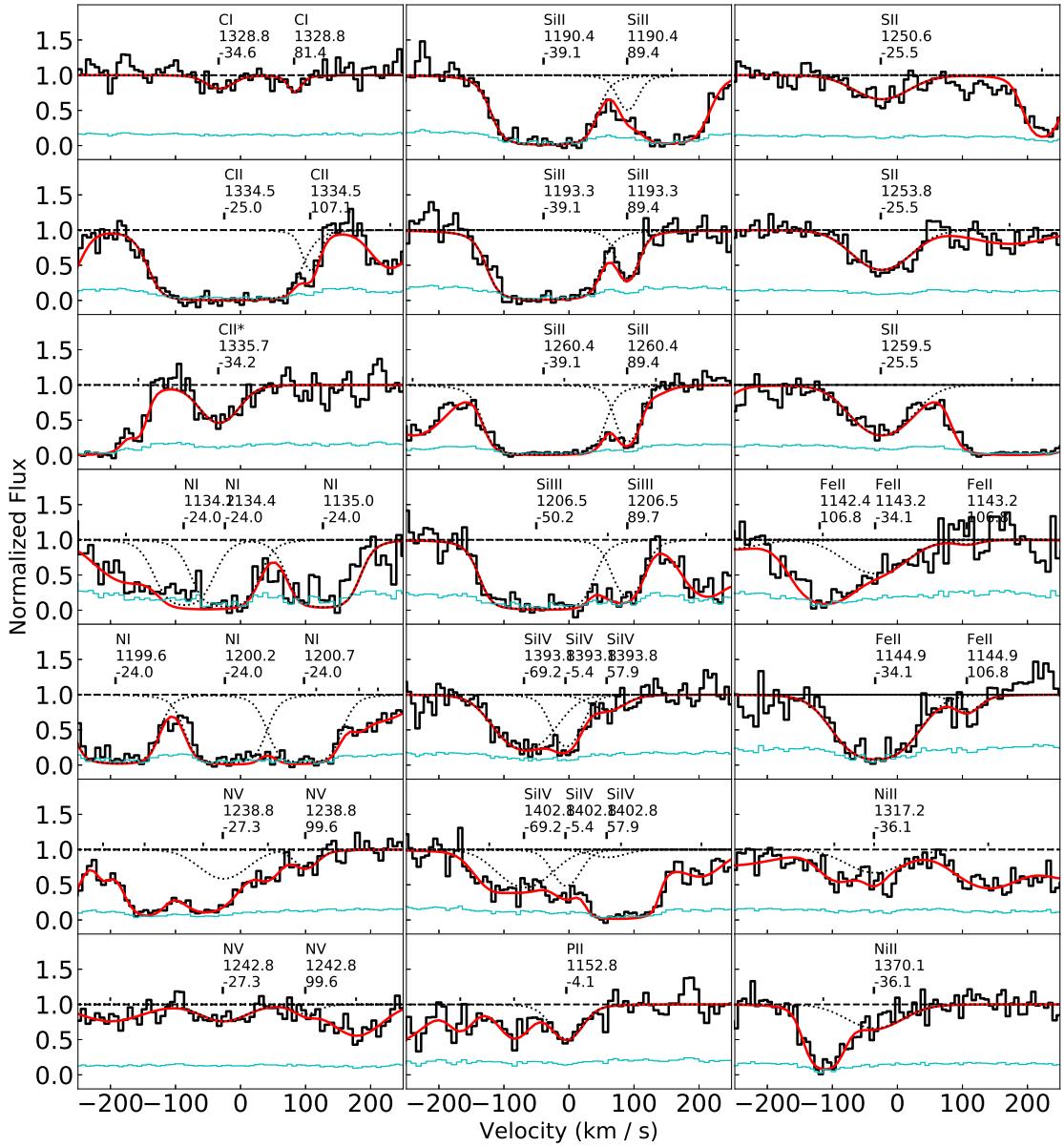

Figure 6.1: The spectra and best-fit models for identified lines for NGC 891. The black histograms are the observed spectrum, while the cyan lines are the error. The red solid lines are the total model for all identified lines, while the black dotted lines are decomposed spectral lines associated with NGC 891. The label for each identified line is the ion, the wavelength and the velocity relative to $z = 0.001761$.

For saturated lines, the column densities are degenerate with b factors that cannot be well determined using single lines. For N I, Fe II, and Si II, multiple lines from the same ion break the degeneracy between the b factor and the column density. N I and Fe II have multiple lines including unsaturated lines, which constrains the column densities and b factors. The situation is different for Si II, since all of the three observed lines are saturated. The simultaneous fitting of multiple lines leads to acceptable measurement uncertainties ($\log N = 15.60 \pm 0.26$ and $b = 39.2 \pm 2.9$). However, this measurement may have additional systematic errors that are dependent on the coadding method and the continuum determination, which is more sensitive for saturated lines. Therefore, besides the direct measurement from the Voigt profile fitting, we also determine a lower limit of $\log N > 14.8$ for Si II at the 1σ level. For Si III, there is only one absorption line, which would result in the lower limit of the column density. One possible solution is using the Si II b factor to constrain the b of Si III. As adjacent ions, Si II and Si III are believed to be in a similar phase, which leads to similar b factors. We adopted the column density by fixed Si III b factor to 40 km s^{-1} (the Si II b factor), leading to a column density of $\log N = 15.11 \pm 0.24$. Otherwise, we obtain the lower limit for Si III similar to Si II, and the 1σ lower limit is $\log N = 14.7$ for Si III. Therefore, we have two sets of measurements for Si II and Si III (Voigt profile fittings and lower limits), which will be used in the modelings (Section 3.1).

For C II, we cannot assume that C II has the same b factor as C I (low significance) or C II*, since a C II b factor of $23 - 33$ km s^{-1} leads to an unrealistically large column density ($\log N > 18$) and wide line wings that are not observed. This might be because C II* is from a dense region with a small b, while the C II line probably includes additional components from low-density ionized gases (e.g., the HVC at $v = -88$ km s^{-1}). However, the line shape of C II cannot be decomposed because it is saturated. Therefore, we varied the b factor to give a lower limit of the column

density. As a constraint, the b factor cannot be lower than 35 km s^{-1} or higher than 66 km s^{-1} (1σ bounds), with $\log N = 18.5$ to 15.8, correspondingly. In the following analysis (Section 3.1), we do not include C II to constrain the photoionization model, but we will consider the consistency of C II with other ions.

In the HVC, we detected absorption lines from C II, Si II, Si III, N V, and Fe II. C I is detected at the significance level of 1.7σ with a velocity separation of 81.4 ± 5.7 km s^{-1}, which is more than 2σ different from most other ions. Si III is contaminated by the Ne VI lines at $z = 1.1655$ (an AGN outflow with multiple components over 1000 km s^{-1}; see the Appendix for details). A possible $v = -170$ km s^{-1} at $z = 1.1655$ component of the AGN outflow (shown by O V, Ne V, and Ar VII) is near the $v = 86$ km s^{-1} component of the NGC 891 Si III line λ1206.5 Å. This AGN outflow component affects the line shape of the HVC Si III line, which may lead to a smaller v value. Both Si III and Ne VI are isolated in the wavelength coverage of the current QSO spectrum, so one cannot break this degeneracy using other lines from these two ions. To remove this degeneracy, we fixed the velocity of Si III to that of Si II (see Appendix) . The b factor of this Si III cannot be well constrained, but it should lie between 15 km s^{-1} (Si II) to 20 km s^{-1} (N V). The adopted column density is $\log N = 13.37 \pm 0.14$ for the Si III HVC component with $b = 20$ km s^{-1} and $\log N = 13.68 \pm 0.25$ with $b = 15$ km s^{-1}. The difference between these two values has complex reasons: the possible saturation of this line and the uncertainty of the AGN outflow Ne VI line. Therefore, we set a lower limit of $\log N = 13.1$ for the HVC Si III, and the upper limit of this ion has a large uncertainty. In Section 3.2, we will show that it is the lower limit of Si III that constrains the photoionization model, so the uncertainty of the upper limit of the HVC Si III will not affect our photoionization modeling (Fig. 6.8). Si IV has a component at $v = 57.9 \pm 21.8$ km s^{-1}, which may or may not be associated with the NGC 891 HVC. In following analysis we assume it is associated with the major component at $v = -30$ km s^{-1}.

For the HVC, we also measure the upper limit of the N I and Si IV column densities, which may have constraints on the physical conditions. The 2σ upper limits for Si IV (λ1393.8Å) and N I (λ1200.7Å) are $\log N < 12.5$ and 13.8 cm^{-2}, respectively.

The COS/NUV G230L spectrum has a lower spectral resolution, so the line measurements (e.g., b factors) are less accurate. There is only one detectable ion (i.e., Fe II) in this band, which is also detected in the FUV band. Therefore, we only use this NUV spectrum to check the consistency of Fe II measurements, and we project the Fe II properties obtained from the FUV spectrum into the NUV lines (Fig. 6.2). The NUV spectrum is consistent with the measurements obtained from the FUV spectrum, although the MW Fe II shows some differences. We suggest that the NUV MW Fe II might be affected by unknown fixed pattern noise. However, the individual exposures have too few counts to check for this effect. The measurements from the FUV spectrum are adopted in the following analysis for three reasons. First, the FUV spectrum shows two matched strong lines with significance $> 6\sigma$, which is unlikely to be by chance. Second, four of the NUV lines from both the MW and NGC 891 are consistent with the FUV measurements. Third, the COS/NUV G230L spectrum is different from the STIS spectrum at the same wavelengths. The STIS spectrum shows stronger absorption around 2382.0 Å (Bregman et al., 2013), which corresponds to the unmatched MW line Fe II λ2382.0 Å in the COS/NUV spectrum.

6.2.1.3 The STIS Spectrum

The STIS spectrum is reduced and reported in Bregman et al. (2013); therefore, we do not describe the STIS observational details here.

From the STIS spectrum, Bregman et al. (2013) obtained the Fe II column density of $\log N = 14.44 \pm 0.14$, the Mg I upper limit of 12.67 (EW $= 0.50 \pm 0.17$ Å), and Mg II of $15.48^{+0.36}_{-0.27}$. Mg I and Mg II can not be measured in the COS data, but

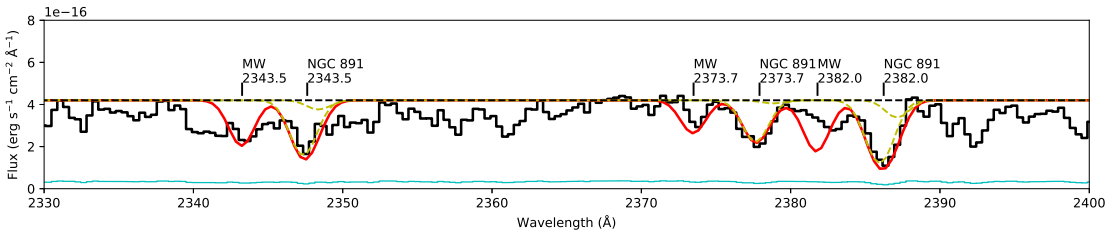

Figure 6.2: The Fe II lines from the FUV spectrum are projected onto the NUV spectrum. The continuum level is set to be a constant at 4.2×10^{-16} erg s^{-1} cm^{-2} Å^{-1}. The solid red line is the projected Fe II using the measurements from the FUV band, while the dashed yellow lines are the major absorption component and the HVC of NGC 891. The NGC 891 Fe II line strengths are consistent between the FUV and the NUV spectra, while the MW Fe II may be affected by fixed pattern noises.

the Fe II measurement from COS is $\log N = 15.10 \pm 0.04$. The Fe II in the STIS spectrum is measured from the line λ2343.5 Å, since two other lines (λ2373.7 Å and λ2382.0 Å) are completely blended with the Galactic Fe II lines. However, the line λ2343.5 Å is also partially blended with the Galactic line. Therefore, we adopt the measurements from the COS/FUV spectrum, which is supported by the matched and separated COS/FUV and COS/NUV spectral lines (Fig. 6.1 and Fig. 6.2).

We update the measurements of Mg I with accurate dynamic information from the high resolution FUV spectrum. Mg I is an isolated line in STIS spectrum with a velocity of $v = -43 \pm 79$ km s^{-1}, which is consistent with lines from N I, C I, and C II*. These ions should be cospatial, considering the major contributor of C I, N I, and Mg I is the neutral phase, and C II* traces the high density gas that is also more neutral than other ions (e.g., C II or Fe II). Therefore, we assume the Mg I also has a b factor of 33 km s^{-1} (the thermal broadening is ignored, which is less than 10 km s^{-1}), which is the b factor from C II* and N I. The C I b factor is not preferred because C I is at a low significance ($< 3\sigma$) leading to a large uncertainty. Then, the Mg I column density is determined to be $\log N = 12.76 \pm 0.24$.

The Doppler b factor of Mg II should be similar to Fe II, Ni II, etc., which have

b factors around 55 km s^{-1}. This b factor is consistent with the previously assumed value of 56 km s^{-1} from the width of the H I 21 cm line (Bregman et al., 2013). However, Bregman et al. (2013) determined the Mg II column density using only the line at Mg II λ2802.7 Å ($\log N = 15.48^{+0.36}_{-0.27}$). For the Mg II λ2795.5. Å line, we measured $\log N = 15.3^{+1.2}_{-0.9}$ (EW $= 2.31 \pm 0.61$ Å assuming $b = 55$ km s^{-1}). There are two undetectable Mg II lines λ1239.9 Å and λ1240.4 Å in COS/FUV spectrum, so we also obtain constraints from these two lines. Using the limiting EW of 12.0 mÅ (1σ), the upper limit of the Mg II column density is $\log N = 15.5$ (2σ) or $\log N = 15.1$ (1σ). Therefore, we prefer the measurement from the Mg II λ2795.5. Å line, and adopt $\log N = 15.3 \pm 0.3$ for the Mg II column density.

6.2.1.4 The H I 21 cm Line

The MW H I 21 cm line is obtained from the Leiden/Argentine/Bonn (LAB) Survey of Galactic H I with an effective beam size of 0.2° around the QSO (Kalberla et al., 2005). The H I 21 cm line data of NGC 891 is from Oosterloo et al. (2007), and extracted around the QSO with a beam size of $< 1.0'$. Both H I 21 cm lines show multiple components, and we fit the spectra using Gaussian functions, shown in Fig. 6.3 and Table 6.2.

For NGC 891, there are two high velocity clouds shown in the H I 21 cm line: -88 km s^{-1} and $+114$ km s^{-1}. The component at $+114$ km s^{-1} is observed in multiple ions, while the HVC at -88 km s^{-1} is only probably detected in Si IV with a velocity difference of ≈ 20 km s^{-1} ($> 2\sigma$). Therefore, we do not consider this component as a separate HVC in the following analysis. The NGC 891 absorption system is divided into two components – the major component at $v = -30$ km s^{-1} and the HVC at $v = +100$ km s^{-1}. The summation of the three low-velocity components leads to a total H I column density of $\log N = 20.06 \pm 0.08$. For the HVC at 110 km s^{-1}, the H I column density is $\log N = 19.08 \pm 0.09$.

Table 6.2: H I 21 cm Line Fitting Results

$\log N$	σ_N	b	σ_b	v	σ_v
MW (LQAC 035+042 003)					
20.32	0.01	27.49	0.62	-24.50	0.87
20.35	0.01	13.11	0.23	-3.34	0.15
19.24	0.01	1.29	0.05	0.53	0.02
20.22	0.01	5.71	0.08	1.64	0.06
19.16	0.02	1.52	0.08	5.15	0.04
NGC 891					
19.05	0.10	10.9	2.4	-88.7	1.6
19.82	0.06	30.5	4.1	-27.4	3.0
19.58	0.10	20.5	2.9	19.0	2.6
19.08	0.09	12.6	2.6	114.7	1.9
MW (3C 66A)					
19.65	0.13	40.93	4.30	-37.39	4.66
20.13	0.02	17.20	0.76	-34.64	0.42
19.70	0.02	6.13	0.21	-19.53	0.12
20.58	0.01	12.02	0.12	-2.26	0.08
19.56	0.03	2.34	0.11	-0.25	0.16
20.14	0.01	2.56	0.04	3.07	0.06

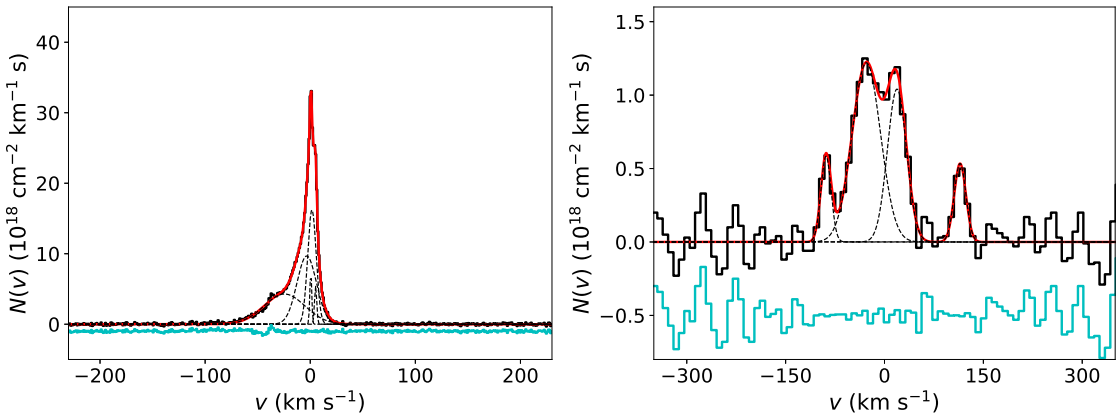

Figure 6.3: The H I 21 cm line fitting results for both the MW (*left panel*) and NGC 891 (*right panel*). Each line is fitted by five (MW) / four (NGC 891) Gaussian components and results are shown in Table 6.2. The data and the fit are shown in the black and red solid lines respectively, while individual components are shown in the black dashed lines. The cyan lines are the residuals shifted by -1×10^{18} cm^{-2} km^{-1} s for the MW and -5×10^{17} cm^{-2} km^{-1} s for NGC 891.

We examine whether the 21 cm line is consistent with the FUV Lyα absorption feature to exclude a possible contamination within the radio beam. The FUV spectrum should be aligned with the H I 21 cm line spectrum, since the COS/FUV spectrum may have a velocity shift up to ≈ 30 km s^{-1} (Wakker et al., 2015). We employ galactic Si III, C I, and C II* lines to do this alignment, since N I may be affected by geocoronal emission. The mean velocity in the FUV spectrum is -16.3 km s^{-1} (13.7 km s^{-1} at $z = -0.0001$), while the peak of the H I 21 cm line is approximately 1.6 km s^{-1}. Therefore, the velocity difference is 17.9 km s^{-1} and the corrected velocities are reported in Table 6.1. Here, the LAB H I 21 cm lines are in the local standard of rest frame, while other spectra are in the heliocentric frame. The difference between these two frames is a constant (1.4 km s^{-1}) over different wavelengths. Applying the velocity shift of 17.9 km s^{-1}, we correct the COS/FUV wavelength calibration, and convert the COS/FUV spectrum into the local standard of rest frame.

In Fig. 6.4, we project the fitted H I from 21 cm lines into the Lyα absorption including the velocity shift. The two components of NGC 891 are plotted separately and the QSO continuum is fitted by a second order polynomial function within $1190-1250$ Å. Against the Lyα wing, other absorption features occurs, so we compare the projected Lyα shape with the continua at $\lesssim 1208$ Å and $\gtrsim 1220$ Å. The red wing of the Lyα ($\lesssim 1224$ Å) matches with the H I 21 cm line projection, while in the blue wing ($\lesssim 1208$ Å), the continuum region around 1205 Å shows consistency between the UV and radio observations. Therefore, we suggest that the average H I in the radio beam is consistent with the FUV Lyα absorption lines.

6.2.2 3C 66A

6.2.2.1 The AGN

3C 66A is a BL Lac AGN at RA = 02h22m39.6s and DEC = +43°02′08″ with the redshift of $z = 0.444$, which is 41.2′ away from the galactic center of NGC 891. This

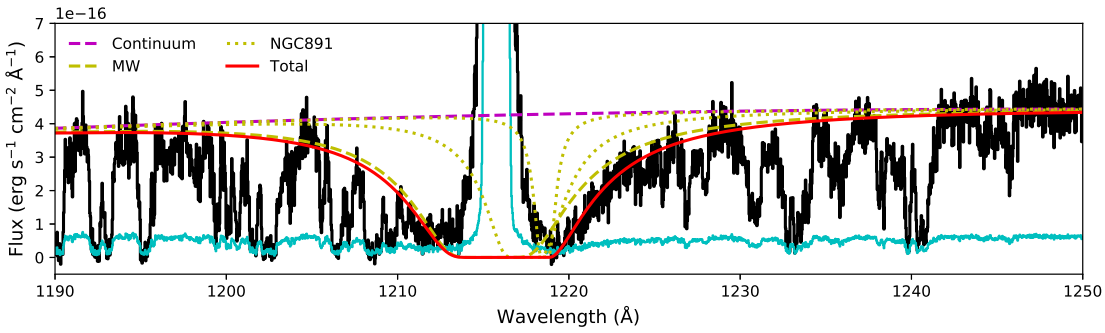

Figure 6.4: The projected Lyα absorption feature. The MW component (the dashed yellow line) is the summation of four Gaussian components fitted to the H I 21 cm line. The NGC 891 contribution is divided into the two components: the major absorption at $v = -30$ km s^{-1} (the broad component in the dotted yellow lines); and the HVC at +100 km s^{-1} (the narrow component). The continuum (the magenta dashed line) is a second order polynomial function. The total model (the red solid line) matches the wing feature of the observed Lyα.

AGN is close to the major axis of NGC 891, which is offset from the position angle of the major axis by 21.8° (clockwise) north of the disk and is in the same side as the QSO LQAC 035+042 003. The impact parameter of this sightline is 108.3 kpc and it is 18.4 kpc above the disk mid-plane.

6.2.2.2 The *HST*/COS Spectrum

The COS spectra of 3C 66A were observed in the *HST* program 12612 (1 Nov 2012; PI: Stocke) and 12863 (8 Nov 2012; PI: Furniss). The total exposure times are 12.6 ks for the G130M and 7.2 ks for the G160M. Using the data reduction processes similar to LQAC 035+042 003, we coadd the COS spectra for 3C 66A. The coadded spectra have median S/N values of 25 for the G130M and 15 for the G160M.

The line list is available in Danforth et al. (2016); therefore, we focus on the absorption system associated with NGC 891. The measured line properties are listed in Table 6.1, while the best-fit models are shown in Fig. 6.5. Our measurements are all consistent with Danforth et al. (2016), except for the detectable C II in our

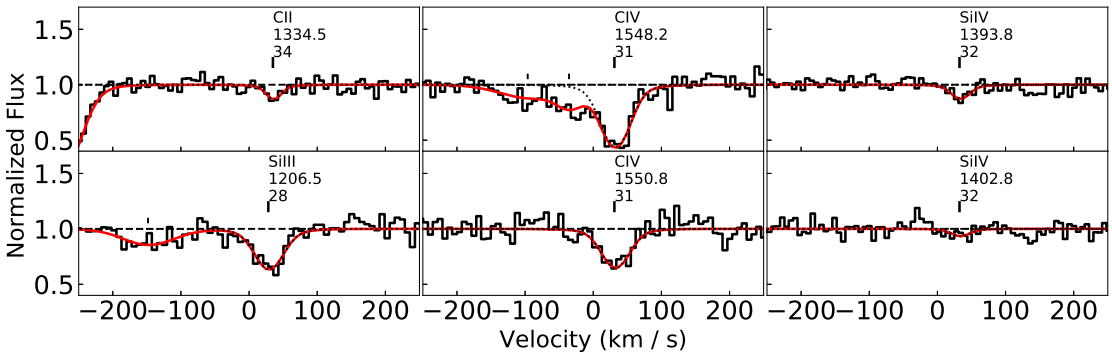

Figure 6.5: The spectra and best-fit models for identified lines toward 3C 66A and near the systemic velocity of NGC 891. The red solid lines are the total model for all identified lines, while the black solid lines are spectral lines associated with NGC 891.

spectrum with a significance of 3.4σ. For these weak features, it is possible that the coadd process could affect the completeness.

We also measure the upper limit for Si II of $\log N < 11.90$ at 2σ, which is obtained from the line Si II λ1260.4 Å assuming $b = 20$ km s^{-1} (similar to Si III).

6.2.2.3 The H I 21 cm Line

The MW H I 21 cm line spectrum is also from the LAB survey. Following the previous steps, we fit the H I 21 cm line and project the shape into the Lyα feature. The fitting results are shown in Table 6.2. The projected Lyα agrees with the FUV spectrum, and there are no obvious components due to the NGC 891 absorption features, which gives an upper limit of $\log N(\mathrm{HI}) < 19.5$ at the 2σ level.

Again, we obtain a velocity of -19.7 km s^{-1} at $z = 0.0$ for the 3C 66A FUV spectrum using the Galactic N I and O I lines, and a shift of 22.8 km s^{-1} between the FUV spectrum and the H I 21 cm line.

6.3 Model

Based on the measured ion column densities, we estimate the ionization parameter, the gas temperature, and the metallicity in the ionization equilibrium model with the photoionization modification. The density of the absorption system with $v = -30$ km s^{-1} can be derived separately from the density sensitive line C II* λ1335.7 Å.

6.3.1 The Low Velocity System at $v = -30$ km s^{-1} toward LQAC 035+042 003

6.3.1.1 The Photoionization Model

To build the photoionization model, we employ the photoionization code Cloudy (version 17.00; Ferland et al. 2013). Due to the proximity to the galactic center of NGC 891, the radiation originating from the galaxy disk cannot be ignored during the calculation. Therefore, the incident field should be the summation of the universal ultraviolet background (UVB) and the escaping light from the disk. However, the escaping light is difficult to determine and there is no published radiation field of NGC 891. We assume the escaping light has the same shape of the UVB at low energies, where the observed low ionization state ions of NGC 891 occur. Then, although the incident field is more intense than the UVB, we can use the UVB-only field to determine the ionization parameter. In this case, we adopt the UVB at $z = 0.0$ from Haardt & Madau (2012) in the following calculation to set the shape of the incident field. The uncertainty of this assumption is discussed in Section 3.1.3.

In the Cloudy model, we fix the neutral hydrogen column density to the measured value from the H I 21 cm line (i.e., $\log N = 20.06$), and the metallicity is fixed to the solar metallicity (Asplund et al., 2009). We explore the parameter space for the density of $\log n_{\rm H} = -5.0$ to -1.5 (roughly ionization parameter $\log U = -1.5$ to -5.0) and the temperature of $\log T = 3.4$ to 4.4.

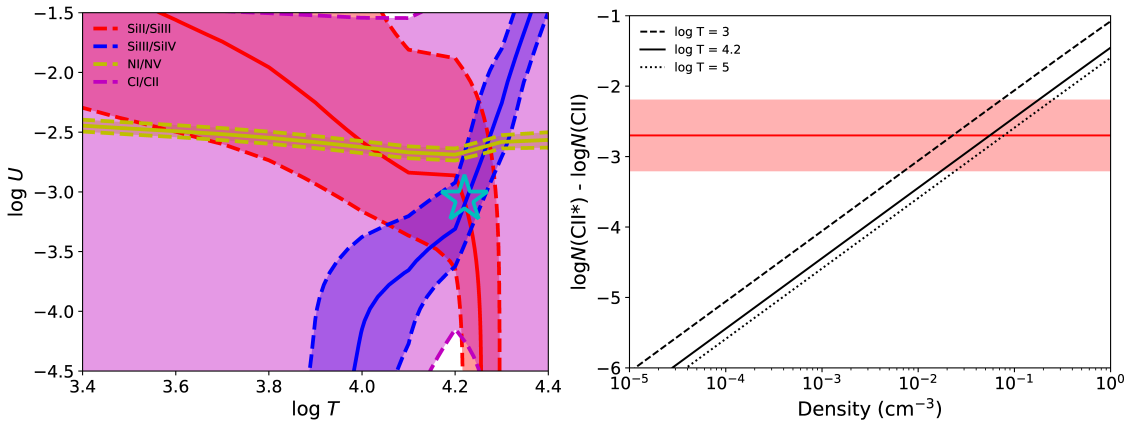

Figure 6.6: *Left panel:* the photoionization model of the $v = -30$ km s^{-1} system. The shadowed belts are the acceptable regions (1σ) for each ion column density ratio. The open cyan star is the preferred solution of $\log U = -3.06 \pm 0.10$ and $\log T = 4.22 \pm 0.04$. *Right panel:* the density measurement from the C II*/C II ratio. The colored bar is the 1σ uncertainty of the observed C II*/C II ratio, while the black lines are the CHIANTI predictions at different $\log T$ of 3.0 (dashed), 4.2 (solid) and 5 (dotted).

Using the different ionization state ions from one element, one can obtain the constraints on the ionization parameter and the temperature without involving element abundances. As shown in Fig. 6.6, we consider three elements: silicon, carbon and nitrogen, which have two or more observed ions. Silicon has three consecutive ions, which could give a best solution for the gas phase properties. Adopting measurements from the Voigt profile fitting, we obtain $\log U = -3.06 \pm 0.10$ ($\log n_{\rm H} = -3.44 \pm 0.10$) and $\log T = 4.22 \pm 0.04$. This solution has a weak dependence on the metallicity; therefore, we use the solar metallicity in our model (Asplund et al., 2009), since NGC 891 is similar to the MW.

Besides this solution, we also build a Markov chain Monte Carlo (MCMC) model to constrain the properties using the lower limits of Si II and Si III. In this model, we follow the method in Fumagalli et al. (2016), adopting the Gaussian function as the likelihood for good measurements (i.e., Si IV), and a rescaled cumulative distribution function for lower limits (i.e., Si II and Si III). We employed *emcee* to sample the

parameter space with 100 walkers and 500 steps, and the first 50 steps are masked out as the thermalization stage (Foreman-Mackey et al., 2013). The final solution is similar to the solution using Voigt fitting results, but with larger uncertainties. As shown in Fig. 6.7, the gas properties are $\log U = -3.14^{+0.07}_{-0.12}$ ($\log n_{\rm H} = -3.36^{+0.12}_{-0.07}$), $\log T = 4.25^{+0.08}_{-0.15}$, and $\log N_{\rm H} = 20.06^{+0.08}_{-0.08}$. There are two reasons for the larger uncertainty: the inclusion of the H I uncertainty in the model; and the lower limits of Si II and Si III. In the ratio-matched model, the H I column density is fixed as a constant, while in the MCMC model, the variation of H I column density could lead to a larger uncertainty. Compared to the measurements with two-sided constraints, only using the lower limits softens the constraints. The reason for the similarity between the two models is because the acceptable parameter space is determined by the lower limit of the Si III column density and the Si IV column density. The measurements of Si IV set a strong constraint of the temperature of $\log T < 4.4$ as shown by the sharp turnover in Fig. 6.7, which is due to the ionization fraction peak of Si IV (the parameter space can extend to $\log T = 5$). The lower limit of Si III leads to a lower limit of the temperature; therefore, the temperature can be determined well. In the MCMC solution, the predicted column densities of these ions has a systematic difference compared to the ratio-matched model. The MCMC model predicts higher column densities by $0.1 - 0.3$ dex for 11/13 metal ions, except for two relatively high ionization state ions (Si IV and N V). This systematic difference occurs because this model predicts a higher H II column density ($\log N = 21.01$ compared to 20.68). With a difference of 0.3 dex, both models predict that the major absorption system is dominated by the ionized gases, which is about $5 - 10$ times more massive than the H I gases.

The ratio between C I and C II has a large uncertainty due to the uncertain C II measurement. Therefore, we only check the consistency between the C II line and the model prediction. Applying the C I to C II ratio of the preferred solution from

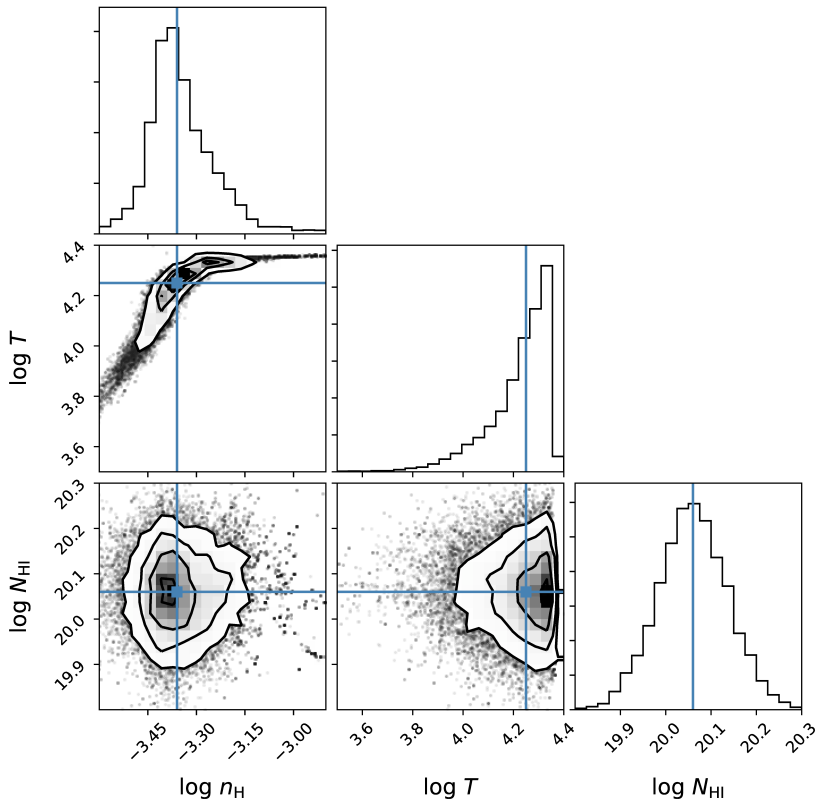

Figure 6.7: The marginalized posterior distributions in MCMC model for the major absorption system at $v \approx 30$ km s^{-1}. The cyan lines indicate the medians for all parameters.

the silicon ions, the predicted C II column density is $\log N = 16.8$. Direct Voigt profile fitting to the C II line leads to $\log N = 16.4 \pm 0.5$ and $b = 53 \pm 8$ km s^{-1} with a total $\chi^2 = 292.6$ and a degree of freedom (dof) of 256. By fixing the b factor at 47 km s^{-1}, the corresponding column density is $\log N = 16.8$ with $\chi^2 = 293.1$, which only increases the χ^2 by 0.5. Therefore, the predictions from the preferred model are consistent with the C II observation.

The ratio between N I and N V is not consistent the preferred solution, as the N V column density is too high, which indicates that N V is not in the same phase as low ionization state ions. The N IV to N V ionization potential, 77.5 eV, is twice the ionization potential from Si III to Si IV (33.5 eV; the second highest potential among detected ions). Therefore, we suggest that N V is not produced in the same

phase of the low ionization state gas.

In the preferred model ($\log U = -3.06$ and $\log T = 4.22$), the total hydrogen column density $\log N = 20.81$. By comparing the model column densities with the observed ion column densities, we calculate the residuals for different ions, which indicates the element abundances. The results are summarized in the Table 6.3. For each element, the relative abundance is calculated as the average value for all ions belonging to the element. The uncertainty of the abundance is affected by two factors – the uncertainty of the photoionization model (assumed to be $\sigma_{\rm PI} = 0.2$ dex) and the observed uncertainty of the total column densities for one element (σ_N). The total uncertainty is $\sigma_{\rm [X/H]} = (\sigma_{\rm PI}^2 + \sigma_N^2)^{1/2}$. For magnesium, the uncertainty is the scatter between the measurement of Mg I and Mg II. As stated previously, we noticed that there is a systematic difference for the column densities of metal ions between the ratio-matched model and the MCMC model, which is mainly due to the higher hydrogen column density in the MCMC model. This difference in column densities leads to a systematic difference of the absolute abundances (related to hydrogen) for the metal elements. This bias is proportional to the total hydrogen column, so it is affected by the H I and H II ratio. Based on our modeling, we found that this ratio is about 5, but could have variation of a factor of 2. Therefore, the absolute metallicity has an uncertainty of 0.3 dex. However, this abundance bias will not affect the relative abundance between metal elements, which indicates that the abundance pattern between metals is relatively robust.

The median metallicity of the three volatiles (C, N, and S) is [X/H] $= -0.3$. Relative to this value, we can see whether the refractory elements have the same metallicity or are lower. This may occur due to depletion onto grains, where Sembach & Savage (1996) show the relative depletions for different types of clouds, including warm diffuse halo clouds. In such clouds, they show that Fe and Ni are depleted (relative to S) by about -0.57 and -0.77 dex, with a range of about 0.1 (after

Table 6.3: Photoionization Model and Metallicity

Ion	$\log N$ obs.	σ_N dex	$\log N$ Ratio	$\log N$ MCMC	[X/H][a] Ion	[X/H][a] Element
H I	20.06	0.10	20.06	20.06	...	...
H II	...	...	20.68	21.01	...	...
C I	13.76	0.17	14.04	14.49	-0.28	-0.3 ± 0.5[b]
C II	15.8	$>$	17.15	17.43	...	
N I	15.71	0.10	15.91	16.02	-0.20	-0.2 ± 0.2
N V	13.97	0.10	13.07	12.86	0.90[c]	
Mg I	12.76	0.24	14.03	14.32	-1.27	-0.9 ± 0.4
Mg II	15.3	0.3	15.86	16.13	-0.6	
Si II	14.8	$>$	16.13	16.34	...	-0.7 ± 0.2
Si III	14.7	$>$	15.79	16.12	...	
Si IV	14.11	0.04	14.80	14.69	-0.69	
P II	13.76	0.09	14.13	14.41	-0.37	-0.4 ± 0.2
S II	15.33	0.02	15.73	16.06	-0.40	-0.4 ± 0.2
Fe II	15.10	0.04	15.88	15.96	-0.78	-0.8 ± 0.2
Ni II	14.19	0.06	14.97	15.24	-0.78	-0.8 ± 0.2

[a] The relative abundances of the ions are calculated using the ratio-matched model. The uncertainty in the photoionization model is assumed to be 0.2 dex.
[b] The abundance of carbon is derived from C I, but the carbon amount is dominated by C II. Therefore, we use the uncertainty from the C II fitting.
[c] N V is not from the same phase of the N I, so we ignore this ion when calculating the nitrogen abundance.

their Fig. 6). We find a similar relative depletion (Table 3) of -0.5 ± 0.1. The relative depletions given by Sembach & Savage (1996) are less for Si (-0.18) and Mg (-0.42) and are consistent with our relative abundance differences of -0.4 ± 0.2 (Si) and-0.6 ± 0.3 (Mg). We conclude that the our absorption line system is similar to warm diffuse Galactic clouds where depletion affects the refractory elements. The depletion-corrected metallicity appears to be about [X/H] $= -0.3 \pm 0.3$.

6.3.1.2 C II Density Sensitive Line

The C II* λ1335.7 Å is absorbed from an excited level, which means the gas density should be high enough to collisionally populate the lower level. Therefore, the strength of this line can be used to determine the density. In collisional ionization equilibrium (CIE),

$$\frac{N(\text{C II}*)}{N(\text{C II})} = \frac{n_\text{e} k_{01}}{n_\text{e} k_{10} + A_{10}}, \tag{6.1}$$

where k_{01} and k_{10} are the upward and downward collisional rate coefficients, and A_{10} is the spontaneous decay rate. Then, the C II*/C II ratio has a dependence on the density (n_e) and the temperature (the temperature is in the terms k_{01} and k_{10}).

We used the atomic data from CHIANTI to calculate the level populations at different temperatures and densities (Del Zanna et al., 2015). Since the C II* cannot be photoionized, radiation transfer is ignored and the ratio between level populations in CIE is the observed column density ratio (Fig. 6.6).

Since the C II column density cannot be well constrained, we adopt the prediction of the photoionization model as $\log N = 16.8$, and the uncertainty is adopted from the direct Voigt profile fitting as 0.5 dex. With the C II* column $\log N = 14.14 \pm 0.04$, the adopted $\log N(\text{CII})/N(\text{CII})$ ratio is -2.7 ± 0.5. As described in the last section, the preferred temperature is $\log T = 4.22 \pm 0.04$, so the expected density is $\log n_\text{H} = -1.26 \pm 0.51$.

Combined with the ionization parameter derived from the photoionization model,

the strength of the incident field is determined to be 150 times larger than the UVB. This value is consistent with the escaping light at 5 kpc for the MW, which is derived from the OB stars (Fox et al., 2005).

In summary, we find that the absorption system at $v = -30$ km s^{-1} has a density of $\log n_{\rm H} = -1.26 \pm 0.51$, and the fixed-temperature photoionization model suggests a temperature of $\log T = 4.22 \pm 0.04$ and a total hydrogen column density of $\log N_{\rm H} = 20.81 \pm 0.20$. Then, the path length of the absorbing gas is $3.8^{+8.5}_{-2.6}$ kpc combining the measured density and the model hydrogen column density.

6.3.1.3 Uncertainties in the Photoionization Model

We made several assumptions to build the photoionization model, which may lead to uncertainties of the derived physical parameters. First, we assumed that the H I column density from the 21 cm line corresponds to the UV absorption system, although the UV line of sight is a pencil beam while the H I emission is from an approximately $1'$ beam. If the gas is rotating, the two components around 0 km s^{-1} seen in the H I 21 cm line are from different sides of the minor axis, while the UV absorption features will only show one component in the red or blue side. However, as discussed in the section 4.1, the line width is not dominated by the rotation, which indicates the line profiles should be similar at both sides of the minor axis. Also, Fig. 6.4 shows the H I 21 cm line is consistent with the Lyα feature.

Second, we assumed that the temperature is a constant, ignoring the radiation transfer. In our model, we varied the temperature rather than adopting the photoionization temperature from the Cloudy calculation because of two reasons. First, The photoionization temperature in the our model is incorrect, where we employ the UVB to obtain the ionization parameter, and increase the density and the incident field correspondingly to account for the escaping flux. This increase could keep the same ionization parameter, but will break the balance between the cooling and the

heating, which have different dependence on the density. Therefore, the calculated photoionization temperature in our model is not the true temperature when we correct the escaping flux. Second, as discussed in Section 4.1, the dynamics of this gas is dominated by the turbulence or the outflow, which indicates the gas is not in a quiescent state. These mechanisms introduce additional heating sources (e.g., the shocks), which raises the photoionization temperature. Therefore, in our model, the temperature is a variable that need to be inferred.

Third, we assumed that the shape of the incident radiation field could be approximated by the cosmic UVB. For NGC 891, although the spectrum of the escaping light is not known, studies of the diffuse ionized gas indicate that the expected incident field is more intense and harder than from the MW, shown by the high helium ionization fraction ($\approx 70\%$) and the high [Ne III]/[Ne II] ratio (Rand, 1997; Rand et al., 2008). Therefore, the escaping flux of NGC 891 may be different from the UVB, since the MW escaping light has a similar shape to the UVB (Fox et al., 2005).

Here, we consider whether the variation of the incident light can affect our modeling of low ionization state ions. The ionization fraction is dominated by the temperature and the incident field strength near the ionization potential. For low and intermediate ionization state ions (lower than Si IV), the escaping light should have a similar shape (at low energies) to the UVB, which is dominated by star light. Modeling of the NGC 891 diffuse ionized halo also suggested that low ionization metal lines (lower than Ne III; 63 eV) can be modeled by a photoionization model with escaping star light (Rand et al., 2008). The temperature in our model is not adopted from the photoionization model, thus, it is not affected by the incident field. Therefore, we suggest that our modeling should not be affected significantly by the variation of the incident field shape with the similar low energy radiation.

The shape of the UVB also leads to variations in the metallicity (Zahedy et al., 2019). This is mainly affected by the relative radiation strength between HI and metal

ions. Roughly, the UVB shapes are approximated as power laws with a constant slope at low energies (lower than Si IV) in different UVB models (Haardt & Madau, 2012; Khaire & Srianand, 2015). Therefore, the uncertainty of the slope leads to biases of relative abundance measurements for different elements in one system. The absolute abundances could be increased or decreased systematically, while the relative abundances between metals should not change significantly.

6.3.2 The High Velocity Cloud at $v = 100$ km s^{-1} toward LQAC 035+042 003

We built a pure photoionization model with $Z = Z_{\odot}$ for this HVC using the UVB-only radiation field. The H I column density is adopted for the $v = 114$ km s^{-1} component, while UV ions are around $v = 90 - 110$ km s^{-1}. As shown in Fig. 6.8, we find a solution with $\log n_{\rm H} = -3.0 \pm 0.3$ ($\log U = -3.4 \pm 0.3$), which is determined by the three silicon ions. This solution is driven mainly due to the overlap between the lower limit of Si III and the upper limits of Si II and Si IV. Therefore, the Si III uncertainty caused by the AGN outflow Ne VI will not affect the photoionization model. In this model, the metal abundances are [C/H] $= -1.9$, [Si/H] $= -1.4$ and [Fe/H] $= -1.1$. The total hydrogen column density is $\log N_{\rm H} = 19.71 \pm 0.36$.

The upper limit of C II* is $\log N < 13.2$ for a 2σ constraint assuming $b = 20$ km s^{-1}. This implies a density of $\log n_{\rm H} < 1$ cm^{-3}, which is much larger than the preferred density in the photoionization model. Similar to the absorption system at $v = -30$ km s^{-1}, the incident radiation field is larger than the UVB-only field. Assuming the incident field is 10 times larger, the density will be 10 times larger correspondingly, hence the path length will also be 10 times smaller ($1.7^{+2.5}_{-1.0}$ kpc). From Section 6.3.1, it is known that the star light is 150 times more intense than the UVB at 5 kpc. A 10 times larger incident field would imply a distance of 19 kpc assuming the radiation is isotropic in all directions. If the distance is 10 kpc (typical distances

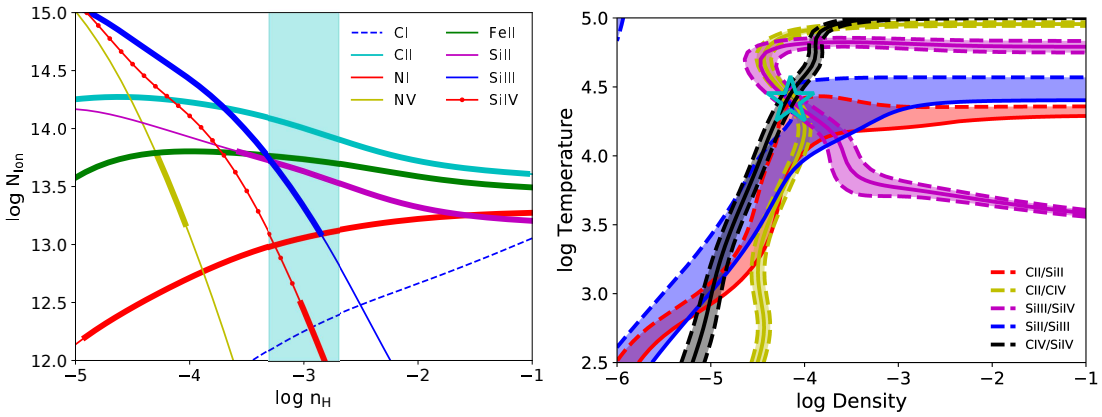

Figure 6.8: *Left panel*: the photoionization model of the HVC at $v = +100$ km s^{-1} with $Z = Z_{\odot}$. The Si IV and N I are upper limit measurements, while the others are detections. The model prediction is in the thin line, while the thick line is the observation constraint. Most ions can be reproduced in the phase of $\log n_{\rm H} = -3.0$. In this model, the relative abundances are [C/H] $= -1.9$, [Si/H] $= -1.3$ and [Fe/H] $= -1.1$. *Right panel*: the solution for the system toward 3C 66A without radiation transfer. The solution is $\log T = 4.40 \pm 0.05$ and $\log n_{\rm H} = -4.15 \pm 0.05$. The solution with radiation transfer agrees with this solution, so this is the final solution for this system. The relative abundance between carbon and silicon are solar (Asplund et al., 2009). Since the Si II column density only has a upper limit, the uncertainty is one-sided. The colored regions are the 1σ uncertainty regions.

for the MW's HVCs; Wakker et al. 2008), the path length will be $0.45^{+0.67}_{-0.27}$ kpc.

In the preferred model, most of the detected ions and the upper limit measurements are reproduced in the same phase, except for C I and N V. The very weak C I ($\approx 2\sigma$) cannot be in the same phase as the much stronger line of C II. Also, the velocity of C I (81 km s^{-1}) is ≈ 20 km s^{-1} offset from the mean velocity of other ions (100 km s^{-1}), which is a $\approx 2\sigma$ difference. Therefore, we suggest that the offset C I at $v = 81$ km s^{-1} might be contaminated by other systems (e.g., a weak Lyα system). The high ionization state ion N V is not in the same phase of the low ionization state ions (i.e., lower than Si IV) and may be related to cooling or mixing between the hot X-ray gas and the warm component.

Table 6.4: Ionization Models for the 3C 66A System

Ion	$\log N$ obs.	σ_N dex	$\log N_{\rm m}$ OS13	$\log N_{\rm m}$ [Z/H] = 0	$\log N_{\rm m}$ [Z/H] = −2
H I	19.5	<	14.91	14.92	16.84
C II	13.03	0.11	13.03	13.02	13.00
C IV	13.79	0.03	13.81	13.81	13.78
Si II	11.9	<	11.50	11.42	11.39
Si III	12.70	0.05	12.79	12.71	12.69
Si IV	12.45	0.10	12.53	12.55	12.54

6.3.3 The Cloud at $v = 30$ km s^{-1} toward 3C 66A

For this system, the Cloudy model is not well-constrained, since there are no precise measurements on the H I column density. Therefore, we try to find a solution, initially ignoring radiation transfer effects. The ionization fractions from Oppenheimer & Schaye (2013) are adopted, which include the UVB-only radiation and assume ionization equilibrium. As shown in the right panel of Fig. 6.8, the preferred solution is $\log T = 4.40 \pm 0.05$ and $\log n_{\rm H} = -4.15 \pm 0.05$. In this model, the required total hydrogen column density is $\log N = 18.06$ assuming solar metallicity.

Using these values, we run a Cloudy model to determine the effect of radiation transfer. In this model, we fix the metallicity at the solar metallicity, the temperature at $\log T = 4.40$, and the density at $\log n_{\rm H} = -4.15$. Adding the radiation transfer does not affect the predicted column densities of all ions (Table 6.4). We also consider a model with lower metallicity $Z = 0.01 Z_\odot$ (and $\log N({\rm H}) = 20.06$), which predicts a higher H I and similar column densities of other ions compared to the solar metallicity model.

The path length of this system varies from $5.26^{+0.64}_{-0.57}$ kpc to 526^{+64}_{-57} kpc for the metallicity of $Z_\odot$ to $0.01 Z_\odot$. Since the impact parameter is 108 kpc, the strength of the galaxy radiation field is about half of the UVB, adopting 150 times the UVB at 5 kpc (Section 3.1.2) and spherical symmetry. Then, the path length is reduced by a factor of 1.5 due to the increased incident field. The metallicity is unlikely to be as

low as $0.01Z_{\odot}$, which leads to a path length larger than the virial radius of NGC 891. If we adopt the extended hot gas metallicity of $0.14Z_{\odot}$ (Hodges-Kluck et al., 2018), the path length is around $20 - 40$ kpc.

6.4 Discussion

6.4.1 The Major System in LQAC 035+042 003

This work presented UV spectra toward a quasar (LQAC 035+042 003) that is projected behind the edge-on galaxy NGC 891 at a height of 5 kpc from the midplane and near the minor axis. A previous *HST*/STIS observation, with the G230L grating, detected absorption lines at the systemic redshift of NGC 891, notably from the ions Fe II and Mg II. The resolution of that observation was 400 km s^{-1} (FWHM) at 2400 Å. The COS FUV G130M spectrum presented here improves on the spectral resolution by about a factor of 25 (15 km s^{-1}), which has been crucial in identifying lines and resolving individual velocity components. Also, the COS spectrum includes lines from elements that are usually not strongly depleted onto grains (C, N, S) as well as elements that, under the right conditions, can be strongly depleted onto grains (Fe, Ni, Si). By measuring the abundance of this range of elements, we obtain the metallicity of the absorbing gas and the degree of depletion, which appears to be low.

Two absorption systems were identified toward LQAC 035+042 003, a broad set of lines from the warm ionized gaseous halo and a lower column cloud that is separated from the main emission by about 110 km s^{-1}, referred to here as the high velocity cloud (NGC 891 HVC). Columns for 13 ions are obtained for the primary absorption, and when modeled with CLOUDY, we obtain a consistent fit with $\log T = 4.22 \pm 0.04$, $\log n_{\rm H} = -1.25 \pm 0.51$, $\log N_{\rm H} = 20.81 \pm 0.20$, and a characteristic size for the absorbing region of ≈ 4 kpc. The metallicity was obtained for eight elements (Table 6.3).

For this warm gas, we obtained a metallicity of [X/H] $= -0.3 \pm 0.3$, which is higher

than that obtained from the X-ray emitting gas. The metallicity of the $kT = 0.2$ keV hot halo is $Z = 0.14^{+0.09}_{-0.04} Z_\odot$ ([X/H] $= -0.85$ for both O and Fe; Hodges-Kluck et al. 2018), about three times lower than the half solar ([X/H] $= -0.3$) that we find in the absorption system. These two metallicities differ at the 2 σ level, so the difference is significant. Metallicity values can be a tracer for the origin of the gas, and one might posit that a hot extended halo is lower metallicity than gas rising up from the disk, which should have a near-solar metallicity. Within this construct, we would identify the X-ray emitting gas as part of the hot extended halo that is accreting onto the galaxy disk. Then, the 10^4 K UV absorbing gas would be understood as a mixture of the disk gas and the hot X-ray emitting medium. Interaction and mixing between the two components has been proposed (Fraternali, 2017), although it is not clear whether this is a viable explanation in detail, as the hot halo mass ($\approx 2.4 \times 10^8\ M_\odot$; Hodges-Kluck & Bregman 2013; Hodges-Kluck et al. 2018) is about order of magnitude less than the neutral and warm ionized gas for scale height < 10 kpc.

The observed UV absorption system could have three origins: infall from beyond the virial radius; outflow from the disk; and a rotating disk. First, infall is not preferred due to the relatively high metallicity of $\approx 0.5 Z_\odot$. Then, to distinguish between outflow and a rotating disk, we consider the dynamical information from the H I 21 cm line and UV metal lines, since the dynamics of observed gases are dominated by the non-thermal broadening, as the thermal broadening at $\log T \approx 4.2$ is only around 16 km s^{-1}. The 21 cm line and the UV lines have similar velocity ranges, lying between -100 km s^{-1} and 50 km s^{-1}, and with b factors of ≈ 50 km s^{-1} (the single component fitting of H I line in Bregman et al. 2013 and Table 6.1). This favors the outflow model rather than the rotating disk. According to Oosterloo et al. (2007), the rotation curve at $z = 4.5$ kpc has a linear dependence on the radius until $R \approx 8$ kpc. With this rotation curve, the rotation velocity dispersion is small at a given projected radius, while the velocity offsets are different at different projected

radii. If the line widths are dominated by the rotation, the H I 21 cm line should have a larger b factor than the UV lines because of the lower spatial resolution (the large beam size) of radio observation. However, the opposite occurs. Therefore, we conclude that the velocity dispersion of this absorption system is non-thermal and not due to rotation, and an additional broadening mechanism is required to reproduce the observations around the galactic center. This is consistent with the studies of extended diffuse ionized gas (Boettcher et al., 2016), which showed the Hα emission line profile favors a ring model with an inner boundary of $\gtrsim 2$ kpc. However, current observation cannot uniquely identify the additional mechanism, which might be random turbulence or a biconical outflow. In the outflow model, the geometry has to be biconical to have the observed radial velocity, since outflows perpendicular to the disk will have a zero radial velocity for edge-on galaxies. Then, the line widths of different ions are mainly determined by the gas density distribution along the sightline (Fox et al., 2015; Savage et al., 2017).

The total hydrogen column is greater than the 21 cm HI column along the same direction, with the ratio being $N(\mathrm{HI}+\mathrm{HII})/N(\mathrm{HI}) = 5-10$. This result is driven by the relatively large columns of singly and doubly ionized elements, mainly C and Si. If the UV absorption system is from a turbulent gaseous disk, then this hydrogen ionization fraction can apply to the low halo material in general ($z < 10$ kpc), which means most of the gaseous mass in the halo is warm ionized gas. The H I halo gas mass is found to be $1.2 \times 10^9\ M_\odot$ (Oosterloo et al., 2007), which is an unusually high value for edge-on galaxies. The presence of this large amount of gas is already challenging to explain (Hodges-Kluck et al., 2018), which becomes worse if a factor of five increase in the mass applies to the whole halo ($\approx 6 \times 10^9\ M_\odot$). These warm gases ($\log T \approx 4$) will be accreted onto the disk. The accretion velocity is assumed to be $v_{\rm ac} = 100$ km s^{-1}, and the dynamical timescale will be about 4.9×10^7 yr at 5 kpc. Applying the factor of 5 to the H I mass, the accretion rate from the warm

gases is $1.2 \times 10^2 v_{100}^{\rm ac}$ $M_\odot$ yr^{-1}, where $v_{100}^{\rm ac}$ is the accretion velocity in the units of 100 km s^{-1}. This accretion rate is much higher than the current star formation rate (SFR) of NGC 891 (3.8 $M_\odot$ yr^{-1}; Popescu et al. 2004), and will likely elevate the star formation rate in the future, probably causing a disk-wide starburst event.

If this warm gas is a biconical outflow from the galactic center, the hydrogen ionization fraction can only apply to the gas around the galactic center. Then, the situation is more complicated, so no estimate can be derived for the accretion rate, but these warm gases cannot be buoyant. Therefore, it is more likely to be a galactic fountain that enhances the gaseous halo.

It is also of interest to consider whether the warm gas is in pressure balance with the hot X-ray emitting gas. Using the *XMM-Newton* and *Chandra* spectrum, the virialized hot halo has an approximate thermal pressure of $n_{\rm H}T = 2.5 \times 10^3$ cm^{-3} K assuming $n_{\rm H} = n_{\rm e}$ (Hodges-Kluck et al., 2018). Considering the filling factor, this value is the lower limit of the pressure, since the density is derived from the normalization parameter ($\int n_{\rm e} n_{\rm H} dV$). The modeling of the UV absorption system leads to a thermal pressure of $n_{\rm H}T = 0.9 \times 10^3$ cm^{-3} K. For the warm gas, the density is obtained from the density sensitive line, which is not affected by the volume filling factor. Therefore, there is a significant pressure difference between the warm and hot gases. This difference may be made up by involving other pressure terms, such as the turbulent pressure or the magnetic pressure, since the thermal pressure is found to be non-dominant in the MW interstellar medium (Cox, 2005).

6.4.2 The HVC in LQAC 035+042 003 – Cold Mode Accretion?

We detected an absorption system at $v = 640$ km s^{-1} (110 km s^{-1} relative to NGC 891), which is not necessarily a HVC of NGC 891. For completeness, it is worth noting that a galaxy group with the central galaxy of NGC 1023 ($v = 637$ km s^{-1}; de Vaucouleurs et al. 1991) is 0.85 Mpc away from LQAC 035+042 003 (Trentham &

Tully, 2009). Although this galaxy group is closer to the absorption system in velocity, we suggest that it is unlikely to be associated with the galaxy group, because the H I column is too high ($\log N > 19$) to be typical of the intragroup medium ($\log N \sim 14$; Stocke et al. 2014). Therefore, the absorption system at 640 km s^{-1} is associated with the galaxy NGC 891 rather than large structures beyond the NGC 891 halo.

The modeling of the HVC at 110 km s^{-1} indicates that it has a metallicity of [X/H] ≈ -1.5, which is lower than the main body of the absorbing gas ([X/H] $= -0.3$) and the X-ray emitting extended halo ([X/H] $= -0.85$). The low metallicity suggests that this gas is accreted from the intergalactic medium (IGM; Lehner et al. 2013; Wotta et al. 2016), or dwarf galaxies within the NGC 891 halo (e.g., UGC 1807; Mapelli et al. 2008). It may represent a cloud or filament due to the cold mode accretion (Kereš et al., 2009; Nelson et al., 2013).

Assuming this system is a spherical cloud, the mass of this HVC is $\log M/M_\odot = 5.8$ at a distance of 19 kpc (the radiation field is approximately 10 times the UVB at this radius) or $\log M/M_\odot = 4.6$ at 10 kpc. Then, the accretion rate from this cloud is around $6.8 \times 10^{-3} M_\odot$ yr^{-1} or $9.2 \times 10^{-4} M_\odot$ yr^{-1} assuming the infall velocity of 200 km s^{-1}. The number of such clouds within each radius is estimated assuming the volume filling factor of HVC is $\approx 2\%$ (Richter, 2012) which leads to 2.0×10^2 or 2.8×10^1 clouds within 10 kpc or 19 kpc. Finally, the accretion from the HVC is $0.2 M_\odot$ yr^{-1} in both cases, which is comparable with the measured accretion rate of the MW HVC ($0.08 M_\odot$ yr^{-1}; Putman et al. 2012). This values set an upper limit of the cold mode accretion rate, since not all of the HVCs have low metallicity. Another way to estimate the HVC mass of NGC 891 is by assuming the HVC has a covering factor of 50% within a radius of 10 kpc or 19 kpc. Then, the total mass of the HVC is $\log M = 8.1$ or $\log M = 8.7$ with the assumed radii, which is also comparable with the MW ($\log M = 7.9$; Putman et al. 2012)

In the MW, studies of sightlines towards the galactic center discovered that HVCs

are common (Fox et al., 2015; Savage et al., 2017). The metallicity measurements indicate the disk origin of these gases with [S/H] = 0.02 or [S/H] = 1.38 (Savage et al., 2017), which are consistent with the outflow from the disk. In the case of NGC 891, we found the HVC in LQAC 035+042 003 cannot be an outflow due to the low metallicity, but it is not clear whether this system is close to the galactic center. It is still possible that this system is at the edge of the NGC 891 disk with a small projected distance to the galactic center.

6.4.3 The Absorption System in 3C 66A

The 3C 66A sightline has an impact parameter of 108 kpc, roughly the major axis direction and 21.8° above the disk. This gas is modeled by a photoionization model, with $\log T = 4.40 \pm 0.05$ and $\log n_{\rm H} = -4.15 \pm 0.05$. Considering the escaping flux from NGC 891, the incident field can be boosted by a factor ≈ 1.5. Then the density is increased correspondingly, which leads to a pressure of $3-5$ cm^{-3} K, which is lower than the expected ambient gas pressure ($50 - 100$ cm^{-3} K) assuming the virial temperature ($\approx 10^6$ K) and the typical density (two hundred times the critical density; $n_{200} \approx 5 \times 10^{-5}$ cm^{-3}).

It is unknown whether this system is assigned to NGC 891, since there are several satellites with smaller projected distances to 3C 66A. GSC2.3 NCIA030805 is found to have a projected distance of 31.2 kpc from 3C 66A, and 95.5 kpc from NGC 891. A spectroscopic redshift is not available for this galaxy, but it is assigned to be in the NGC 891 group by its color (Schulz, 2014). Another dwarf galaxy is UGC 1807 (or GSC2.3 NBZ5012371), which is projected 59.8 kpc away from 3C 66A and 75.9 kpc from NGC 891. This galaxy is believed to be within the virial radius of NGC 891, based on leading interaction features on the H I disk (Mapelli et al., 2008).

The radial velocity (583 km s^{-1}) of the UV absorption system is opposite to the rotation of NGC 891. The gaseous halo is more likely to be co-rotating with the disk

out to the half of the virial radius (Ho et al., 2017). Therefore, this absorption system towards 3C 66 is unlikely to be a part of the extended co-rotating gaseous halo of NGC 891. Perhaps this gas was stripped from the nearby dwarf or it is accreting onto one of these galaxies from the near side.

6.5 Summary

We analyzed the *HST*/COS spectra to detect the gaseous components in the NGC 891 halo either close to the minor axis (LQAC 035+042 003) or further away along the major axis (3C 66A). Three absorption systems are detected in these two sightlines. Our results are summarized as:

- In the spectrum of LQAC 035+042 003, the primary absorption system near $v = -30$ km s^{-1} at $z = 0.001761$ is modeled as a gas with $\log T = 4.22 \pm 0.04$, $\log n_{\rm H} = -1.26 \pm 0.51$, and $\log N_{\rm H} = 20.81 \pm 0.20$. Abundances are measured for eight elements, showing a typical depletion pattern seen in the MW warm diffuse gas. The volatile elements (C, N, S) show a metallicity of [X/H] $= -0.3 \pm 0.3$, which suggests that the high-metallicity disk-originating gas is mixed with the virialized hot halo ($Z \approx 0.14 Z_{\odot}$) seen in the X-rays (Hodges-Kluck et al., 2018). This leads to a more massive warm gas disk than the H I disk from 21 cm emission, and along this sightline; the H/H I ratio is about 5 ± 1.

- The HVC in LQAC 035+042 003 is separated from the primary system by $\approx +110$ km s^{-1}, with $\log U = -3.4 \pm 0.3$ and the metallicity is lower than $0.1 Z_{\odot}$ with an average value of [X/H] $= -1.5$ for C, Si, and Fe. This is different from the HVC seen in the MW (about solar metallicity) around the galactic center (Savage et al., 2017), which are about the solar metallicity. Therefore, we suggest that this low metallicity HVC in NGC 891 is likely to be an accreted cloud from the more distant halo and has not mixed effectively with the hot

halo or the warm gas closer to the disk.

- The absorption system in the 3C 66A spectrum is suggested to be associated with a satellite around NGC 891 rather with NGC 891 itself, which is mainly because the velocity of this system is opposite to the rotational velocity of the H I disk.

CHAPTER VII

The Mass and Absorption Columns of Galactic Gaseous Halos

7.1 Introduction

Recently, more and more observational evidence has been found to show the importance of gaseous components (the circumgalactic medium; CGM) in galaxy halos (Anderson & Bregman 2010; Ménard et al. 2010; Werk et al. 2014; see the review of Tumlinson et al. 2017). These gaseous components surrounding the galaxy disk are formed during the galaxy formation and are modified by various feedback processes, such as stellar feedback and active galactic nucleus (AGN) feedback (White & Frenk, 1991). The existence of a CGM also modifies the evolution of the galaxy by providing fresh materials for star formation (Kereš et al., 2005; Sancisi et al., 2008; Kereš et al., 2009), and by heating materials accreted from the intergalactic medium (IGM) through the gravitational potential release and the accretion shock (Mo et al., 2010).

The existence of gaseous halos is also helpful to explain various observational issues, such as the missing baryon problem (the baryonic fraction is significantly lower than the cosmic baryonic fraction of 0.16; Dai et al. 2010; McGaugh & Schombert 2015; Planck Collaboration et al. 2016a). One solution is that the missing baryons stay in the galaxy but in an invisible phase (low density and high temperature), which

could be the hot gaseous halo (Fukugita & Peebles, 2006; Bregman & Lloyd-Davies, 2007). Theoretically, simulations found that the cool gas (10^4 K) in the early Universe ($z > 4$) is heated, becoming a warm-hot intergalactic medium ($10^5 - 10^7$ K) during galaxy formation, which accounts for more than 30% of total baryons (Weinberg et al., 1997; Cen & Ostriker, 1999).

The final temperature of these heating processes is about the virial temperature of the galaxy, which is determined by the galaxy halo mass. Massive galaxies have higher virial temperatures than low-mass galaxies, and the virial temperature of low-mass galaxies ($M_{\rm h} \sim 10^{11}\ M_{\odot}$) is around $10^{5.5}$ K, which is also the peak temperature of the radiative cooling curve and can lead to rapid cooling with a cooling timescale of < 1 Gyr. Therefore, whether the gaseous halo exists is a result of the competition between various heating processes and the radiative cooling, and this competition results in a multi-phase medium in the gaseous halo (Oppenheimer et al., 2016).

Multi-wavelength observations of both emission and absorption reveal different phase mediums in the gaseous halo. The hot components in the gaseous halo can be detected in emission by direct X-ray imaging (Anderson & Bregman, 2010; Bogdán et al., 2013a; Goulding et al., 2016; Li et al., 2016), and in absorption or emission from high ionization state ions (e.g., O VII, Ne VIII and Mg X; Nicastro et al. 2002; Savage et al. 2005; Miller & Bregman 2015; Qu & Bregman 2016). These studies found that the mass of the hot gaseous halo is comparable to the stellar mass of the galaxy, and about half of total baryons are still missing. Some studies show that the hot gas may account for all missing baryons in the Milky Way (MW; Gupta et al. 2012; Nicastro et al. 2016a), however, they overestimate the emission measurement by more than one order of magnitude (Bregman et al., 2018; Li et al., 2018a). Ultraviolet (UV) absorption line studies on low and intermediate ionization state ions show the existence of cool clouds in the halos, but the mass is model-dependent with a variation from 6% to 40% of the total baryon mass (Werk et al., 2014; Stern et al., 2016).

With a large amount of gas in the halo, radiative cooling may lead to a significant cooling flow onto the galaxy disk, which will be transformed into the stellar content of the disk through star formation (Sancisi et al., 2008). This astrophysical connection between the radiative cooling and the star formation suggests that the cooling rate and the star formation rate (SFR) should be comparable with each other. Although the net cooling rate is also modified by heating from galactic feedback or accretion from the IGM, observations showed that the cooling rate is approximately the SFR for star-forming galaxies (with large scatter; Li et al. 2014).

In this paper, our starting point is that the SFR is balanced by the radiative cooling rate of the gaseous halo within the cooling radius. Then, we employ a set of assumptions for the gaseous halo – the density profile, the temperature distribution, hydrostatic and ionization equilibrium, and build up a halo model to connect the properties of the gaseous halo (i.e., mass and ion column density) to other galaxy properties (i.e., stellar mass and star formation rate). The details of the model assumptions are described in Section 2. In Section 3, we present the mass and column density of the gaseous halos, and their dependence on model parameters (e.g., stellar mass, SFR, or metallicity). The comparison with observations and implications are discussed in Section 4; our results are summarized in Section 5.

7.2 Model

We consider a spherical volume-filling gaseous halo model to connect the galaxy properties with the gaseous halo properties. In this section, the employed assumptions will be described and discussed.

7.2.1 General Picture

During the formation of the galaxy, the accreted material is heated by the released gravitational potential through the accretion shock. Without radiative energy losses,

the final temperature of a gravitationally self-bound system is the virial temperature that is determined by the total mass. However, a realistic gaseous halo suffers from radiative cooling, which is crucial for the formation of galaxy disk.

Once the galaxy disk is formed, star formation leads to stellar feedback, injecting gas, dust, and energy into the gaseous halo. Stellar feedback affects the galaxy in several ways: stellar winds of massive stars; mass-loss of asymptotic giant branch stars; and supernovae from either massive stars or degenerate stars (Zaritsky et al., 1994; Willson, 2000; Scannapieco et al., 2008). Another main feedback channel is the central supermassive black halo that is in an active galactic nuclei (AGN) phase, which injects ionizing photons and high-energy particles (Fabian, 2012). These feedback processes can offset radiative cooling, or reheat the cooled gas (Li et al., 2015). Although these processes are poorly resolved and implemented with different subgrid models in cosmological simulations, their effects on the galaxy evolution have been confirmed showing that no single feedback channel can dominate across all galaxy masses (Vogelsberger et al., 2014; Schaye et al., 2015; **?**). However, the relative contributions for different processes are still controversial (**?**Suresh et al., 2017).

Besides the feedback from the galaxy disk, accretion from the IGM also provides additional energy to the gaseous halo as material falls deeper into the gravitational potential well. Then, the energy conservation of the gaseous halo leads to

$$L_{\rm net,cl} = L_{\rm rad} - L_{\rm net,acc} - L_{\rm fb}, \tag{7.1}$$

where symbols denote the net cooling, the radiative cooling, the net accretion heating and the feedback heating. For simplicity, we ignore the heating from the accretion of the IGM gas in our models, since the actual value of accretion heating depends on several uncertain factors – the accretion rate from IGM, the accretion shock process and the structure around the virial radius. However, an estimation shows that

the contribution from accretion heating is not significant when the hot gaseous halo already exists. Assuming the accreted material is virialized at the virial radius, the released gravitational potential energy is $2k_{\rm B}T_{\rm vir}$, which is slightly larger than the internal energy of the virialized halo of $3/2k_{\rm B}T_{\rm vir}$. Additionally, the energy to ionize electrons from atoms will increase the internal energy by several tens of eV per atom, which is equivalent to a temperature around $10^5 - 10^6$ K (depending on the ionization state that is proportional to the virial temperature). Therefore, the energy used to ionize atoms cannot be transformed into internal energy, which decreases the net heating from the IGM accretion. Finally, we consider the net cooling rate that is only related to the radiative cooling and the heating due to galactic feedback.

The net cooling flux is related to the accretion flow since the cooled gas cannot be buoyant in the halo due to the gravitational potential. Once the gas from the halo is accreted onto the disk, it will interact with the disk interstellar medium or outflows launched from the disk, which leads to the disruption of the cool gas and the condensation of the hot gas (Marinacci et al., 2010; Scannapieco & Brüggen, 2015). Additionally, various processes are involved in this interaction, such as the disk dynamics and the thermal conduction, which lead to complex situations in different galaxies (Oosterloo et al., 2007; Armillotta et al., 2016; Zheng et al., 2017). These phenomenon are beyond the scope of this paper, therefore, we assume that the accreted cold gas could be mixed with the existed ISM instantly to avoid detailed interactions between disk and halo gases.

Studies of the MW molecular clouds showed that the star formation timescale is comparable to the dynamical timescale of the cloud ($\sim 1 - 10$ Myr), and the star formation efficiency is less than 2% (Larson, 1981; Myers et al., 1986; Leroy et al., 2008). Considering the SFR of the MW as $\approx 1\ M_\odot\ {\rm yr}^{-1}$ (Robitaille & Whitney, 2010), around 100 $M_\odot\ {\rm yr}^{-1}$ gas should be transformed into the star-forming molecular clouds since the lifetime of molecular clouds is short ($\lesssim 20$ Myr ; Larson 1981, 1994). The

total atomic gas mass in the MW is around 7×10^9 $M_\odot$ (Nakanishi & Sofue, 2016), which means that the atomic gas will be refreshed in around 70 Myr. Therefore, the timescale is around several 10^7 yr to form stars using accreted cool gas from the gaseous halo. This timescale is comparable with the timescale of current measurement methods (i.e., UV/IR) of SFR for external galaxies, which measure the average SFR over 10^7 to 10^8 yr (Madau & Dickinson, 2014). In this sense, the measured net cooling flow mass has a physical connection with the measured SFR.

The cold mode accretion provides an additional gas origin besides the hot mode accretion (the radiative cooling and accretion of the virialized halo), which requires the density of at least one order of magnitude higher than n_{200} ($10^{-3}-10^{-4}$ cm^{-3}) and the low temperature (10^{4-5} K) for the gas to remain cool during the accretion (Kereš et al., 2005). The cold mode accretion leads to cool gas filaments in the halo, directly connecting the disk and the IGM and transporting gases into the disk (Kereš et al., 2009). However, the existence of a hot ambient halo ($T \approx T_{\rm vir}$) near hydrostatic equilibrium could destroy these cold gas filaments by the mixing and interaction, which makes the contribution from the cold mode accretion less than one-third of the hot mode in the low redshift universe ($z < 2$; Nelson et al. 2013). Therefore, involving cold mode accretion will not break the balance between the cooling flow and the star formation, so we adopt the assumption that the net cooling rate is equal to the SFR.

Feedback processes must the included, as they will offset some of the radiative cooling. For a star-forming galaxy without a merger, the gas for star formation is originally from the gaseous halo, and the accretion from a gaseous halo is modified by the strength of stellar feedback (i.e., proportional to the SFR) when the redshift is low. Therefore, for a galaxy dominated by stellar feedback (with a dim AGN or without an AGN), the stellar feedback strength is proportional to the radiative cooling rate, which can be modeled as $\dot{M}_{\rm stellar,h} = \alpha \dot{M}_{\rm rad,cl}$. Then, a simple relationship between

the SFR and the radiative cooling rate is

$$\mathrm{SFR} = \gamma \dot{M}_{\mathrm{rad,cl}}, \tag{7.2}$$

where $\gamma = 1 - \alpha$ is smaller than unity to account the heating by stellar feedback, and $\dot{M}_{\mathrm{rad,cl}}$ is the total radiative cooling rate of the gaseous halo. For simplicity, we assume that γ is unity for the following calculation; the effect of variations in this γ factor is discussed in Section 4.

This relationship will be broken by several physical processes, such as feedback from an AGN or a starburst event. For AGN feedback, there is no direct connection with the SFR, therefore, there is no direct relationship between AGN feedback heating and the radiative cooling. For merging galaxies that trigger starburst events, the connection between the SFR and the radiative cooling rate is not valid either, since the interaction between gases in the two galaxies triggers the star formation, which is not related to the gaseous halo cooling. Therefore, Equation (2) is only applicable for stably-evolving star-forming galaxies without powerful AGNs.

Therefore, in our model, the SFR and radiative cooling from the gaseous halo are tightly connected. This model is most applicable to field galaxies, rather than group or cluster galaxies, which can be greatly affected by the intragroup or intracluster medium (Balogh et al., 1998). With these constraints, we adopt the conditions where the SFR is equal to the radiative cooling rate of the gaseous halo. The radiative cooling rate is limited within the cooling radius, where the cooling timescale is equal to the Universe age (13.8 Gyr; Planck Collaboration et al. 2016a) or the cosmic epoch at a given redshift. In the following calculation, we use $H_0 = 67.8$ km s^{-1} Mpc^{-1}, $\Omega_{\mathrm{m}} = 0.308$, and $\Omega_{\mathrm{b}} = 0.0483$ (Planck Collaboration et al., 2016a).

7.2.2 Galaxy and Gaseous Halo Properties

To construct sample galaxies, we adopt several empirical relationships. For a given stellar mass, we obtain the halo mass based on the stellar mass-halo mass (SMHM) relationship (Behroozi et al., 2013; Kravtsov et al., 2018). These two SMHM relationships sdiverge when $M_{\rm h} > 10^{11.5}\ M_{\odot}$, and Kravtsov et al. (2018) has a higher stellar mass than Behroozi's relationship. At the halo mass of $10^{13.5}\ M_{\odot}$, the stellar mass difference is around 0.5 dex. We choose the Kravtsov's SMHM relationship, since it describes the case that is more similar to the MW, where a $\approx 2 \times 10^{12}\ M_{\odot}$ halo hosts a $5 - 8 \times 10^{10}\ M_{\odot}$ galaxy disk. Once the halo mass is determined, the virial radius and the virial temperature are calculated as:

$$\begin{aligned} R_{\rm vir} &= R_{200} = \frac{M_{\rm h}}{4\pi\Delta_{\rm vir}\rho_{\rm crit}/3}, \\ V_{\rm c}^2 &= \frac{GM_{\rm h}}{R_{\rm vir}} = 100 H_0^2 R_{\rm vir}^2, \\ T_{\rm vir} &= \frac{\mu m_{\rm p}}{2k_{\rm B}} V_{\rm c}^2, \end{aligned} \tag{7.3}$$

where $\Delta_{\rm vir} = 200$ is the collapse factor, and $\rho_{\rm crit} = 3H_0^2/8\pi G$ is the cosmic critical density. The quantities $R_{\rm vir}$ and $T_{\rm vir}$ are input parameters of our models and can be varied by introducing additional factors (as the model of the MW in Section 4.5). Therefore, the choice of the SMHM relationship does not affect our results significantly.

The star formation rate can be inferred using the star formation-stellar mass plane (Renzini & Peng, 2015; Morselli et al., 2016):

$$\log({\rm SFR}) = (0.72 \pm 0.02) \log M_{\star} - 7.12, \tag{7.4}$$

in the stellar mass range of $M_{\star} = 10^{8.5} - 10^{11.25} M_{\odot}$. Therefore, we set the range of halo mass to $10^{10.5} - 10^{13.5}\ M_{\odot}$. The star formation also has a dependence on the

redshift (Pannella et al., 2009):

$$\overline{\mathrm{SFR}} \approx 270 \frac{M_\star}{10^{11}\ M_\odot} \left(\frac{t}{3.4 \times 10^9\ \mathrm{yr}} \right)^{-2.5} \frac{M_\odot}{\mathrm{yr}}, \tag{7.5}$$

where t is the cosmic epoch. This relationship can be rewritten as a dependence on the redshift directly sSFR $\propto (1+z)^3$ at $z < 2$ (Lilly et al., 2013).

The structure of the gaseous halo is also fixed to reduce the degree of freedom, and we adopt the β-model for gaseous halos for all galaxies with different masses, which has the density profile:

$$\rho(r) = n_0 \left(1 + \frac{r^2}{r_\mathrm{c}^2} \right)^{-3\beta/2}, \tag{7.6}$$

where n_0 is the normalization parameter, and r_c is the core radius. Normally, core radii for galaxies are small, and cannot be modeled for isolated galaxies (Li et al., 2016). Then, we rewrite the profile as

$$\rho(r) = \frac{n_0 r_\mathrm{c}^{3\beta}}{r^{3\beta}}, \tag{7.7}$$

which is valid for $r >> r_\mathrm{c}$, and then the degeneracy of $n_0 r_\mathrm{c}^{3\beta}$ will not be broken. X-ray imaging studies on nearby massive galaxies showed that the β factor is around 0.5 within the radius $\leq$ 50 kpc (Anderson et al., 2016). Recently, the Circum-Galactic Medium of MASsive Spirals (CGM-MASS) project shows that β is a constant of ≈ 0.4 extended to around the half of virial radius ($\approx$ 200 kpc for massive star-forming spiral galaxies; Li et al. 2018b). Therefore, we adopted β as a constant over all of the radius range for one gaseous halo, but β can be varied for different models.

Since the total mass of the β-model is not convergent with increasing radius, we need to set the radius range for this model. In the inner region, other physical processes occur (e.g., the interaction with disk gases), therefore, the hydrostatic as-

sumption is broken, and the β-model may not be applicable. This radius is set by the competition between the free-fall timescale and the radiative cooling timescale, which is around $5 - 10$ kpc using the radiative cooling timescale of the MW from Miller & Bregman (2015). Massive galaxies have larger inner radii that can be larger than 10 kpc, but our model does not show significant dependence on the innermost radius. From 5 kpc to 10 kpc, the mass of the gaseous halo is increased by up to 15%, which is only for the most massive galaxies ($M_{\rm h} > 10^{13}\ M_{\odot}$) due to their small cooling radii. For L^* galaxies, this change is smaller than 10%, therefore, we fix the innermost radius as 5 kpc for all galaxies. For the outer region, the maximum radius is set to the virial radius for a given halo mass, which means that the density goes to zero at the virial radius. However, it is shown that the massive system (galaxy cluster) could have detectable gas reaching R_{200}, which implies that the gaseous component could extend beyond the virial radius (Baldi et al., 2012). Therefore, this assumption may not be correct, however, there are no other means to set an unbiased boundary condition.

The normalization parameter n_0 is calculated based on the assumption that the SFR is equal to the radiative cooling rate:

$$\mathrm{SFR} = \int_{5\mathrm{kpc}}^{\min\{R_{200},R_{\rm cl}\}} \frac{\overline{\Lambda}(r)n^2(r)}{\overline{\epsilon}(r)}\mu m_{\rm p} 4\pi r^2 \mathrm{d}r, \tag{7.8}$$

where $\overline{\Lambda}(r)$ is the average radiative cooling emissivity, while the $\overline{\epsilon}(r)$ is the average internal energy at a given radius, defining as

$$\overline{\Lambda} = \frac{\int_{T_{\rm min}}^{T_{\rm max}} M(T)n(T)\Lambda(T)\mathrm{d}T}{\int_{T_{\rm min}}^{T_{\rm max}} M(T)n(T)\mathrm{d}T}, \tag{7.9}$$

$$\overline{\epsilon} = \int_{T_{\rm min}}^{T_{\rm max}} M(T)\frac{3}{2}k_{\rm B}T\mathrm{d}T. \tag{7.10}$$

$M(T)$ is the mass distribution depending on the temperature, which has the normalization of $\int_{T_{\rm min}}^{T_{\rm max}} M(T){\rm d}T = 1$. Here, we also assume that the average mass of particles (μ) is 0.59 for the temperature range considered ($T > 10^{4.5}$ K), since this value is dominated by the ionization state of the hydrogen, which is almost completely ionized in this temperature range. The choice on the radiative cooling model will be discussed in the following section.

The radial dependence of temperature is still observationally poorly constrained for isolated galaxies. X-ray studies on galaxy clusters showed that the temperature variation is less than one order of magnitude within R_{500} (Baldi et al., 2012). For isolated star-forming galaxies, Anderson et al. (2016) showed that NGC 1961 also has a small variation, but only out to $\sim$ 50 kpc. Here, we assume that there is no radius-dependence of the temperature.

7.2.3 Cooling Emissivity

The radiative cooling rate is directly affected by the emissivity, which has a dependence on the temperature, the density and the metallicity. For the temperature range of a gaseous halo ($\sim 10^{4.5} - 10^{7}$ K), the radiative cooling is dominated by lines of various ions. Therefore, for a given temperature and density, the ionization state of different ions can be determined and the cooling rate is calculated involving the metallicity. Here, we assume that the gaseous halo is in ionization equilibrium, and consider two ionization processes – collisional ionization and the modification due to photoionization.

For collisional ionization equilibrium (CIE), we adopt the emissivity calculated using CHIANTI (version 8.0.6; Del Zanna et al. 2015). In this calculation, the metallicity is set to 0.1 $Z_{\odot}$, 0.3 $Z_{\odot}$, 1.0 $Z_{\odot}$ and 2.0 $Z_{\odot}$, and the solar metallicity of $Z_{\odot} = 0.0142$ is adopted from Asplund et al. (2009).

The photoionization due to the ultraviolet background (UVB) can modify the

ionization distribution of different elements (Wiersma et al., 2009), and the photoionization model is employed to model the low and intermediate ionization ions in intervening systems (Savage et al., 2014; Werk et al., 2014). Also, the high ionization state ions might be photoionized at low densities of $\lesssim 10^{-5}$ cm^{-3}, which is the expected density in the outskirts of gaseous halos (Hussain et al., 2015, 2017). Therefore, we include the photoionization from the UVB to compare with the pure collisional ionization mode.

Galaxies also provide a part of the ionizing flux to photoionize the CGM or nearby IGM, which is known as the escaping ionizing flux. The escape fraction is believed to be large ($\gtrsim 10\%$) in the early Universe ($z > 6$) to contribute to the re-ionization (Mitra et al., 2013), while studies of the low redshift IGM ($z < 2$) found the escape fraction is several percent (Khaire & Srianand, 2015). The small escape fraction has the implication that those ionizing photons mainly affect the innermost $\sim$ 50 kpc region of the gaseous halo, thus, we ignore ionizing photons from the galaxy disk (Suresh et al., 2017).

For the photoionization equilibrium (PIE), we adopt the calculation from Oppenheimer & Schaye (2013), who tabulated results for different redshifts, densities, and temperatures. Several UVB models have been provided, and we choose the UVB form Haardt & Madau (2012) in our models. In this database, authors also include the cosmic microwave background (CMB), with the dependence on the redshift. The existence of the CMB provides a large number of low-energy photons, which can be heated by inverse Compton scattering, thereby cooling the high-temperature electrons.

In Fig. 7.1, we show the comparison between CIE and PIE cooling curves. High energy photons from the UVB photoionize low ionization state ions to higher states, which suppresses the cooling in the low-temperature region. Due to the lack of H I, the first peak around 2×10^4 K is missing. The photoionization also changes the ionization fraction of metals and contributions to the radiative cooling, suppressing

low ionization state cooling (e.g., C II and O II) and increasing high ionization cooling (e.g., O VI). Therefore, the cooling emissivity is lower in the low-temperature regime for the PIE model than the CIE model. Inverse Compton cooling due to CMB dominates the high temperature and low-density gas. The emissivity of inverse Compton scattering is proportional to nT, while the free-free emission has the dependence $n^2T^{1/2}$. Therefore, there is always a critical combination of temperatures and densities, above which the inverse Compton cooling is dominant. However, in the low redshift Universe ($z < 2$), the number density of CMB photons is sufficiently low so that gases have a cooling timescale longer than the Hubble timescale. Therefore, the effect due to the CMB can be ignored for the low redshift ($z < 2$) Universe. The effect of the radiative cooling model will be described in details in Section 3.

7.2.4 Temperature Dependence of the Mass Distribution

Multi-phase gas in gaseous halos have been detected by various observations (Nicastro et al., 2002; Danforth & Shull, 2008; Anderson et al., 2013; Werk et al., 2013; Savage et al., 2014; Qu & Bregman, 2016). Unfortunately, obtaining an accurate distribution of the multi-phase medium by mass remains a challenge both observationally or theoretically (e.g., the divergence on O VI abundance; Oppenheimer et al. 2016; Suresh et al. 2017). Therefore, for the simplest model, we assume that the gaseous halo is a single phase medium at the virial temperature.

We also consider a stable cooling model, which is a time-independent solution. In this model, we assume the mass cooling rate is the same at all temperatures:

$$L(T) = \Lambda(T)n^2(T)\frac{M(T)}{\mu m_{\rm p} n(T)} = const., \tag{7.11}$$

where $L(T)$ is the luminosity at a given temperature T, and $M(T)$ is the mass distribution dependence on the temperature. Another assumption is the pressure balance,

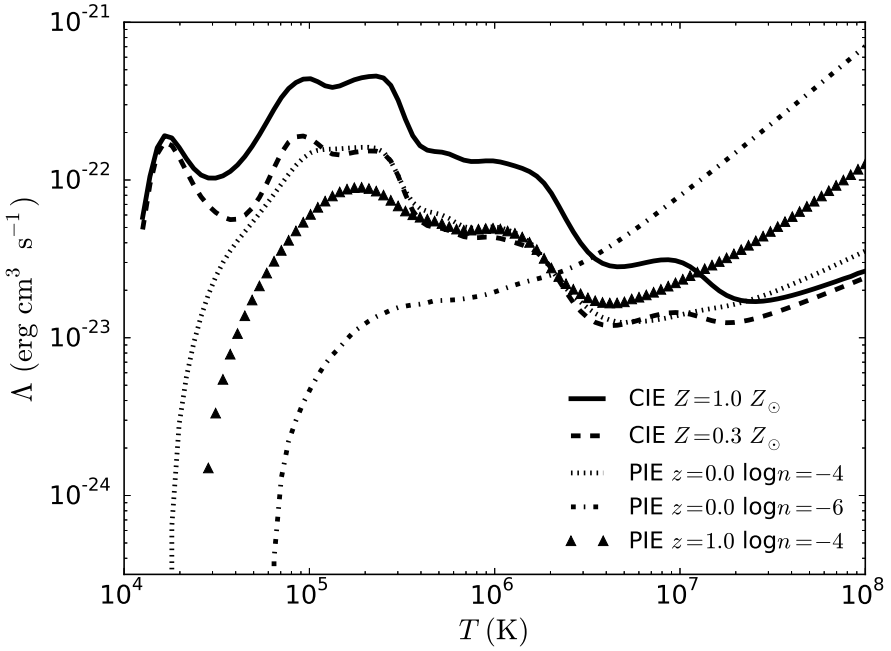

Figure 7.1: Comparison between the cooling curve for pure collisional ionization (CIE) and with the modification from photoionization (PIE). The cooling curves in CIE have metallicities of 1 $Z_\odot$ (the solid line) and 0.3 $Z_\odot$ (the dashed line). The three PIE cooling curves all have the same metallicity of 0.3 $Z_\odot$. The dotted line has a density of 10^{-4} cm^{-3} (typical of the density of the inner gaseous halo) and at $z = 0$, while the dash-dotted line has a lower density of 10^{-6} cm^{-3} (typical of the density in the halo outskirts) at the same redshift. The up-triangle shows the cooling curve at $z = 1$ with a density of 10^{-4} cm^{-3}.

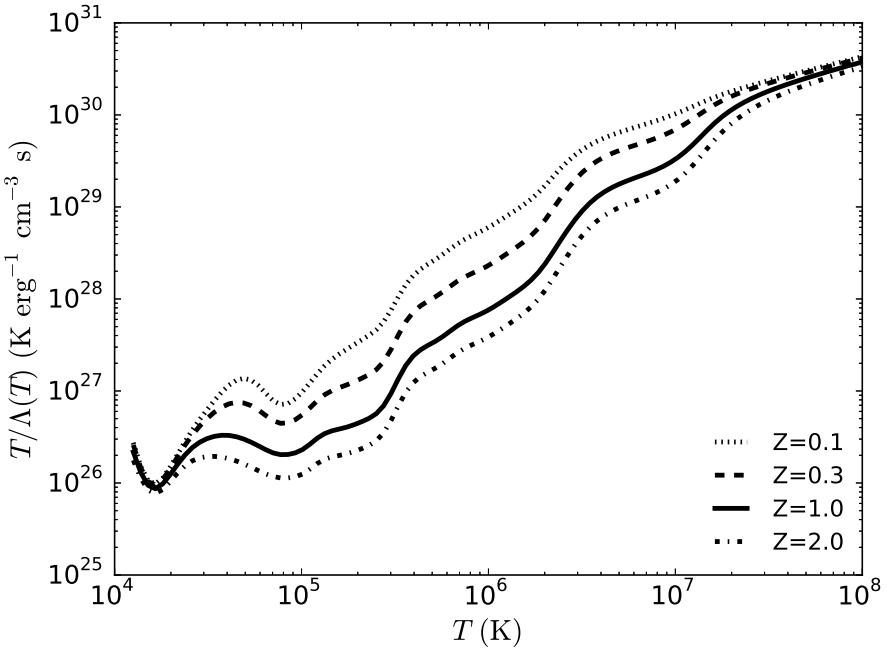

Figure 7.2: The unnormalized mass distribution for cooling gas as a function of temperature. `CIE` cooling curves with metallicities of 0.1 $Z_\odot$, 0.3 $Z_\odot$, 1.0 $Z_\odot$ and 2.0 $Z_\odot$ are shown in dotted, dashed, solid and dot-dashed lines, respectively. With temperature limits, which are related to the galaxy mass, this function can be normalized as $\int_{T_{\rm min}}^{T_{\rm max}} M(T){\rm d}T = 1$ to obtain the mass distribution $M(T)$.

which implies $n(T) \propto 1/T$. Thus, the mass distribution is

$$M(T) = \frac{T}{\Lambda(T)} \Big/ \int_{T_{\rm min}}^{T_{\rm max}} \frac{T}{\Lambda(T)} {\rm d}T, \tag{7.12}$$

the temperature upper limit ($T_{\rm max}$) is set to the virial temperature, while the lower limit is fixed to $10^{4.5}$ K, under which forbidden lines dominate the cooling, along with dust and molecules. An example of $M(T)$ without normalization is shown in Fig. 7.2.

Our model does not include all relevant physics that occurs in galaxy halos (e.g., thermal instabilities), but it allows us to explore a wide range of parameter space and to identify robust results. Detailed calculations show that the stable cooling

model has applicability for the cooling in a temperature range of 10^4 K to $10^{6.5}$ K in stellar feedback dominated galaxies (Thompson et al., 2016). Their breaking of this cooling assumption in the high-temperature range is mainly because they consider the hot gas from the stellar feedback, which softens the assumed boundary condition that the high-temperature gas can be supplied infinitely. However, in the gaseous halo scenario, this condition could be satisfied when a hot and long radiative-cooling timescale gaseous halo exists.

7.3 Results

We calculate three models with different cooling models and temperature distributions – `CIE`: the single temperature collisional ionization model; `PIE`: the single temperature photoionization model; `TCIE`: the collisional ionization model with the mass distribution described in Section 2.4. In this section, we show our main results for these models on the gaseous halo mass and the ion column density.

7.3.1 Fiducial Galaxies

There are four factors affecting the properties of the gaseous halo in our simplified models – the metallicity (Z), the specific star formation rate (sSFR defined as SFR/$M_\star$), the slope of the β-model (β) and the redshift (z). Based on these four dimensions, we have fiducial galaxies defining as $\log M_{\rm h} = 10.5 - 13.3$, $Z = 0.3\ Z_\odot$ (cosmic metallicity), sSFR $= 10^{-10}$ yr^{-1} (star-forming), $\beta = 0.5$ (hydrostatic equilibrium structure) and $z = 0$. For each modeled gaseous halo, we calculate the gaseous halo mass enclosed in the radius range of 5 kpc to the virial radius, and the cooling radius. The calculation results are shown in the Fig. 7.3.

For the fiducial case, all three models have masses of gaseous halos that are smaller than corresponding stellar masses around the (sub-)L^* galaxies. The largest difference of ≈ 0.5 dex occurs at sub-L^* galaxies ($M_{\rm h} \approx 4 \times 10^{11}\ M_\odot$). Overall, the `CIE` model

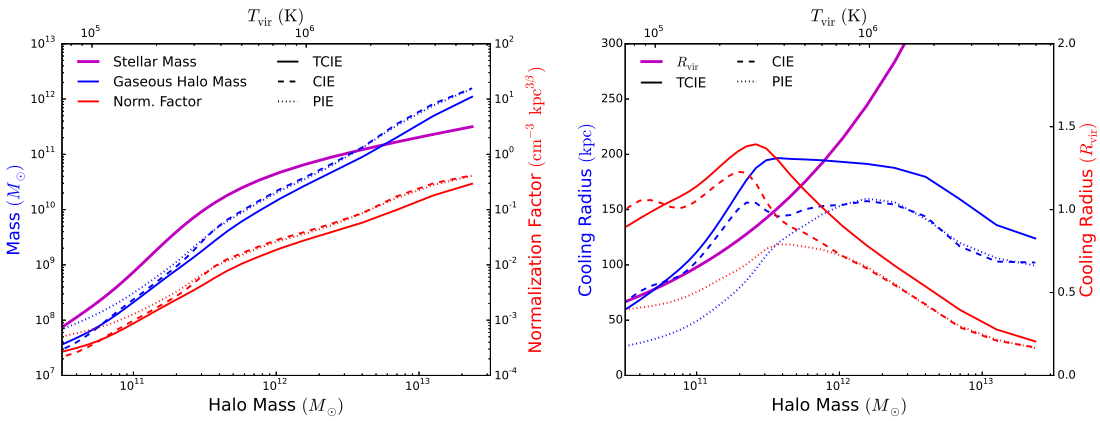

Figure 7.3: *Left panel*: The gaseous halo mass and the normalization factor of different models at $z = 0$. The blue lines are the gaseous halo masses, while the red lines are the normalization factors in the β-model. `CIE`, `PIE` and `TCIE` models are shown in dash-dotted, dashed, and solid lines. The magenta line is the stellar mass from stellar mass-halo mass relationship (Kravtsov et al., 2018). *Right panel*: The cooling radius, the radius within which the cooling time equals the local Hubble time, as a function of halo mass. The blue lines are the absolute cooling radius (left scale), while the red lines are the cooling radius in the unit of the virial radius (right scale). The range in the cooling radius only changes by a factor of four over the range in which the halo mass changes by three orders of magnitude.

shows convergence with TCIE in the low-mass region and converges with PIE for massive galaxies. With the halo mass decreasing, the temperature range for TCIE (with $T_{\rm min} = 3 \times 10^4$) is also decreasing, which leads to the similarity with CIE. Both of collisional ionization models have lower mass gaseous halos than the PIE model because they have a higher radiative emissivity in the low temperature, and the photoionization due to the UVB can support a relatively more massive halo for low-mass galaxies.

In the massive galaxy range, the radiative cooling is reduced at high temperatures, which results in a massive gaseous halo, consistent with theoretical expectations (Mo et al., 2010). These halos are supported by their buoyancy even for the PIE model. The convergence between CIE and PIE is due to the higher density in massive galaxies – in the inner region (inside of the cooling radius), the average density is higher than 10^{-4} cm^{-3}. This high density corresponds to the low ionization parameter ($U = n_{\rm ph,ionizing}/n_{\rm H}$), indicating the weakening of the photoionization. As shown in Fig. 7.1, the CIE cooling is consistent with the PIE cooling with a density of 10^{-4} cm^{-3}. TCIE has a lower mass gaseous halo than CIE or PIE, due to its higher average emissivity since this model always has low-temperature gas with a higher radiative emissivity.

Overall, the cooling radius varies only modestly over the halo mass range in each model. Specifically, the variation is less than one order of magnitude, and this variation corresponds to the changes in the average emissivity. With the higher emissivity, the cooling radius is larger, however, the changes in the cooling radius is smaller than the emissivity changes. Meanwhile, the cooling radius shows a similar convergence as the gaseous halo mass between CIE and TCIE for low-mass galaxies, and between CIE and PIE for massive galaxies.

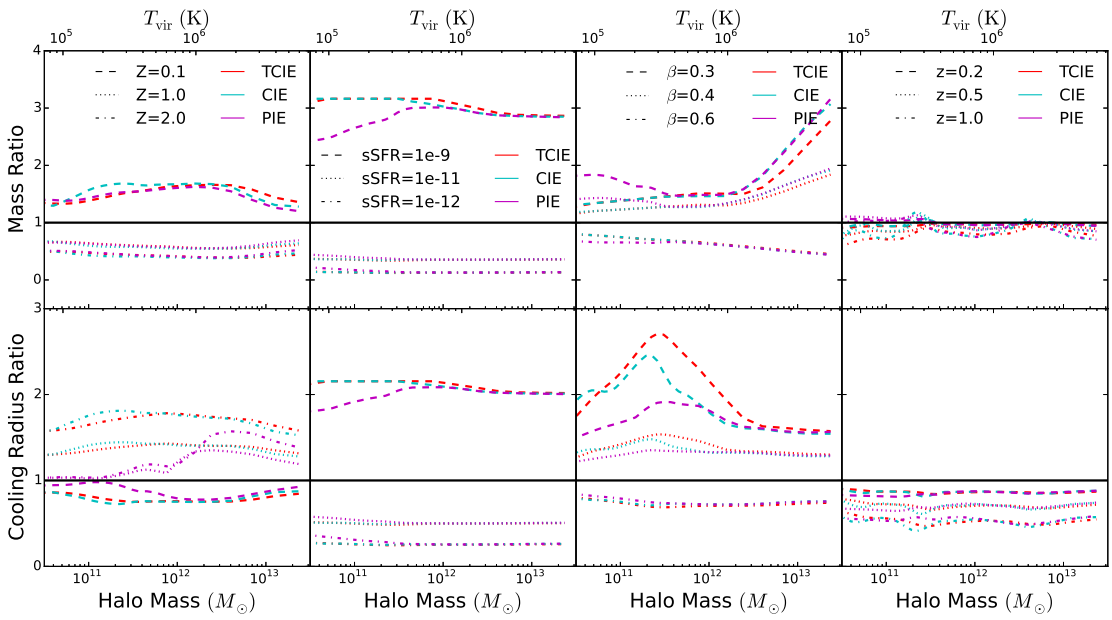

Figure 7.4: Gaseous halo properties as a function of the halo mass for variations in the metallicity (left), the sSFR, the slope of the density profile, and the redshift (right). `CIE`, `PIE` and `TCIE` models are shown in cyan, magenta and red, and the ratios are the values relative to the functional form of the fiducial galaxy has parameters of $Z = 0.3\ Z_\odot$, sSFR $= 10^{-10}$ yr^{-1}, $\beta = 0.5$, and $z = 0$ (in the solid black lines).

7.3.2 The Effect of Galaxy Properties

By changing the four parameters (Z, sSFR, β and z), we show the effect of these parameters on the resulting hot halo and column densities. For each parameter, we have four choices: the metallicity – 0.1 $Z_\odot$, 0.3 $Z_\odot$, 1 $Z_\odot$, or 2 $Z_\odot$; the specific SFR – 10^{-9} yr^{-1}, 10^{-10} yr^{-1}, 10^{-11} yr^{-1}, or 10^{-12} yr^{-1}; the β parameter – 0.3, 0.4, 0.5, or 0.6; and the redshift – 0, 0.2, 0.5, or 1. In Fig. 7.4, we show the change corresponding to these parameters as the ratio between varied models and the fiducial model.

The high metallicity increases the cooling emissivity, which reduces the normalization parameter in the β-model, and subsequently the halo mass. With the variation of metallicity in the range $0.1 - 2.0\ Z_\odot$, the change of the gaseous halo mass is less than a factor of 5, whereas the change of metallicity is a factor of 20. This implies

that lower metallicity gaseous halos have a lower total metal mass to account for the same cooling rate. The cooling radius of `CIE` and `TCIE` models has a positive dependence on the metallicity due to the increase of emissivity. However, inclusion of photoionization shows a similar cooling radius for different metallicities in the low-mass end, which indicates that the radiative cooling due to the low ionization metal ions is suppressed by the photoionization.

A sSFR of 10^{-11} yr^{-1} is used as a boundary between a star-forming galaxy and a quiescent galaxy, while normal star-forming galaxies have sSFR around 10^{-10} (Renzini & Peng, 2015). By increasing the sSFR, the total radiative cooling rate is increased, which means that a massive gaseous halo is needed. For `CIE` and `TCIE`, this effect is almost a constant over all mass regions, and `PIE` shows a similar tendency in the high mass region ($> 10^{12}$ $M_\odot$). However, for low-mass galaxies, `PIE` models with different sSFR values show a significant convergence of the gaseous halo mass, which indicates the effect of a changing sSFR is not as large as `CIE` or `TCIE`. The reason for these phenomena is that there are two ways to increase the radiative cooling rate – higher density or higher emissivity. In `CIE` and `TCIE` models, the emissivity cannot be increased when the temperature distribution is fixed. Therefore the only way to raise the cooling rate is by increasing the density, which makes the density proportional to the square root of the sSFR for all halo masses. In the `PIE` model, the emissivity has a dependence on the density as shown in Fig. 7.1. Within the cooling radius, the density is higher than 10^{-4} cm^{-2}, and the PIE cooling curve does not deviate from the CIE cooling curve significantly in the temperature range of $\approx 10^{5.5} - 10^6$ K. For galactic gaseous halos with these temperatures ($M_{\rm h} > 10^{12}$ $M_\odot$), the emissivity shows a similar behavior as the CIE models, therefore, the change of the density (and the gaseous halo mass) is also similar to the CIE models. For low-mass galaxies with low-temperature halos, the PIE cooling deviates from the CIE cooling curve significantly since the cooling is suppressed for low ionization state ions. Raising the

density decreases the photoionization effect, and increases the emissivity to the value of CIE models. Therefore, in the `PIE` model, the high density not only increases the cooling rate by the squared dependence on the density itself but also increases the emissivity, which leads to a smaller change in the density to account for the high sSFR.

The variation of the sSFR is equivalent to changing the γ factor with the sSFR unchanged. For an example, sSFR $= 10^{-9}$ with $\gamma = 1$ is the same model as sSFR $= 10^{-10}$ but with $\gamma = 0.1$. Therefore, our models show that the gaseous halo mass has a square root dependence on the inverse γ factor.

With a larger β, the gas is more concentrated in the central region (at the same gas mass), which leads to the higher emissivity. Since the mass is linearly dependent on the density, the larger β results in a smaller gaseous halo mass. Due to the concentrated emission, the cooling radius is also decreases as β is increases. The effect of larger β also has a dependence on the halo mass – with a more massive halo, the ratio of masses is larger, as shown in Fig. 7.4. This correlation occurs because the massive galaxy has a relatively small cooling radius compared to the virial radius, and the flat β-model can host more mass in the region out of the cooling radius.

A higher redshift can affect the gaseous halo through three means – the higher gas density, the younger Universe age and the more intense cosmic background. First, due to the Universe expansion, the higher redshift Universe has a higher density, which leads to the smaller virial radius, and hence higher virial temperature. Second, the younger Universe age at the higher redshift determines a shorter cooling timescale, which reduces the cooling radius and the total cooling rate within this radius. Since `CIE` and `TCIE` models have no photoionization involved, these two models are only affected by these two factors. The gaseous halo mass has an anti-correlation with the cooling emissivity of the gas, but the emissivity is a result of a competition of two factors – the increasing emissivity due to the higher density and the changing due

to virial temperature. Together, these complex effects leads to a small variation of the gaseous halo mass, with small variations reflecting the shape of the cooling curve (i.e., the bump around $T_{\rm vir} \approx 10^{5.5}$ K, also the peak of the cooling curve). For the cooling radius, the effect is clear that the higher redshift leads to a smaller cooling radius. The cooling radius of a $z = 0$ galaxy is about 1.5 times larger than the same mass galaxy at $z = 1$ galaxies.

The cosmic background includes two parts – the UVB and the CMB. As stated in Section 2.3, the inverse Compton cooling is negligible in the low-redshift universe ($z < 6$), but the UVB changes the ionization state distribution, leading to the reduced radiative cooling in the low-temperature region. Therefore, for the low-mass galaxies ($M_{\rm h} \lesssim 10^{11.3}\ M_{\odot}$), a more massive gaseous halo is required to account for the same SFR with the UVB increasing at the higher redshift, which results in the mass ratio being slightly larger than 1. For the high-temperature end, the `PIE` model converges with the `CIE` model, which is expected.

7.3.3 The Ion Column Densities

With the calculated density profile and the temperature distribution, we calculate the column density for ions of interests (mainly high ionization state ions), which are more common in the hot ambient medium. For `CIE` and `TCIE` models, we adopt the ionization distributions from Bryans et al. (2006), which only has a dependence on the temperature. The `PIE` ionization fraction is adopted from Oppenheimer & Schaye (2013), which is tabulated based on the redshift, the metallicity, the density and the temperature.

For the `TCIE` model, we calculate the average ionization fraction using

$$\overline{f}_{\rm i} = \int_{T_{\rm min}}^{T_{\rm max}} f_{\rm i}(T) M(T) {\rm d}T. \tag{7.13}$$

Here, we assume that multi-phase medium has similar covering factors around 1, which implies that the multi-phase medium is well-mixed. This assumption should be good for high ionization state ions. Werk et al. (2013) shows that intermediate ionization ions (i.e., C III, Si III, Si IV) and high ionization ions (i.e., O VI) have comparable covering factors around 0.8, except that O VI seems to be less in quiescent galaxies. However, this is probably caused by quiescent galaxies that are usually massive galaxies with higher virial temperatures (Oppenheimer et al., 2016).

In Fig. 7.5, we compare the three models (`CIE`, `TCIE` and `PIE`), showing ion column densities for star-forming galaxies (i.e., $Z = 0.3\ Z_{\odot}$, $z = 0$, sSFR $= 10^{-10}$ yr^{-1} and $\beta = 0.5$). To show the dependence on the stellar mass, we fix the impact parameter to 0.3 $R_{\rm vir}$, which is a typical impact parameter in the COS-Halos program and also leads to a similar column for ions observed in the MW from the Sun. Similar to the result of the gaseous halo mass, `CIE` and `PIE` shows the convergence of H I column densities from $M_{\rm h} = 4 \times 10^{11}\ M_{\odot}$ and above, which indicates that the cooling emissivity is almost the same. However, other ions do not show the same similarity, which indicates that the ionization fractions are not similar. Only the most massive halo ($M_h > 10^{13}\ M_{\odot}$) has similar ionization fractions for `CIE` and `PIE` due to the relatively higher density. In low-mass galaxies (at the left side of the ionization peak for different ions), `PIE` leads to extended tails for high ionization state ions (e.g., O VI and O VII) because of the low density.

Compared to `CIE` or `PIE` without cooling temperature distributions, `TCIE` does not show the shape of the ionization fraction function directly, but it shows a flattened peak for high ionization state ions. For O VI and O VII, column density peaks are $\gtrsim 10^{14}$ cm^{-2} and 7×10^{15} cm^{-2}, respectively. O VI is higher than $10^{13.5}$ cm^{-2} over a halo mass range of $2 \times 10^{11}\ M_{\odot}$ to $4 \times 10^{12}\ M_{\odot}$. Ne VIII and Mg X show comparable flattened column density distributions in the range of $10^{13.5} - 10^{14.0}$ cm^{-2}, while Ne VIII occurs in lower mass galaxies compared to Mg X.

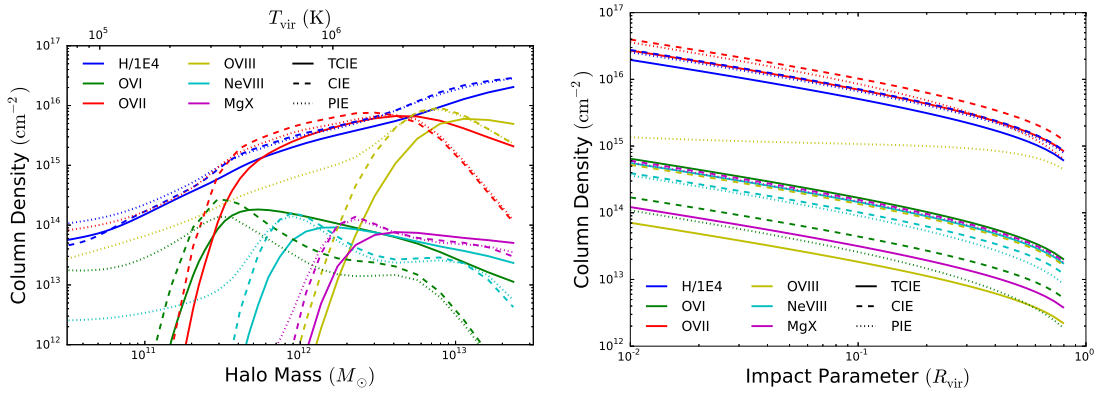

Figure 7.5: Comparison of the ion column density between three models, `CIE`, `PIE` and `TCIE` at $z = 0$, which are shown in dashed, dotted and solid lines, respectively. Different ions are shown in different colors: blue – hydrogen (reduced by a factor of 10^4); green – O VI; red – O VII; yellow – O VIII; cyan – Ne VIII; and magenta – Mg X. *Left panel*: The column density dependence on the halo mass. The galaxy sample is the fiducial galaxy locus, and the impact parameter is fixed to 0.3 $R_{\rm vir}$. *Right panel*: The column density dependence on the impact parameter for the galaxy with $M_\star = 7 \times 10^{10}\ M_\odot$, and SFR $= 3\ M_\odot\ {\rm yr}^{-1}$, $Z = 0.3\ Z_\odot$, and $\beta = 0.5$.

To show the ion column density dependence on the impact parameter, we choose a MW-like galaxy with $M_\star = 7 \times 10^{10}\ M_\odot$, SFR $= 3\ M_\odot\ {\rm yr}^{-1}$, $Z = 0.3$, $\beta = 0.5$ and $z = 0$. In `CIE` and `TCIE` models, the ionization fraction does not have a dependence on the density, so the average ionization fraction has no dependence on the impact parameter. Therefore, all columns follow a general radial decrease of the β-model. For the `PIE` model, the significant flattening of O VIII in the small impact parameter region shows that the ionization fraction in the inner region is much smaller than the outer region, where the photoionization generates more O VIII (Oppenheimer & Schaye, 2013). The turnover point is about the half of the virial radius, where about half of O VIII is produced beyond this radius.

We consider the redshift dependence of the `PIE` model in Fig. 7.6, which is otherwise similar to Fig. 7.5. At higher redshifts, the more intense UVB leads to a stronger tail of high ionization state ions in low-mass galaxies. Also, high ionization ions (e.g.,

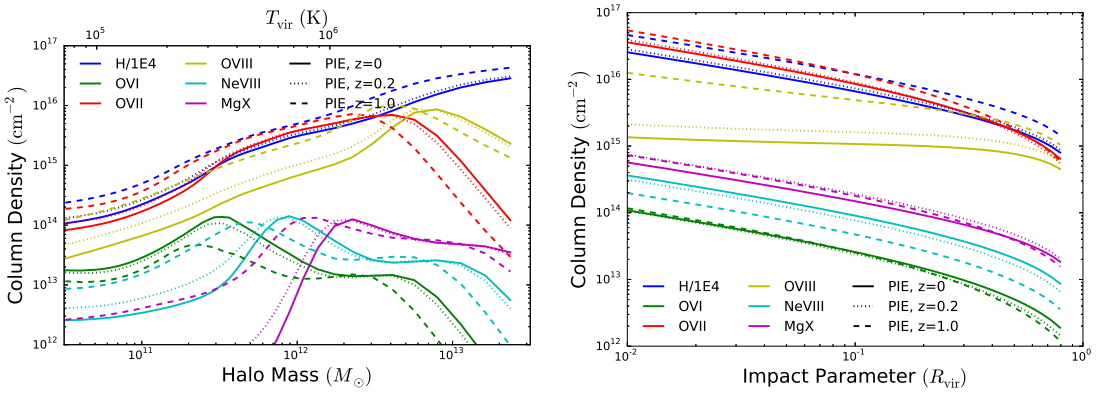

Figure 7.6: Comparison of the ion column density of the `PIE` model at different redshifts. Ions are encoded in the same colors as Fig. 7.5, while solid, dotted, and dot-dashed lines are `PIE` models with $z = 0$, $z = 0.2$, $z = 1.0$, respectively. The galaxy sample configuration is also the same as Fig. 7.5. *Left panel*: The column density dependence on the halo mass. Since the virial temperature has the dependence on the redshift, the shown $T_{\rm vir}$ is at $z = 0$. *Right panel*: The column density dependence on the impact parameter. The higher redshift leads to a higher virial temperature, and shifts the peaks of ions to lower-mass galaxies. Both the higher virial temperature and more intense UVB increase the higher ionization state ion column densities for higher redshift galaxies.

O VIII) show peaks at the lower halo mass for the high redshift galaxy, as the O VIII column density peak moves from $M_{\rm h} \approx 7 \times 10^{12}\ M_\odot$ ($z = 0$) to $M_{\rm h} \approx 4 \times 10^{12}\ M_\odot$ ($z = 1$). This is mainly due to the increasing virial temperature at higher redshifts. For these higher virial temperatures, the O VIII column density is no longer flat in the small impact parameter region at $z = 1$, which means that the ionization of O VIII is no longer dominated by the photoionization. Although the high density in the inner region still reduces the ionization fraction of O VIII, a significant amount of O VIII is produced in the inner region through collisional ionization.

7.3.4 Galaxies with the SFR Main Sequence

Using the relationship between the SFR and the stellar mass (Morselli et al., 2016), we generate a set of galaxies with typical SFR, and calculate the ion column densities,

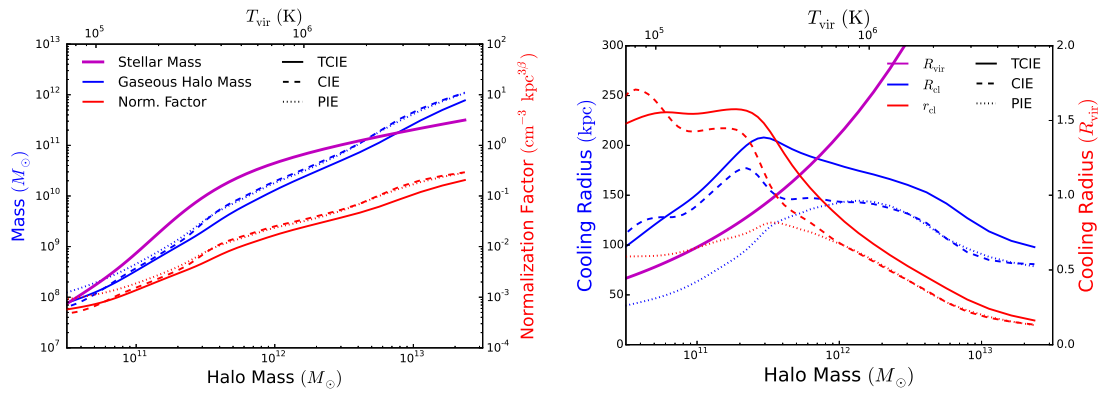

Figure 7.7: The gaseous halo mass and the cooling radius of galaxies where the SFR is given by the mean fundamental plane SFR-stellar mass relationship of Morselli et al. (2016). *Left panel*: The gaseous halo mass and the normalization factor. *Right panel*: The cooling radius dependence on the halo mass. These two plots are encoded in the same way as Fig. 7.3. The relatively higher sSFR for low-mass galaxies, leads to more massive gaseous halos and larger cooling radius, while massive galaxies have lower mass and smaller cooling radius compared to Fig. 7.3.

showing the result in Fig. 7.7. The sSFR has a weak dependence on the stellar mass as sSFR $\propto M_\star^{-0.28}$, so the changes are modest compared to Fig. 7.3, where the sSFR is constant for different galaxies. Due to the high sSFR of low-mass galaxies ($M_{\rm h} < 10^{11}\ M_\odot$), these galaxies have higher normalization factors in the β-model and gaseous halo masses. The gaseous halo mass at the high-mass end ($M_{\rm h} \approx 10^{13}\ M_\odot$) is decreased by a factor of two, due to the small sSFR. The cooling radius has a moderately narrow range of 50 kpc to 200 kpc as a function of the halo mass for a given model. Therefore, the increasing $R_{\rm vir}$ leads to a decrease of the relative cooling radius in units of $R_{\rm vir}$. Compared to Fig. 7.3, the cooling radius in the low-mass range is raised until $M_{\rm h} \approx 10^{11.5}\ M_\odot$, while it is suppressed for the massive galaxy, corresponding to the change of sSFR. For dwarf galaxies ($M_{\rm h} \lesssim 5 \times 10^{11}\ M_\odot$), the entire gaseous halo is radiatively cooling in `CIE` or `TCIE` models, while the `PIE` model always shows the cooling radius smaller than the virial radius.

We also consider the SFR modification on the ion column density, shown in Fig.

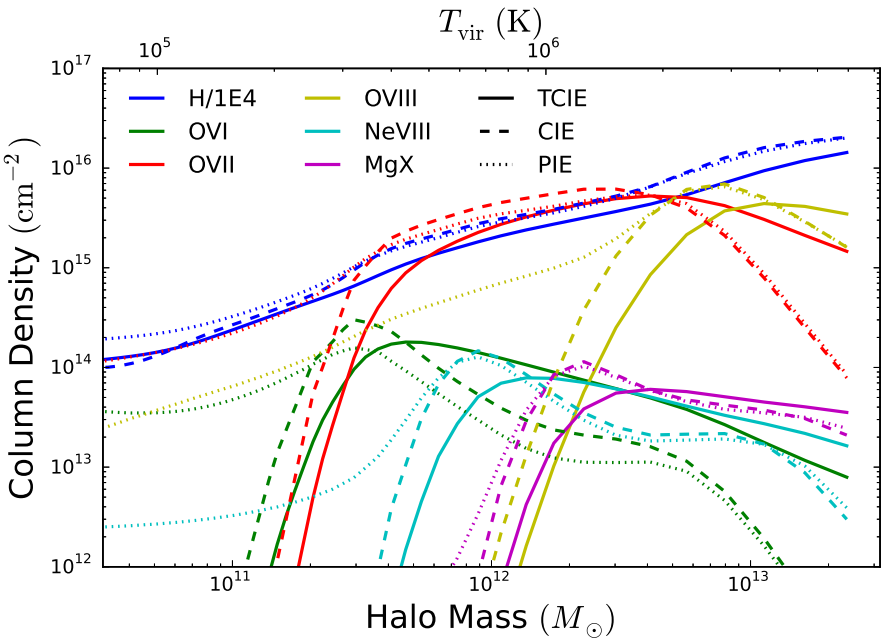

Figure 7.8: The column density dependence on the halo mass of galaxies with fundamental plane SFR. The ion colors are same as Fig. 7.5. Similar to the comparison between Fig. 7.7 and Fig. 7.3, the changing of sSFR leads to higher column densities for low-mass galaxies, and lower column densities for massive galaxies, compared to Fig. 7.5.

7.8. Due to the more massive gaseous halo of low-mass galaxies, the total hydrogen column density is increased significantly, while high ionization state ions (e.g., O VII and O VIII) changes within a factor of 1.5. The massive galaxy shows ions with column densities slightly smaller than Fig. 7.5. Overall, the sSFR dependence on stellar mass does not change the phenomena illustrated by the fixed sSFR models, such as the convergence between models.

7.4 Discussion

Currently, modeling of gaseous components in halos often assume a single-temperature CIE model or a photon-heated PIE model (Stocke et al., 2013; Werk et al., 2014; Miller & Bregman, 2015; Nicastro et al., 2016a; Faerman et al., 2017). Improvements

in such assumptions are warranted by observations that indicate the presence of multi-phase medium and temperature variations over different radii (Anderson et al., 2016; Tumlinson et al., 2017). However, both of these two temperature issues are not well constrained observationally – there is not a universal temperature distribution for multi-phase gas or a universal radial-dependence of the temperature (Anderson et al., 2016; Bogdán et al., 2017; Tumlinson et al., 2017).

Besides the gas temperature, the contribution by photoionization is controversial regarding the effect on high ionization state ions. The photoionization model is employed to explain the low and intermediate ionization state absorption system seen against the UV spectrum of background QSOs (Werk et al., 2014). High ionization state ions (e.g., O VI and Ne VIII) are normally explained in the collisional ionization model (Savage et al., 2005; Narayanan et al., 2012; Meiring et al., 2013; Pachat et al., 2017), while they are also possible to be modeled by photoionization (Hussain et al., 2015, 2017).

In the last decade, the effect of the photoionization and the radiative cooling has been considered in theoretical calculations (Wiersma et al., 2009; Oppenheimer & Schaye, 2013; Gnat, 2017). Benefiting from these numerical calculations, we apply two improvements to the modeling of gaseous halos – the photoionization modification and the radiative cooling multi-phase medium. These two improvements change the radiative cooling rate of the gaseous halo, subsequently the mass of the gaseous halo, and ions hosted by the halo. In this section, we compare our models with observations and theoretical simulations, and discuss implications and limitations.

7.4.1 The Most Applicable Models

In our gaseous halo model, we consider the modification of the photoionization and the effect of the radiatively cooling multi-phase medium, separately. In general, the photoionization mainly affects the low temperature or the low-density regions. In

the context of a gaseous halo, the low temperature gas is most common in low-mass galaxies, while the low-density gas is on the outskirts of gaseous halos. Meanwhile, the radiative cooling mainly occurs within the cooling radius, where the density is high enough for the effective radiative cooling. However, these modifications have several limitations, which should be considered when one evaluates the applicability of these models.

For the photoionization of the gaseous halo, there are two main limitations – the lack of ionizing photons from the host galaxy and the lack of the radiation transfer inside the halo. First, we only employ the UVB to supply ionizing photons, however, it is not the only source of the high-energy ionizing photons. The host galaxy also provides ionizing radiation from the star formation or soft X-rays from shock heated gases due to stellar winds and supernovae. Assuming an escape fraction of the unity of soft X-rays, Suresh et al. (2017) show that the impact of the photoionization due to the host galaxy is limited to the inner 50 kpc traced by the O VI. Typically, the escape fraction is only several percent for low-redshift galaxies ($z < 2$; Grimes et al. 2009; Khaire & Srianand 2015), which indicates that the galaxy escaping ionizing flux dominates the innermost region within the cooling radius. Second, ionizing UVB photons will be diluted by the absorption inside the gaseous halo, which leads to the suppression of the photoionization with the decreasing radius. The decreased photoionization means that the medium in the inner region is more likely to be collisionally ionized. Therefore, the UVB-only `PIE` model is more likely the case for the outer region of massive halos.

We assume a time-independent cooling model for the multi-phase radiatively cooling medium, where the mass cooling rate is constant over all temperatures. This model has two assumptions – the gases at different temperatures are "well-mixed" and the hot medium can always be supplied to keep the cooling time independent. The first assumption means that the multi-phase ionic structure should have a physi-

cal connection (mixture) at various temperatures to keep the same mass cooling rate, and the cooling is only due to the radiative losses of the whole gaseous halo. However, some of the physical aspects surrounding the cooling are still uncertain, which is related to various processes besides the pure radiative cooling – the galactic fountain, the accretion from IGM and even the tidal effect due to nearby galaxies (Bregman, 1980; Kwak & Shelton, 2010; Marinacci et al., 2010; Gnat, 2017). These processes introduce perturbations to the gaseous halo, which leads to denser regions and possible thermal instabilities that might enhance the radiative cooling (Armillotta et al., 2016, 2017). These processes cannot be investigated in our analytic model, but might find solutions in the highest resolution cosmological simulations, which is beyond the scope of this paper. However, Thompson et al. (2016) show that the cooling can follow the constant mass cooling rate model in a detailed radiative-cooling hot-wind model with mass-loading and energy transfer. In their calculation, the stable cooling model is evident in the large mass-loading factor $\dot{M}_{\rm hot}/{\rm SFR} \gtrsim 1$ case, which is related to another assumption on the boundary condition.

This boundary condition – an infinite ambient hot medium – is required in a steady state model to balance the cooling rate of the gas. Without this boundary condition, the cooling will reduce the mass and the density of the hot gas, and subsequently reduce the cooling rate in the high temperature region, which violates the constant mass cooling rate assumption. In Thompson et al. (2016), the low mass-loading case shows the flattened $\mathrm{d}L/\mathrm{d}\ln T$ in the high temperature region, indicating the lower cooling rate, which directly results from the weakening of the boundary condition. In the context of our gaseous halo model, this boundary condition could be satisfied automatically when the cooling radius is significantly smaller than the virial radius, which means that the gas beyond the cooling radius can be treated as the ambient hot phase gas to supply the cooling medium.

Based on above discussions, we suggest that gaseous halos should be divided

into two categories based on their host galaxy masses. For the low-mass galaxy ($M_{\rm h} \lesssim 4 \times 10^{11}\ M_{\odot}$), the `PIE` model is a good assumption, since its halo size is small, and the virial temperature is low. For such a gaseous halo, the photoionization must be considered, since it provides additional heating to support a more massive gaseous halo, and changes the distribution of ionization states significantly. Also, low-mass galaxies normally have lower SFR ($\lesssim 1\ M_{\odot}\ {\rm yr}^{-1}$), which reduces the ionizing flux from the host galaxy, and it is approximately correct to assume the UVB-dominated photoionization. However, one potential issue is that the stellar feedback is stronger with the decreasing halo mass, which implies the feedback heating is higher and the γ factor is smaller in Equation (2). Considering this effect, the low-mass galaxy may host a higher mass halo than the `PIE` model predicts. Considering the radiative cooling, we could use the `TPIE` model, which is more realistic, since the cooling radius is smaller than the virial radius as shown in Fig. 7.7. In the next section, we will show that the photoionization modification on the `TCIE` model is similar to its effect on the `CIE` model.

For a high-mass galaxy ($M_{\rm h} \gtrsim 4 \times 10^{11}\ M_{\odot}$), the virial temperature is high ($> 10^{5.5}$ K) and the cooling radius is smaller than the virial radius. Therefore, we suggest that the whole gaseous halo should be divided into two parts – the inner high-density region within the cooling radius and the outskirts , which is a low-density region. In the inner region, the cooling produces a multi-phase medium, therefore, the `TCIE` model is preferred. Also, in this case the boundary condition is satisfied to maintain the system in a steady-state. Beyond the cooling radius, the `PIE` model is appropriated due to the density of $\lesssim 5 \times 10^{-5}\ {\rm cm}^{-3}$.

7.4.2 The Multi-Phase Cooling Medium With Photoionization

The `TPIE` model – the stable radiative cooling model with the photoionization – is a more complex extension of the earlier models, and there are two potential

issues with such a model. First, with the effect of photoionization increasing, the gas could be in a net heating phase, which could break our assumption on the stable radiative cooling model. This phenomenon is important where the photoionization might support gaseous components in special situations, such as at 10^4 K and within ~ 1 kpc of the plane (as occurs in the Milky Way – the gaseous disk). However, this case is not the aim of our models. Second, the `TPIE` model leads to a radial dependence in the temperature distribution, since `PIE` cooling curves have a dependence on the density. This involves the modeling of the cooling flow, which is not included in our models. Meanwhile, as we will show below, the `TCIE` and `PIE` models can be a good approximation for the `TPIE` model in different situations.

In the `TPIE` model, there are two modifications compared to the previously defined model. First, the lower limit of temperature in `TPIE` is no longer fixed at $10^{4.5}$ K due to the potential heating. We set a minimum emissivity of 10^{-26} erg cm^3 s^{-1} (corresponding to a minimum temperature), which sets a dynamic range of more than three orders of magnitude for the emissivity. If this temperature is higher than $10^{4.5}$ K, then the local minimum temperature is changed to the new temperature with the minimum emissivity. In practice, only few percent of gas has the new lower limit of temperature (about 5×10^4 K to 10^5 K), which is not far from our fixed minimum temperature (3×10^4 K). Second, for different temperatures, the density is also different due to the pressure balance, which leads to different cooling curves. However, this involves radiative transfer to obtain the photon spatial distribution in the gaseous halo. Therefore, we ignore such an effect and use the cooling curve of the total density to calculate the mass-temperature distribution for all different temperatures.

In the calculation of `TPIE`, we use the galaxy sample with the typical SFR dependence on the stellar mass. Other parameters are fixed, including the metallicity of $Z = 0.3\ Z_\odot$, redshift of $z = 0$, $\beta = 0.5$, and the impact parameter of $0.3\ R_{\rm vir}$. The

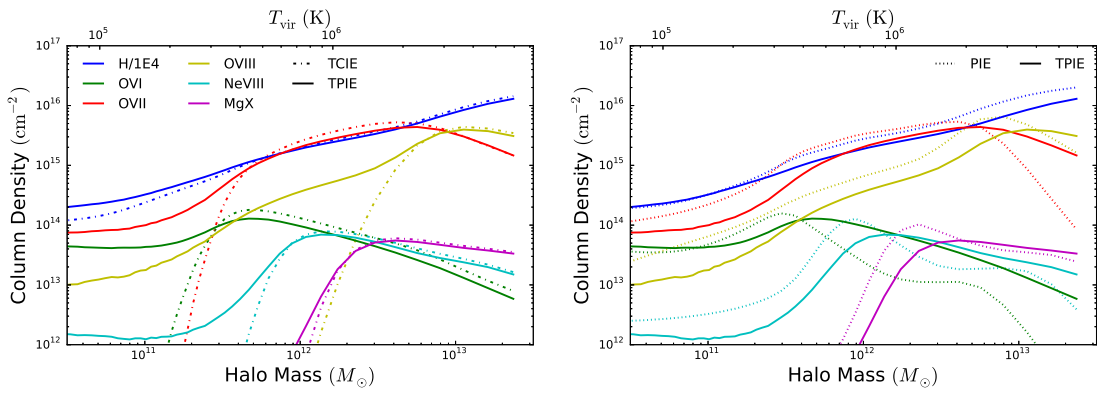

Figure 7.9: The comparison between PIE, TCIE, and TPIE models. Ions have the same colors as in Fig. 7.5, while solid, dotted and dot-dashed lines are TCIE, PIE, TPIE models, respectively. *Left panel*: We compare the TCIE and TPIE models, which are the most realistic. For $T_{\rm vir}$ values below the peak column densities of the TCIE model, the column is considerably enhanced for the metal ions due to the photoionization modification. *Right panel*: We compare the PIE and TPIE models, where more relatively low ions for massive galaxies (e.g., O VI) is produced due to the cooling of the high temperature medium.

results are compared to TCIE and PIE models, as shown in Fig. 7.9.

The gaseous halo mass is proportional to the normalization factor in the β-model, which is also indicated by the hydrogen column density. For the gaseous halo mass, the TPIE model converges to the TCIE model for massive galaxies ($\gtrsim 10^{12.5}\ M_\odot$), and show similarities with the PIE model (with the shift to the high mass galaxy) for low-mass galaxies ($\lesssim 10^{11.5}\ M_\odot$) as expected. Overall, the TPIE is roughly a direct summation of the effect of the photoionization and the cooling temperature distribution. For massive galaxies, the TCIE model is a good approximation of the TPIE model, which has enhanced "low" ionization state ions (e.g., O VII from the cooling of O VIII). In the low-mass range, the gaseous halo is mainly dominated by the photoionization, which enriches the high ionization state abundance at low temperatures (e.g., O VI or O VII). Therefore, the TPIE model can be approximated by a combination of PIE and TCIE models for all mass ranges.

7.4.3 The γ Factor

In our model, we introduce a γ factor in Equation (2) to account for the stellar feedback heating. In the previous calculation, this γ factor is fixed at unity for simplicity. However, the γ factor varies over different galaxies, which is determined by the detailed physics of the stellar feedback – supernovae (SNe), stellar winds, photoionization due to the star light and the radiation pressure (**?**). **?** shows that the SN feedback dominates the stellar feedback, although only SN feedback cannot produce observations.

SNe can launch a galactic wind that ejects materials and energy into the gaseous halo or beyond the virial radius (Fielding et al., 2017a). The strength of the galactic wind can be modeled by the mass-loading factor η as $\dot{M}_{\rm out} = \eta \rm SFR$. The mass-loading factor (at 0.25 $R_{\rm vir}$) has a dependence on the galaxy halo mass (Muratov et al., 2015):

$$\begin{aligned} \eta &= 2.9(1+z)^{1.3} \left(\frac{V_c}{60 \text{ km s}^{-1}} \right)^{-3.2}, \ V_c \leq 60 \text{ km s}^{-1}, \\ \eta &= 2.9(1+z)^{1.3} \left(\frac{V_c}{60 \text{ km s}^{-1}} \right)^{-1.0}, \ \text{otherwise}, \end{aligned} \tag{7.14}$$

where V_c is the circular velocity. This is a specific wind model obtained by parametrizing the galactic winds in the FIRE simulations (Hopkins et al., 2014). For the energy carried by the galactic wind, we only consider the kinetic energy, ignoring the internal energy, since the temperature of the galactic wind is found to be much lower than the virial temperature in simulations (Fielding et al., 2017a). For the wind internal energy, Thompson et al. (2016) showed a semi-analytic model for the cooling wind, and found a drop of the temperature at the radius of $5-10$ kpc for high mass-loading cases ($\eta > 0.8$), which agree with Muratov et al. (2015). The wind temperature is only about one tenth of the virial temperature, when it enters the innermost radius in our model. Therefore, the internal energy of the wind is negligible compared to the virial temperature of the halo.

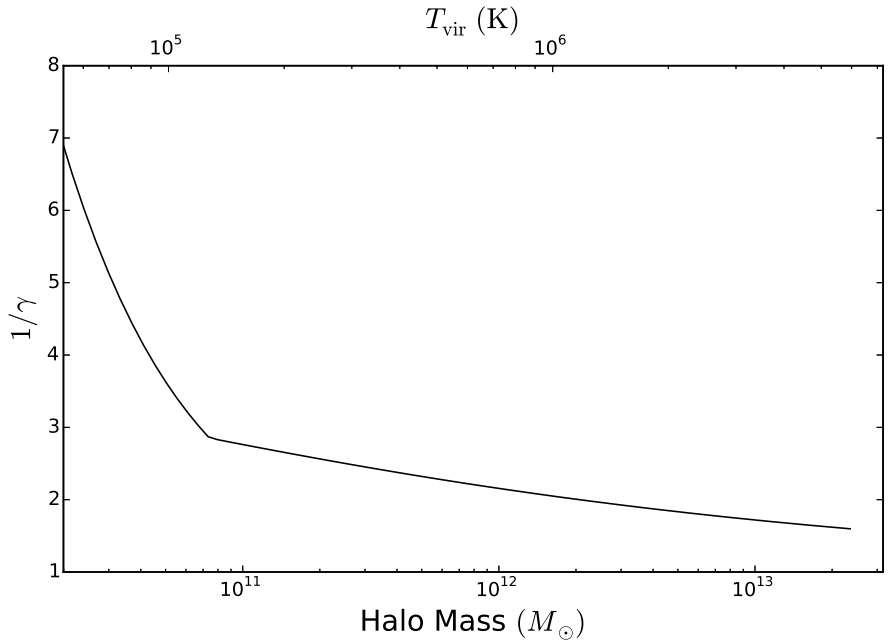

Figure 7.10: The stellar feedback parameter γ as a function of halo mass, where higher $1/\gamma$ indicates stronger stellar feedback heating.

The wind velocity is $V_{\rm wind} = 0.85 V_c^{1.1}$, which is also measured at 0.25 $R_{\rm vir}$ (Muratov et al., 2015). Based on these relationships, we can set an upper limit for the stellar feedback, since not all of the kinetic energy can be converted into the internal energy of the gaseous halo. Some of the galactic wind will be recycled before it is well-mixed with the gaseous halo, and some will be ejected out of the galaxy halo. Therefore, the lower limit of γ factor is calculated by:

$$\frac{1}{\gamma} = 1 + \eta(V_{\rm c})(\frac{V_{\rm wind}^2}{V_{\rm c}^2} - 1), \tag{7.15}$$

Then, the γ factor is around 0.14 for the lowest mass galaxies, and around 0.5 for galaxies with masses higher than 10^{11} $M_\odot$. We show the halo mass dependence of γ in Fig. 7.10.

7.4.4 The O VI Puzzle

From our models, we find that the O VI column lies in a moderately narrow range close to 10^{14} cm^{-2} for all masses of galaxies due to either the photoionization (in low-mass galaxies) or the low-temperature cooling medium (in massive galaxies; Fig. 7.11). Current observations show that the O VI has a significant dependence on the star formation rather than the stellar mass (Tumlinson et al., 2011), which seems to be reproduced by the `TPIE` model. Therefore, we compared the prediction from our models with observations, and we adopt three samples – COS-Halos (Werk et al., 2013), Johnson et al. (2015) and Johnson et al. (2017). Our models have the parameters $Z = 0.3\ Z_{\odot}$, $\beta = 0.5$ and the SFR is from the main-sequence relationship (also modified using redshift; sSFR $\propto (1+z)^3$). The impact parameters of 0.3 $R_{\rm vir}$ and 0.6 $R_{\rm vir}$ are shown since the COS-Halos sample is limited to $< 0.55\ R_{\rm vir}$. The redshift is set to 0.2 since most of the O VI samples have $\bar{z} \approx 0.2$. As shown in Fig. 7.11, the `TPIE` model can be approximated by the combination of `PIE` and `TCIE` with a broad transition around $M_{\rm h} \approx 3 \times 10^{11} M_{\odot}$. Therefore, in the following discussion, the `TPIE` designation represents the combination of `PIE` and `TCIE` models. For low-mass galaxies ($M_{\rm h} \lesssim 3 \times 10^{11} M_{\odot}$), the O VI is mainly ionized through photoionization for the whole gaseous halo, while for the higher mass galaxies, the cooling medium corresponds to the majority of observed O VI. The `TPIE` model predicts a narrow range of column densities from $M_{\rm h} = 3 \times 10^{10}\ M_{\odot}$ to $2 \times 10^{13}\ M_{\odot}$. In most mass regions, the `TPIE` model predicts an O VI column density of $10^{13.5}$ cm^{-2} to $10^{14.1}$ cm^{-2}.

For the COS-Halos sample, the line shape of O VI usually shows multiple components, which can be separated by using the Voigt profile fitting. However, in addition to component separation, there is the issue of the host galaxy. Werk et al. (2013) assigned one galaxy for each multi-component absorption system and calculated the SFR. Therefore, we adopt their measurements based on the apparent optical depth method, which does not separate different components. One caveat is that this treat-

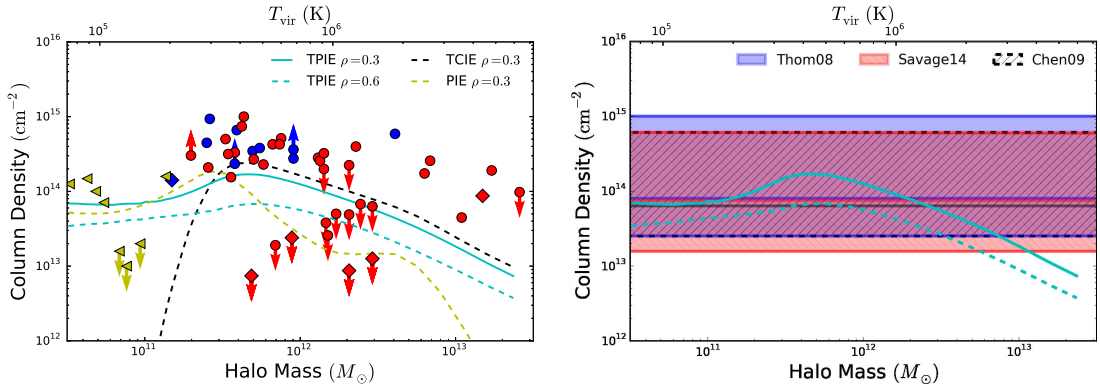

Figure 7.11: Comparison of O VI columns in our models and observations. *Left panel*: Comparison with O VI-galaxy pairs. The cyan lines are the `TPIE` model, and the solid line has an impact parameter of 0.3 $R_{\rm vir}$, while the dashed cyan line is 0.6 $R_{\rm vir}$; most observations fall between these two impact parameters. The black dashed line is the `TCIE` model with an impact parameter of 0.3 $R_{\rm vir}$, while the yellow dashed line is `PIE` model with the same impact parameter. The filled circle marks the O VI column in Werk et al. (2013), and the red color indicates that the SFR is lower than the typical SFR, while the blue color indicates higher SFR values. The upper limit for column density is the detection threshold. The sample of Johnson et al. (2015) is shown by diamond symbols, and the color indicates whether the galaxy is early-type (red) or late-type (blue). The sample of Johnson et al. (2017) is shown in yellow left triangles. The COS-Halos sample lies about 0.5dex over our models. *Right panel*: Comparison with blind O VI surveys. Three samples are marked in blue, black slashed, and red slashed regions for Thom & Chen (2008a), Chen & Mulchaey (2009), and Savage et al. (2014), respectively. The median value for these samples are shown in corresponding solid lines, which are consistent with our models.

ment of different components might give higher O VI column densities than the isolated gaseous halo. Several galaxies in the COS-Halos sample have other lower mass galaxies at the same redshift in the same field or lie in galaxy groups, which may introduce contamination from the other galaxies or from the intragroup medium. Since the COS-Halos sample also provides the SFR for each galaxy, we mark with blue a galaxy that has a SFR higher than the SFR calculated from the SFR main sequence, while a lower one is red. For galaxies with non-detections of O VI, we set the upper limit as the detection limit if it is available.

The Johnson 2015 sample considered galaxies in groups or clusters with isolated galaxies, so we used only isolated galaxies with impact parameters smaller than the virial radius. Johnson et al. (2015) do not have information on the SFR, but they report the galaxy type. Therefore, we assign early-type galaxies with red colors and late-type with blue colors. This color encoding is different from the COS-Halos sample, but will not affect the general tendency. The Johnson 2017 sample focuses on dwarf galaxies with stellar masses in $\log M_\star = 7.7 - 9.2$ (Johnson et al., 2017). For these galaxies, no color is assigned, since no SFR information is available.

In Fig. 7.11, most of the detected O VI have column densities of $\gtrsim 10^{14}$ cm^{-2}, no matter whether the SFR is above or below the typical SFR. Overall, the difference is about $0.3 - 0.5$ dex, which may be accounted for by two explanations. One is the heating from the stellar feedback, which might produce a smaller γ factor in Equation (2). A factor of 4 to 10 can raise the normalization factor in the β-model by a factor of 2 to 3, which also raises the O VI column density by the same ratio. Similarly, McQuinn & Werk (2018) showed that a cooling flow with 100 $M_\odot$ yr^{-1} can account for the observed O VI column density, and that most of the cooling flow might be destroyed by stellar feedback. However, the galactic wind only feedback model is unlikely to be sufficiently energetic based on our calculation in Section 4.3. Another possibility is that the observed O VI is overestimated due to the intragroup medium

contamination or the overlap of multiple gaseous halos in the sightline (Stocke et al., 2014).

To address this possibility further, we do not limit the sample to O VI-galaxy pairs, but also consider all intervening O VI absorption systems from blind surveys. We consider three samples – Thom & Chen (2008a), Chen & Mulchaey (2009), and Savage et al. (2014). These three samples have some overlap with each other, but since the detection methods are not the same, they are also complementary to each other. In Thom & Chen (2008a), the median O VI column density is $\log N(\mathrm{OVI}) = 13.9$ with a standard deviation of 0.4 dex, while in Chen & Mulchaey (2009), the O VI column density has a median value of $\log N(\mathrm{OVI}) = 13.8$ and a scatter of 0.4 dex. In Savage et al. (2014), the components are reported separately. The median column density of single O VI components is $\log N(\mathrm{OVI}) = 13.68$ with a range of 13.00 to 14.59. The average number of components per O VI absorption system is around 1.6, which leads to the average O VI column density for each O VI system of $\log N(\mathrm{OVI}) = 13.87$. These three surveys are consistent with each other in terms of the median and range of $N(\mathrm{OVI})$.

Although these intervening O VI systems currently do not have detected host galaxies, it is possible that they are also the gaseous halo of galaxies, whose luminosities are below 0.1 L^* ($M_h < 3 \times 10^{11}\ M_\odot$; the detection limit of the COS-Halos galaxy sample). If this is the case, these O VI observations show a significant difference from the COS-Halos sample, whose median is $\log N(\mathrm{OVI}) = 14.5$ with a scatter of 0.26 dex (only accounting for the detected O VI).

Since the COS-Halos sample provides the SFR for each O VI-galaxy pair, we built a specific model (with γ) for individual systems based on its stellar mass, SFR, and impact parameter from Werk et al. (2014). We only use the physical impact parameter from the COS-Halos sample, and we recalculate the relative impact parameter using R_{vir} calculated from Equation (3) with a mean halo density of $200\rho_{\mathrm{crit}}$ rather than

$200\rho_{\rm matter}$. These recalculated virial radii are smaller than those presented in Werk et al. (2014) by a factor of $\approx 30-40\%$ within the redshift range of $z = 0.14 - 0.36$. This modification leads to larger relative impact parameters. For the QSO-galaxy pair J1437+5045 and 317_38 (here we use the same notation of COS-Halos sample – position angle and angular separation), our calculation leads to the virial radius of 140.2 kpc, which indicates that the absorption system is beyond the virial radius at $z = 0.246$ with the impact parameter of 143 kpc. Although different stellar mass-halo mass relationships and different cosmological constants can lead to different results on the virial radius, the systems with reported $\rho/R_{\rm vir} > 0.5$ are actually further out in the halo ($\rho/R_{\rm vir} > 0.8$).

Our calculations for the O VI column density are shown in Fig. 7.12. If the SFR of a galaxy is the upper limit, we can only derive the upper limit of the O VI column density. Among 30 systems with detectable O VI, there are five that do not have measurable SFRs. It is clear that some of these five systems are in galaxy groups – the galaxy 211_33 of QSO J1133+0327 has a similar redshift ($\Delta z < 0.0002$) to the galaxy 110_5 adopted in the COS-Halos study, and the galaxy 35_14 of QSO J0910+1014 has the similar redshift of the galaxy 242_34. For these O VI absorption systems, it is possible that they are due to the intragroup medium or smaller galaxies that are closer, since we have shown that the O VI column density can be detected for low-mass galaxies ($M_{\rm h} < 3\times10^{11}\ M_\odot$), which is consistent with observations (Johnson et al., 2017). Such contamination may also explain some of the difference between the model and the observation. As shown in Bregman et al. (2018), there are two small galaxies surrounding QSO J1009+0713 with a redshift of 0.3556 similar to the galaxy 170_9 (0.3557). For this system, the O VI has four components, which have velocities of -95 km s^{-1}, 25 km s^{-1}, 117.2 km s^{-1}, and 200.7 km s^{-1}. For the galaxy 170_9, our model predicts $\log N({\rm OVI}) = 14.41$, while the two components of two high velocities are 14.21 ± 0.16 and 14.34 ± 0.05, respectively. The two components at low

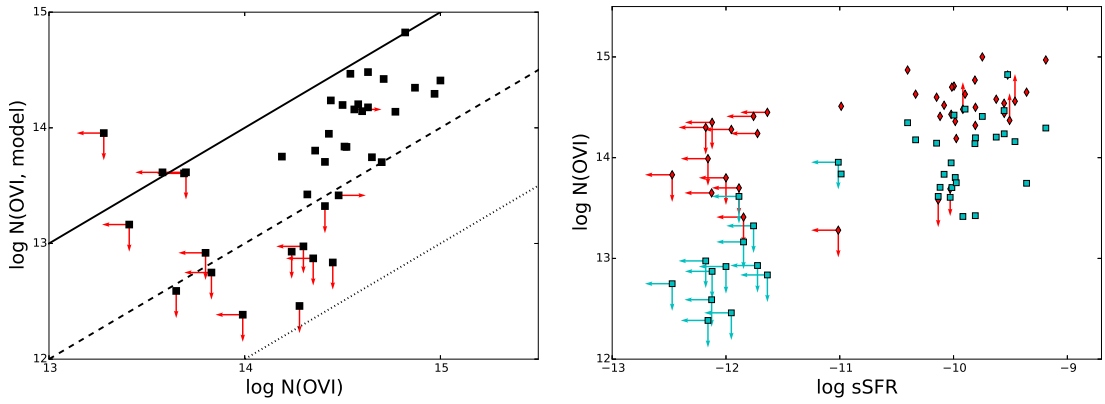

Figure 7.12: Specific models for the COS-Halos O VI sample. *Left panel*: For each system, the predicted O VI column density is calculated with the reported stellar mass, the SFR, and the impact parameter. If the SFR is only an upper limit, then our models predict an upper limit. The solid, dashed, and dotted lines indicate models are equal to observations, 10%, and 1% of observations. For detected objects, the model are typically a factor of $3-5$ lower than the observations, which is consistent with Fig. 7.11. *Right panel*: The sSFR dependence of the O VI column density. The red diamonds are the observations, while the cyan squares are our models.

velocities are larger contributors (14.61 ± 0.05 and 14.52 ± 0.12) to the total O VI column density of 15.00 ± 0.03, and we suggest that they may be associated with the two small galaxies with slightly lower redshifts. Overall, our specific models show a difference of 0.5 dex smaller than the detected O VI from COS-Halos, which is similar to our general comparison shown in Fig. 7.11.

In Fig. 7.12, we also show the relationship between the sSFR and the O VI column density. Our models show results similar to the Evolution and Assembly of GaLaxies and their Environments (EAGLE) simulation (Oppenheimer et al., 2016). For star-forming galaxies, the predicted O VI column densities are about 0.5 dex lower than the observation, while we predict lower O VI column densities for passive galaxies (our upper limit is lower than those simulated in EAGLE; Oppenheimer et al. 2016). The difference for passive galaxies may be due to the lack of AGN heating in our models. The AGN feedback is also proposed to explain the strong O VI in

star forming galaxies (**?**), but as discussed above, this difference is possibly due to contamination in COS-Halos sample.

7.4.5 The Galactic O VII/O VIII

The O VII and O VIII ions have resonant lines in the X-ray band at 21.60 Å and 18.97 Å. However, the detection of these two ions is limited by the current X-ray observatory sensitivity, and only O VII and O VIII in the Milky Way have been confirmed in both absorption and emission (Nicastro et al., 2002; Wang et al., 2005; Henley & Shelton, 2012). The modeling of the O VII and O VIII emission lines shows that the gaseous halo of the MW has a normalization parameter of $1.35 \pm 0.24 \times 10^{-2}/Z$ cm^{-3} kpc$^{-1.5}$ (Miller & Bregman, 2015). For the MW model, we adopt $M_\star = 7 \times 10^{10}$ $M_\odot$, $M_{\rm h} = 1.7 \times 10^{12}$ $M_\odot$, $Z = 0.3$ $Z_\odot$ and a SFR of 1 $M_\odot$ yr^{-1}. This MW model leads to a normalization parameter of 1.75×10^{-2} cm^{-3} kpc$^{-1.5}$, 1.62×10^{-2} cm^{-3} kpc$^{-1.5}$, 1.24×10^{-2} cm^{-3} kpc$^{-1.5}$ and 1.15×10^{-2} cm^{-3} kpc$^{-1.5}$ for the `CIE`, `PIE`, `TCIE` and `TPIE` models, respectively. For a distance to the galactic center of 8 kpc, the sightline with the galactic latitude of 90° has a column density that is half of the sightline with an impact parameter of 0.03 $R_{\rm vir}$ (8 kpc). Then, the predicted column density is $\log N({\rm OVII}) = 15.6$, 15.7, 15.8, 15.6 for `CIE`, `PIE`, `TCIE` and `TPIE`, respectively. These column densities lead to an EW of 12 mÅ ($\log N({\rm OVII}) = 15.7$), which is less than the most of the observations as summarized in Hodges-Kluck et al. (2016b), where the mean in this direction ($b > 60°$) is about 25 mÅ. The corresponding O VIII column densities are 13.9, 14.7, 13.0 and 14.4 for our four models, which is about one order of magnitude lower than observations (Gupta et al., 2012). These modelings show two issues – the ratio of $N({\rm OVIII})/N({\rm OVII})$ is too low and the total amount of oxygen is less than the observation.

For the $N({\rm OVIII})/N({\rm OVII})$ ratio, there are two ways of improving the agreement with Galactic observations – raising the maximum temperature or extending

the gaseous halo beyond the virial radius. First, for a $M_{\rm h} = 1.7 \times 10^{12}\ M_{\odot}$ halo, the virial temperature is around 10^6 K, while the measured hot gas temperature is around $1.5 - 2 \times 10^6$ K (Henley & Shelton, 2012; Miller & Bregman, 2015; Nevalainen et al., 2017). Also, it is evident that the hot gas temperature is higher than the virial temperature for most elliptical galaxies (Davis & White, 1996; Brown & Bregman, 1998; Goulding et al., 2016). This higher temperature can increase the N(OVIII)/N(OVII) ratio significantly, since the O VIII ion traces the higher temperature gas. Second, an extended gaseous halo also changes this ratio involving the photoionization modification as shown in the Section 3.3. Therefore, increasing the maximum radius helps to increase the N(OVIII)/N(OVII) ratio.

To increase the total amount of the oxygen, there are also two approaches – having an extended gaseous halo and increasing the metallicity. For the MW, the cooling radius is smaller than the virial radius, which means that the larger maximum radius will not reduce the normalization factor in the β-model, so this modification only increases the gaseous component surrounding the galaxy, hence the metal mass. As stated in Section 3.2, for a given galaxy-gaseous halo pair (fixed the SFR and the halo mass), higher metallicity leads to a higher total metal mass, although the gaseous halo mass is reduced. Therefore, a higher solar metallicity halo can solve the problem of the small O VII column density in our model.

To illustrate these possibilities, we construct a `TPIE` model to match the galactic O VII and O VIII observations. In the modified model, we vary two parameters – the maximum temperature $T_{\rm max} = \alpha T_{\rm vir}$ and the metallicity. We use the observation summarized in Faerman et al. (2017), which has $N(\mathrm{OVII}) = 1.4(1.0-2.0) \times 10^{16}$ cm^{-2} and $N(\mathrm{OVIII}) = 0.36(0.22-0.57) \times 10^{16}$ cm^{-2} (also see Gupta et al. 2012; Fang et al. 2015). The O VI is also considered to show whether it can be reproduced in the same model, and the column density of halo O VI is $\log N(\mathrm{OVI}) = 13.95 \pm 0.34$ (Sembach et al., 2003). For the O VI column density, the contribution from the disk is excluded

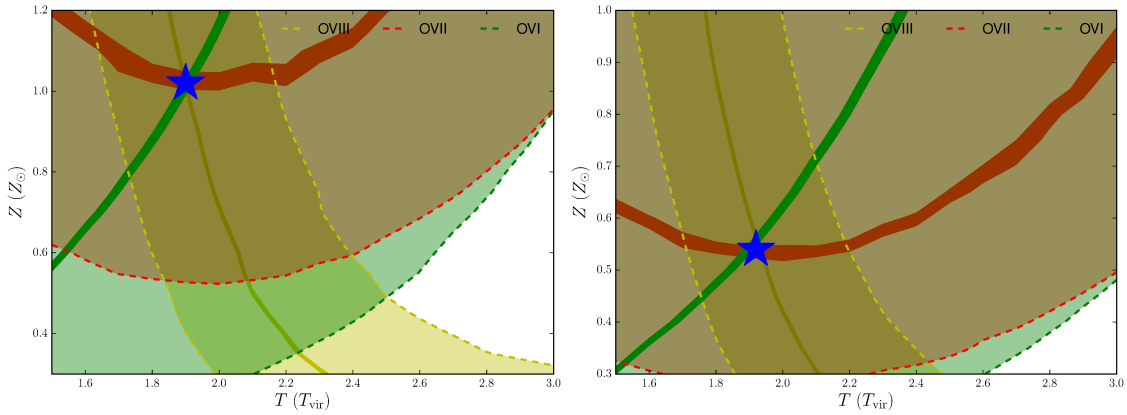

Figure 7.13: Modified model for Galactic O VII and O VIII, constrained by observations, as a function of metallicity and temperature. *Left panel*: Models with the nominal value for γ (= 1). The dashed lines indicate the acceptable region for each ion within 1σ. O VIII, O VII, and O VI are in yellow, red, and green, respectively. The thick colored lines indicates the median value of different ions. The blue star indicates the preferred solution with $T \approx 1.90 \times 10^6$ K and $Z = 1.02\ Z_\odot$. *Right panel*: Models with enhanced stellar feedback ($\gamma = 0.5$), as given in Fig. 7.10. The symbols are the same as the left panel, but the preferred solution is $T \approx 1.93 \times 10^6$ K and $Z = 0.55\ Z_\odot$.

based on the velocity criterion (Savage et al., 2003).

In Fig. 7.13, we explore the parameter space of $\alpha = 1.5 - 3$ and $Z = 0.3 - 1.2\ Z_\odot$, which is determined by the $N(\mathrm{OVIII})/N(\mathrm{OVII})$ ratio and column densities. The acceptable region for each ion is constrained by the observational limits, therefore, the overlap region indicates the preferred parameter space, while the cross of lines indicates the preferred model. Our modified model suggests a super-solar metallicity of 1.02 $Z_\odot$ and a maximum temperature of 1.9×10^6 K. This high metallicity solution is not favored since it is very unlikely for the gaseous halo to have higher metallicity than the galaxy disk. This high metallicity is caused by the high oxygen column density in the observation, which can be solved when the γ factor is considered.

Involving the γ factor in Equation (2) can lead to a higher mass gaseous halo, since a $\gamma < 1$ leads to a higher radiative cooling rate. The typical γ factor for the MW is around 0.5. Applying this modification to our model, we will obtain lower metallicity

solutions, since the small γ factor leads to a more massive gaseous halo and more metals. Then it is not necessary to have high metallicities to account for observed oxygen. We obtain the best model of the MW gaseous halo with the metallicity of 0.55 $Z_{\odot}$ and the maximum temperature of 1.9×10^6 K, showing column densities of $\log N = 13.95$, 16.15 and 15.53 for O VI, O VII, and O VIII ions, respectively. The normalization factor of the β-model is 1.91×10^{-2} cm^{-3} kpc$^{3\beta}$, and the gaseous halo mass is 1.94×10^{10} $M_{\odot}$, which contributes 7% to the total baryon mass. The emission line studies of O VII show a normalization factor of $3.39^{+0.67}_{-0.55} \times 10^{-2}$ cm^{-3} kpc$^{3\beta}$ with 0.3 $Z_{\odot}$ (Li et al., 2017b), which is equivalent to 1.85×10^{-2} cm^{-3} kpc$^{3\beta}$ with 0.55 $Z_{\odot}$. Therefore, our MW gaseous halo solution also matches with the emission line study.

We now consider the magnitude of column density increases when the gaseous halo is extended beyond the virial radius. Assuming the maximum radius is twice the virial radius, the change in the column density is about 5% to 8%, which is not enough to account for the observed O VII and O VIII column density. Therefore, compared to the heating due to the stellar feedback, extending of the maximum radius is a secondary effect for the column density, although it leads to a significant increase in the mass, which will be discussed in Section 4.7.

7.4.6 Intervening Ne VIII/Mg X Systems

The Ne VIII and Mg X occurs in the extreme UV band (770 Å and 610 Å respectively), which can only be detected for extragalactic galaxies due to the wavelength limit of Galactic absorption (912 Å) and due to the UV observing band of *HST*/COS ($1150 - 1750$ Å). The Ne VIII is detectable in the redshift of 0.5 to 1.3, while the Mg X is detectable between $z = 0.9$ and 1.8. At higher redshift, galaxies have a higher mean sSFR, which results in a more massive gaseous halo. In the redshift range of $z = 0.7$ to $z = 1.2$, the SFR is raised by a factor of $5 - 10$, which makes the gaseous halo $2 - 3$ times more massive, with a similar increase in the column density

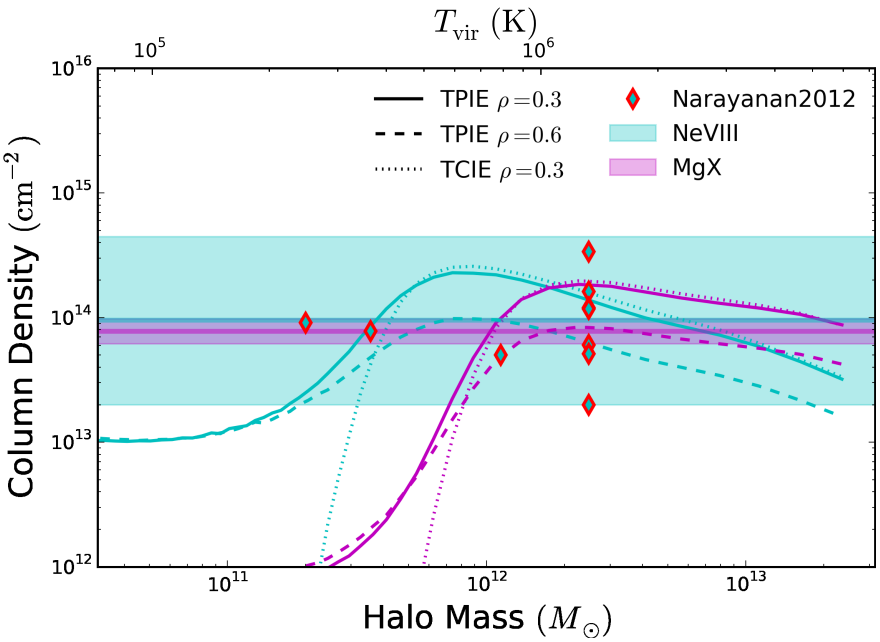

Figure 7.14: Comparison of Ne VIII (cyan) and Mg X (magenta) in our models and observations. The solid, dashed, and dotted lines are the `TPIE` model with impact parameters of 0.3 $R_{\rm vir}$, 0.6 $R_{\rm vir}$, and the `TCIE` model with 0.3 $R_{\rm vir}$. The Ne VIII-galaxy pair data is from Narayanan et al. (2012), while the Ne VIII absorption in PG 1206+459 is broken into seven components, and it is not clear which one corresponds to the reported galaxy (Tripp et al., 2011).

of Ne VIII and Mg X. In Fig. 7.14, we show our models of the Ne VIII and Mg X columns at the redshift of 1.

As summarized in Pachat et al. (2017), the median of the detected Ne VIII is $\log N(\mathrm{NeVIII}) = 13.98 \pm 0.31$, varying in the range of $\log N(\mathrm{NeVIII}) = 13.30$ to 14.65. The observed Ne VIII column density shows consistency with our model in a wide galaxy mass range. For the host galaxy, current observations show it varies from 0.08 L^* to ≈ 2 L^*(Narayanan et al. 2012 and reference herein), which is also well matched with our models. For MgX, there is only one detection towards LBQS 1435-0134, with the column density of $\log N(\mathrm{MgX}) = 13.89 \pm 0.10$ (Qu & Bregman, 2016), which is also consistent with the model for a (sub-)L^* galaxy.

The Mg X system in LBQS 1435-0134 is a good example to study the multi-phase medium in the gaseous halo since it has a wide ionization state coverage (i.e., from O III to Mg X), and most of them are high ionization state ions (higher than O IV). In Qu & Bregman (2016), it is modeled by a three-temperature `CIE` model or a power law model of the column density-temperature distribution with an index of 1.55. This power law model has a total χ^2 of 3.3 with 7 degrees of freedom. We notice the power law index is approximately the slope of the mass-temperature distribution $M(T)$ in the cooling model, therefore we fit this Mg X system using the `TCIE` model (Fig. 7.15). The only one variable is the stellar mass, and the SFR is calculated based on the stellar mass and modified by the redshift of 1.2. We use three different impact parameters of 0.2, 0.3 and 0.6. The fitting results are $\log M_\star = 10.76$ ($\log M_\mathrm{h} = 12.1$) with total $\chi^2 = 65.7$ ($dof = 10$), 10.64 (12.0) with $\chi^2 = 30.0$ (10) and 10.56 (11.9) with $\chi^2 = 131.1$ (10), respectively. Therefore, the Mg X system is likely to be a (sub-)L^* galaxy at the redshift of 1.2. For the best model with $\rho = 0.3\ R_\mathrm{vir}$, the most of χ^2 (22.0/30.0) is from three ions H I, O IV and Ne VIII. These deviations may be caused by the uncertainty in the lower and the upper limits of the temperature distribution. Extending the lower limit can increase the low and intermediate ionization state ions, while extending the upper limit can decrease the Ne VIII column density as shown in Fig. 7.14 regarding the $\log M_\mathrm{h} = 12.0$. Therefore, although the best reduced χ^2 is around 3, it is a valuable step in modeling such a complex object (the gaseous halo) with a simple physical model.

7.4.7 Mass Budget

The galaxy missing baryon problem is a crucial aspect of both observation and theory for galaxy formation and evolution, so we also check whether our gaseous halo model can address this issue. In Fig. 7.16, we show the baryonic fraction for models considered for typical star-forming galaxies. In all mass regions, the cosmic baryonic

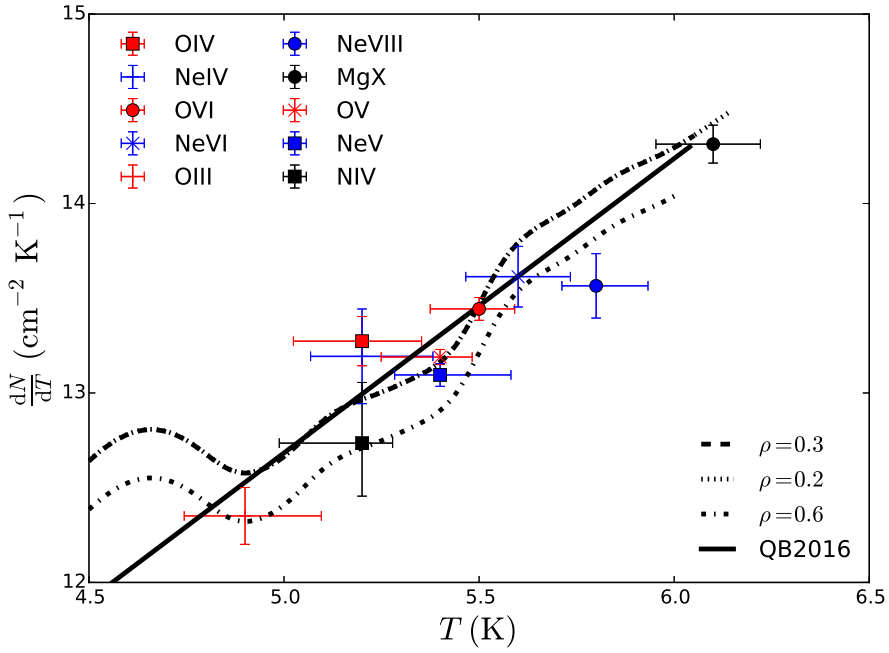

Figure 7.15: The fitting result of `TCIE` for the Mg X system in the sightline towards LBQS 1435-0134 (Qu & Bregman, 2016). For each ion, the temperature is the peak temperature of the ionization fraction, and the error bar is the full width of the half maximum, while the y axis value is the normalized column density gradient, which is given by $\frac{dN_{\rm H,ion}}{dT} = \frac{dN_{\rm H,model}}{dT} \times N_{\rm ion,observed}/N_{\rm ion,model}$. The solid line is the power law model in Qu & Bregman (2016), while dashed, dotted, dash-dotted lines are stable cooling models with impact parameters of 0.3 $R_{\rm vir}$, 0.2 $R_{\rm vir}$, and 0.6 $R_{\rm vir}$, respectively. Note that the $\rho = 0.2$ $R_{\rm vir}$ line overlaps with the $\rho = 0.3$ $R_{\rm vir}$ line. Therefore, it is clear that the observed power law column density distribution is actually a result of the cooling medium.

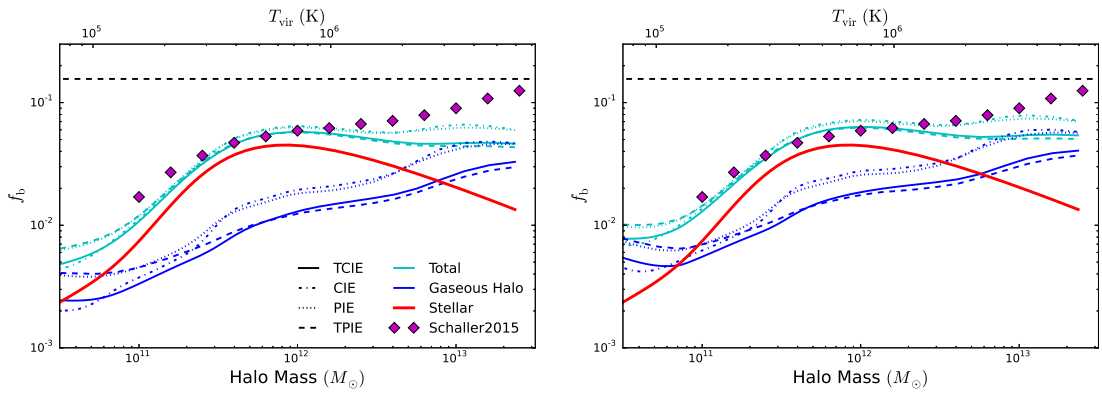

Figure 7.16: The baryonic fraction dependence on the halo mass. *Left panel*: The `CIE`, `PIE`, `TCIE` and `TPIE` models are shown in dot-dashed, dotted, solid and dashed lines, while the black dashed line is the cosmic baryonic fraction, and the red solid line is the stellar content baryonic contribution. Blue lines are the gaseous-halo-only baryonic fraction, while cyan lines are the total baryonic fraction enclosed in the virial radius. The magenta diamonds are the baryonic fraction from the EAGLE simulation (Schaller et al., 2015). *Right panel*: The baryonic fraction due to the gaseous halo is increased for the enhanced stellar feedback given in Fig. 7.10. The largest increases occur at lower masses and points at which the stellar and gaseous halos are equal occur at $M_{\rm h} = 6 \times 10^{10}\ M_\odot$ for the `TPIE` model.

fraction is significantly higher than the total baryonic fraction of galaxies, which indicates that the gaseous halo within the virial radius cannot account for missing baryons of galaxies in the mass region considered. The overall tendency shows that the low-mass galaxy is more baryon-poor than the massive galaxy, showing a sharp rise between $M_{\rm h} \sim 10^{11}\ M_\odot$ and $4 \times 10^{11}\ M_\odot$. The baryonic fraction is almost a constant $f_{\rm b} \approx 0.05 - 0.06$ for galaxies with higher masses than $5 \times 10^{11}\ M_\odot$.

These baryonic fractions are the median values for galaxies at different masses, while it is possible to have significant scatter due to the SFR scatter. With the SFR scatter of 0.4 dex (Renzini & Peng, 2015), the baryonic fraction could have a scatter of 0.2 dex based on the square root relationship between the sSFR and the gaseous halo mass. This scatter is consistent with cosmological simulations, which shows the baryonic fraction can vary between 20% to 100% of the cosmic baryonic fraction

(Marinacci et al., 2014; Muratov et al., 2015; Schaller et al., 2015; Suresh et al., 2017).

That low-mass galaxies have a low $f_{\rm b}$ is the direct result of both low stellar mass and the high cooling rate. Although they have a relatively high sSFR, the gaseous halo is still low mass and comparable to the stellar mass within a factor of 2. This tendency is consistent with the simulation effort (EAGLE) when the halo mass is smaller than $\approx 3 \times 10^{12}\ M_{\odot}$ (Schaye et al., 2015; Schaller et al., 2015). EAGLE has prescriptions for the star formation, stellar evolution, stellar feedback and AGN feedback. The discrepancy between the EAGLE simulations and our models in the high mass region is due to the lack of heating from the AGN feedback in our model, which is positively related to the halo mass rather than the stellar mass. In the low-mass region, the baryonic fraction in our model is slightly less than Schaller et al. (2015) by a factor of $\lesssim 2$ at the halo mass of $10^{11}\ M_{\odot}$. This might emphasize the importance of the stellar feedback for the low-mass galaxies, and a γ factor of $0.1-0.2$ can account for such a difference. Involving the γ factor described in Section 4.3, we set the upper limits for the baryonic fraction in our models, which is also shown in Fig. 7.16. The modification on the γ factor leads to higher baryonic fraction in low-mass galaxies, which is consistent with our hypothesis that low-mass galaxies have higher stellar feedback heating.

However, the trend of increasing baryonic fraction with the halo mass is significantly different from the Illustris simulation, which also has full stellar physics and AGN feedback (Vogelsberger et al., 2014). The Illustris simulation shows the opposite tendency with the low-mass galaxy having more baryonic material (even higher than the cosmic baryonic fraction) enclosed in the virial radius (Suresh et al., 2017). This result may be a result of the photoionization, which is included in Illustris but not EAGLE. Our models show that the photoionization modification is important for low-mass galaxies, since it can support a more massive gaseous halo. Nevertheless, the divergence between Illustris and EALGE is very unlikely to be caused by the

photoionization modification, since it has also been shown that the photoionization can only raise the gaseous halo mass by a factor of about 2, down to the stellar mass of $8 \times 10^7\ M_\odot$ (see Section 3.1). This difference is more likely to be caused by the weak stellar feedback employed in Illustris, which is set to keep gas inside the halo (Suresh et al., 2017).

Another consideration that might moderate the missing baryon problem is having a gaseous halo extending beyond the virial radius. When we change the outermost radius for the gaseous halo from one virial radius to twice the virial radius, the gaseous halo mass is increased by a factor of the $2-3$. For an L^* galaxy ($M_h = 1.7 \times 10^{12}\ M_\odot$, SFR $= 5\ M_\odot\ \mathrm{yr}^{-1}$), the cooling radius is 173 kpc (less than the virial radius of 253 kpc), which indicates that the increasing of outermost radius will not change the normalization factor in the β-model. Modifying the outermost radius raises the mass from $2.6 \times 10^{10}\ M_\odot$ to $7.4 \times 10^{10}\ M_\odot$, raising the baryon fraction from 0.055 to 0.083. Therefore, in the case that the cooling radius is smaller than the virial radius, the factor is fixed to 2.83, otherwise, the factor is slightly smaller but still around 2. This would raise the baryonic fraction, but still not enough to account for all of the missing baryons for L^* galaxies. For the high mass and the low-mass end of the galaxy distribution, the total baryonic fraction is raised by a factor of ≈ 2, since most of the mass is in the gaseous halo rather than the stellar content.

7.4.8 Future Observations

An issue highlighted by this work is that one needs measurements for ions that are the dominant volume filling ions, which traces the gas that is near hydrostatic equilibrium and is at the temperature of most of the gaseous mass. In practice, this requires that we obtain O VII and O VIII absorption line data for galaxies with $M_\mathrm{h} > 3 \times 10^{11}\ M_\odot$. Absorption in O VII is available for the MW for about two dozen sight lines and in O VIII for a handful of objects (Fang et al., 2015; Hodges-

Kluck et al., 2016b). A significant advance can be realized through improved S/N for O VII and especially O VIII as well as for a larger number of sightlines. This will not happen with existing instruments (*XMM-Newton* and *Chandra*), which have already devoted about 20 Msec of observing time toward bright objects, so improvements would require several times this amount.

For external galaxies, no O VII or O VIII absorption lines have been detected (Nicastro et al., 2016b). Sight lines through the halos of external galaxies ($0.3-1\ R_{\rm vir}$) are expected to be nearly an order of magnitude weaker than those from the MW. The failure to see these lines is consistent with model predictions, given the sensitivity of current instruments and the amount of redshift space that has been probed.

Detecting O VII and O VIII through a sample of external galaxy halos will require a new instrument with capabilities that offer at least an order of magnitude improvement. Such an instrument would also offer a breakthrough in the study of these lines in the MW. This level of improvement is possible through *Arcus* (Smith et al., 2016b), an Explorer class mission that will have nearly an order of magnitude improvement in both spectral resolution and in collecting area, relative to the *XMM-Newton*/RGS (and a larger improvement relative to the *Chandra*/LETG). The spectral resolution will be about 3000 (100 km s^{-1}), providing kinematic information as well as insights into turbulence. The *Athena* mission will also add to our understanding of these absorption systems, but its spectral resolution is poorer than that of *XMM-Newton* (1300 km s^{-1}), so kinematic information will be limited (Barcons et al., 2017). The *Lynx* mission concept will offer another order of magnitude increase in collecting area, relative to *Arcus* and with double the resolution (50 km s^{-1}), which approaches the thermal width of gas at 2×10^6 K (Gaskin et al., 2016). It will be sensitive to much weaker lines and will provide excellent kinematic information.

7.5 Summary

We report upon a gaseous halo model connecting the SFR and the radiative cooling rate, including photoionization and a multi-phase medium. This model predicts a comparable gaseous halo mass to the stellar mass, and can be employed to understand observations of high ionization state ions (i.e., O VI, O VII, Ne VIII, Mg X, and O VIII). We summarize our major results:

1. Photoionization is the most important physical process in determining the relative ion distribution in the entire extended gaseous halo of low-mass galaxies and the outskirts of massive galaxies. For low-mass galaxies ($M_{\rm h} < 3 \times 10^{11}\ M_{\odot}$), photoionization supports a more massive gaseous halo, and generates high ionization state ions (e.g., O VI and O VII). For more massive galaxies, photoionization leads to more high ionization state ions in the outskirts (i.e., the O VIII of the MW).

2. The multi-phase medium within the cooling radius can be modeled by the distribution of $M(T) \propto T/\Lambda(T)$. This multi-phase medium leads to a flattened dependence of high ionization state ion column densities with galaxy halo mass. More relatively low ionization state ions (compared to the virial temperature) are generated because of the cooling from the high temperature medium.

3. Overall, our models predict the mass of the gaseous halo is comparable to the stellar mass (within one order of magnitude) for star forming galaxies over all halo masses. The cooling radius is expected to vary between $50-200$ kpc, which is a small variation when compared to the two order of magnitude range in the halo mass.

4. O VI has a narrow range ($\log N({\rm OVI}) = 13.5 - 14.3$) for galaxies with $M_{\rm h} < 10^{13}\ M_{\odot}$. Above $M_{\rm h} = 3 \times 10^{11}\ M_{\odot}$, the O VI is mainly from the collisional

ionization, while below this mass, photons from the UVB ionizes most of O VI ions. The predicted O VI column density range is consistent with blind O VI surveys.

5. A modified model is constructed for the Galactic O VII and O VIII, with changes in the standard metallicity of 0.55 $Z_{\odot}$ and a maximum temperature of 1.93×10^6 K, which is above the virial temperature but similar to that derived from emission ratios. Such a gaseous halo leads to a hot halo mass of 1.9×10^{10} $M_{\odot}$ within the virial radius, which contributes to 7% of the total baryonic mass of the MW.

6. For intervening Ne VIII and Mg X at $z = 0.5 - 1.3$, our models predict column densities of $\approx 10^{14}$ cm^{-2}, which is consistent with observations and informs the detection limit for future observations.

7. Such a gaseous halo cannot close the census of the galaxy missing baryons within $R_{\rm vir}$. Where it is possible to compare, our models results are similar to those of the EAGLE simulations, and about the half of baryons are still missing for L^* galaxies within the virial radius.

CHAPTER VIII

The Mass and Absorption Column Densities of Galactic Gaseous Halos. II. The High Ionization State Ions

8.1 Introduction

During the formation and evolution of galaxies, gases in the cool intergalactic medium (IGM; $T \sim 10^4$ K) fall into dark matter halos and are heated to form the warm-hot intergalactic medium (WHIM; $10^5 - 10^7$ K) by accretion shocks and various galactic feedback processes (Weinberg et al., 1997; Cen & Ostriker, 1999). These warm-hot gases could account for $30 - 40\%$ of the total baryon contents and exist in different forms: the hot galactic gaseous halo; the intra-group (cluster) medium; and the cosmic web (Cen & Ostriker, 2006). However, these warm-hot gases are difficult to detect because of their low densities and high temperatures.

Currently, direct X-ray imaging can detect the intra-group (cluster) medium extending to about the virial radius, while for isolated galaxies, X-ray imaging can only detect the emission from hot gases surrounding nearby massive galaxies within about 50 kpc (Anderson & Bregman, 2010; Bogdán et al., 2013a; Goulding et al., 2016). An alternative detection approach is to stack microwave images to measure the average Sunyaev-Zel'dovich (SZ) effect, which is useful for systems with masses

above $\log M_{\rm h} = 12.3$ (Lim et al., 2018). Stacking galaxy pairs also reveals the existence of hot cosmic filaments between galaxy pairs within ≈ 15 Mpc, which account for $20 - 30\%$ of the total baryonic content of the universe (**??**). However, smaller galaxies ($< L^*$) have too weak an SZ signal, even in a stack ($< 5\sigma$), to measure a useful constraint on the mass or temperature. A third way to detect the hot gaseous component in the universe is by measuring absorption lines from high ionization state ions towards background AGNs – O VI, Ne VIII, O VII, Mg X, and O VIII – which can trace the gas with temperatures from 10^5 K (O VI) to 5×10^6 K (O VIII).

In the past decade, several observational studies of these ions have constrained the column density distributions and the cosmic abundances (Meiring et al., 2013; Savage et al., 2014; Danforth et al., 2016; Frank et al., 2018). The lithium-like ions O VI, Ne VIII and Mg X have strong resonant doublets in the far-ultraviolet (FUV) band with wavelengths of 1031.9 Å, 770.4 Å, and 609.8 Å, respectively (for the strongest of the doublet lines). Using the current FUV instruments (i.e., *Hubble Space Telescope*/Cosmic Origin Spectrograph; *HST*/COS), these ions are detectable in the redshift range of around $0.1 - 0.7$, $0.5 - 1.3$, and $0.9 - 1.9$. O VI has the largest sample among these high ionization state ions because of the low redshift and the high abundance of oxygen (Tripp et al., 2008; Thom & Chen, 2008a). Ne VIII and Mg X are more difficult to detect because they are less abundant than oxygen and require a higher continuum S/N ratio (> 20). Currently, fewer than 10 sightlines have reported Ne VIII absorption lines (see the summary in Pachat et al. 2017 and references therein), while there is only one intervening Mg X detection (in the sightline toward LBQS 1435-0134; Qu & Bregman, 2016). O VII and O VIII occur in the X-ray band and have resonant lines at 21.60 Å and 18.96 Å. The detection of O VII and O VIII absorption lines is limited to the Milky Way (MW; Nevalainen et al. 2017), as detections around external galaxies are still controversial (Fang et al., 2010; Nicastro et al., 2016a). A larger sample of O VII and O VIII will only be feasible with

next-generation X-ray telescopes (e.g., *Arcus*; Smith et al. 2016b).

Absorption lines from high ionization state ions make it possible to study the connection between galaxies and their halos. For example, O VI is more frequently around star forming galaxies, using the COS-Halos sample (Tumlinson et al., 2011; Werk et al., 2016). This phenomenon is also confirmed for star forming dwarf galaxies, which host O VI absorption of $\approx 10^{14}$ cm^{-2} (Johnson et al., 2017).

However, the contributions of gaseous halo to the cosmic high ionization state ions remain as a question, since it is controversial regarding the total baryonic content and the dominant component of gaseous halos. Both the cool gas ($\approx 10^4 - 10^5$ K) and the hot gas ($\approx 10^6$ K) are claimed to account for the missing bayons in L^* galaxies (Gupta et al., 2012; Werk et al., 2014; Nicastro et al., 2016a; Prochaska et al., 2017). Meanwhile, there are other observational studies and theoretical predictions that the total amount of the gases in halos is $\lesssim 30\%$ of the total baryon mass for L^* galaxies (Miller & Bregman, 2015; Schaller et al., 2015; Li & Bregman, 2017; Bregman et al., 2018).

In Qu & Bregman (2018b, hereafter, QB18), we proposed a semi-analytic galactic gaseous halo model (GGHM) that is consistent with most observations of the high ionization state ions. This model enables us to consider the contribution to the cosmic high ionization state ions due to galactic gaseous halos. In this paper, we estimate the column density distribution originating from the galactic gaseous halo by combining the GGHM model with the spatial density of galaxies (i.e., the stellar mass function; SMF). By comparing the predicted column density distribution to observations, we obtain the relative contribution due to the galaxy and constrain the GGHM model. In Section 2, we give a brief summary of the GGHM model and the assumptions required to predict the column density distribution. In Section 3, we find the preferred model parameters, while in Section 4, we discuss our results and implications.

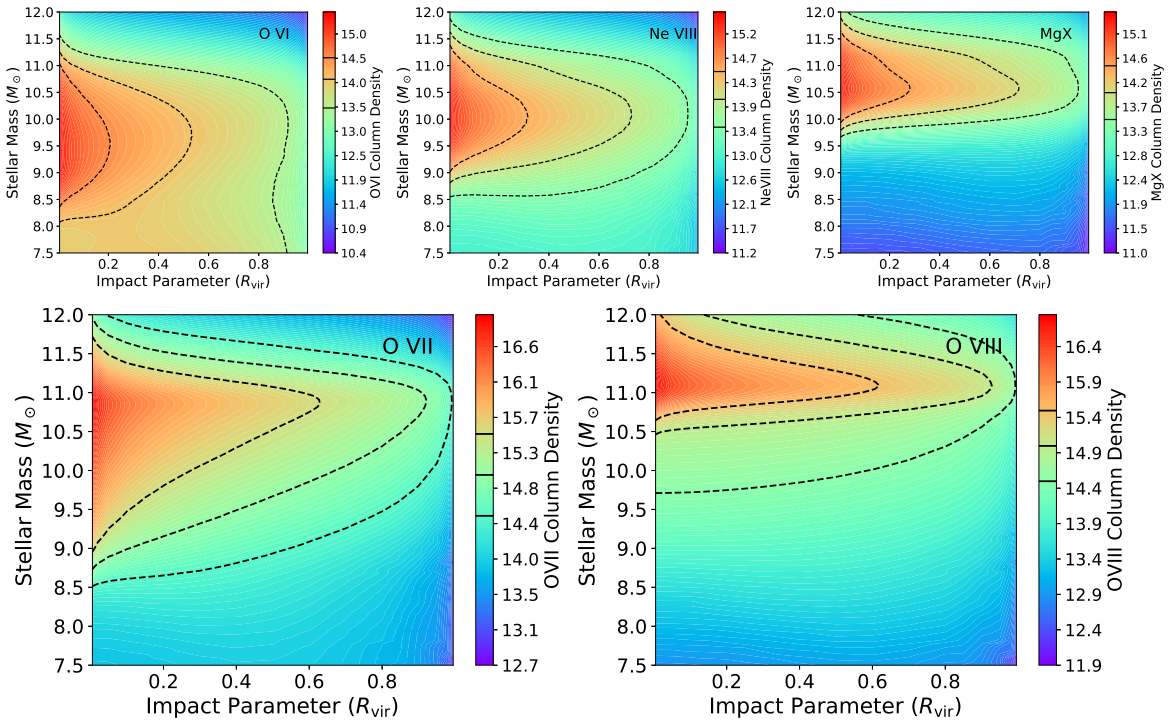

Figure 8.1: The GGHM model for high ionization state ions (i.e., O VI, Ne VIII, O VIII, Mg X, O VIII). The fiducial model has $Z = 0.5Z_\odot$, $T_{\rm max} = 2T_{\rm vir}$, $R_{\rm max} = R_{\rm vir}$ at $z = 0$. For UV ions (i.e., O VI, Ne VIII, Mg X; upper panels), the dashed contour lines are 13.5, 14.0 and 14.5 respectively. The X-ray ions (i.e., O VII and O VIII; lower panels), the contour levels are 14.5, 15.0 and 15.5, respectively.

8.2 Methods

To calculate the galaxy contribution to high ionization state ions in the universe, one needs a galactic gaseous halo model and the galaxy number density (i.e., the star-forming galaxy SMF). We adopted the gaseous halo model introduced in QB18, which connects the galaxy disk and the gaseous halo for star-forming galaxies. Subsequently, the column density distribution is derived by convolving the gaseous halo model with the SMF.

8.2.1 The Gaseous Halo Model

The gaseous halo model is the `TPIE` model in QB18, including the photoionization modification due to the ultraviolet background (UVB) and a time-independent model of the radiative-cooling multi-phase medium. To summarize, our basic assumption is that the star formation rate (SFR) of the galaxy disk is balanced by the radiative cooling rate of the gaseous halo within the cooling radius, where $t_{\rm cooling} = t_{\rm Hubble}$. In QB18, we also consider heating due to feedback processes, which could modify the properties of the gaseous halo. Specifically, we included a galactic wind model from the FIRE simulation (Muratov et al., 2015), which is believed to have a tight relationship with the SFR. In our modeling, a γ factor (SFR $= \gamma \dot{M}_{\rm cooling}$) is introduced to include the heating by stellar feedback, which varies from 0.14 to 0.70 from low-mass galaxies ($M_\star = 3 \times 10^7\ M_\odot$) to massive galaxies ($M_\star = 10^{12}\ M_\odot$). Therefore, once the SFR of the galaxy is obtained, the radiative cooling rate is determined, which will be used to calculate the density of the gaseous halo. The SFR is fixed for different stellar masses and redshifts using the star formation main sequence (Pannella et al., 2009; Morselli et al., 2016). Generally, the low-mass galaxies have lower SFR values but higher specific SFR (sSFR = SFR/$M_\star$) and higher redshift galaxies have higher SFR, roughly $\overline{\rm SFR} \propto (1+z)^3$.

Our multi-phase medium model assumes that there is a hot ambient gas supplying

the "steady-state" gaseous halo and the mass cooling rate is constant over different temperatures, which lead a universal distribution for the mass-temperature distribution (QB18). Photoionization modifies the cooling curve and the ionization fractions at different temperatures; ionization equilibrium is assumed. The gas density profile is fixed as a β-model ($\rho(r) = \rho_0 r^{-3\beta}$) and β is fixed to 0.5 such that the halo is near hydrostatic equilibrium. In the GGHM model, there are also free parameters – the upper temperature limit ($T_{\rm max}$; the ambient gas temperature), the lower temperature limit ($T_{\rm min}$; setting the cooling temperature range), the metallicity (Z) and the maximum radius ($R_{\rm max}$; setting the cutoff of the β-model). Since we only consider the high ionization state ions, our results are not sensitive to the lower temperature limit, therefore, it is fixed to the fiducial value (3×10^4 K) in QB18.

We explore the effect of varying the other parameters ($T_{\rm max}$, Z, and $R_{\rm max}$) in Section 8.3, but here present a fiducial model. We adopt twice the virial temperature as the fiducial $T_{\rm max}$. QB18 showed that a gaseous halo at the virial temperature significantly underestimates the total amount of O VIII gases of the MW. The preferred model indicated that the MW has an ambient gas temperature about twice the virial temperature. This is consistent with X-ray observations of external galaxies, which shows that the gas temperature is about twice the virial temperature (Goulding et al., 2016). In the same model, the derived metallicity of the MW gaseous halo is $0.5-0.6\ Z_\odot$ (as argued by Faerman et al. 2017 and Bregman et al. 2018). The column density measured around the MW is not sensitive to $R_{\rm max}$ in the β-model. Raising the maximum radius from the virial radius to twice the virial radius only increases the O VII and O VIII column densities by 8% (within the measurement errorbar $\approx 20\%$). Therefore, the maximum radius is unconstrained by Galactic observations, but a larger halo does significantly increase the detectable cross-section (Section 8.3). Thus, our fiducial model has $T_{\rm max} = 2T_{\rm vir}$, $Z = 0.5Z_\odot$, and $R_{\rm max} = R_{\rm vir}$.

In Fig. 8.1, we show the high ionization state ion column densities in the fiducial

model, quantifying the dependence on the stellar mass and the impact parameter. In the GGHM model, the origins of high ionization state ions (i.e., O VI, Ne VIII, O VII, Mg X, O VIII) could be divided into three categories: the photoionized virialized gaseous halo; the collisional virialized gaseous halo; and the radiatively-cooling flow (QB18). As galaxy mass increases, collisional ionization becomes more important than photoionization, with the transition at the mass where the virial temperature corresponds to the peak ionization fraction for each ion. Each ion also has the highest column density around the galaxies with the transition mass, which is set by the ionization potential. The transition galaxy mass for O VI is around $M_\star \approx 3 \times 10^9\ M_\odot$ or halo masses of $M_{\rm h} \approx 2 \times 10^{11}\ M_\odot$, while the transition stellar masses are $1 \times 10^{10}\ M_\odot$, $4 \times 10^{10}\ M_\odot$, $8 \times 10^{10}\ M_\odot$, and $1 \times 10^{11}\ M_\odot$ for Ne VIII, O VII, Mg X, and O VIII, respectively. Above the transition mass, the ions are generated in the cooling flows from the hotter ambient gas. The radial dependence of the column density decreases as one expects from the β-model since the ionization fraction is constant over different radii. Below the transition mass, photoionization becomes more important, which weakens the column density dependence on the radius (showing a flattened distributions in the inner region) and allows high ionization state ions to exist for a wide range of stellar masses (see QB18 for details).

8.2.2 The Contribution of Galaxies

To consider the cosmic galaxy contribution, we adopt the SMF to represent the galaxy number density in the universe. The adopted redshift-dependent SMF is from Tomczak et al. (2014), where the SMF is calculated in redshift bins of $\Delta z \approx 0.2$. In Fig 8.2, we show the path-length density (detection rate) of galactic gaseous halos at different redshifts where the maximum radius equals the virial radius. Since the difference between the SMF at $z = 0.0$ and $z = 0.5$ is small ($< 10\%$; Behroozi et al. 2013), we use the same SMF at $0.2 < z < 0.5$ for these two redshifts (Tomczak et al.

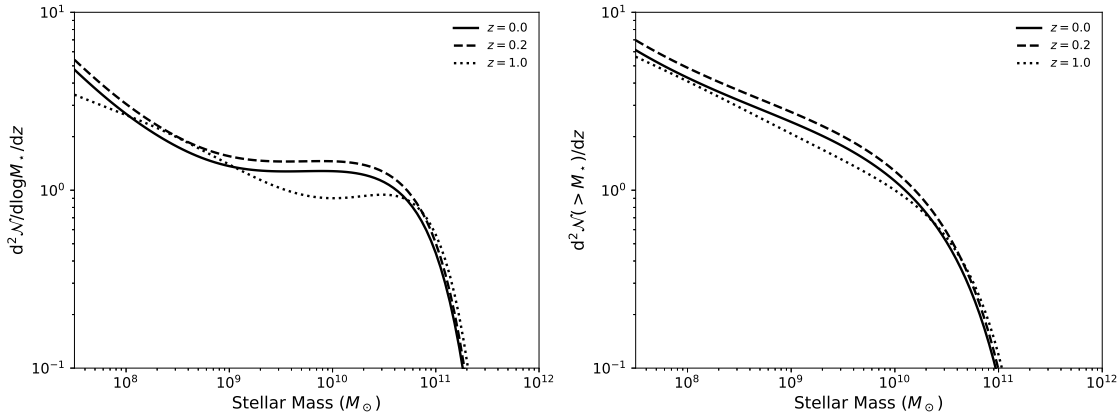

Figure 8.2: *Left panel*: The differential detection rate of gaseous halos as a function of galaxy stellar mass assuming the maximum radius is the virial radius. The adopted SMF is only for star-forming galaxies (Tomczak et al., 2014). *Right panel*: The cumulative detection rate of gaseous halos.

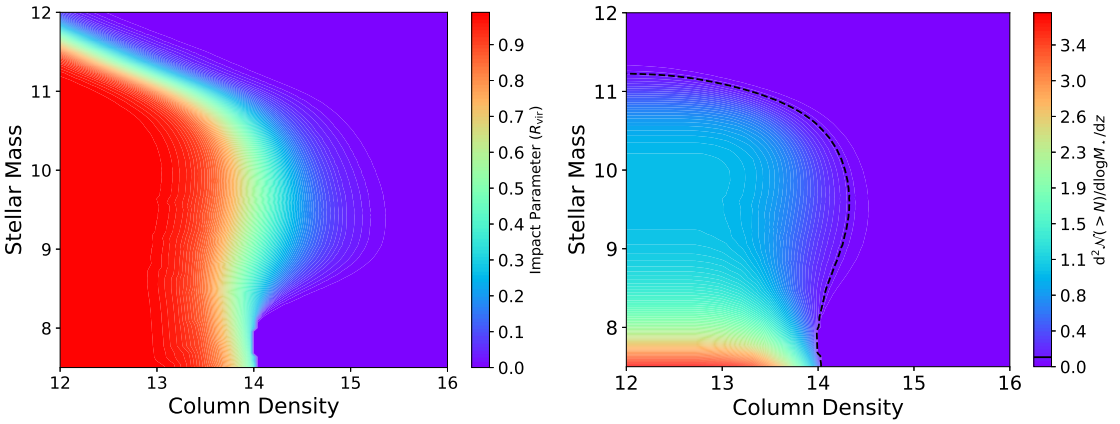

Figure 8.3: *Left panel*: The relative impact parameter of O VI at different column densities. Within the relative impact parameter, the O VI column density is larger than the given value as marked by the x-axis. *Right panel*: The cumulative O VI column density distribution at different stellar masses. The black dashed line shows the contour of a detection rate of 0.1 dex^{-1} per unit redshift, which indicates sub-L^* galaxies are the major contributors to the high O VI column density systems.

2014; in $\log M_\star = 8.00 - 11.25$). At $z = 1.0$, we use the SMF for the redshift bin of $z = 0.75 - 1$, which is measured in the stellar mass range of $\log M_\star = 8.50 - 11.25$. As the redshift increases, the comoving galaxy density decreases, while the comoving covering area per gaseous halo increases due to increasing of the scale factor. Overall, the detection rates at different redshifts are similar, showing total cross section values of $\mathrm{d}\mathcal{N}/\mathrm{d}z = 6.0$, 6.8 and 5.5 at $z = 0.0$, 0.2, and 1.0, respectively. However, the similarity of total detection rate does not imply that the column density distribution is also similar to each other.

For a given column density, only a part of the gaseous halo cross section contributes to the detection of systems that are higher than the column density. To represent the cross sections of different column densities, we define the relative impact parameter (or radius), within which the column density due to the gaseous halo is higher than the given column density (the left panel of Fig. 8.3 for O VI). Since the inner regions typically have higher column densities, this treatment applies in most stellar mass ranges for all ions; while for the most low-mass galaxies, there is a modest decrease in the inner region (of 0.2 dex) because of the photoionization modification (QB18). However, one expects that there are ionizing photons escaping from the galaxy disk, which will boost the high ionization state ion column density in the inner region, although the treatment of an escaping flux contribution is beyond the scope of this paper. Therefore, we ignore the decrease in the innermost regions of low-mass galaxies and apply the relative impact parameter to all galaxies and all column densities.

Applying the relative impact parameter ($r_{\rm cf}$), we calculate the cumulative detection rates at different column densities for different stellar masses:

$$\frac{\mathrm{d}^2\mathcal{N}(>N)}{\mathrm{d}z\mathrm{d}M_\star} = \pi(r_{\rm cf}R_{\rm vir}(1+z))^2 \times \mathcal{F}(M_\star), \tag{8.1}$$

where z is the redshift to account for the scale factor and $\mathcal{F}(M_\star)$ is the comoving

SMF at different stellar masses. Our results are shown in the right panel of Fig. 8.3 for O VI, showing that the high O VI column density ($N > 10^{14}$ cm^{-2}) systems are mainly from the galaxies with stellar masses between $10^{8.5}$ $M_\odot$ and $10^{10.5}$ $M_\odot$, while low column density systems occur in all galaxies. The cumulative column density distribution is calculated by integrating over all stellar masses:

$$\mathcal{F}(N) = \frac{\mathrm{d}\mathcal{N}(>N)}{\mathrm{d}z} = \int \frac{\mathrm{d}^2\mathcal{N}(>N)}{\mathrm{d}z\mathrm{d}M_\star}\mathrm{d}M_\star, \tag{8.2}$$

where $\mathcal{F}(N)$ is the cumulative detection rate for different column densities. Meanwhile the column density distribution function is defined as

$$f(N) = \frac{\mathrm{d}\mathcal{N}(>N)}{\mathrm{d}z\mathrm{d}N} = \frac{\mathrm{d}\mathcal{F}(N)}{\mathrm{d}N}. \tag{8.3}$$

In the following sections, we mainly use the cumulative column density distribution for comparison with observations, while the column density distribution function is used to compare with cosmological simulations.

8.3 The High Ionization State Ions

Once the ion column density distribution is calculated, we can compare the model with observations to constrain the free parameters and the physical conditions of observed systems. For O VI systems, there are a variety of observations to be compared with, while for other ions, we mainly show the predictions of the galaxy contributions.

8.3.1 Intervening O VI at $z \approx 0.2$

Observations constrain the column density as a function of impact parameter. In Fig. 8.4, three data sets are shown – the COS-Halos sample (Werk et al., 2013, 2014), the Johnson et al. (2015) sample, and a dwarf galaxy sample (Johnson et al., 2017).

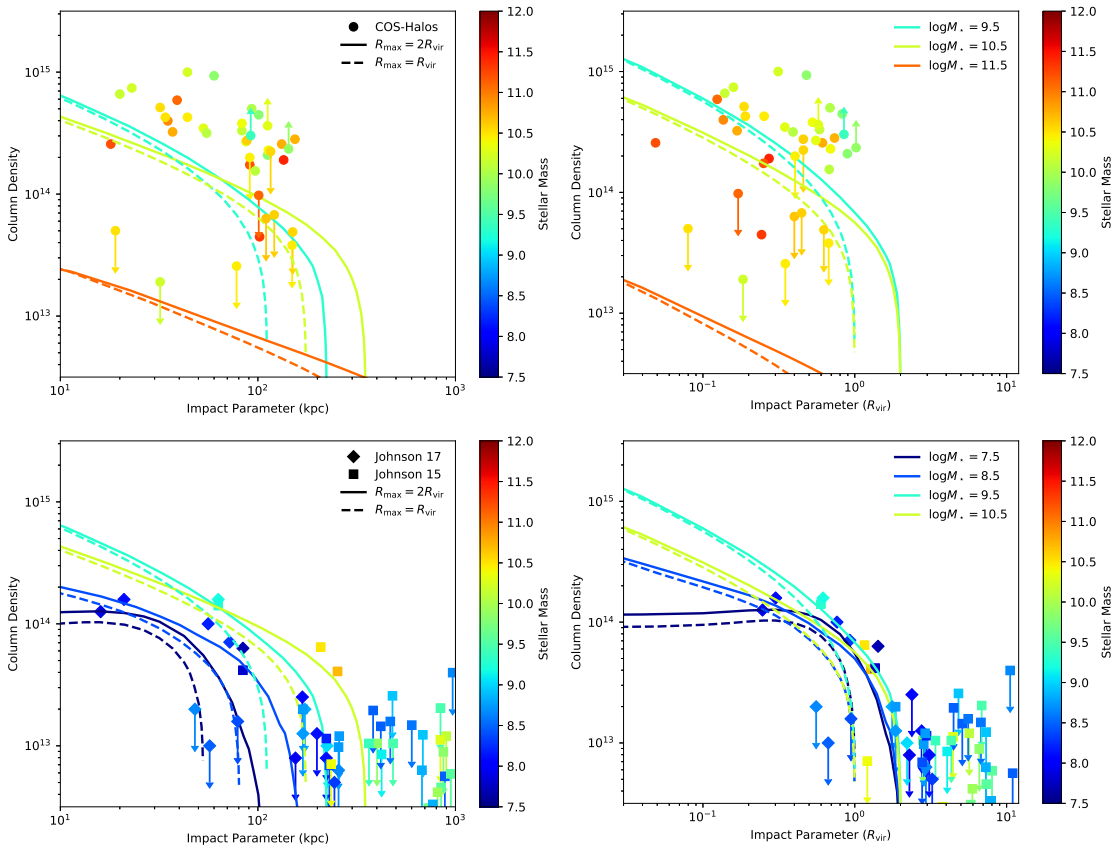

Figure 8.4: The radial dependence of O VI in the GGHM models and observations. The GGHM models are for galaxies with stellar masses of $\log M_\star = 7.5$, 8.5, 9.5, 10.5, and 11.5 at $z = 0.2$, respectively. The observations are from COS-Halos (Werk et al. 2014; marked as circles; upper panels), and the surveys of (Johnson et al. 2015; square; lower panels), and (Johnson et al. 2017; diamond; lower panels). Both the models and the observations are color-coded by the stellar masses. *Left panels*: Dependence on the physical impact parameter. *Right panels*: Dependence on the impact parameter in the units of the virial radius. Low mass galaxies ($\log M_\star < 8.5$) have a flattened radial dependence, which is consistent with Johnson's sample. Higher mass galaxies ($\log M_\star > 8.5$) show a decline with radius, which is consistent with the COS-Halos sample, but the O VI column density from COS-Halos is systematically higher than our model predictions.

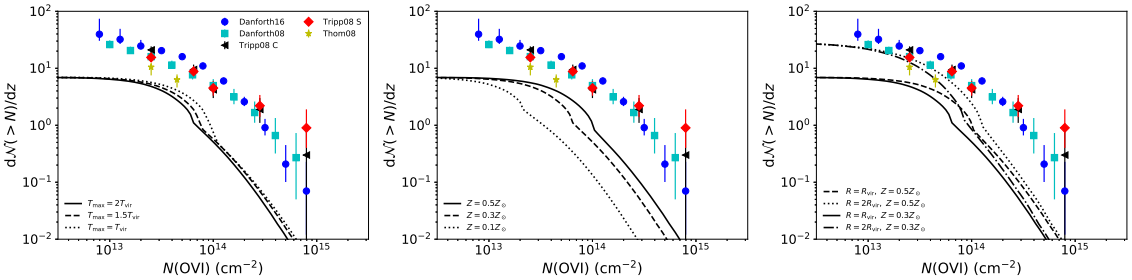

Figure 8.5: The predicted column density distributions in the GGHM models with varied parameters at $z = 0.2$. The data consist of intervening O VI with or without galaxy information. The data are from Danforth & Shull (2008), Thom & Chen (2008a), Tripp et al. (2008), and Danforth et al. (2016). For Tripp et al. (2008), two column density distributions are shown for components ("C") or systems ("S"). In each panel, we show the result of varying one parameter while keeping the others fixed at the fiducial values ($T_{\rm max} = 2T_{\rm vir}$, $Z = 0.5Z_\odot$, and $R_{\rm max} = R_{\rm vir}$). *Left panel*: The dependence on $T_{\rm max}$. *Middle panel*: The dependence on Z. *Right panel*: The dependence on $R_{\rm max}$.

For the comparison models, we adopt $z = 0.2$ with $R_{\rm max} = R_{\rm vir}$ or $R_{\rm max} = 2R_{\rm vir}$, since each sample has a median redshift $z \approx 0.2$. The COS-Halos sample selected L^* galaxies ($\log M_\star = 9.7 - 11.5$) within the virial radius, while Johnson et al. (2017) focus on dwarf galaxies ($\log M_\star = 7.7 - 9.2$). The Johnson et al. (2015) work shows a QSO-selected sample with impact parameters up to ten times the virial radius, which probes beyond the halo itself, and we selected isolated and late-type galaxies from this sample. Savage et al. (2014) presented an O VI absorption-based sample of galaxy-absorption pairs, which is biased to detect O VI absorption features not near known galaxies; therefore, we do not include this sample in the comparison (see discussion in Section 8.4.4). In the comparison with the COS-Halos, our models underestimate the observed O VI column densities by a factor of ≈ 0.3 dex systematically, which is discussed in detail in QB18. Nevertheless, the radial decline of the $\approx L^*$ galaxies ($M_\star \gtrsim 10^{10}\ M_\odot$) is reproduced with the similar magnitude. The maximum O VI column density systems occur in around $M_\star \approx 10^{9.5}-10^{10.5}\ M_\odot$. For low mass galaxies ($M_\star \lesssim 10^{8.5}\ M_\odot$), our models appear to match the data showing the turnover in the

radial direction (the flattened radial distribution; Johnson et al. 2017). Also, the modeling favors the solution with the $R_{\rm max} = 2R_{\rm vir}$ to best reproduce the observations based on measurements and non-detections of the Johnson et al. (2015) sample.

We also consider O VI absorption blind survey samples that are different from galaxy-QSO pair samples. In Fig. 8.5, we show the comparison with these four samples – Danforth & Shull (2008), Thom & Chen (2008b),Tripp et al. (2008), and Danforth et al. (2016), which have median redshifts of 0.20, 0.25, 0.22, and 0.29. In these four samples, the detected O VI systems may not have galaxy information and all of the detected O VI contributes to the total column density distribution. Specifically, these samples have redshift regions of $z < 0.36$, $0.1 < z < 0.5$, $z < 0.5$, $0.1 < z < 0.7$, respectively. For Danforth & Shull (2008) and Danforth et al. (2016), we used the reported differential column density distribution to calculate the cumulative column density distribution. For Tripp et al. (2008), we assume a Doppler b factor of 30 km s^{-1} to convert the rest-frame equivalent width (EW) into a column density, since the average b factor is 27 ± 14 km s^{-1} in this sample. In Tripp et al. (2008), there are two reported column density distributions based on whether a system is broken into separate components – components ("C") and systems ("S"). Therefore, the "S" column density distribution is more flattened, having more high column systems. Our fiducial model has the parameters $Z = 0.5\ Z_{\odot}$, $T_{\rm max} = 2\ T_{\rm vir}$, and $R_{\rm max} = R_{\rm vir}$ at $z = 0.2$. The results of varied Z, $T_{\rm max}$ and $R_{\rm max}$ are also shown in Fig. 8.5.

All of the GGHM models underestimate the detection rate of the observed O VI, showing a gap with a factor of $\approx 4-10$ over all column densities (Fig. 8.5). However, the GGHM models predict the general shape of the observed column density distribution. Danforth et al. (2016) shows that the column density distribution can be fitted by a broken power law with a break point at $\log N({\rm OVI}) = 14.0 \pm 0.1$ and two power law indices of 2.5 ± 0.2 (high column density end) and 0.56 ± 0.16 (low column density

end). Our models show a similar break around $\log N(\mathrm{OVI}) = 14$, which is indicated by a relatively sharp decrease of the detection rate. As we will show in Section 4, this decrease is due to the contribution from low-mass galaxies and the break indicates that there is a lower column density limit for O VI systems with galaxy origins. As shown in Fig. 8.1, the majority of the gaseous halos have $N(\mathrm{OVI}) \approx 10^{14}$ cm^{-2} for low-mass galaxies ($\lesssim 10^{8.5}\ M_\odot$), which leads to the sharp decrease of the cumulative column density distribution around the break point.

Increasing the maximum temperature moves the O VI transition galaxy mass from $\log M_\star = 10.2$ ($T_{\rm max} = T_{\rm vir}$) to 9.5 ($T_{\rm max} = 2T_{\rm vir}$) and affects the column density distribution by changing the detection rate of the corresponding galaxies. As shown in Fig. 8.2, the detection rate of galaxies changes only modestly from $10^{10}\ M_\odot$ ($T_{\rm max} = T_{\rm vir}$) to $10^{9.5}\ M_\odot$ ($T_{\rm max} = 2T_{\rm vir}$), which corresponds to high column density O VI systems. Therefore, the high column density end of the O VI column density distribution does not change significantly. Higher ionization state ions (e.g., O VII and O VIII) could be affected significantly, since there are many fewer massive galaxies. We also notice that the break point is slightly smaller for the high temperature model. This is mainly because the high temperature model predicts lower column densities in the low-mass galaxies that contribute to the break. In low-mass galaxies, the radiative cooling is suppressed by photoionization, and increasing the temperature reduces the impact of photoionization (see Fig 1. in QB18). The high radiative cooling emissivity could reduce the gas density in high temperature gaseous halo models, which leads to lower O VI column densities.

Increasing the metallicity helps with the problem that our models lie below the observation, since raising the metallicity increases the O VI column density in all galaxies (QB18). This effect moves all column density toward higher values, which can make up some of the gap at the high column density end (shown in the middle panel of Fig. 8.5). However, varying only the metallicity cannot make up the entire

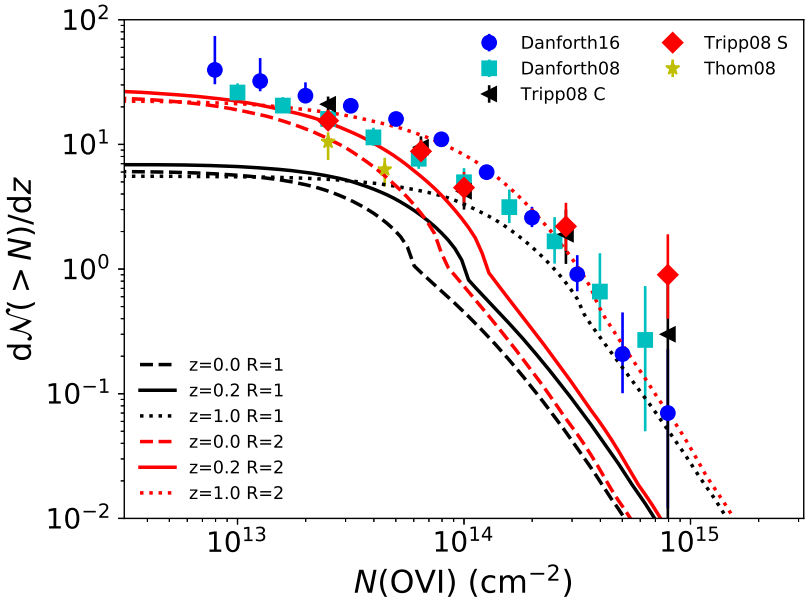

Figure 8.6: The redshift evolution of the O VI column density distribution. The observations used are color-coded as Fig. 8.5. The higher redshift leads to the higher specific SFR, which raises the O VI columns of all galaxies.

gap between the model and observations, since it cannot increase the total detection rate of O VI in the low-column density range.

The total model detection rate of galactic gaseous halos (≈ 6 per unit redshift) is far below the observed detection rate of O VI systems (≈ 40 per unit redshift at $\log N = 12.8$; Danforth et al. 2016). Increasing the maximum radius can increase the halo cross section; therefore, we consider models with the maximum radius of twice the virial radius, which is shown in the right panel of Fig. 8.5. With a larger maximum radius, the low column density system ($\log N(\mathrm{OVI}) < 14$) is raised significantly by factor > 2, while the high column density system detection rate is only increased by several percent and is still significantly underestimated. At low column densities, the difference cannot be made up completely by the extension of the maximum radius. The gaseous halo has a non-zero lower bound for the column density (see Fig. 8.1), which means that the differential distribution would decrease to zero at a given column density. However, the observed column density distributions do not show such a

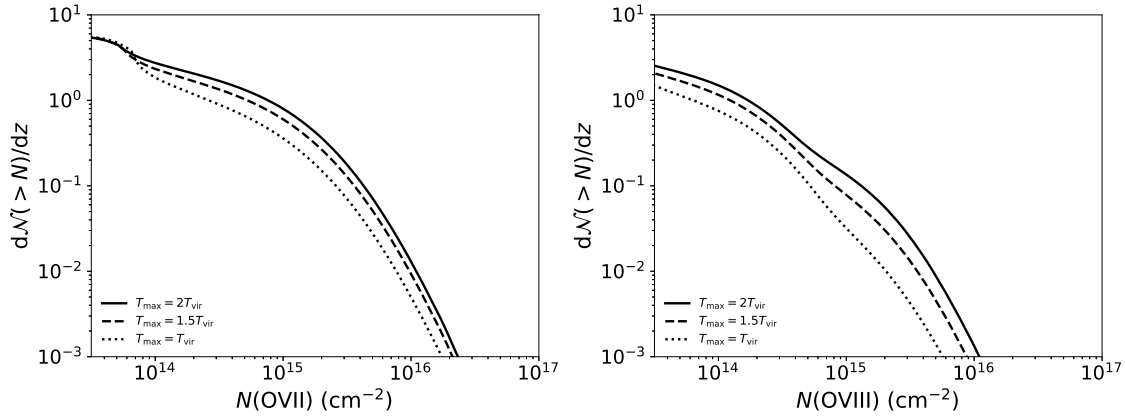

Figure 8.7: The effect of varying maximum temperature on O VII (*Left panel*) and O VIII (*Right panel*). Increasing the maximum temperature could increase the detection rate for O VII and O VIII by a factor of $0.2-0.3$ dex at high column densities.

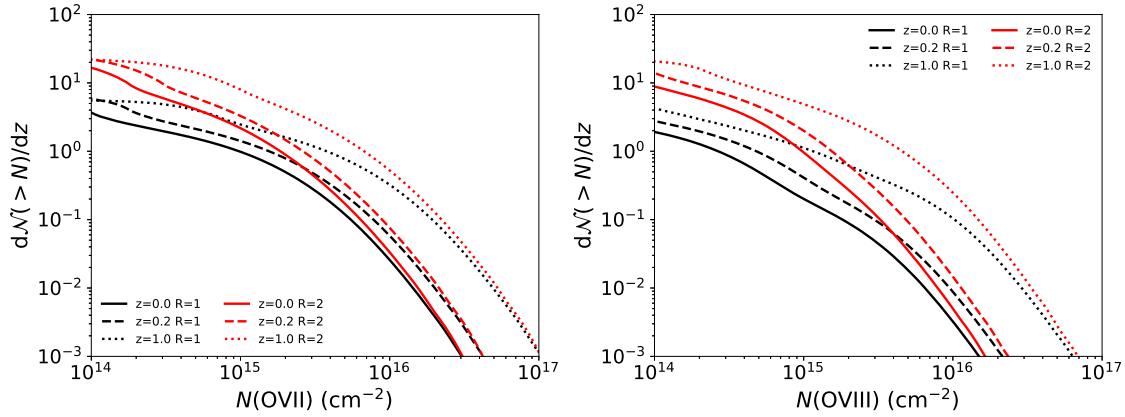

Figure 8.8: The redshift evolution of O VII (*Left panel*) and O VIII (*Right panel*). The predicted column detection rate of O VII and O VIII are about $2-20$ and $0.2-7$ per unit redshift with limiting EW of 1 mÅ at $z = 0.0-1.0$.

decrease. Therefore, we suggest that the cosmic filaments (gas not associated with galaxy halos) might be another origin for low O VI column density systems, which is discussed in Section 4.4.

Finally, we consider the redshift evolution of the O VI column density distribution. Since the redshift dependence of sSFR is approximately $\propto (1+z)^3$, the high redshift ($z \gtrsim 1$) leads to a significant higher SFR, which affects a gaseous halo by increasing the density (QB18). This higher density occurs because the higher rate of star formation requires a higher cooling rate of mass from the halo. The increase of the gaseous halo density is approximately the root square of the sSFR, therefore a significant increase of the O VI column density is expected for high redshift galaxies (Fig. 8.6). The $z = 1.0$ column density distribution fits the observed distribution in the high column density end phenomenally, although this fitting is non-physical, because the observation samples have smaller redshifts ($z \approx 0.2$). Since the redshift mainly affect the SFR, the $z = 1.0$ model is equivalent to a higher SFR model (see discussion in Section 8.4.1) or a stronger feedback model (larger γ than our assumption from a galactic wind model) at low redshifts.

8.3.2 O VII and O VIII in the Local Universe

The O VII and O VIII ions show similar predicted column density distributions to O VI, while the break point is moved to a higher column density about 10^{15} cm^{-2}. This change of the break point is mainly because these two ions have higher ionization fractions than O VI and are associated with more massive galaxies, which normally have higher total hydrogen column densities. Increasing the metallicity will move the distribution toward higher column densities, and increasing the maximum radius raises the detection rate of low-column density systems.

Increasing the maximum temperature increases the detection rates of both O VII and O VIII at high column densities, which is due to the higher ionization potentials

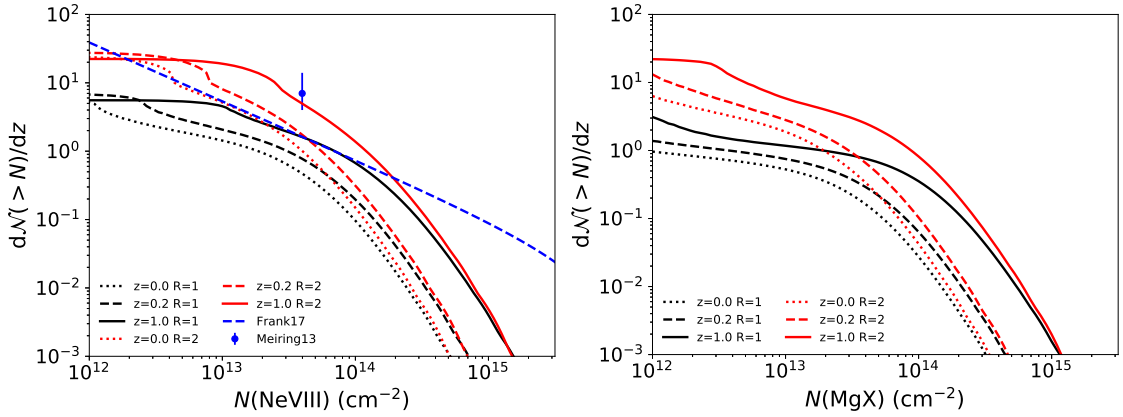

Figure 8.9: The redshift evolution of Ne VIII (*Left panel*) and Mg X (*Right panel*). The predicted column detection rate of Ne VIII and Mg X are about $2-5$ and $1-3$ per unit redshift with limiting column density of $\log N = 13.7$ at $z = 1.0$. Current observations are not consistent for Ne VIII at $\log N = 13.4$, an issue that needs to be resolved in order to constrain the models.

of these two ions. Once the maximum temperature is increased, O VII and O VIII occur in lower mass galaxies, which have higher number densities and larger detection rates (Fig. 8.2). Specifically, the abundance of O VII detections are ≈ 0.3 dex higher for high column density systems ($> 10^{15}$ cm^{-2}), and this effect is more significant for O VIII systems (≈ 0.7 dex).

Fig. 8.8 shows the redshift evolution of the O VII and O VIII column density distribution, which is similar to the O VI column density distribution in Fig. 8.6. With the maximum radius varying between 1 or 2 $R_{\rm vir}$, our model predicts the detection rate of O VII is $1-10$ in the redshift range $z = 0.0-1.0$ with a limiting column density of 10^{15} cm^{-2} (EW ≈ 3 mÅ), or $2-20$ with a limiting column density of 3×10^{14} cm^{-2} (EW ≈ 1 mÅ). For O VIII, the predicted detection rate is $0.2-7$ in the redshift range $z = 0-1$ with a limiting column density of 10^{15} cm^{-2} (EW ≈ 1 mÅ).

8.3.3 Intervening Ne VIII/Mg X near $z = 1.0$

The Ne VIII and Mg X column density distributions have similar characteristics as O VII and O VIII, since Ne VIII and Mg X have similar ionization potentials to O VII and O VIII, respectively. Fig. 8.9 shows the redshift evolution and the effect of extending the maximum radius for these two ions. Our models predict the detection rate of Ne VIII and Mg X are about $1 - 2$ and $0.4 - 1$ systems per unit redshift, respectively, at $z = 1$ with a limiting column density of 10^{14} cm^{-2}, which requires a continuum $S/N \geq 15$ at a spectral resolution of *HST*/COS.

For Ne VIII, there are observational studies on the detection rate that can constrain the GGHM models. Meiring et al. (2013) shows three Ne VIII absorption systems in the sightline of PG 1148+549 around $z = 0.7$ with matched O VI absorption features. Based on this sightline, the derived Ne VIII detection rate is $\mathrm{d}\mathcal{N}/\mathrm{d}z = 7^{+7}_{-4}$ with a limiting column density of $10^{13.7}$ cm^{-2}. However, the detection rate from Meiring et al. (2013) seems to be inconsistent (at the 2σ level) with a stacking Ne VIII study (Frank et al., 2018). The non-detections in the stacked Ne VIII spectrum set an upper limit of the Ne VIII column density distribution; otherwise, the weaker doublet line should show up in the stacked spectrum. Meanwhile, individual detections of high Ne VIII column density systems set the lower limit of the Ne VIII abundance; otherwise, there should not be so many detected systems. Combining these two constraints, Frank et al. (2018) gives a preferred single power law distribution of the Ne VIII column density, and the detection rate at $z = 0.88$ is $\mathrm{d}\mathcal{N}/\mathrm{d}z = 1.4^{+0.9}_{-0.8}$ with $\log N > 13.7$.

As shown in Fig. 8.9, these two measurements can constrain the maximum radius of the gaseous halo model. The extended maximum radius model is consistent with (Meiring et al. 2013; slightly lower by a factor of 0.2 dex). The stacked spectrum study prefers the fiducial model with the maximum radius set to the virial radius (Frank et al., 2018), although the single power law distribution significantly differs

from our model at high column densities, which shows a break around $\log N = 13.6$. However, for the detectable Ne VIII systems ($14.5 > \log N > 13.6$), the fiducial model is consistent with the observations.

Frank et al. (2018) suggested that the Ne VIII detections in PG 1148+549 are due to unresolved large cosmic structures, which leads to a high detection rate of Ne VIII. Therefore, the measurement in Meiring et al. (2013) is an upper limit for the detection rate of Ne VIII. However, the individual detected Ne VIII systems used by Frank et al. (2018) are incomplete (e.g., only the most prominent system is reported in PG 1206+459), and so underestimate the constraint of the lower limit of the Ne VIII detection rate. Therefore, we suggest that the true value is between the two measurements of Frank et al. (2018) and Meiring et al. (2013). Resolving this discrepancy will require a large and complete survey of Ne VIII systems. Current observations only constrain that the the maximum radius of the hydrostatic gaseous halo is between the virial radius and twice the virial radius.

8.4 Discussion

8.4.1 The Effect of the SFR Scatter

The SFR is a crucial parameter to determine the density of the gaseous halo in the GGHM model and the density is approximately proportional to the square root of the SFR (QB18). In the previous calculation, we use the typical SFR from the star formation main sequence (Morselli et al., 2016), which is the logarithmic mean value at different stellar masses. Once the SFR scatter is considered, the arithmetic mean is larger than the typical SFR used in our model, which leads to variations of the final column density distribution.

The accurate way to account for the SFR scatter is by integrating over the SFR-$M_\star$ plane instead of fixing the SFR. However, this integration is extremely computer

intensive, so we assumed that the magnitude of the scatter is same at different stellar masses, and follows a log-normal distribution for star-forming galaxies. Then, we use two ways to estimate the effect of the SFR scatter. First, we use the arithmetic mean of SFRs instead of the logarithmic mean. Because of the log-normal distribution, the arithmetic mean is larger than the logarithmic mean by a constant factor of $10^{\sigma/2}$, where σ is the standard deviation of the log-normal distribution. For L^* galaxies ($\log M_\star = 10.5$), the standard deviation is about 0.4 dex (Renzini & Peng, 2015), which is applied to all galaxies, leading to 1.6 times larger SFR values. The results of this modification are shown in Fig. 8.10, which focuses on O VI. Compared to the logarithmic mean, the new column density distribution moves to higher column densities. For high column density systems ($\gtrsim 10^{14}$ cm^{-2}), our modification increases the detection rate by a factor about 1.7, while for low column density systems, the rate hardly changes because they are limited by the geometrical covering factor of galaxy halos.

Another way to estimate the SFR scatter is by using the approximation that the column density is proportional to the square root of the SFR, so $N \propto x^{1/2}$, where x is the ratio between the SFR and the logarithmic mean SFR. Then, a convolution is calculated to estimate the final column density distribution,

$$\mathcal{F}_{\rm final}(N) = \int_0^\infty \frac{1}{\sqrt{2\pi\sigma^2}} e^{-\frac{\log x^2}{2\sigma^2}} \times \mathcal{F}(Nx^{-1/2}) {\rm d}x, \tag{8.4}$$

where $\mathcal{F}(N)$ is the column density distribution calculated in Equation 1, and $\mathcal{F}_{\rm final}(N)$ is the final column density distribution with the SFR scatter considered. This final column density distribution is shown in Fig. 8.10. This full scatter estimation shows a relationship that is similar to the first treatment (i.e., the arithmetic mean) within a difference of 0.1 dex. At all redshifts, the convolution solution has higher detection rates than the arithmetic mean solution for high column density systems. This is

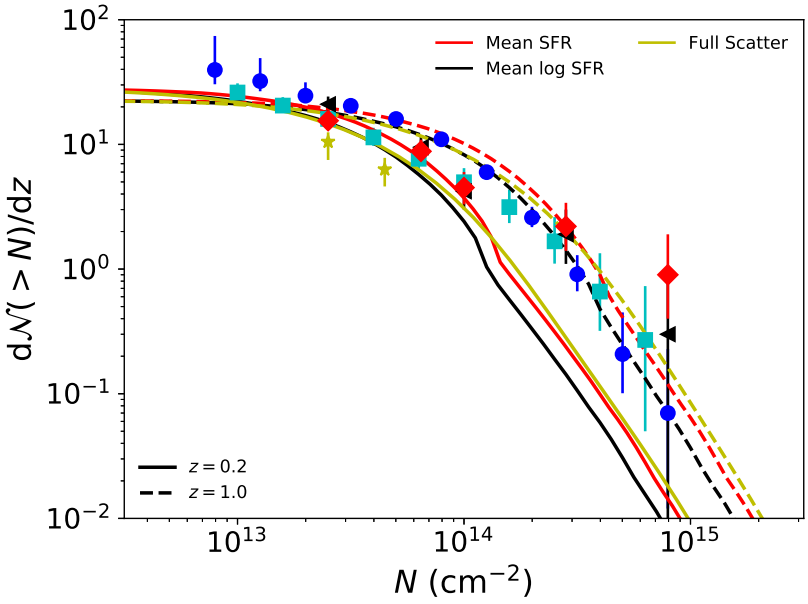

Figure 8.10: The effects of SFR scatter. The observation points are encoded in the same colors as Fig. 8.5. The black lines are the fiducial models using the logarithm mean of SFR from the star formation main sequence. The red lines use the arithmetic mean instead of the logarithm mean, while the yellow lines are the convolution results (see the text for details).

because the high SFR wing leads to higher column density systems. The low SFR wing affects the distribution in the opposite direction, which decreases the detection rate in the column density range near the break point. Meanwhile, the sharp decrease around the break point is smoothed by the convolution of the SFR, which is more consistent with the observations.

When accounting for scatter in the SFR, the detection rate of high column density systems is increased. Although our model at $z = 0.2$ is still below measurements obtained around $z = 0.1 - 0.7$ (Danforth et al., 2016), the model at $z = 1.0$ lies above the observation, which indicates that involving the SFR scatter moderates the tension between the observation and our models.

8.4.2 Collisional Ionization or Photoionization

The physical conditions of high ionization state ions are important for understanding the properties of the hot gaseous components in the universe. However, high ionization state ions can be produced either through collisional ionization (CI) at high temperatures or photoionization (PI) at low densities, so we must determine the ionization mechanism.

Observationally, the line width (b factor) of different ions help to define the physical conditions (Tripp et al., 2008; Savage et al., 2014). Using the matched H I and O VI line components, the thermal and the non-thermal velocity components can be decomposed by assuming a single temperature model. Subsequently, the temperature is derived from the thermal velocity and the physical conditions are determined by comparison with the collisional ionization temperature of O VI ($\approx 10^{5.5}$ K). Employing a threshold of $\approx 10^5$ K ($< 10^{5.3}$ K for PI and $> 10^{4.7}$ K for CI), about the half of O VI (or less) are collisionally ionized (Savage et al., 2014).

This method is only applied to the ion O VI, since H I and O VI have comparable wavelengths for their resonant lines. For higher ionization state UV ions (i.e., Ne VIII and Mg X), it is very difficult to obtain similar quality spectra for both H I and these two ions, since Ne VIII and Mg X have much shorter wavelengths, which puts H I in the COS/NUV band with lower resolution and sensitivity. An alternative way to determine the physical condition is to check whether a single phase PI model could reproduce high ionization state ions. Most previous studies show that the observed Ne VIII column density cannot be generated in PI models, which require unrealistically low densities and hence extremely large sizes (> 1 Mpc; Savage et al. 2005; Narayanan et al. 2012; Meiring et al. 2013; Qu & Bregman 2016; Pachat et al. 2017).

Recently, Hussain et al. (2017) argued that PI models can reproduce all Ne VIII systems using the UVB prescription from Khaire & Srianand (2015). Compared to

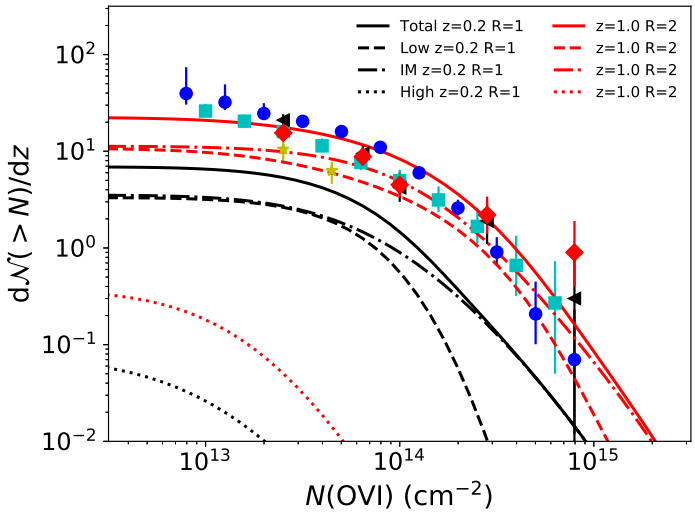

Figure 8.11: The contributions from galaxies with different masses. The observation points are encoded in the same colors as Fig. 8.5. The three galaxy mass ranges are $\log M_\star = 7.5 - 8.0$ (low mass – "Low"; dashed), $8.0 - 11.0$ (intermediate mass – "IM"; dotted-dashed), and $11.0 - 12.0$ (high mass – "High"; dotted). The intermediate and high mass galaxies are collisionally ionized in GGHM models, while the low mass galaxies are photoionized.

Haardt & Madau (2012), the UVB in Khaire & Srianand (2015) is 0.5 dex higher at and above the Ne VIII and Mg X ionization edges ($E > 10$ Ryd). This modification increases the density in the absorbing system for the PI model and reduces the size of the absorption gas to $\lesssim 100$ kpc. However, the UVB at the high energy band is mainly from QSOs, which is uncertain observationally. Khaire & Srianand (2015) used the *HST*/COS QSO composite spectrum from Stevans et al. (2014), which has a harder spectral index $\alpha = -1.41 \pm 0.15$ ($L_\nu \propto {}^\alpha$), compared to $\alpha = -1.57 \pm .0.17$ (Telfer et al., 2002, from *HST*/Faint Object Spectrograph) used in Haardt & Madau (2012). However, both of these observations only go down to 500 Å ($E = 1.8$ Ryd), which is extrapolated to 25 Å ($E \approx 100$ Ryd) to obtain the UVB at the high energy band. Therefore, the actual value of the UVB is still uncertain in the high energy regime (for Mg X, Ne VIII, and even O VI).

In the GGHM models, PI and CI systems can be distinguished in another way

based on statistical properties. Phenomenally, O VI absorption systems that originate from PI and CI show different radial dependences as shown in Fig. 8.1 and Fig. 8.4. This is consistent with observations – the dwarf galaxy sample shows a flatter radial dependence (Johnson et al., 2017), while L^* galaxies show a radial decrease (2.9σ), which is defined and dominated by "broad" features (Werk et al., 2016). Therefore, we select a threshold for the PI to CI transition at a the stellar mass of 10^8 $M_\star$, above which we assume that O VI is predominantly collisionally ionized.

Using this criterion, the contribution of PI and CI are shown for two models: the fiducial model at $z = 0.2$ and the extended radius model at $z = 1.0$ in Fig. 8.11. For these models, there is a significant difference between the upper limit column density for PI and CI O VI, which indicates high column density O VI systems are all collisionally ionized. The PI contribution shows a sharp decrease around the break point for both models, which is because the PI O VI leads to in a narrow range of column densities near $\approx 10^{14}$ cm^{-2} at $z = 0.2$ (Fig. 8.1). For the current detection limit of O VI ($\log N(\mathrm{OVI}) \approx 13$), the ratio between CI and PI systems is around 1 for gaseous halos, so about the same amount of O VI is excited by each process. However, our model with $R_{\mathrm{max}} = 2R_{\mathrm{vir}}$ still underestimates the detection rate of low column density systems. Assuming this difference is mainly caused by unvirialized IGM gas that is photoionized (discussed further in Section 4.4), one will obtain a CI/PI ratio about 0.3 when the CI contribution is fixed to our gaseous halo model.

This CI/PI ratio (≈ 0.3) is consistent with observations (Savage et al., 2014); however, our model and the observations have different criteria for distinguishing CI from PI. Savage et al. (2014) set a threshold temperature of $\log T = 4.7$ for CI, whose O VI ionization fraction is $< 10^{-10}$ in collisional ionization equilibrium (CIE). If we use $\log T = 5.0$ as the threshold, the observed CI/PI ratio is less than the GGHM model prediction of 0.3. As stated above, the current method to determine the physical condition is using the Doppler b factor, which requires a detectable broad

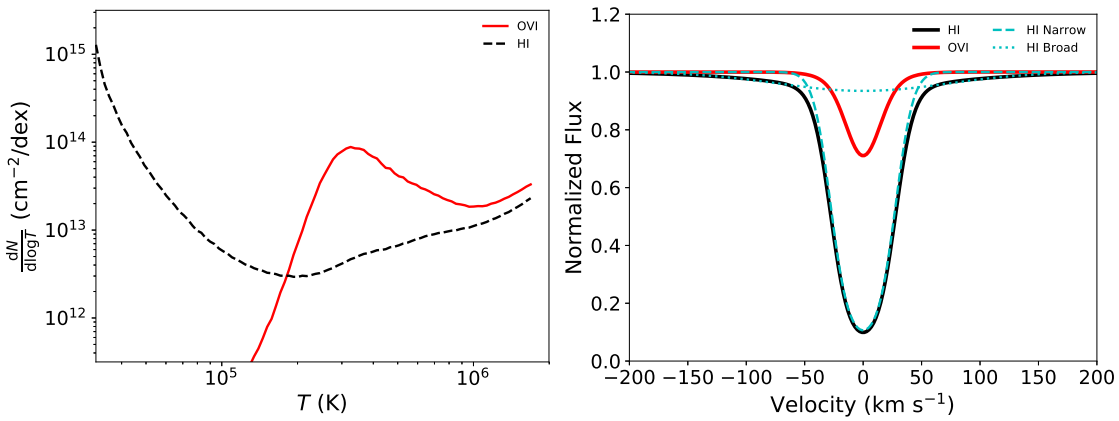

Figure 8.12: Example of the multi-phase medium in the gaseous halo, with galaxy parameters $M_\star = 10^{10.5} M_\odot$, SFR $= 3 M_\odot$ yr^{-1}, $Z = 0.3 Z_\odot$, $R_{\rm max} = 2 R_{\rm vir}$, $T_{\rm max} = 2 T_{\rm vir}$ at $z = 0.2$. The impact parameter of this absorption is $0.3 R_{\rm vir}$. *Left panel*: The column density dependence on the temperature. *Right panel*: The composite line shapes for Lyα and the strong line of O VI. The Lyα line can be decomposed to two components – broad ($\log T = 5.8$) and narrow ($\log T = 4.5$).

H I features ($b > 70$ km s^{-1}) to obtain the high temperature ($T \gtrsim 10^5$ K). However, these broad H I features are difficult to detect, especially when there are also narrow features at the same velocity.

We consider an L^* galaxy with $M_\star = 10^{10.5} M_\odot$, SFR $= 3 M_\odot$ yr^{-1}, $Z = 0.3 Z_\odot$, $R_{\rm max} = 2 R_{\rm vir}$, $T_{\rm max} = 2 T_{\rm vir}$, and the impact parameter is 0.3 $R_{\rm vir}$ at $z = 0.2$. In the left panel of Fig. 8.12, we show the temperature dependence of the column density for H I and O VI. The temperature distribution is a combination of two factors – the mass-temperature distribution of the multi-phase medium (QB18) and the ionization fraction. It is clear that O VI is mainly from collisional ionization, which leads to the peak around $10^{5.5}$ K. The H I columns are mainly generated in a lower temperature phase, while there is also a weak, broad H I feature at high temperature ($\approx 10^6$ K). With these column density distributions, the composite line shapes are also shown in Fig. 8.12, where we only consider the thermal broadening. The Lyα is decomposed into two components: $\log N_1 = 13.86$ with $b_1 = 24.5$ km s^{-1} ($\log T = 4.5$); and

$\log N_2 = 12.96$ with $b_2 = 102.0$ km s^{-1} ($\log T = 5.8$), while the O VI strong line is well modeled by a single component model with $\log N = 13.54$ and $b = 21.4$ km s^{-1} ($\log T = 5.7$).

In such a system, although the O VI is collisionally ionized (associated with the broad component of H I), it can be mistaken as being photoionized, if the O VI is assigned to the narrow component. Unfortunately, the broad component of Lyα is difficult to detect since the central depth is only about 5%, which is easily buried by the noise, especially in the situation that it is blended with the narrow component. This situation may occur in observed systems with comparable O VI and H I b factors, which are marked as PI currently (Savage et al., 2014).

8.4.3 Comments on the Origins of O VI

As stated in Section 2.1, there are three different origins of high ionization state ions in our analytic models: PI for low-mass galaxies; CI in ambient gases at the virial temperature; and CI in cooling flows in massive galaxies. Different ions have different halo masses corresponding to their ionization potentials, and the O VI occurs in ambient gases of galaxies with $M_\star \approx 10^9 - 10^{10}\ M_\odot$.

Several recent theoretical works also attempt to understand the origins of O VI (Bordoloi et al., 2017a; McQuinn & Werk, 2018). McQuinn & Werk (2018) argued that the cooling flow in the gaseous halo is the main source of O VI, and the authors suggested a large cooling rate ($10 - 100\ M_\odot$ yr^{-1}) and a dense gaseous halo ($P/k \approx 100$ cm^{-3} K) to account for the observed O VI column density ($10^{14.5}$ cm^{-3}) in the COS-Halos sample ($\approx L^*$ galaxies). This massive cooling flow requires energetic feedback processes originating from the galaxy disk to disrupt the cooling flow at the low temperatures ($\approx 10^4$ K). Although, O VI in GGHM models are also in the cooling flow, it is shown that galactic winds cannot be energetic enough to support such a massive cooling flow if we adopt a galactic wind model from the FIRE simulations

(Hopkins et al. 2014; Muratov et al. 2015; QB18).

Bordoloi et al. (2017a) suggested that all observed intervening O VI could be explained in the CIE model, involving an additional parameter – the cooling flow velocity. This flow velocity is a non-thermal velocity applied to the gas diffusion or gas flow, and larger flow velocities could lead to higher column densities. Therefore, one can find solutions for every single OVI systems in CIE models and the modeled temperatures are all higher than $10^{5.3}$ K. However, for narrow features, although it can be modeled as a cooling flow, the total line width may be too large ($v_{\rm cool}^2 + v_{\rm th}^2 > \Delta v^2$; notations from Bordoloi et al. 2017a).

For individual O VI systems, Werk et al. (2016) considered their connections with host galaxies. Specifically, O VI in COS-Halos are divided into three categories – "broad" features ($b \gtrsim 40$ km s^{-1}), "narrow" features ($b \approx 25$ km s^{-1}), and "no-low" features (no corresponding low ionization state ions; Werk et al. 2016). The "broad" features show a significant decrease with increasing radius, and typically have high column densities ($\gtrsim 10^{14.5}$ cm^{-2}), while "no-low" are also broad features ($b > 50$ km s^{-1}), but typically have lower column density ($\lesssim 10^{14.5}$ cm^{-2}). We suggest that these two types of O VI could correspond to the $M_\star \gtrsim 10^{8.5}$ $M_\odot$ galaxies and the difference between "broad" and "no-low" features are mainly due to the impact parameter. In our model, with smaller impact parameters, it is more possible to have a cool medium because of a larger cooling rate (higher density). Therefore, "no-low" features are all in the outer region (impact parameter $\rho > 50$ kpc) and O VI in inner 50 kpc regions all have corresponding low ionization state ions (see Fig. 10 in Werk et al. 2016).

The "narrow" features have small b factors (≈ 25 km s^{-1}), which are also seen in dwarf galaxies (Johnson et al., 2017). In the dwarf galaxy sample, all detected O VI absorption lines are narrow ($b \lesssim 30$ km s^{-1}), except for one system with $b \approx 60$ km s^{-1}. These narrow-feature O VI lines in dwarf galaxies are photoionized

and associated with low-density gaseous halos ($\approx 10^{-5}$ cm^{-3}) in our model. However, in the COS-Halos sample, the"narrow" features also occur in massive galaxies ($> L^*$). In addition, Werk et al. (2016) suggested that the UVB-only PIE model is disfavored by the ratio of N(NV)/N(OVI). We suggest that these differences may be due to the contamination from dwarf galaxies in the fields, where the identification of such galaxies is limited by the depth of the current galaxy survey. The failure of the UVB-only PIE model has two potential solutions – the uncertainty of the UVB (as discussed in Section 4.2) and the additional radiation sources (the escaping flux from the galaxy disk; Werk et al. 2016), which are beyond the scope of this paper.

8.4.4 The Contribution of Galaxies and the IGM

Our preferred model is $Z = 0.5Z_{\odot}$, $R_{\rm max} = 2R_{\rm vir}$, and $T_{\rm max} = 2T_{\rm vir}$ for the galactic gaseous halo based on the modeling of the observed O VI column density distribution. Also, the SFR is crucial to determine the gaseous halo density and hence the column density, which leads to a strong dependence of the column density distribution on the redshift. Using an approximation to the relationship between the SFR and the ion column densities, we introduce the SFR scatter to show that the observed O VI column density lies between our $z = 0.2$ and $z = 1.0$ models.

For the simplicity, we use the constant metallicity for all galaxies with different SFR values and stellar masses. Observationally, Prochaska et al. (2017) studied the metallicity of circumgalactic medium at $z \approx 0.2$ using the COS-Halos sample, finding a median metallicity of -0.51 dex with scatter ≈ 0.5 dex. Assuming the metallicity distribution is a log-normal distribution, the arithmetic mean of the metallicity will be around $0.5 - 0.6Z_{\odot}$, which is consistent with the preferred model. This constraint on the metallicity is also consistent with the O VI gas in the Illustris-TNG simulation (Nelson et al., 2018). A direct metallicity measurement of warm O VI ($\log T > 5$) by Savage et al. (2014) also shows a wide range of the metallicity (about [Z/H] = -2

to 0). Compared to Prochaska et al. (2017), the median metallicity is lower with [Z/H] $= -0.96$ for six systems. Due to the uncertainty of the small number statistics, it is still uncertain whether this sample is in conflicts with our assumption and other phase gases.

The maximum radius is constrained by the O VI column density distribution, and an extended model ($R_{\rm max} = 2R_{\rm vir}$) is preferred. However, as stated in Section 8.3.3, there is a possible disagreement between Ne VIII and O VI, where the stacking Ne VIII result supports the fiducial model with the virial radius (but the direct detection of Ne VIII systems goes in the opposite sense). This disagreement may be solved obtaining more Ne VIII observations. Currently, the O VI observations favor the extended radius model for low-mass galaxies, while for massive galaxies, more Ne VIII sample is needed.

The predicted O VI column density distributions have a strong dependence on the redshift due to the evolution of the cosmic SFR. However, there is no reported redshift evolution of the shape of the O VI column density distribution at $z < 1$, while the detection rate of O VI is found to increase with redshift at the limiting column density of $\log N = 13.4$ (Danforth et al., 2016). The detection rate is modeled as a power law $(1+z)^{\gamma}$ with a positive index of $\gamma = 1.8 \pm 0.8$ for O VI. As shown in Fig. 8.6, the O VI detection rate is dominated by the galactic gaseous halo contributions above $\log N = 13.4$, and the detection rates also increase with the redshifts in our model. In our model, the slope of this dependence is not well constrained, but an estimate of this slope is around 1 using the model points at $\log N = 13.4$ in Fig. 8.6.

With the preferred galactic gaseous halo model, there are two remaining issues – the differences in the high-column density region ($\gtrsim 10^{14}$ cm^{-2}) and at low-column densities ($\lesssim 10^{13.5}$ cm^{-2} for O VI). The difference at high column densities may be solved by varying the galaxy properties (i.e., the metallicity or the SFR), while the low column density difference indicates the existence of other origins for the high

ionization state ions. We suggest that the intra-group or cluster medium, and/or the cosmic filaments contribute about a comparable number of absorption systems as galaxies at low column densities.

The properties of the intra-group or cluster medium are still not well constrained. Stocke et al. (2014) suggests that the detected broad Lyα features (with O VI) are associated with the smaller galaxy groups rather than the member galaxies. However, for a single system within a larger galaxy redshift survey, Stocke et al. (2017) finds that a broad O VI is more likely associated with a single galaxy halo (with an impact parameter of $1.1R_{\rm vir}$ and $\Delta v \approx 50$ km s^{-1}). For the Virgo galaxy cluster, Yoon & Putman (2017) found that five of six systems with metal lines (up to C IV) have nearby galaxies within 300 kpc and 300 km s^{-1}. They also concluded that the detected Lyα features are IGM around galaxy clusters rather than the intra-cluster medium (Yoon et al., 2012; Yoon & Putman, 2017).

The properties of cosmic filaments are also rarely constrained in observations due to the difficulty in defining a filament. Wakker et al. (2015) measured the Lyα for two nearby filaments at $cz \approx 3000$ km s^{-1}, and found the broad Lyα features ($b > 40$ km s^{-1}) are all along the defined filament axes. However, the corresponding high ionization state ions (i.e., O VI) are out of the wavelength coverage. For O VI, one possible sample is from Savage et al. (2014), where some of the O VI absorption features are beyond twice the virial radius (up to $\approx 5-10\ R_{\rm vir}$). Since the detection limits of the galaxy survey are about 0.01 L^*, it is still possible that these features are due to smaller galaxies. Assuming $R_{\rm max} = 2R_{\rm vir}$, the detection rate is ≈ 13 per unit redshift for galaxies with masses $10^{7.5} - 10^{8.5}\ M_\odot$ ($0.001 - 0.01\ L^*$). Therefore, we expect that more O VI absorption systems are not associated with galactic halos in this situation, since we require a detection rate of 20 per unit redshift for cosmic filaments (comparing our models with Danforth et al. 2016). Based on this assumption, O VI in cosmic filaments has an upper limit of $\approx 10^{14}$ cm^{-2}, obtained from

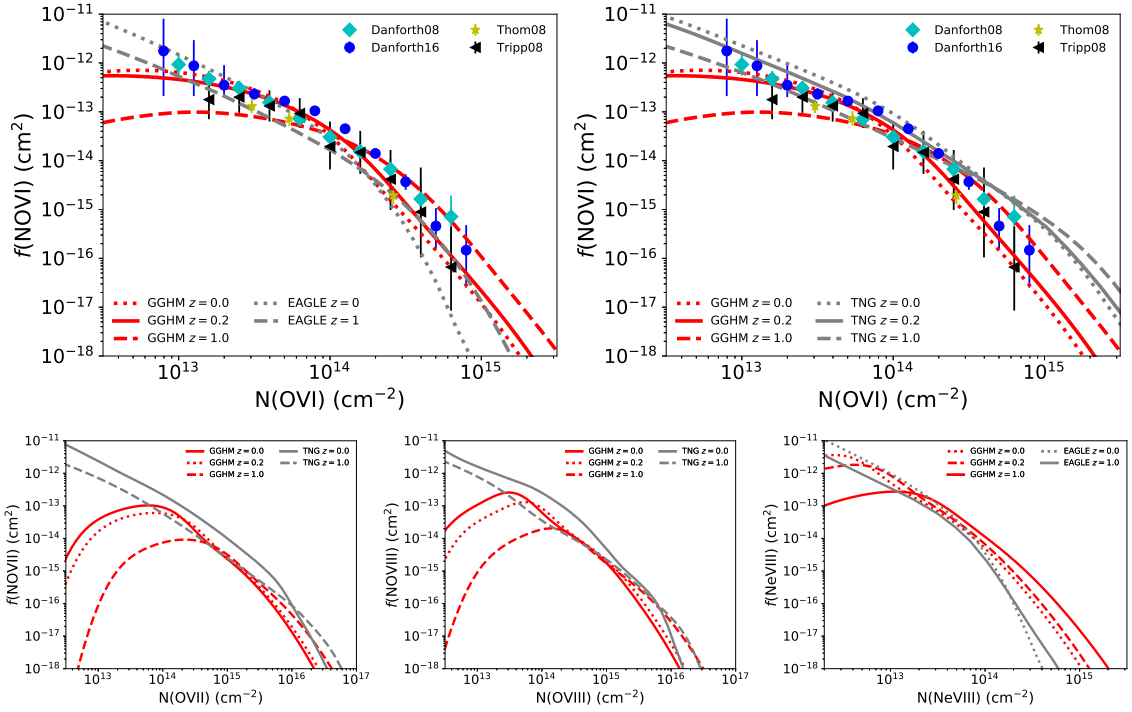

Figure 8.13: The comparison of the column density distribution function (Equation 3) between the GGHM models and cosmological simulations, EAGLE and Illustris-TNG. For EAGLE, we compared the O VI and Ne VIII, while O VI, O VII and O VIII are available for Illustris-TNG. Three models show comparable column density distributions and similar decrease for high column density systems. The divergence at the low density end indicates the necessity of additional origins for high ionization state ions.

Savage et al. (2014) O VI systems that are > 500 kpc from known galaxies. These values satisfy our requirements of the additional O VI systems beyond the gaseous halo (Fig. 8.6).

The high ionization state ions beyond galactic gaseous halos may have different origins due to their ionization potentials. It is unlikely that O VI can be the dominant ion in galaxy groups or clusters, since the ionization fraction will be very low ($\lesssim 10^{-4}$) at high temperatures ($\log T > 6.5$). However, higher ionization state ions (i.e., O VII and O VIII) could be dominant in these large structures. Therefore, additional O VI may be from the cosmic web, while additional O VII and O VIII are more likely from galaxy groups or clusters.

8.4.5 Comparison to Galaxy Simulations

We also compare our models with cosmological simulations to obtain insights into the contributions beyond galactic gaseous halos. In Fig. 8.13, we show the comparison with two cosmological simulations – EAGLE (Schaye et al., 2015; Rahmati et al., 2016) and Illustris-TNG (Pillepich et al., 2018; Nelson et al., 2018). Although there are several systematic differences, our model and these simulations are similar in that low-column density systems have a larger detection rate at $z = 0$, while high-column density systems are more abundant at $z = 1$ for all high ionization state ions. From the high$-z$ universe to the local universe, the decrease of high column density systems is associated with the decreasing cosmic SFR in our model, which is consistent with the evolution from $z = 2$ to $z = 0$ in simulations (Rahmati et al., 2016; Nelson et al., 2018).

In our model, the increasing detection rate of low-column density O VI features is due to the low SFR at $z = 0$. However, as shown in Fig. 8.13, the galaxy contribution does not dominate the low column density end for all high ionization state ions; therefore, it is necessary to consider the unvirialized gases (cosmic filaments), which

is discussed in Section 8.4.4.

There are some systematic differences between our model and simulations, which might be explained by the variation of the SMF. We employed the observed SMF, while EAGLE and Illustris-TNG both produce their own SMF obtained from the simulations. The EAGLE SMF is lower than the observation by a factor of 0.2 dex in the range of $M_\star = 10^{10} - 10^{11}\ M_\odot$ (the major contributor of Ne VIII; Schaye et al. 2015), which could lead to a lower Ne VIII column density distribution than our models at high column densities. For the Illustris-TNG, the O VI is overestimated at high column densities mainly due to the 0.2 dex higher spatial density in their simulations for galaxies with $M_\star = 10^9 - 10^{10}\ M_\odot$ (Pillepich et al., 2018). Besides the difference in the SMF, different treatments of physical processes also lead to different column density distributions. Our model predicts $0.1-0.2$ dex more baryonic material than EAGLE for galaxies of $M_\star = 10^{10} - 10^{11}\ M_\odot$ (QB18), which also contributes to the difference in the Ne VIII column density distribution. However, this kind of comparison is too small to distinguish between current models, so we do not include such a comparison.

8.5 Summary

Following QB18, we calculate the column density distribution of high ionization state ions (i.e., O VI, Ne VIII, O VII, Mg X, and O VIII) originating from galactic gaseous halos. We convolved the GGHM models from QB18 with the redshift-dependent SMF from Tomczak et al. (2014) to obtain the redshift evolution of the column density distributions. We summarize our major results as follows:

1. In the GGHM model, there are three processes that lead to high ionization state ions: photoionization and collisional ionization in the virialized halo; and a radiative cooling flow that forms around sufficiently massive galaxies. Colli-

sional ionization becomes dominant for a halo mass whose virial temperature corresponds to the excitation potential of a given ion.

2. Our model reproduces the Johnson et al. (2015) and Johnson et al. (2017) samples at $z \approx 0.2$, while underestimates the COS-Halos sample at the same redshift but with higher masses, which is discussed in QB18.

3. Observationally, the O VI column density distribution is modeled as a broken power law (Danforth et al., 2016). The power law at high column densities could be reproduced by the galaxies around the transition mass of O VI ($M_\star = 3 \times 10^9\ M_\odot$; see Fig. 8.6 and Fig. 8.11). Based on O VI observations, a typical gaseous galaxy halo has $T_{\rm max} = 2T_{\rm vir}$, $R_{\rm max} = 2R_{\rm vir}$ and $Z = 0.5Z_\odot$. The predicted column density distributions are shown in Fig. 8.13.

4. In our models, the differential column density distributions have turnovers at low column densities (Fig. 8.13), which is because gaseous halos have the non-zero lower limits of the column densities for all high ionization state ions. However, such turnovers are not observed for O VI and do not occur in simulations. Therefore, additional hosts are required to account for the gaps between our models and observations or simulations. We suggest that these additional contributions are from the cosmic filaments (IGM) and the intra-group/cluster medium. The non-galactic O VI systems are more likely to be associated with the IGM due to its low ionization potential, although the physical properties of IGM are still highly uncertain. Additional O VII, O VIII, Ne VIII, and Mg X could originate in galaxy groups or the outer parts of poor clusters, which contribute to the total column density distributions.

5. The extended radius model ($R_{\rm max} = 2R_{\rm vir}$; for low-mass galaxies) is favored by the both the absorption-galaxy pair sample and intervening column density distribution studies of O VI. This model may be in tension with the current

Ne VIII observation studies, although the column density distribution is still uncertain and requires more observations. Combining the O VI and Ne VIII column density distributions could give more constraints on the maximum radius of the gaseous halo.

6. The total O VI column density distribution is not sensitive to the temperature of the ambient gas, although the ambient temperature affects the O VI column densities in individual galactic gaseous halos. The detection rate of O VII and O VIII are raised by a factor of $0.3 - 0.5$ dex at the limiting column density of 10^{15} cm^{-2} (Fig. 8.7), which could be distinguished by future X-ray observations.

7. In GGHM models, the redshift evolution of the column density distribution is dominated by the cosmic SFR at high column densities, which is consistent with cosmological simulations and O VI observations (Danforth et al., 2016).

CHAPTER IX

Summary and Future Work

The understanding of the warm-hot circumgalactic (CGM) has been dramatically improved during the past decade. In this dissertation, I focused on the warm-hot CGM in both observation and physical modeling at low redshift $z \lesssim 1$, and provided a comprehensive picture of the warm-hot CGM and its co-evolution with the galaxy disk in three parts. The first part dealt with developing methods optimized for warm-hot CGM detection (i.e., weak and diffuse features). To detect the hot gas, I developed a new spectral reduction method that is sensitive to weak absorption features, which leads to the first detection of the Mg X intervening system (the hot phase in CGM; §2). In the local Universe, I also developed a model-dependent extraction method of large-scale SZ signals, which significantly improved the detected signals. This method makes it possible to study the SZ signal from the MW and the Local Group (LG) medium (i.e., the detection of the Local Hot Bridge; §3), which is the first detection of the hot LG medium.

The second part of this dissertation dealt with converting the observed 2-dimensional projected features (integral over sight line direction; e.g., SZ signals or column densities) to 3-dimensional physical properties directly, such as density distributions or velocities. By introducing the kinematical distance to the absorption line modeling, I found that the warm gas in the MW is co-rotating with the stellar disk (§5). This

method is currently only applied to the MW, but it also applicable to observations of external galaxies (and their CGM) with sufficient resolutions.

In the last part, I developed a semi-analytic model to study the relationship between the warm-hot CGM and the disk (§7 and §8). This model provides a self-consistent picture for disk-CGM co-evolution for a wide mass range of different galaxies – the star formation in the disk correlates with the radiative cooling in the CGM. Our model successfully reproduced the observed O VI column density dependence on the stellar mass down to $\log M_* \approx 8$ (private communications with Kirill Tchernyshyov and Jessica Werk; in preparation), while numerical simulations significantly underestimate O VI column densities for low-mass galaxies. Our results suggest that photoionization is crucial to understand warm-hot CGM in low-mass galaxies, which is currently poorly resolved in numerical simulations.

9.1 Significant Conclusions

The particular remarks of individual studies are summarized as:

- **The first detection of an intervening Mg X absorption system tracing the hot CGM near virial equilibrium at** $z \approx 1$. Specifically, I applied the Bayesian method to spectral data to characterize features in the UV spectra, which leads to the first (and the only) intervening Mg X absorption systems (§2). This method is sensitive to the hot CGM at $z \approx 1$, where other methods (e.g., detection of X-ray emission) cannot detect the hot gas at large radii. Therefore, our Mg X absorption detection make it possible to obtain a full coverage of warm-hot gas up to $\log T \approx 6.1$ in the CGM, together with intermediate ionization state ions (e.g., O IV, O V, and Ne VIII).

- **The discovery of the massive Local Hot Bridge between the MW and M31**. In §3, I developed a model-dependent extraction method to reproduce

the large-scale SZ features ($> 5°$), which includes the MW hot gas (both disk and CGM) and the intra-group medium of the Local Group. I applied this method to the archival *Planck* and *WMAP* data, and detected an SZ-bright diffuse source (radius $\approx 20°$) toward the M31 direction. The archival X-ray data also show an enhancement above the MW hot gas foreground. Combining X-ray and SZ observations, we suggested that it may be a hot bridge connecting the MW and M31, as a massive contributor ($\approx 10^{11}\ M_{\odot}$) to the Local Group baryon budget.

- **A comprehensive study of the warm gas distribution and kinematics in the MW revealing the feedback origin of the warm gas**. §4 and §5 are a series of papers to develop a comprehensive model of the warm gas in the MW. Previous efforts found there is a significant gap between the modeling of the stellar sightlines and the AGN sightlines (Zheng et al., 2019a). In §4, I solved this tension by introducing the radial profile of the warm gas disk and the north-south asymmetry for the gas distribution (i.e., above and below the disk middle, the gas distributions are different). This leads to a 2D disk and CGM model, where the total column density is reproduced by the warm gas spatial distribution. Based on this model, I concluded that the stellar and the AGN sightline samples are consistent with each other.

  This 2D disk and CGM model is further developed in §5 by including kinematics. With kinematics information, I modeled both the total column density and the line shape of the MW Si IV-bearing gas. This model provides a novel way to de-project the integral effect when viewing out from the MW disk. I found that the warm gas is co-rotating with the stellar disk within at least 20 kpc. The north-south asymmetry is also seen in kinematics as the northern sky has a net inflow of $0.6 M_{\odot}\mathrm{yr}^{-1}$. On top of the bulk velocity field (i.e., rotation and inflow), we found inflows and outflows with a physical size of 5 kpc, which suggested

the feedback origin (Galactic fountain) of the warm gas in the MW.

- **A unique case study of the interaction layer between the disk and the CGM of NGC891**. The cool-warm CGM of the NGC 891 was investigated in §6. With a unique sight line projected 5 kpc around the edge-on disk of NGC 891, I directly measured the column density of various ions close to the NGC 891 disk, and determine the metallicity of the gas. The depletion pattern of the warm gas is similar to the warm gas in the MW disk, indicating a disk-origin (and mixing) of the warm gas close to the disk. In the same sight line, I detected an HVC with a much lower metallicity than the majority gas, which could be a cloud accreted directly from the IGM. Therefore, the warm gas is ejected, accreted, and recycled around the disk, which is a crucial part of the baryonic cycle in galaxy evolution.

- **A semi-analytic model of the disk-CGM co-evolution to study the warm-hot CGM**. §7 and §8 describe an analytic model of the warm-hot CGM of star-forming galaxies. In §7, I described the basic assumptions and main results of the warm-hot CGM, while the cosmological implication of this model is introduced in §8. In this model, I assumed a static solution of disk-CGM co-evolution that the star formation rate in the disk is supplied by the net cooling accretion from the warm-hot CGM. The net cooling is a result of radiative cooling and the heating from feedback processes. Although this is a model without full prescriptions of all individual feedback processes, it reproduced observed column densities of O VI, Ne VIII, and Mg X at $z \lesssim 1$. According to some recent studies, this model is even better than most popular cosmological simulations like EAGLE and IllustrisTNG for low-mass galaxies (halo mass less than 10^{11} $M_{\odot}$; private communications with Kirill Tchernyshyov and Jessica Werk). By combining this warm-hot CGM model with the spatial distribution

of star-forming galaxies, I predicted the cosmic column density distribution associated with galaxies in §8. This column density distribution is consistent with the observed column density distribution at the high column density domain, which indicates that the warm-hot CGM is dominant contributor to the total warm-hot gas in the low-redshift Universe at $z \lesssim 1$.

9.2 Future Work

There are two direct followups of this dissertation work. First, the archival *HST* data also provides a large sample of another intermediate ionization state ion C IV, which has not been reduced and analyzed in the kinematical model framework. With excitation potential between Si IV and oxygen ions (O VI, O VII, and O VIII), C IV is of great importance to investigate the cooling from the hot gas to the cooler gas. The reduction and analyses of the C IV sample is in progress, where I will study its correlation with Si IV and higher ionization state ions. Second, I am still developing a better SZ extraction for the MW SZ signal to suppress the dust contamination. The MW signal is more contaminated by the foreground dust emission compared to the M31 direction, so one must be more careful to exclude the dust component. The SZ signal is complementary to the existing X-ray emission data, which can significantly improve the extraction of the hot gas distribution in the MW. Therefore, these followups will provide a more comprehensive understanding of the MW warm-gas as the most valuable case study to resolve the disk-CGM co-evolution.

The methods and models developed in the dissertation can benefit future observations and theories, which will be significantly improved in the coming decade. In observations, there are various on-going or in-planning missions aiming at observations of the warm-hot CGM. For example, Aspera (PI: Carlos Vargas; expected 2024; Vargas et al. 2021) was selected to detect O VI line emissions in the local Universe, and Hot Universe Baryon Surveyor (HUBS; PI: Wei Cui; expected 2030+; Cui et al.

2020) was planned for the X-ray emitting gas. These dedicated missions for the warm-hot CGM will provide high resolution data in both spatial and spectral spaces. Therefore, detailed modeling and analyses are needed for these coming missions as what we have done for the MW warm gas in §4 and §5. For the SZ signals, further improvements are expected by missions introducing more channels, such as the probe concept *PICO* with 21 channels (Hanany et al., 2019) or improving spatial resolution, such as CMB-S4 (Carlstrom et al., 2019). These missions make it possible to extend our diffuse SZ studies to high redshifts, which is complementary to future X-ray missions (e.g., HUBS). More general missions (e.g., Lynx, Athena, and JWST) will also contribute to the warm-hot CGM field. For example, JWST makes it possible to detect warm gas at high redshifts, which is crucial to study the cosmological evolution of the warm CGM. Although Lynx and Athena are not dedicated X-ray missions to the hot CGM, their can provide even higher spatial and spectral resolution observations than HUBS (but with low efficiency for diffuse features), which will be great for substructure detections in the CGM.

BIBLIOGRAPHY

BIBLIOGRAPHY

Anders, E., & Grevesse, N. 1989, *Geochim. Cosmochim. Acta*, 53, 197

Anderson, M. E., & Bregman, J. N. 2010, *ApJ*, 714, 320

Anderson, M. E., Bregman, J. N., & Dai, X. 2013, *ApJ*, 762, 106

Anderson, M. E., Churazov, E., & Bregman, J. N. 2016, *MNRAS*, 455, 227

Arav, N., Borguet, B., Chamberlain, C., Edmonds, D., & Danforth, C. 2013, *MNRAS*, 436, 3286

Armillotta, L., Fraternali, F., & Marinacci, F. 2016, *MNRAS*, 462, 4157

Armillotta, L., Fraternali, F., Werk, J. K., Prochaska, J. X., & Marinacci, F. 2017, *MNRAS*, 470, 114

Arnaud, M., Pratt, G. W., Piffaretti, R., et al. 2010, *A&A*, 517, A92

Arrigoni Battaia, F., Prochaska, J. X., Hennawi, J. F., et al. 2018, *MNRAS*, 473, 3907

Asplund, M., Grevesse, N., Sauval, A. J., & Scott, P. 2009, *ARA&A*, 47, 481

Baldi, A., Ettori, S., Molendi, S., & Gastaldello, F. 2012, *A&A*, 545, A41

Balogh, M. L., Schade, D., Morris, S. L., et al. 1998, *ApJ*, 504, L75

Banday, A. J., & Górski, K. M. 1996, *MNRAS*, 283, L21

Barcons, X., Barret, D., Decourchelle, A., et al. 2017, Astronomische Nachrichten, 338, 153

Barger, K. A., Haffner, L. M., Wakker, B. P., et al. 2012, *ApJ*, 761, 145

Behroozi, P., Becker, M., Bosch, F. C. v. d., et al. 2019, *BAAS*, 51, 125

Behroozi, P. S., Conroy, C., & Wechsler, R. H. 2010, *ApJ*, 717, 379

Behroozi, P. S., Wechsler, R. H., & Conroy, C. 2013, *ApJ*, 770, 57

Bell, E. F., McIntosh, D. H., Katz, N., & Weinberg, M. D. 2003, *ApJ*, 585, L117

Bennett, C. L., Larson, D., Weiland, J. L., et al. 2013, *ApJS*, 208, 20

Boettcher, E., Zweibel, E. G., Gallagher, III, J. S., & Benjamin, R. A. 2016, *ApJ*, 832, 118

Bogdán, Á., Bourdin, H., Forman, W. R., et al. 2017, *ApJ*, 850, 98

Bogdán, Á., Forman, W. R., Kraft, R. P., & Jones, C. 2013a, *ApJ*, 772, 98

Bogdán, Á., Forman, W. R., Vogelsberger, M., et al. 2013b, *ApJ*, 772, 97

Bogdán, Á., Vogelsberger, M., Kraft, R. P., et al. 2015, *ApJ*, 804, 72

Bordoloi, R., Wagner, A. Y., Heckman, T. M., & Norman, C. A. 2017a, *ApJ*, 848, 122

Bordoloi, R., Lilly, S. J., Knobel, C., et al. 2011, *ApJ*, 743, 10

Bordoloi, R., Tumlinson, J., Werk, J. K., et al. 2014, *ApJ*, 796, 136

Bordoloi, R., Fox, A. J., Lockman, F. J., et al. 2017b, *ApJ*, 834, 191

Boroson, B., Kim, D.-W., & Fabbiano, G. 2011, *ApJ*, 729, 12

Borthakur, S., Heckman, T., Strickland, D., Wild, V., & Schiminovich, D. 2013, *ApJ*, 768, 18

Borthakur, S., Heckman, T., Tumlinson, J., et al. 2015, *ApJ*, 813, 46

Bouma, S. J. D., Richter, P., & Fechner, C. 2019, *A&A*, 627, A20

Bovy, J., & Rix, H.-W. 2013, *ApJ*, 779, 115

Bowen, D. V., Chelouche, D., Jenkins, E. B., et al. 2016, *ApJ*, 826, 50

Bowen, D. V., Jenkins, E. B., Tripp, T. M., et al. 2008, *ApJS*, 176, 59

Bregman, J. N. 1980, *ApJ*, 236, 577

—. 2007, *ARA&A*, 45, 221

Bregman, J. N., Alves, G. C., Miller, M. J., & Hodges-Kluck, E. 2015, Journal of Astronomical Telescopes, Instruments, and Systems, 1, 045003

Bregman, J. N., Anderson, M. E., Miller, M. J., et al. 2018, *ApJ*, 862, 3

Bregman, J. N., & Lloyd-Davies, E. J. 2007, *ApJ*, 669, 990

Bregman, J. N., Miller, E. D., Seitzer, P., Cowley, C. R., & Miller, M. J. 2013, *ApJ*, 766, 57

Brown, B. A., & Bregman, J. N. 1998, *ApJ*, 495, L75

Bruhweiler, F. C., Kondo, Y., & McCluskey, G. E. 1980, *ApJ*, 237, 19

Brüns, C., Kerp, J., Staveley-Smith, L., et al. 2005, *A&A*, 432, 45

Bryans, P., Badnell, N. R., Gorczyca, T. W., et al. 2006, *ApJS*, 167, 343

Burchett, J. N., Tripp, T. M., Wang, Q. D., et al. 2018, *MNRAS*, 475, 2067

Burchett, J. N., Tripp, T. M., Prochaska, J. X., et al. 2015, *ApJ*, 815, 91

—. 2019, *ApJ*, 877, L20

Butsky, I. S., Fielding, D. B., Hayward, C. C., et al. 2020, *ApJ*, 903, 77

Cai, Z., Cantalupo, S., Prochaska, J. X., et al. 2019, *ApJS*, 245, 23

Cantalupo, S., Pezzulli, G., Lilly, S. J., et al. 2019, *MNRAS*, 483, 5188

Carlstrom, J., Abazajian, K., Addison, G., et al. 2019, in Bulletin of the American Astronomical Society, Vol. 51, 209

Cen, R., & Ostriker, J. P. 1999, *ApJ*, 514, 1

—. 2006, *ApJ*, 650, 560

Chen, H.-W., & Mulchaey, J. S. 2009, *ApJ*, 701, 1219

Chen, H.-W., Zahedy, F. S., Boettcher, E., et al. 2020a, arXiv e-prints, arXiv:2005.02408

Chen, Y., Steidel, C. C., Hummels, C. B., et al. 2020b, *MNRAS*, 499, 1721

Chen, Y., Steidel, C. C., Erb, D. K., et al. 2021, arXiv e-prints, arXiv:2104.10173

Condon, J. J., Cotton, W. D., Greisen, E. W., et al. 1998, *AJ*, 115, 1693

Cowie, L. L., Jenkins, E. B., Songaila, A., & York, D. G. 1979, *ApJ*, 232, 467

Cox, D. P. 2005, *ARA&A*, 43, 337

Cui, W., Bregman, J. N., Bruijn, M. P., et al. 2020, in Society of Photo-Optical Instrumentation Engineers (SPIE) Conference Series, Vol. 11444, Society of Photo-Optical Instrumentation Engineers (SPIE) Conference Series, 114442S

Dai, X., Bregman, J. N., Kochanek, C. S., & Rasia, E. 2010, *ApJ*, 719, 119

Danforth, C. W., Keeney, B. A., Stocke, J. T., Shull, J. M., & Yao, Y. 2010, *ApJ*, 720, 976

Danforth, C. W., & Shull, J. M. 2008, *ApJ*, 679, 194

Danforth, C. W., Keeney, B. A., Tilton, E. M., et al. 2016, *ApJ*, 817, 111

Darling, J., Macdonald, E. P., Haynes, M. P., & Giovanelli, R. 2011, *ApJ*, 742, 60

Davis, D. S., & White, III, R. E. 1996, *ApJ*, 470, L35

de Boer, K. S., & Savage, B. D. 1983, *ApJ*, 265, 210

de Kool, M., & de Jong, T. 1985, *A&A*, 149, 151

de Vaucouleurs, G., de Vaucouleurs, A., Corwin, Jr., H. G., et al. 1991, Third Reference Catalogue of Bright Galaxies. Volume I: Explanations and references. Volume II: Data for galaxies between 0^h and 12^h. Volume III: Data for galaxies between 12^h and 24^h.

Deason, A. J., Belokurov, V., & Sanders, J. L. 2019, *MNRAS*, 490, 3426

Del Zanna, G., Dere, K. P., Young, P. R., Landi, E., & Mason, H. E. 2015, *A&A*, 582, A56

Delabrouille, J., Cardoso, J. F., Le Jeune, M., et al. 2009, *A&A*, 493, 835

Delhaye, J. 1965, Solar Motion and Velocity Distribution of Common Stars (the University of Chicago Press), 61

Dickey, J. M., & Lockman, F. J. 1990, *ARA&A*, 28, 215

Einasto, J., & Lynden-Bell, D. 1982, *MNRAS*, 199, 67

Eriksen, H. K., Banday, A. J., Górski, K. M., & Lilje, P. B. 2004, *ApJ*, 612, 633

Fabian, A. C. 2012, *ARA&A*, 50, 455

Faerman, Y., Sternberg, A., & McKee, C. F. 2017, *ApJ*, 835, 52

—. 2020, *ApJ*, 893, 82

Falkendal, T., Lehnert, M. D., Vernet, J., De Breuck, C., & Wang, W. 2021, *A&A*, 645, A120

Fang, T., Buote, D., Bullock, J., & Ma, R. 2015, *ApJS*, 217, 21

Fang, T., Buote, D. A., Humphrey, P. J., et al. 2010, *ApJ*, 714, 1715

Farber, R., Ruszkowski, M., Yang, H. Y. K., & Zweibel, E. G. 2018, *ApJ*, 856, 112

Ferland, G. J., Korista, K. T., Verner, D. A., et al. 1998, *PASP*, 110, 761

Ferland, G. J., Porter, R. L., van Hoof, P. A. M., et al. 2013, RMxAA, 49, 137

Fielding, D., Quataert, E., Martizzi, D., & Faucher-Giguère, C.-A. 2017a, *MNRAS*, 470, L39

Fielding, D., Quataert, E., McCourt, M., & Thompson, T. A. 2017b, *MNRAS*, 466, 3810

Finkbeiner, D. P. 2003, *ApJS*, 146, 407

Finn, C. W., Morris, S. L., Crighton, N. H. M., et al. 2014, *MNRAS*, 440, 3317

Foreman-Mackey, D., Hogg, D. W., Lang, D., & Goodman, J. 2013, *PASP*, 125, 306

Foster, A. R., Ji, L., Smith, R. K., & Brickhouse, N. S. 2012, *ApJ*, 756, 128

Fox, A. J., Richter, P., Ashley, T., et al. 2019, *ApJ*, 884, 53

Fox, A. J., Savage, B. D., Wakker, B. P., et al. 2004, *ApJ*, 602, 738

Fox, A. J., Wakker, B. P., Savage, B. D., et al. 2005, *ApJ*, 630, 332

Fox, A. J., Wakker, B. P., Barger, K. A., et al. 2014, *ApJ*, 787, 147

Fox, A. J., Bordoloi, R., Savage, B. D., et al. 2015, *ApJ*, 799, L7

Fox, A. J., Lehner, N., Lockman, F. J., et al. 2016, *ApJ*, 816, L11

Fox, A. J., Barger, K. A., Wakker, B. P., et al. 2018, *ApJ*, 854, 142

Frank, S., Pieri, M. M., Mathur, S., Danforth, C. W., & Shull, J. M. 2018, *MNRAS*, 476, 1356

Fraternali, F. 2017, in Astrophysics and Space Science Library, Vol. 430, Gas Accretion onto Galaxies, ed. A. Fox & R. Davé, 323

Fukugita, M., & Peebles, P. J. E. 2006, *ApJ*, 639, 590

Fumagalli, M., O'Meara, J. M., & Prochaska, J. X. 2016, *MNRAS*, 455, 4100

Gaskin, J., Özel, F., & Vikhlinin, A. 2016, in *Proc. SPIE*, Vol. 9904, Space Telescopes and Instrumentation 2016: Optical, Infrared, and Millimeter Wave, 99040N

Gaspari, M., Temi, P., & Brighenti, F. 2017, *MNRAS*, 466, 677

Ghez, A. M., Salim, S., Weinberg, N. N., et al. 2008, *ApJ*, 689, 1044

Ginolfi, M., Maiolino, R., Nagao, T., et al. 2017, *MNRAS*, 468, 3468

Gnat, O. 2017, *ApJS*, 228, 11

Gnat, O., & Sternberg, A. 2007, *ApJS*, 168, 213

Gnat, O., Sternberg, A., & McKee, C. F. 2010, *ApJ*, 718, 1315

Goulding, A. D., Greene, J. E., Ma, C.-P., et al. 2016, *ApJ*, 826, 167

Green, J. C., Froning, C. S., Osterman, S., et al. 2012, *ApJ*, 744, 60

Grimes, J. P., Heckman, T., Aloisi, A., et al. 2009, *ApJS*, 181, 272

Guo, Y., Maiolino, R., Jiang, L., et al. 2020, *ApJ*, 898, 26

Gupta, A., Mathur, S., Krongold, Y., Nicastro, F., & Galeazzi, M. 2012, *ApJ*, 756, L8

Haardt, F., & Madau, P. 1996, *ApJ*, 461, 20

—. 2012, *ApJ*, 746, 125

Haffner, L. M., Reynolds, R. J., & Tufte, S. L. 2001, *ApJ*, 556, L33

Hanany, S., Alvarez, M., Artis, E., et al. 2019, in Bulletin of the American Astronomical Society, Vol. 51, 194

Henley, D., & Shelton, R. 2012, *ApJS*, 202, 14

Henley, D. B., & Shelton, R. L. 2013, *ApJ*, 773, 92

Hewett, P. C., Foltz, C. B., & Chaffee, F. H. 1995, *AJ*, 109, 1498

Hewett, P. C., & Wild, V. 2010, *MNRAS*, 405, 2302

Hilton, M., Sifón, C., Naess, S., et al. 2021, *ApJS*, 253, 3

Ho, S. H., Martin, C. L., Kacprzak, G. G., & Churchill, C. W. 2017, *ApJ*, 835, 267

Hodges-Kluck, E., & Bregman, J. N. 2014, *ApJ*, 789, 131

Hodges-Kluck, E., Cafmeyer, J., & Bregman, J. N. 2016a, *ApJ*, 833, 58

Hodges-Kluck, E. J., & Bregman, J. N. 2013, *ApJ*, 762, 12

Hodges-Kluck, E. J., Bregman, J. N., & Li, J.-T. 2017, in AAS/High Energy Astrophysics Division, Vol. 16, AAS/High Energy Astrophysics Division #16, 107.06

Hodges-Kluck, E. J., Bregman, J. N., & Li, J.-t. 2018, *ApJ*, 866, 126

Hodges-Kluck, E. J., Miller, M. J., & Bregman, J. N. 2016b, *ApJ*, 822, 21

Hopkins, P. F., Kereš, D., Oñorbe, J., et al. 2014, *MNRAS*, 445, 581

Howk, J. C., & Savage, B. D. 2000, *AJ*, 119, 644

Howk, J. C., Savage, B. D., Sembach, K. R., & Hoopes, C. G. 2002, *ApJ*, 572, 264

Huang, Y., Liu, X. W., Yuan, H. B., et al. 2016, *MNRAS*, 463, 2623

Hummels, C. B., Smith, B. D., Hopkins, P. F., et al. 2019, *ApJ*, 882, 156

Hussain, T., Khaire, V., Srianand, R., Muzahid, S., & Pathak, A. 2017, *MNRAS*, 466, 3133

Hussain, T., Muzahid, S., Narayanan, A., et al. 2015, *MNRAS*, 446, 2444

Jenkins, E. B. 1978, *ApJ*, 219, 845

Ji, S., Oh, S. P., & Masterson, P. 2019a, *MNRAS*, 487, 737

Ji, S., Chan, T. K., Hummels, C. B., et al. 2019b, arXiv e-prints, arXiv:1909.00003

Johnson, S. D., Chen, H.-W., & Mulchaey, J. S. 2015, *MNRAS*, 449, 3263

Johnson, S. D., Chen, H.-W., Mulchaey, J. S., Schaye, J., & Straka, L. A. 2017, *ApJ*, 850, L10

Joung, M. R., Putman, M. E., Bryan, G. L., Fernández, X., & Peek, J. E. G. 2012, *ApJ*, 759, 137

Kaaret, P., Koutroumpa, D., Kuntz, K. D., et al. 2020, Nature Astronomy, 4, 1072

Kafle, P. R., Sharma, S., Lewis, G. F., Robotham, A. S. G., & Driver, S. P. 2018, *MNRAS*, 475, 4043

Kalberla, P. M. W., Burton, W. B., Hartmann, D., et al. 2005, *A&A*, 440, 775

Kalberla, P. M. W., & Dedes, L. 2008, *A&A*, 487, 951

Karim, M. T., Fox, A. J., Jenkins, E. B., et al. 2018, *ApJ*, 860, 98

Karwin, C. M., Murgia, S., Campbell, S., & Moskalenko, I. V. 2019, *ApJ*, 880, 95

Karwin, C. M., Murgia, S., Moskalenko, I. V., et al. 2021, *Phys. Rev. D*, 103, 023027

Kaufmann, T., Bullock, J. S., Maller, A. H., Fang, T., & Wadsley, J. 2009, *MNRAS*, 396, 191

Keeney, B. A., Danforth, C. W., Stocke, J. T., France, K., & Green, J. C. 2012, *PASP*, 124, 830

Keeney, B. A., Stocke, J. T., Danforth, C. W., et al. 2017, *ApJS*, 230, 6

Kereš, D., Katz, N., Davé, R., Fardal, M., & Weinberg, D. H. 2009, *MNRAS*, 396, 2332

Kereš, D., Katz, N., Weinberg, D. H., & Davé, R. 2005, *MNRAS*, 363, 2

Khaire, V., & Srianand, R. 2015, *MNRAS*, 451, L30

Kim, C.-G., & Ostriker, E. 2018, *ApJ*, 853, 173

Kovács, O. E., Bogdán, Á., Smith, R. K., Kraft, R. P., & Forman, W. R. 2019, *ApJ*, 872, 83

Kravtsov, A. V., Vikhlinin, A. A., & Meshcheryakov, A. V. 2018, Astronomy Letters, 44, 8

Kwak, K., & Shelton, R. L. 2010, *ApJ*, 719, 523

Kwak, K., Shelton, R. L., & Henley, D. B. 2015, *ApJ*, 812, 111

Lallement, R., Welsh, B. Y., Vergely, J. L., Crifo, F., & Sfeir, D. 2003, *A&A*, 411, 447

Lan, T.-W., & Mo, H. 2018, *ApJ*, 866, 36

Larson, R. B. 1981, *MNRAS*, 194, 809

Larson, R. B. 1994, in Lecture Notes in Physics, Berlin Springer Verlag, Vol. 439, The Structure and Content of Molecular Clouds, ed. T. L. Wilson & K. J. Johnston, 13

Lehner, N., & Howk, J. C. 2011, Science, 334, 955

Lehner, N., Howk, J. C., Thom, C., et al. 2012, *MNRAS*, 424, 2896

Lehner, N., Howk, J. C., & Wakker, B. P. 2015, *ApJ*, 804, 79

Lehner, N., Jenkins, E. B., Gry, C., et al. 2003, *ApJ*, 595, 858

Lehner, N., Zech, W. F., Howk, J. C., & Savage, B. D. 2011, *ApJ*, 727, 46

Lehner, N., Howk, J. C., Tripp, T. M., et al. 2013, *ApJ*, 770, 138

Lehner, N., Berek, S. C., Howk, J. C., et al. 2020, *ApJ*, 900, 9

Leroy, A. K., Walter, F., Brinks, E., et al. 2008, *AJ*, 136, 2782

Leroy, A. K., Walter, F., Martini, P., et al. 2015, *ApJ*, 814, 83

Li, J.-T., Bregman, J. N., Wang, Q. D., Crain, R. A., & Anderson, M. E. 2016, *ApJ*, 830, 134

—. 2018a, *ApJ*, 855, L24

Li, J.-T., Bregman, J. N., Wang, Q. D., et al. 2017a, *ApJS*, 233, 20

Li, J.-T., Crain, R. A., & Wang, Q. D. 2014, *MNRAS*, 440, 859

Li, J.-T., Hodges-Kluck, E., Stein, Y., et al. 2019, The Astrophysical Journal, 873, 27

Li, J.-T., & Wang, Q. D. 2013, *MNRAS*, 428, 2085

Li, J.-T., Ballet, J., Miceli, M., et al. 2018b, *ApJ*, 864, 85

Li, M., & Bryan, G. L. 2020, *ApJ*, 890, L30

Li, M., Bryan, G. L., & Ostriker, J. P. 2017b, *ApJ*, 841, 101

Li, M., & Tonnesen, S. 2020, *ApJ*, 898, 148

Li, Y., & Bregman, J. 2017, *ApJ*, 849, 105

Li, Y., Bryan, G. L., Ruszkowski, M., et al. 2015, *ApJ*, 811, 73

Li, Y.-S., & White, S. D. M. 2008, *MNRAS*, 384, 1459

Liang, C. J., & Remming, I. 2020, *MNRAS*, 491, 5056

Licquia, T. C., & Newman, J. A. 2015, *ApJ*, 806, 96

Lilly, S. J., Carollo, C. M., Pipino, A., Renzini, A., & Peng, Y. 2013, *ApJ*, 772, 119

Lim, S. H., Mo, H. J., Li, R., et al. 2018, *ApJ*, 854, 181

Lim, S. H., Mo, H. J., Lu, Y., Wang, H., & Yang, X. 2017, *MNRAS*, 470, 2982

Liu, R.-Y., Yan, H., Wang, X.-Y., Shao, S., & Li, H. 2019, *ApJ*, 871, 40

Lockman, F. J., Di Teodoro, E. M., & McClure-Griffiths, N. M. 2020, *ApJ*, 888, 51

Luo, Y., Fang, T., & Ma, R. 2018, *ApJS*, 235, 28

Luo, Y., Heckman, T., Hwang, H.-C., et al. 2021, *ApJ*, 908, 183

Madau, P., & Dickinson, M. 2014, *ARA&A*, 52, 415

Mapelli, M., Moore, B., & Bland-Hawthorn, J. 2008, *MNRAS*, 388, 697

Marasco, A., & Fraternali, F. 2011, *A&A*, 525, A134

Marinacci, F., Binney, J., Fraternali, F., et al. 2010, *MNRAS*, 404, 1464

Marinacci, F., Pakmor, R., Springel, V., & Simpson, C. M. 2014, *MNRAS*, 442, 3745

Martin, A. M., Papastergis, E., Giovanelli, R., et al. 2010, *ApJ*, 723, 1359

Martin, D. C., O'Sullivan, D., Matuszewski, M., et al. 2019, Nature Astronomy, 3, 822

Martizzi, D., Vogelsberger, M., Artale, M. C., et al. 2019, *MNRAS*, 486, 3766

Mateo, M. L. 1998, *ARA&A*, 36, 435

McGaugh, S. S., & Schombert, J. M. 2015, *ApJ*, 802, 18

McGaugh, S. S., Schombert, J. M., de Blok, W. J. G., & Zagursky, M. J. 2010, *ApJ*, 708, L14

McQuinn, M., & Werk, J. K. 2018, *ApJ*, 852, 33

Meiring, J. D., Tripp, T. M., Werk, J. K., et al. 2013, *ApJ*, 767, 49

Melso, N., Bryan, G. L., & Li, M. 2019, *ApJ*, 872, 47

Ménard, B., Scranton, R., Fukugita, M., & Richards, G. 2010, *MNRAS*, 405, 1025

Miller, M., & Bregman, J. 2015, *ApJ*, 800, 14

Miller, M. J., & Bregman, J. N. 2013, *ApJ*, 770, 118

—. 2016, *ApJ*, 829, 9

Miller, M. J., Hodges-Kluck, E. J., & Bregman, J. N. 2016, *ApJ*, 818, 112

Misawa, T., Charlton, J. C., Eracleous, M., et al. 2007, *ApJS*, 171, 1

Mitra, S., Ferrara, A., & Choudhury, T. R. 2013, *MNRAS*, 428, L1

Mo, H., van den Bosch, F. C., & White, S. 2010, Galaxy Formation and Evolution (Cambridge: Cambridge Univ. Press)

Morselli, L., Renzini, A., Popesso, P., & Erfanianfar, G. 2016, *MNRAS*, 462, 2355

Mulchaey, J. S. 2000, *ARA&A*, 38, 289

Mulchaey, J. S., & Chen, H.-W. 2009, *ApJ*, 698, L46

Muratov, A. L., Kereš, D., Faucher-Giguère, C.-A., et al. 2015, *MNRAS*, 454, 2691

Murray, N., Ménard, B., & Thompson, T. A. 2011, *ApJ*, 735, 66

Muzahid, S., Kacprzak, G. G., Charlton, J. C., & Churchill, C. W. 2016a, *ApJ*, 823, 66

Muzahid, S., Srianand, R., Arav, N., Savage, B. D., & Narayanan, A. 2013, *MNRAS*, 431, 2885

Muzahid, S., Srianand, R., Bergeron, J., & Petitjean, P. 2012a, *MNRAS*, 421, 446

Muzahid, S., Srianand, R., & Charlton, J. 2015, *MNRAS*, 448, 2840

Muzahid, S., Srianand, R., Charlton, J., & Eracleous, M. 2016b, *MNRAS*, 457, 2665

Muzahid, S., Srianand, R., Savage, B. D., et al. 2012b, *MNRAS*, 424, L59

Myers, P. C., Dame, T. M., Thaddeus, P., et al. 1986, *ApJ*, 301, 398

Nakanishi, H., & Sofue, Y. 2016, *PASJ*, 68, 5

Nakashima, S., Inoue, Y., Yamasaki, N., et al. 2018, *ApJ*, 862, 34

Narayanan, A., Savage, B. D., & Wakker, B. P. 2012, *ApJ*, 752, 65

Narayanan, A., Savage, B. D., Wakker, B. P., et al. 2011, *ApJ*, 730, 15

Nelson, D., Vogelsberger, M., Genel, S., et al. 2013, *MNRAS*, 429, 3353

Nelson, D., Kauffmann, G., Pillepich, A., et al. 2018, *MNRAS*, 477, 450

Nevalainen, J., Wakker, B., Kaastra, J., et al. 2017, *A&A*, 605, A47

Nicastro, F., Senatore, F., Gupta, A., et al. 2016a, *MNRAS*, 457, 676

—. 2016b, *MNRAS*, 458, L123

Nicastro, F., Zezas, A., Drake, J., et al. 2002, *ApJ*, 573, 157

Nicastro, F., Kaastra, J., Krongold, Y., et al. 2018, *Nature*, 558, 406

Nuza, S. E., Parisi, F., Scannapieco, C., et al. 2014, *MNRAS*, 441, 2593

Oosterloo, T., Fraternali, F., & Sancisi, R. 2007, *AJ*, 134, 1019

Oppenheimer, B. D., & Schaye, J. 2013, *MNRAS*, 434, 1043

Oppenheimer, B. D., Segers, M., Schaye, J., Richings, A. J., & Crain, R. A. 2018, *MNRAS*, 474, 4740

Oppenheimer, B. D., Crain, R. A., Schaye, J., et al. 2016, *MNRAS*, 460, 2157

Osmond, J. P. F., & Ponman, T. J. 2004, *MNRAS*, 350, 1511

O'Sullivan, D. B., Martin, C., Matuszewski, M., et al. 2020, *ApJ*, 894, 3

O'Sullivan, E., Vrtilek, J. M., David, L. P., et al. 2014, *ApJ*, 793, 74

Pachat, S., Narayanan, A., Khaire, V., et al. 2017, *MNRAS*, 471, 792

Pannella, M., Carilli, C. L., Daddi, E., et al. 2009, *ApJ*, 698, L116

Peeples, M., Tumlinson, J., Fox, A., et al. 2017, The HSLA, Tech. rep., STScI

Peeples, M. S., Werk, J. K., Tumlinson, J., et al. 2014, *ApJ*, 786, 54

Peeples, M. S., Corlies, L., Tumlinson, J., et al. 2019, *ApJ*, 873, 129

Péroux, C., & Howk, J. C. 2020, *ARA&A*, 58, 363

Piffaretti, R., Arnaud, M., Pratt, G. W., Pointecouteau, E., & Melin, J. B. 2011, *A&A*, 534, A109

Pildis, R. A., & McGaugh, S. S. 1996, *ApJ*, 470, L77

Pillepich, A., Nelson, D., Hernquist, L., et al. 2018, *MNRAS*, 475, 648

Planck Collaboration, Ade, P. A. R., Aghanim, N., et al. 2013, *A&A*, 550, A131

—. 2016a, *A&A*, 594, A13

—. 2016b, *A&A*, 594, A26

—. 2016c, *A&A*, 596, A101

Planck Collaboration, Aghanim, N., Akrami, Y., et al. 2018, *A&A*, 617, A48

—. 2020, *A&A*, 641, A1

Popescu, C. C., Tuffs, R. J., Kylafis, N. D., & Madore, B. F. 2004, *A&A*, 414, 45

Prasad, D., Voit, G. M., O'Shea, B. W., & Glines, F. 2020, *ApJ*, 905, 50

Pratt, C. T., & Bregman, J. N. 2020, *ApJ*, 890, 156

Pratt, C. T., Qu, Z., & Bregman, J. N. 2021, arXiv e-prints, arXiv:2105.01123

Predehl, P., Sunyaev, R. A., Becker, W., et al. 2020, *Nature*, 588, 227

Prochaska, J. X., Werk, J. K., Worseck, G., et al. 2017, *ApJ*, 837, 169

Putman, M. E., Peek, J. E. G., & Joung, M. R. 2012, *ARA&A*, 50, 491

Qu, Z., & Bregman, J. N. 2016, *ApJ*, 832, 189

—. 2018a, *ApJ*, 862, 23

—. 2018b, *ApJ*, 856, 5

—. 2019, *ApJ*, 880, 89

Qu, Z., Bregman, J. N., Hodges-Kluck, E., Li, J.-T., & Lindley, R. 2020, *ApJ*, 894, 142

Qu, Z., Bregman, J. N., & Hodges-Kluck, E. J. 2019, *ApJ*, 876, 101

Qu, Z., Huang, R., Bregman, J. N., & Li, J.-T. 2021, *ApJ*, 907, 14

Rahmati, A., Schaye, J., Crain, R. A., et al. 2016, *MNRAS*, 459, 310

Rand, R. J. 1997, *ApJ*, 474, 129

Rand, R. J., Wood, K., & Benjamin, R. A. 2008, *ApJ*, 680, 263

Rasmussen, A., Kahn, S. M., & Paerels, F. 2003, in Astrophysics and Space Science Library, Vol. 281, The IGM/Galaxy Connection. The Distribution of Baryons at z=0, ed. J. L. Rosenberg & M. E. Putman, 109

Rasmussen, J., & Pedersen, K. 2001, *ApJ*, 559, 892

Read, A. M., Ponman, T. J., & Strickland, D. K. 1997, *MNRAS*, 286, 626

Renzini, A., & Peng, Y.-j. 2015, *ApJ*, 801, L29

Rephaeli, Y. 1995, *ARA&A*, 33, 541

Richter, P. 2012, *ApJ*, 750, 165

Richter, P. 2017, in Astrophysics and Space Science Library, Vol. 430, Gas Accretion onto Galaxies, ed. A. Fox & R. Davé, 15

Richter, P., Nuza, S. E., Fox, A. J., et al. 2017, *A&A*, 607, A48

Riess, A. G., Fliri, J., & Valls-Gabaud, D. 2012, *ApJ*, 745, 156

Robitaille, T. P., & Whitney, B. A. 2010, *ApJ*, 710, L11

Roman-Duval, J., Jenkins, E. B., Williams, B., et al. 2019, *ApJ*, 871, 151

Rubin, D., & Loeb, A. 2014, JCAP, 2014, 051

Rubin, K., & MaNGA Team. 2016, in American Astronomical Society Meeting Abstracts, Vol. 227, American Astronomical Society Meeting Abstracts #227, 312.10

Rubin, K. H. R., Diamond-Stanic, A. M., Coil, A. L., Crighton, N. H. M., & Stewart, K. R. 2018, *ApJ*, 868, 142

Ryu, D., Kang, H., Hallman, E., & Jones, T. W. 2003, *ApJ*, 593, 599

Sancisi, R., Fraternali, F., Oosterloo, T., & van der Hulst, T. 2008, *A&A Rev.*, 15, 189

Savage, B. D., & de Boer, K. S. 1981, *ApJ*, 243, 460

Savage, B. D., Kim, T.-S., Wakker, B. P., et al. 2014, *ApJS*, 212, 8

Savage, B. D., Lehner, N., & Narayanan, A. 2011a, *ApJ*, 743, 180

Savage, B. D., Lehner, N., Wakker, B. P., Sembach, K. R., & Tripp, T. M. 2005, *ApJ*, 626, 776

Savage, B. D., Meade, M. R., & Sembach, K. R. 2001, *ApJS*, 136, 631

Savage, B. D., Narayanan, A., Lehner, N., & Wakker, B. P. 2011b, *ApJ*, 731, 14

Savage, B. D., & Sembach, K. R. 1991, *ApJ*, 379, 245

—. 1996, *ARA&A*, 34, 279

Savage, B. D., Sembach, K. R., & Lu, L. 1997, *AJ*, 113, 2158

Savage, B. D., & Wakker, B. P. 2009, *ApJ*, 702, 1472

Savage, B. D., Sembach, K. R., Wakker, B. P., et al. 2003, *ApJS*, 146, 125

Savage, B. D., Kim, T.-S., Fox, A. J., et al. 2017, *ApJS*, 232, 25

Scannapieco, C., Tissera, P. B., White, S. D. M., & Springel, V. 2008, *MNRAS*, 389, 1137

Scannapieco, E., & Brüggen, M. 2015, *ApJ*, 805, 158

Scargle, J. D. 1998, *ApJ*, 504, 405

Scargle, J. D., Norris, J. P., Jackson, B., & Chiang, J. 2013, *ApJ*, 764, 167

Schaller, M., Frenk, C. S., Bower, R. G., et al. 2015, *MNRAS*, 451, 1247

Schaye, J., Crain, R. A., Bower, R. G., et al. 2015, *MNRAS*, 446, 521

Schulz, E. 2014, *ApJ*, 790, 76

Sembach, K. R., & Savage, B. D. 1992, *ApJS*, 83, 147

—. 1996, *ApJ*, 457, 211

Sembach, K. R., Savage, B. D., & Jenkins, E. B. 1994, *ApJ*, 421, 585

Sembach, K. R., Savage, B. D., & Tripp, T. M. 1997, *ApJ*, 480, 216

Sembach, K. R., Wakker, B. P., Savage, B. D., et al. 2003, *ApJS*, 146, 165

Shapiro, P. R., & Field, G. B. 1976, *ApJ*, 205, 762

Shelton, R. L., & Kwak, K. 2018, *ApJ*, 866, 34

Shull, J. M., & Danforth, C. W. 2019, *ApJ*, 882, 180

Shull, J. M., Jones, J. R., Danforth, C. W., & Collins, J. A. 2009, *ApJ*, 699, 754

Shull, J. M., & Slavin, J. D. 1994, *ApJ*, 427, 784

Sidher, S. D., Sumner, T. J., & Quenby, J. J. 1999, *A&A*, 344, 333

Simcoe, R. A., Onoue, M., Eilers, A.-C., et al. 2020, arXiv e-prints, arXiv:2011.10582

Smith, M. W. L., Eales, S. A., De Looze, I., et al. 2016a, *MNRAS*, 462, 331

Smith, R. K., Brickhouse, N. S., Liedahl, D. A., & Raymond, J. C. 2001, *ApJ*, 556, L91

Smith, R. K., Abraham, M. H., Allured, R., et al. 2016b, in *Proc. SPIE*, Vol. 9905, Space Telescopes and Instrumentation 2016: Ultraviolet to Gamma Ray, 99054M

Snowden, S. L., Egger, R., Freyberg, M. J., et al. 1997, *ApJ*, 485, 125

Sokołowska, A., Babul, A., Mayer, L., Shen, S., & Madau, P. 2018, *ApJ*, 867, 73

Srianand, R., Petitjean, P., Ledoux, C., Ferland, G., & Shaw, G. 2005, *MNRAS*, 362, 549

Stern, J., Faucher-Giguère, C.-A., Hennawi, J. F., et al. 2018, *ApJ*, 865, 91

Stern, J., Fielding, D., Faucher-Giguère, C.-A., & Quataert, E. 2019, *MNRAS*, 488, 2549

Stern, J., Hennawi, J. F., Prochaska, J. X., & Werk, J. K. 2016, *ApJ*, 830, 87

Stevans, M. L., Shull, J. M., Danforth, C. W., & Tilton, E. M. 2014, *ApJ*, 794, 75

Stocke, J. T., Keeney, B. A., Danforth, C. W., et al. 2017, *ApJ*, 838, 37

—. 2013, *ApJ*, 763, 148

—. 2014, *ApJ*, 791, 128

Strickland, D. K., Heckman, T. M., Colbert, E. J. M., Hoopes, C. G., & Weaver, K. A. 2004, *ApJS*, 151, 193

Su, M., Slatyer, T. R., & Finkbeiner, D. P. 2010, *ApJ*, 724, 1044

Sulentic, J. W., Marziani, P., & Dultzin-Hacyan, D. 2000, *ARA&A*, 38, 521

Suresh, J., Rubin, K. H. R., Kannan, R., et al. 2017, *MNRAS*, 465, 2966

Suto, Y., Makishima, K., Ishisaki, Y., & Ogasaka, Y. 1996, *ApJ*, 461, L33

Tamm, A., Tempel, E., Tenjes, P., Tihhonova, O., & Tuvikene, T. 2012, *A&A*, 546, A4

Telfer, R. C., Zheng, W., Kriss, G. A., & Davidsen, A. F. 2002, *ApJ*, 565, 773

Teng, S. H., Veilleux, S., & Baker, A. J. 2013, *ApJ*, 765, 95

Tepper-García, T., Richter, P., & Schaye, J. 2013, *MNRAS*, 436, 2063

Thom, C., & Chen, H.-W. 2008a, *ApJS*, 179, 37

—. 2008b, *ApJ*, 683, 22

Thompson, T. A., Quataert, E., Zhang, D., & Weinberg, D. H. 2016, *MNRAS*, 455, 1830

Tomczak, A. R., Quadri, R. F., Tran, K.-V. H., et al. 2014, *ApJ*, 783, 85

Travascio, A., Zappacosta, L., Cantalupo, S., et al. 2020, *A&A*, 635, A157

Trentham, N., & Tully, R. B. 2009, *MNRAS*, 398, 722

Tripp, T. M., Sembach, K. R., Bowen, D. V., et al. 2008, *ApJS*, 177, 39

Tripp, T. M., Meiring, J. D., Prochaska, J. X., et al. 2011, Science, 334, 952

Tully, R. B., Pomarède, D., Graziani, R., et al. 2019, *ApJ*, 880, 24

Tully, R. B., Courtois, H. M., Dolphin, A. E., et al. 2013, *AJ*, 146, 86

Tumlinson, J., Peeples, M. S., & Werk, J. K. 2017, *ARA&A*, 55, 389

Tumlinson, J., Thom, C., Werk, J. K., et al. 2011, Science, 334, 948

—. 2013, *ApJ*, 777, 59

Vargas, C. J., Hamden, E., & Chung, H. 2021, in American Astronomical Society Meeting Abstracts, Vol. 53, American Astronomical Society Meeting Abstracts, 215.04

Veilleux, S., Cecil, G., & Bland-Hawthorn, J. 2005, *ARA&A*, 43, 769

Verner, D. A., Tytler, D., & Barthel, P. D. 1994, *ApJ*, 430, 186

Vogelsberger, M., Genel, S., Springel, V., et al. 2014, *MNRAS*, 444, 1518

Voges, W., Aschenbach, B., Boller, T., et al. 1999, *A&A*, 349, 389

Voit, G. M., Donahue, M., Zahedy, F., et al. 2019, *ApJ*, 879, L1

Voit, G. M., Bryan, G. L., Prasad, D., et al. 2020, *ApJ*, 899, 70

Wakker, B. P. 1991, *A&A*, 250, 499

—. 2001, *ApJS*, 136, 463

Wakker, B. P. 2004, in Astrophysics and Space Science Library, Vol. 312, High Velocity Clouds, ed. H. van Woerden, B. P. Wakker, U. J. Schwarz, & K. S. de Boer (Springer, Dordrecht), 25

Wakker, B. P., Hernandez, A. K., French, D. M., et al. 2015, *ApJ*, 814, 40

Wakker, B. P., Savage, B. D., Fox, A. J., Benjamin, R. A., & Shapiro, P. R. 2012, *ApJ*, 749, 157

Wakker, B. P., York, D. G., Wilhelm, R., et al. 2008, *ApJ*, 672, 298

Wakker, B. P., Savage, B. D., Sembach, K. R., et al. 2003, *ApJS*, 146, 1

Wang, Q. D., Yao, Y., Tripp, T. M., et al. 2005, *ApJ*, 635, 386

Weinberg, D. H., Miralda-Escudé, J., Hernquist, L., & Katz, N. 1997, *ApJ*, 490, 564

Werk, J. K., Prochaska, J. X., Thom, C., et al. 2012, *ApJS*, 198, 3

—. 2013, *ApJS*, 204, 17

Werk, J. K., Prochaska, J. X., Tumlinson, J., et al. 2014, *ApJ*, 792, 8

Werk, J. K., Prochaska, J. X., Cantalupo, S., et al. 2016, *ApJ*, 833, 54

Werk, J. K., Rubin, K. H. R., Bish, H. V., et al. 2019, *ApJ*, 887, 89

White, S. D. M., & Frenk, C. S. 1991, *ApJ*, 379, 52

White, S. D. M., & Rees, M. J. 1978, *MNRAS*, 183, 341

Wiersma, R. P. C., Schaye, J., & Smith, B. D. 2009, *MNRAS*, 393, 99

Wijers, N. A., Schaye, J., & Oppenheimer, B. D. 2020, arXiv e-prints, arXiv:2004.05171

Willson, L. A. 2000, *ARA&A*, 38, 573

Wotta, C. B., Lehner, N., Howk, J. C., O'Meara, J. M., & Prochaska, J. X. 2016, *ApJ*, 831, 95

Xue, X. X., Rix, H. W., Zhao, G., et al. 2008, *ApJ*, 684, 1143

Yoon, J. H., & Putman, M. E. 2017, *ApJ*, 839, 117

Yoon, J. H., Putman, M. E., Thom, C., Chen, H.-W., & Bryan, G. L. 2012, *ApJ*, 754, 84

Yu, X., Li, J.-T., Qu, Z., et al. 2021, *MNRAS*, 505, 4444

Zahedy, F. S., Chen, H.-W., Johnson, S. D., et al. 2019, *MNRAS*, 484, 2257

Zahedy, F. S., Chen, H.-W., Rauch, M., Wilson, M. L., & Zabludoff, A. 2016, *MNRAS*, 458, 2423

Zaritsky, D., Kennicutt, Jr., R. C., & Huchra, J. P. 1994, *ApJ*, 420, 87

Zhang, B., Zhu, M., Wu, Z.-Z., et al. 2021a, *MNRAS*, 503, 5385

Zhang, Y., Liu, R.-Y., Li, H., et al. 2021b, *ApJ*, 911, 58

Zheng, Y., Emerick, A., Putman, M. E., et al. 2020, *ApJ*, 905, 133

Zheng, Y., Peek, J. E. G., Putman, M. E., & Werk, J. K. 2019a, *ApJ*, 871, 35

Zheng, Y., Peek, J. E. G., Werk, J. K., & Putman, M. E. 2017, *ApJ*, 834, 179

Zheng, Y., Putman, M. E., Peek, J. E. G., & Joung, M. R. 2015, *ApJ*, 807, 103

Zheng, Y., Putman, M. E., Emerick, A., et al. 2019b, *MNRAS*, 490, 467

Zsargó, J., Sembach, K. R., Howk, J. C., & Savage, B. D. 2003, *ApJ*, 586, 1019